Modelling and Simulation of Turbulence in Unsteady Separated and Suddenly-Expanded Flows

By

Konstantinos Karantonis

A thesis submitted to the Cranfield University
In Partial Fulfillment of the Requirements
for the Degree of
Doctor of Philosophy

Cranfield University
Department of Aerospace Sciences
Cranfield, UK
July 2012

Typeset in LaTeX 2ε.

Except where acknowledged in the customary manner, the material presented in this thesis is, to the best of my knowledge, original and has not been submitted in whole or part for a degree in any university.

Konstantinos Karantonis

Modelling and Simulation of Turbulence in Unsteady Separated and Suddenly-Expanded Flows

Konstantinos Karantonis

July 4, 2012

CRANFIELD UNIVERSITY

SCHOOL OF ENGINEERING

PH.D. THESIS

ACADEMIC YEAR: 2007-2011

KONSTANTINOS KARANTONIS

MODELLING AND SIMULATION OF TURBULENCE IN UNSTEADY SEPARATED AND SUDDENLY-EXPANDED FLOWS

SUPERVISORS:
PROF. DIMITRIS DRIKAKIS & DR. BEN THORNBER

Abstract

The scope of this PhD thesis is the simulation of turbulence in time-dependent, separated and suddenly-expanded channel flows. High-resolution and very high-order numerical methods have been employed in the framework of Implicit Large Eddy Simulation (ILES) to elucidate open questions about the physics in flows with sudden expansion.

It is well known that the planar sudden expansion (PSE), despite its simple and symmetric geometry it produces a very complex behaviour and a distinctly asymmetric flow pattern ascribed mainly to the Coanda effect. Such flows are encountered in a wide range of practical engineering applications, such as combustion, hydraulic and fluidic devices, air ducts, and mixing equipments. It is of great importance, therefore, to understand the mechanisms that dominate flows with separation and reattachment of the shear layers, as well as flows with regions of strong reversed motion.

This thesis has for the first time analysed in detail the turbulent kinetic energy budget (TKEB) for the PSE. This analysis has been extended to examine the influence of Mach number on each individual component of the TKEB. The resulting data can be used as reference for further development of turbulence models capable of accurately resolving the flow behaviour in suddenly-expanded flows.

A comprehensive study is carried out with aim at clarifying to what extent can ILES in conjunction with very high-order methods (i.e., 3^{rd}- and 5^{th}-order MUSCL, 5^{th}-order WENO schemes) capture the flow features and the mean flow paths in suddenly-expanded flows. For that purpose, sophisticated inflow boundary conditions were implemented and used throughout the numerical simulations, while several statistical tools were produced to investigate in depth the mean flow characteristics and structures, particularly at high Reynolds numbers.

The influence of different Reynolds numbers (at $Re = 10^4$ and $Re = 4 \cdot 10^4$) on the mean and fluctuating flow velocities, the Reynolds shear stresses, the turbulent kinetic

energy, as well as on the reattachment lengths of the primary and secondary recirculation vortices was thoroughly examined. Results indicated that the peak turbulence intensity, and subsequently, the peak turbulent kinetic energy is larger for the smallest *Re* under investigation. Moreover, the size of the primary recirculation zones, and particularly the size of the larger vortex, increases with increasing *Re*.

Measurements on the TKEB showed that in the free-shear layer regions, the turbulence production and energy dissipation are the most dominant terms. However, in the near-wall region turbulence production found to approach zero, whereas viscous diffusion and energy dissipation contribute positively and negatively to the energy budget, respectively. The transport terms, i.e., turbulent diffusion and velocity-pressure correlations, extract energy from the mean flow and transfer it towards the inner part of the shear layers, as well as towards the upper and lower walls of the channel.

It was also observed that the effect of compressibility on the turbulence intensities and the reattachment lengths is significant. Calculations of the mean flow path revealed that the reattachment length of the larger vortex increases with increasing Mach number, whereas the size of the shorter bubble remains almost intact. Comparisons between Mach 0.1 and Mach 0.8 in terms of TKEB showed that turbulence production and energy dissipation increases substantially with Mach number. On the other hand the influence of Mach number on the viscous diffusion term is rather weak, apart from the near-wall regions where its peak value, at Mach 0.8, is considerably higher than that observed at the lower Mach number.

Acknowledgements

First and foremost I would like to express my deepest gratitude to my supervisor, Prof. Dimitris Drikakis, for his guidance and support throughout my research, and for giving me the opportunity to enter the CFD world.

My thanks must go also to Dr. Ben Thornber for his constant support and valuable input during my research. His continuous encouragement and numerous fruitful discussions and suggestions helped me enhance my knowledge in turbulent flows considerably.

Also I am very grateful to all the people within the FMACS group I had the privilege to work with; Antonis Antoniadis, Nikolas Asproulis, Matyas Benke, Marco Hahn, Felipe Baranda Inok, Ioannis Kokkinakis, Dimitris Mantzalis, Antonis Milonas, Benjamin Obadia, Zeeshan Rana, Panagiotis Tsoutsanis, Chris Vamvakoulas and Bowen Zhong. I would like to especially thank Chris Vamvakoulas for his friendship and endorsement, since 2001.

Very special thanks to my partner Anastasia for her continuous support and love during the last nine years. Her understanding and endless patience are so much appreciated.

Last but not least, I would like to express from the bottom of my heart, my sincere thanks to my parents Dimitris and Efterpi for their invaluable support throughout the duration of my studies at Cranfield University. Without their devotion to me, I would not have been able to overcome the difficult moments in my student life. My gratitude goes also to my brother Fotis, who was always there whenever I needed him.

I would like to thank, of course, all my relatives and friends in Greece that helped me fill

up my time with pleasant and sprightly moments.

This PhD thesis is dedicated to my parents Dimitris and Efterpi, my brother Fotis and my partner Anastasia.

Konstantinos Karantonis

Contents

List of Figures

List of Tables

Abbreviations

Acronyms

BWFS	Backward Facing Step
CFD	Computational Fluid Dynamics
CFL	Courant-Friedrichs-Lewy Condition
CPU	Computer Processor Unit
CV	Control Volume
DNS	Direct Numerical Simulation
ENO	Essentially Non-Oscillatory
EoS	Equation of State
FVM	Finite Volume Method
HLL	Harten-Lax-van Leer
HLLC	Harten-Lax-van Leer Contact
ILES	Implicit Large Eddy Simulation
LDA	Laser Doppler Anemometry
LES	Large Eddy Simulation
LHS	Left Hand Side
LMNT	Low Mach Number Treatment
MILES	Monotonically Integrated LES
MUSCL	Monotone Upstream-centred Schemes for Conservation Laws
NFV	Non-oscillatory FVM
NSE	Navier Stokes Equations
ODE	Ordinary Differential Equations

PDE	Partial Differential Equations
PIV	Particle Image Velocimetry
PSE	Planar Sudden Expansion
RANS	Reynolds Averaged Navier Stokes
RHS	Right Hand Side
RK	Runge-Kutta
RM	Richtmyer-Meshkov
RT	Rayleigh-Taylor
SEF	Sudden Expansion Flows
SGS	Sub Grid Scale
TKEB	Turbulent Kinetic Energy Budget
TVD	Total Variation Diminishing
WENO	Weighted Essentially Non-Oscillatory

Latin Letters

A	Area
AR	Aspect ratio
b_{ij}	Reynolds stress anisotropy tensor
b_j	Filter coefficient
C	CFL number
c	Speed of characteristic
C_F	Skin-friction coefficient
C_{ij}	Cross-stress tensor
CK	Convection term
C_P	Wall-pressure coefficient
c_p	Specific heat at constant pressure
c_v	Specific heat at constant volume
D	Height of the main channel
d	Height of the inlet channel
dA	Elemental surface area
DK	Viscous diffusion term

dV	Elemental volume
E	Total energy per unit mass
e	Internal energy
$E(f)$	Energy spectrum
EK	Energy dissipation term
ER	Expansion ratio
f	Frequency
$\vec{f}_b$	Body forces
$\vec{F}_c$	Vector of convective fluxes
$\vec{F}_v$	Vector of viscous fluxes
H	Enthalpy
h	Step height
IS	Smoothness indicators
J	Jacobian
k	Thermal conductivity coefficient
KE	Kinetic energy
l	Characteristic length scale
L_{ij}	Leonard stresses term
M	Mach number
$\vec{n}$	Unit normal vector
NF_x	Filter size
p	Pressure
PK	Turbulence production term
$\vec{Q}$	Vector of the source terms
$\dot{q}$	Heat flux
R	Specific gas constant
r	Slope
Re	Reynolds number
Re_c	Critical Reynolds number
Re_L	Turbulent Reynolds number
Re_λ	Taylor microscale Reynolds number
Re_τ	Friction Reynolds number

R_{ij}	Reynolds stresses tensor
S_{ij}	Rate of strain tensor
$S_j(U)$	Limiter slopes
S_{max}	Maximum wave velocity
T	Absolute static temperature
t	Real time
t_c	Convective time scale
TK	Turbulent diffusion term
$\vec{u}$	Velocity vector
$u^{'}$	Fluctuating velocity
u_0	Centreline velocity
U_b	Inlet bulk velocity
u_η	Kolmogorov velocity scale
u_τ	Friction velocity
V	Volume
VPK	Velocity-pressure correlation
x_R	Reattachment length
y^+	Non-dimensional wall distance term

Greek Letters

α	Speed of sound
α_{ij}	Prescribed Reynolds stress tensor
β	Universal constant
γ	Specific heat ratio
Δ	Cell width
δ_{ij}	Kronecker delta symbol
ε	Dissipation rate
ε_{num}	Numerical dissipation rate
η	Kolmogorov length scale
Θ	Work of viscous stresses
κ	Thermal conductivity coefficient

λ	Second viscosity coefficient
μ	Dynamic viscosity coefficient
ν	Kinematic viscosity
Π	Weighted average polynomial function
π	Polynomial function
ρ	Density
$\overline{\overline{\tau}}$	Shear stress tensor
τ_η	Kolmogorov time scale
τ_{ij}^h	Numerical stress
τ_{ij}^R	Residual stress tensor
τ_{ij}^{SGS}	Subgrid-scale stress tensor
τ_l	Lagrangian time-scale
τ_w	Wall shear stress
ϕ	Arbitrary quantity
ω	Slope limiter function

Introduction

1 Introduction

1.1 Background

Almost everything in our planet either is a fluid or moves within or near a fluid. Fluid dynamics, which constitutes one of the main branches of fluid mechanics, is dealing with the fluid flow motion. It has a wide range of engineering applications, including calculating forces around an airplane, predicting climate patterns, estimating the mass flow rate of petroleum through pipes and understanding nebulae in interstellar space. The governing equations of fluid dynamics are the **N**avier-**S**tokes **E**quations (NSE), which were firstly introduced by Claude-Louis Navier and George Gabriel Stokes in 1822. The NSE are a set of non-linear **P**artial **D**ifferential **E**quations (PDE), which can also be expressed in integral form, consisted of the system of mass, momentum and energy equations. To date, there is no solution for the NSE, mainly due to the complexity of the form of the momentum and energy equation. In most of the flows and geometries (apart from very simple flows, such as the Poiseuille flow, Couette flows, laminar boundary layer, and so on) these equations cannot be solved analytically, which does not imply that no general solution exists. The only effective way of solving this system of PDEs is by applying appropriate

numerical techniques combined with high-speed digital computers.

During the last 50 years the increase of computational power gave birth to a new challenging field known as **C**omputational **F**luid **D**ynamics (CFD). CFD is one of the most important approaches in fluid dynamics along with pure theory and experiment. State of the art numerical algorithms lay the foundations of the CFD development. Furthermore, powerful supercomputers were designed, especially the last two decades, for solving very complex flows in high Reynolds numbers regimes. Today, the use of CFD as a scientific tool is as important as the experiment and theory for solving fluid dynamics problems.

(a) Laminar flow

(b) Laminar to turbulence

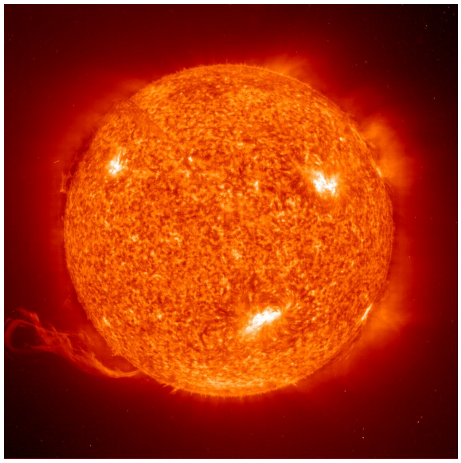

(c) Interstellar Turbulence

FIGURE 1.1: Laminar, Transitional and Turbulent flows in nature (after Jefferey [60]).

The types of flows in fluid mechanics can be separated in laminar, transitional and turbulent. Laminar flows Figure 1.1(a) are characterised by a smooth motion where the flow layers are parallel to each other and there is no mixture among them. In such flows the momentum diffusion is high, while the momentum convection low. On the other hand,

turbulent flows Figure 1.1(c) have an irregular and chaotic behavior which usually leads to the creation of vortices having many different length and time scales. Contrary to laminar flows, in turbulent flows the momentum convection is high and the momentum diffusion low. The transitional regime Figure 1.1(b) takes place between the laminar and turbulent state where the flow can be characterised as laminar with regions of sporadic bursts of turbulence. The parameter that determines whether the flow is laminar, transitional or turbulent is the Reynolds number (Re) taken its name from the physicist Osborne Reynolds who used it in his experiments in 1883.

The majority of the flows in nature are turbulent. Turbulent flows are of great importance in many scientific fields from aerospace engineering (Figure 1.2(a)) to meteorology (Figure 1.2(b)) and environmental engineering (Figure 1.2(c)), to name but a few. It is well known that turbulence causes the formation of eddies of many different length scales. However, most of the kinetic energy of the turbulent motion is contained in the large scale structures. This energy is then transferred from the large scales to smaller and smaller scales until, at the smallest scales, viscous dissipation of energy takes place. It is important to point out that the range of sizes of the eddies can be very large, so with the current computational power it is impossible to calculate all of the structures. Thus, in order to perform simulations on turbulent flows we have to use statistical models for the smaller scales and resolve only the larger scales.

There are several ways of modelling turbulent flows. The most common approaches of simulating such flows are the **D**irect **N**umerical **S**imulation (DNS), the **R**eynolds **A**veraged **N**umerical **S**imulation (RANS), and the **L**arge **E**ddy **S**imulation (LES). Each of the aforementioned techniques has its strengths and weaknesses. The selection of the turbulence modelling method should be carried out by taking into account the pros and cons of each technique, the type of fluid flow problem (e.g. compressible or incompressible, viscous or inviscid, steady or unsteady, wall-bounded flow or free shear flow, moderate Re number flow or high Re number flow) and the limits of computational power.

DNS method solves the unsteady, three-dimensional Navier-Stokes equations numerically by resolving all the spatial and temporal scales of fluid motion (from larger scales to smaller scales). Unlike other modelling techniques, in DNS there is no approximation involved in the numerical solution of PDEs. However it is important to point out that the computational time as well as the computer memory requirements increase rapidly with Reynolds number.

(a) Wing tip vortices behind an airplane

(b) Weather forecasting

(c) Turbulent flow development after volcanic eruption

FIGURE 1.2: Turbulence in different scientific fields (after Jefferey [60]).

The number of grid points (N) that is required to capture all the length scales in a three dimensional turbulent flow simulation is the following ([94]):

$$N \propto \left(\frac{u^{'} l}{\nu}\right)^{9/4} = Re_L^{9/4}$$

where the turbulence Reynolds number $Re_L = u^{'} l/\nu$ is the ratio of the fluctuating velocity $u^{'}$ times the characteristic length scale of the flow l to the kinematic viscosity ν. The number of time iterations is given by:

$$N_t = \frac{T}{l/u} Re_L^{3/4}$$

The total computational time $N_x \cdot N_t$ can then be written as:

$$N_x N_t = \frac{T}{l/u} Re_L^3$$

For example a numerical simulation which is performed at 1 gigaflop at $Re_L = 2.4 \times 10^4$, according to the above equations, would need 3.8×10^{10} total modes, 7.4×10^4 time steps and 90 years to complete [94]. It is obvious that DNS simulations are impracticable for high Re ($Re_L \gtrapprox 1.5 \times 10^3$) and are mainly limited to flows with low or moderate Reynolds numbers. Furthermore, there are two uncertainties arising in DNS, which can lead to inaccurate numerical solutions.

1. Flow instabilities can be formed by the lack of precise initial and boundary conditions of the smallest scales.

2. Lack of unique solutions - in a strict mathematical sense - as well as the possibility of numerical instabilities and spurious solutions can arise from the nonlinear nature of the advective terms in the NSE [31–33].

DNS, where it can be applied, has proved extremely important in providing us with such knowledge that is very difficult, and in some cases impossible, to be supplied from experiments (near-wall turbulence, interaction of turbulence with supersonic boundary layers). A comprehensive study of DNS as a research tool for modelling turbulent flows can be found in [87].

RANS method is based on the Reynolds decomposition technique, and is less computationally expensive compared to DNS and LES. According to the Reynolds decomposition, a quantity can be separated into its time-averaged and fluctuating part. Assume that we have an instantaneous quantity φ in space and time decomposed to its time-averaged part and fluctuating part. Thus we obtain the following:

$$\varphi(x,y,z,t) = \overline{\varphi(x,y,z,t)} + \varphi^{'}(x,y,z,t)$$

where $(\overline{\varphi})$ and $(\varphi^{'})$ the time-averaged and the fluctuating quantity φ, respectively. The above technique when applied to the NSE lead to a simplified form of time-averaged equations containing a non-linear term $\rho\overline{u_i^{'}u_j^{'}}$ known as Reynolds stress. It can be shown that averaging the NSE equations leads to additional unknown terms (closure problem of RANS method), which have to be defined to close the system. For that reason several turbulence models have been developed, which determine the Reynolds stresses. Algebraic models, one-equation models and two-equation models are extensively analysed in

[129]. The RANS method is used in practical engineering applications mainly for predicting steady-state flows. For time-dependent flows this approach is not appropriate, as the Reynolds-averaging assumes a statistically steady flow. In this latter case URANS (Unsteady Reynolds Averaged Navier-Stokes) approaches are alternatively used to model unsteady and transient flows.

LES is another method of predicting turbulent flows, lying between RANS and DNS. The main features of this method are the separation between large and small scales and the calculation of low-frequency modes only. In LES the large scale structures are computed explicitly, whereas the smallest scales are modelled by a subgrid-scale model (SGS). Compared with DNS, LES is computationally less expensive, as the explicit representation of the small-scale motions is avoided. Furthermore, LES can be more accurate and reliable than RANS method for flows with unsteady separation and vortex shedding. The main steps followed in LES are summarised below:

1. A low-pass filtering operation in space and time is applied to the NSE decomposing the velocity field U_i into the sum of a resolved term $\tilde{U}_i$ and a SGS component $u_i^{'}$. The filtered component $\tilde{U}_i$ represents the motion of the large eddies.

2. The filtered momentum equation contains the SGS term, which has to be modelled usually by an eddy-viscosity model for the closure of the system.

$$\frac{\partial \tilde{U}_j}{\partial t} + \frac{\partial \widetilde{U_i U_j}}{\partial x_i} = -\frac{1}{\rho}\frac{\partial \tilde{p}}{\partial x_j} + \nu \frac{\partial^2 \tilde{U}_j}{\partial x_i \partial x_i}$$

   where $\widetilde{U_i U_j} = \tilde{U}_i \tilde{U}_j + \tau_{ij}^R$ and τ_{ij}^R the residual-stress tensor.

3. Finally, the filtered NSE are solved numerically for $\tilde{U}_i$ providing an approximation for the motion of the large eddies in one realisation over time.

In the context of LES approach, a number of studies have been carried out over the last 50 years. Most of those studies focus on the development of efficient models for the residual stress tensor which are necessary for the closure of the filtered NSE. The first SGS model was developed in 1963 by Smagorinsky for the simulation of the dynamics of the atmosphere's air currents [106] and many more followed by Smagorinsky et al. [107], Fischer [41] and Kasahara et al. [66]. Deardorff [23] was the first to use the Smagorinsky model for the prediction of turbulent shear flow within a channel (plane Poiseuille flow) at large Reynolds numbers. Leonard [74] introduced a different decomposition technique

for the residual-stress tensor from that presented in step two. The SGS stresses were written in a triple decomposition form $\tau_{ij}^R = L_{ij} + C_{ij} + R_{ij}$ where $L_{ij} = \widetilde{\tilde{U}_i\tilde{U}_j} - \tilde{U}_i\tilde{U}_j$, $C_{ij} = \widetilde{\tilde{U}_i u'_j} - \widetilde{u'_i\tilde{U}_j}$ and $R_{ij} = \widetilde{u'_i u'_j}$. The Leonard stresses term L_{ij} represents the interactions between the resolved scales (the large scales of the flow). The term C_{ij} is the cross stresses and represents interactions between the unresolved and the resolved scales, while the SGS Reynolds stresses term R_{ij} represents interactions between the unresolved scales (the small scales of the flow). However, Speziale [111] proved that two of the three component stresses (L_{ij} and C_{ij}) in Leonard's approach are not Galilean-invariant (i.e. description of turbulence is not the same in all inertial frames of reference). The above model, therefore, cannot be of any general applicability, since it is inconsistent with the fundamental physics of the problem, which requires the description of turbulence be the same in all inertial frames of reference (i.e., the Newton's laws can then be applied). Germano [45] proposed an improved approach for the decomposition of the residual-stress tensor where all of the stress terms are Galilean-invariant. Since then a number of major contributions in the field of SGS modelling have been made by Bardina et al. [8], Germano et al. [47], Germano [46], Lilly [76], Scotti et al. [100] and Medeveau et al. [83] to name but a few.

1.2 ILES Background

Boris et al. (1992) [13] introduced a totally different approach within the context of LES technique which is known as Monotone Integrated Large Eddy Simulation (MILES) or Implicit Large Eddy Simulation (ILES). According to ILES, no explicit SGS model should be used and no explicit filtering should be performed. Instead, an appropriate numerical scheme should be used to solve the Navier-Stokes equations. In the conventional LES method the unresolved scales are explicitly modelled, while in ILES the smallest scales in the energy cascade are implicitly modelled by the numerical method. Several studies in the past have clearly shown that high-resolution numerical schemes for hyperbolic PDEs have an implicit (built-in) turbulence model ([27], [51], [52]). The different philosophy between LES and ILES can be expressed through the modified equation analysis (MEA). The modified equation is a partial differential equation satisfied by the numerical solution. Applying that equation to the LES (filtering) momentum equation we end up with the following expression:

$$\frac{\overline{DU}_j}{\overline{D}_t} = \nu \frac{\partial^2 \overline{U}_j}{\partial x_i \partial x_i} - \frac{1}{\rho}\frac{\partial \overline{p}}{\partial x_j} - \frac{\partial}{\partial x_i}(\tau_{ij}^R + \tau_{ij}^h)$$

where τ_{ij}^R the modelled residual stress and τ_{ij}^h the numerical stress related to the truncation error of the numerical method used for the discretisation of the NSE. The additional numerical stress depends on the grid spacing h. In standard LES method, the grid spacing h should be chosen to be small enough for a given filter width Δ, such that the numerical stress τ_{ij}^h is negligible compared to the residual stress τ_{ij}^R. On the other hand, in ILES no explicit filtering takes place and obviously the residual stress term is zero ($\tau_{ij}^R = 0$). However, significant numerical stresses can arise from the fact that the grid spacing h is not fine enough to resolve the solution to the Navier-Stokes equations. Thus the numerical dissipation (viz. the amount of energy that is removed from the resolved motions of the flow) depends exclusively on the numerical method used and each mean rate is obtained by:

$$\langle \varepsilon \rangle \equiv -\tau_{ij}^h \overline{S}_{ij}$$

where $\overline{S}_{ij}$ is the rate of strain given by $\overline{S}_{ij} = \frac{1}{2}(\frac{\partial \overline{U}_i}{\partial x_j} + \frac{\partial \overline{U}_j}{\partial x_i})$. It is worth pointing out that the type of the numerical method chosen is crucial and has an imminent effect on the numerical stress τ_{ij}^h.

The ability of ILES to accurately model practical engineering flow problems has been extensively examined in the past. Adams [3] performed simulations on shock-wave interactions with solenoidal velocity fluctuations, using MILES approach in conjunction with third order essentially non-oscillatory scheme (ENO) based on a Roe-flux formulation with entropy fix [104]. Comparisons have been made with a dynamic Smagorinsky model and the direct deconvolution method (DDM). Results, however, showed that the DDM method gave a more accurate representation of the shock-velocity wave interaction than that of the ENO scheme without subgrid model.

Fureby and Grinstein [43] used the ILES approach to conduct simulations on high-Reynolds-number free and wall bounded flows. Its ability to model complex unsteady flows were examined focusing mainly on the isotropic decaying turbulence, transitional jets and channel flows. Comparison of ILES of transitional free jets showed good agreement with DNS of homogeneous turbulence, and similar results were obtained. Furthermore, comparisons between ILES and conventional LES in inhomogeneous channel flows

as well as in free shear flows revealed that ILES approach is not less accurate than standard LES.

Margolin et al. [81] used a non-oscillatory finite volume method (NFV) without any explicit subgrid-scale model to perform high Reynolds number flow simulations. Specifically, the Multidimensional Positive Definition Advection Transport Algorithm (MPDATA) was used for the simulation of decaying turbulence of a homogeneous incompressible fluid in a triply periodic cube. They found that NFV methods free of explicit subgrid models can accurately predict turbulent flows exhibiting both large physical viscosity and vanishing physical viscosity.

Drikakis et al. [29] employed high-resolution numerical methods for simulating low- and high-speed flows featuring instabilities, symmetry-breaking and turbulence mixing in the context of ILES. Both Richtmyer-Meshkov (RM) and Rayleigh-Taylor (RT) instabilities in very high Reynolds number regimes were examined, where turbulence mixing occurs. The robust results obtained for RM and RT mixing calculations indicates that ILES technique is capable of performing simulations of turbulent mixing in very complex problems which contain shocks and initial density discontinuities. Besides, they pointed out that implicit LES model is not only computational simpler but also more economical than conventional LES.

An extended study related to MILES was carried out by Grinstein and Fureby [50] using flux-limiting algorithms (non-linear numerical algorithms) to imitate the flow features in the high wave number end of the inertial subrange of turbulent flows. The Flux-Corrected Transport (FCT) algorithm was used in the context of MILES and its performance was demonstrated in several selected test cases including canonical flows (turbulent channel flows, homogeneous isotropic turbulence), complex flows (rectangular jets and flow past a prolate spheroid) and very-complex flows in terms of geometrical characteristics and flow features (submarine hydrodynamics).

Drikakis et al. [30] assessed several high-resolution and high-order schemes to check the ability of ILES to model complex flows. Particularly the numerical schemes used, ranged from the second-order monotone upstream-centred scheme to very high-order WENO schemes up to ninth-order. Simulations were performed on swept-wing configurations, deep open cavity flows, shock-induced turbulent mixing and homogeneous decaying turbulence. Comparisons showed that the numerical results obtained in all the above

test cases were in excellent agreement with experimental results indicating that high-resolution numerical schemes in ILES can accurately predict flows in the high-Reynolds-number regime featuring physical complexity with well designed algorithms.

During the last two decades ILES has been widely used for simulating a large number of fundamental engineering problems. Its robustness and accuracy have placed the grounds to use this technique in flows that exhibit large regions of separation and reattachment. Studies on separated and reattached flow have been extensively conducted, and the backward-facing step (BWFS) geometry has received most of the attention. Although the geometry is very simple, the flow through it contains the most important characteristics encountered in more complex geometries. Most of the works on BWFS flow examined the effects of different Reynolds numbers (i.e. laminar, transitional and turbulent flow regimes), aspect ratios, expansion ratios, step heights and Prandtl numbers, on the behavior of the flow.

In the next section of this chapter a number of past studies on laminar and turbulent flows over the BWFS geometry configuration are presented. Previous experimental and numerical results on the turbulent kinetic energy budget (TKEB) have been extensively used in the present study to compare against the ILES results obtained from the sudden expansion test case. It is, therefore, of great importance to mention that measurements of the TKEB on the sudden expansion geometry have not been addressed in the past (either numerically or experimentally), so comparisons were made using exclusively the data from the BWFS.

1.3 Studies on the BWFS geometry

Considerable work has been devoted to the study of BWFS at high Reynolds numbers. Abbott and Kline ([1], 1962) carried out an experimental investigation of a subsonic turbulent flow over single and double BWFS flows. They found that downstream from the step a complex flow pattern with three distinct stall regions is present. Furthermore, they used a wide range of Reynolds numbers and turbulence intensities to examine their effect on the reattachment length and flow pattern. They concluded that there is totally no effect, provided that the flow is fully turbulent before the step. Finally a good agreement with other experimental data was found in the region close to the step, but poor agreement near the reattachment region.

Experimental investigation of turbulent flow over BWFS was conducted by Eaton

and Johnston ([37], 1981). They demonstrated several previous studies related to the measurement of the reattachment length and addressed five system parameters that have an effect on flow reattachment. The parameters examined were a) the initial boundary-layer state, b) the initial boundary-layer thickness, c) the freestream turbulence, d) the pressure gradient and e) the aspect ratio (the ratio of the channel width to the step height). In addition, measurements of turbulence intensities and Reynolds stresses showed that there is a peak value approximately one step height upstream of the reattachment and then a rapid decay. It is important to underline that the turbulence intensity as well as the Reynolds stress decay were found slower close to the step wall than away from the wall.

Neto et al. ([88], 1993) conducted a numerical study of the coherent structures in turbulence behind a backward-facing step. DNS, LES (Smagorinsky model and structure-function subgrid model) and ILES techniques were used for the simulations in three dimensions. Two different geometries were examined with aspect ratios 1.25 (high-step) and 2.5 (low-step). The Reynolds numbers based on the step height and the mean velocity at the inlet were 6000 and 38 000 for the low-step and high-step, respectively. In the high-step two-dimensional simulations Kelvin-Helmholtz vortices of low pressure were found behind the step undergoing various pairings, while for the low-step case, the separation behind the step causes the detachment of the boundary layer at the upper wall. On the other hand, in the high-step three-dimensional case, primary vortices shed behind the step and secondary longitudinal hairpin vortices are stretched in between. The numerical results were in good agreement with experiments, apart from the near-wall regions where significant variations were found mainly due to the poor resolution.

Papadopoulos et al. ([92], 1995) carried out an experimental study of separating and reattaching flow structure in a BWFS geometry. The main objective was to investigate the influence of different aspect ratios on the flow structure. The Re number was 26 500 based on the freestream velocity and the step height of the rectangular duct. They found that for aspect ratios greater than four ($AR > 4$) the flow is almost two-dimensional with a minor side wall effect on the centerplane mean velocity, whereas for $AR = 2$ and $AR = 4$ there is a strong indication of the three-dimensionality of the flow. Furthermore, a flow separation on the flat wall approximately five step heights downstream of the step were also found. Finally, a relation between aspect ratio and reattachment length was presented and the results were in a good agreement with those of de Brederode and Bradshaw ([21],1972). According to it, as the aspect ratio decreases, so does the reattachment length x_R.

Le et al. ([73], 1997) performed direct numerical simulation of a turbulent flow over

a BWFS. The Re number based on the step height h and the freestream velocity was 5100. Calculation of the skin friction coefficient, C_f, for $Re = 5100$ showed that its magnitude is 2.5 times more than the value measured at experiments with much higher Reynolds number. Measurements at 20 step heights behind the separation revealed that the turbulent boundary layer is not fully recovered. Moreover, the mean reattachment length was found $6.28h$, while its variation was approximately 2% and 3%. Finally, the budgets of all Reynolds stress components along with up to third-order statistics at all locations in the flow field were computed.

Experimental and numerical study of laminar, transitional and turbulent flow behind a two-dimensional BWFS carried out by Armaly et al. ([6], 1983). The influence of Reynolds number on the reattachment length of the reversed flow regions was mainly examined. The Reynolds numbers ranged between 70 and 8000. They found that the separation length behind the step increases with increasing Re in the laminar-flow region up to $Re = 1200$. On the other hand, the mean separation region attached to the step in the transitional regime (laminar to turbulent flow state) sensibly decreases. Comparisons between numerical and experimental results were in good agreement for low Reynolds numbers up to 400. Above this value, strong deviations between measurements and predictions started to appear, mainly due to the three-dimensionality of the experimental flow. A reversed flow region at the flat wall opposite the step wall was also predicted by the numerical scheme, showing that the strong adverse pressure gradient taken place thanks to the change of the cross-section, can cause the formation of an additional separation region at the wall opposite the step location.

Nie and Armaly ([90], 2004) continued the study of Armaly et al. [6] on a three-dimensional BWFS flow. The geometry used provided an expansion ratio ($ER = D/d$) of 2.02 and an aspect ratio ($AR = W/h$) of 8. They found that as the Reynolds number increases, the reattachment length, x_R adjacent to the flat wall and side wall increases and moves further downstream in the laminar flow regime. In the transitional flow regime, x_R decreases and moves upstream, while it remains constant or diminishes in the turbulent flow regime. In the laminar flow regime numerical results agreed well with experiments of Armaly et al. (1983) and reasonably well in the turbulent region.

Kaiktsis et al. ([64], 1991) and ([63], 1996) performed a numerical study (DNS) of transition to turbulence in flow over a backward-facing step. Investigation of the onset of three-dimensionality in the step flow due to secondary instability of the primary two-dimensional flow was undertaken. They concluded that above a characteristic (critical)

Reynolds number ($Re \geqslant Re_c \approx 700$), a primary source of discrepancies in comparisons of two-dimensional numerical predictions and experimental data starts to appear, due to the bifurcation of the steady, two-dimensional laminar flow to three-dimensional flow.

Kasagi et al. ([65], 1995) conducted an experimental study (PIV) of a turbulent flow over a BWFS. Emphasis was given to turbulent flow measurements (Reynolds stresses, turbulent kinetic energy, triple velocity correlations, reattachment lengths, to name but a few) and, particularly, to the calculation of the terms of the TKEB. They stated that the turbulent diffusion term of the energy budget plays a significant role in the transport of the Reynolds stresses, particularly in the separation shear layer region and the reattachment location. Note that comparisons (of the TKEB calculations) between the ILES results and the experimental data of Kasagi et al. are presented later in Chapter 5.

In the past, considerably work has been reported for the nominally two-dimensional flow over a double-sided expansion. Flow through a channel with symmetric sudden expansion exhibits separation, reattachment and recirculation. The most important characteristic in such flows is that while the geometry is symmetric, asymmetric flow condition takes place under certain Reynolds numbers and geometric properties. It is well known that the flow up to a certain Reynolds number is symmetric and two separation regions of equal length develop on either side of the expanding channel. As the Reynolds number increases, the flow becomes asymmetric about its centerline and separation regions of unequal length arise and remain in the flow field even up to high Reynolds numbers (turbulent flow conditions). The transition from a symmetric state to an asymmetric one is also referred as Coanda effect [130] in the literature. The critical Reynolds number and the conditions of the asymmetry were extensively examined theoretically, experimentally and numerically.

1.4 Laminar Studies on PSE

Most of the studies on plane sudden expansion (PSE) channels have been conducted in the laminar flow regime.

Durst et al. ([35], 1974) performed laser anemometer measurements for low Reynolds number flow over a plane symmetric sudden expansion with an expansion ratio of 3 : 1 and aspect ratio of 9.2 : 1 downstream of the expansion. They stated that the flow was markedly dependent on the Reynolds number and at high velocities three-dimensional, even away from the channel corners. The flow at Reynolds number 56, based on the

upstream height of the duct and on the maximum upstream velocity, was found to be symmetric with two separation regions of equal length. However, above that value and specifically at Reynolds number 114 two separation regions were found of different length scales, leading to asymmetric velocity profiles. Furthermore, a third recirculation region downstream of the smaller of the two recirculation zone adjacent to the step appeared at Reynolds number equal to 252. The authors pointed out that in the region of PSE the flow can exhibit a three-dimensional nature even for low Reynolds numbers.

Experimental investigation of low Reynolds number flow over symmetric channels with sudden expansion was carried out by Cherdron et al. ([18], 1978). The Laser-Doppler anemometer (LDA) technique used to provide an in-depth description of the velocity characteristics of a flow through a symmetric sudden expansion duct with $ER = 2$ and $AR = 8$. A strong relationship was found between the ER, the AR and the critical Reynolds number value. A decrease in the ER and AR had a stabilising effect, which extended the range of Reynolds number over which a symmetric flow can exist. Besides, the flow was symmetric at Reynolds number approximately 150, but asymmetric at Reynolds number 185. They also investigated the physical origin of the asymmetry and they concluded that the instability of the shear layer between the recirculation region and the main stream causes the transition of the flow from a symmetric state to an asymmetric one. Finally, vortex-shedding structures were detected further downstream of the step resulting from the interaction between the two shear layers of the two sides of the intake stream.

Acrivos et al. ([2], 1982) conducted a theoretical investigation of a laminar flow in a two-dimensional duct in the limit of large Reynolds number flow. The boundary layer equation was solved numerically by a finite difference scheme to examine the relationship between the Reynolds number and λ(the ratio of the upstream channel half-width to the step height). For this reason, a parabolic inlet velocity profile, as well as a uniform inlet profile were used. Steady solutions were found for all values of λ when the former profile was used. On the other hand, when the latter profile was used steady solutions obtained only for values $\lambda \leq \lambda_c = 1.54$ and $\lambda \leq \lambda_c = 3.67$ for the two-dimensional and the axisymmetric case, respectively. The term λ_c is the critical value above which the solution becomes unsteady.

A theoretical study of a steady flow past sudden expansions has also been undertaken by Milos and Acrivos ([84], 1986). They found that for uniform flows and small expansion ratios the separated eddy length l increases linearly with Re up to a certain point. For sufficiently large Reynolds numbers where the flow becomes unsteady, this linear

relationship will no longer exist. Similar results were obtained for a two-dimensional, laminar, incompressible flow past a bluff body. They also showed that the linear increase of l with Re takes place up to a certain value. For $\lambda > \lambda_c$ that linear relation of l and Re should no continue.

Sobey and Drazin ([109], 1986) carried out a bifurcation analysis of two-dimensional channel flows. The flows under consideration were the Jeffery-Hamel (JH) flow, i.e. a steady radial flow of a viscous incompressible fluid between two inclined plane walls, and the symmetric channel flow configuration. They found that the nature of the symmetry-breaking in the above two examples is not the same. Particularly, in JH flows a subcritical pitchfork bifurcation occurs where the flow above a certain value of either Reynolds number or maximum angle between the channel walls becomes unstable. On the contrary, in symmetric plane channel flows a supercritical pitchfork bifurcation causes the flow to become steady asymmetric for high Reynolds number values.

Milos et al. ([85], 1987) used a global Newton method to obtain finite-difference solutions to the steady Navier-Stokes equations up to Reynolds number of 1000. The inlet velocity profile was uniform and the calculations revealed that for large expansion ratio the eddy length increases linearly with Re and the flow features are identical with those predicted by the boundary-layer solutions, indicating the eddy flow in those cases remains viscous as $Re \to \infty$. The calculations for smaller values of the expansion ratio showed that as the Re increases, the solution to the Navier-Stokes equations approaches the limit of an inviscid eddy length.

The origin of steady asymmetric flows in a symmetric sudden expansion was both experimentally and numerically examined by Fearn et al. ([40], 1990). The flow features were studied in a single channel of expansion ratio 3 and aspect ratio 8. They found that the asymmetry arises at symmetry-breaking bifurcation taking place at a critical value of Reynolds number $Re_c = 40.45 \pm 0.17\%$ based on the upstream channel half-height and the maximum inlet velocity (or $Re_c = 80.9$ based on the upstream channel height). A third region of recirculating flow was also observed at a Reynolds number of 125 on the same wall of the small recirculation region and opposite the downstream end of the large recirculation. In addition, further increase of Reynolds number leads to flow unsteadiness where the flow is characterised by the shedding vortices arising at the shear layers. Finally, the authors found that the observed time-dependent flows were a consequence of three-dimensional effects in the channel and not of a two-dimensional Hopf bifurcation.

Shapira et al. ([101], 1990) performed a linear stability analysis of viscous flow in

two-dimensional channels with symmetric changes in width. They found that the flow is symmetric downstream of the expansion for Reynolds numbers below a critical value and that a transition from a symmetric flow pattern to an asymmetric one occurs as the Reynolds number increases more. Two different expansion ratios were used to investigate the value of the critical Reynolds number above which steady non-symmetrical solutions exist. Thus for $ER = 2$, the flow pattern becomes unstable for Reynolds numbers beyond 215, while for $ER = 3$ the transition occurs at Reynolds number of 82.6.

The flow through a nominally two-dimensional channel with a symmetric sudden expansion has been thoroughly investigated both numerically and experimentally by Durst et al. ([36], 1993). The expansion ratio used throughout the calculations was equal to 2. Both the experiments and the numerical simulations confirmed a symmetry-breaking bifurcation of the flow leading to one short and one long recirculation region for Reynolds numbers beyond 125, based on the upstream channel height and the maximum inlet velocity. The relation between the Reynolds number and the length of the separation regions was additionally reported. It was observed that as the Reynolds number increases above the critical value of 125, the short separation region remains almost constant in length whereas the length of the long region increases.

Foumeny et al. ([42], 1996) performed a numerical investigation of an incompressible Newtonian fluid downstream of a plane symmetric sudden expansion to determine the critical value of Reynolds number, above which the flow turns out to be asymmetric. They found that for $ER = 3$, the critical Reynolds number is approximately 80. For $Re > Re_c \simeq 80$ the flow becomes asymmetric with one small and one large separation region adjacent to the walls.

Alleborn et al. ([4], 1997) carried out a bifurcation analysis to study the flow in a plane symmetric channel with sudden expansion. For this reason, Arnoldi-based iterative methods were used to track the variation of the eigenvalues of the least-stable modes with respect to Reynolds number. Several expansion ratios were examined in the range of $0 < Re < 800$. For $ER = 2$, two symmetry-breaking bifurcations were detected at $Re_{c1} = 218$ and $Re_{c2} = 542$. The critical Reynolds number for the first bifurcation agrees well with the results obtained by Shapira et al. [101]. In addition, they found that for values of expansion ratio larger than 2 the symmetry-breaking bifurcations take place at lower Reynolds number. Specifically, for $ER = 3$ the flow found to be asymmetric at $Re > Re_c \simeq 80$, while for $ER = 5$ at $Re > Re_c \simeq 45$. They also pointed out that the distance between the first and second bifurcation points decrease with increasing ER. Finally, the

flow asymmetry and the reattachment lengths grow more rapidly with increasing ER.

Numerical simulations and bifurcation calculations of low Reynolds number flows in symmetric channels were also conducted by Battaglia et al. ([11], 1997). Three important statements were made in their work: a) the critical Reynolds number decreases with increasing expansion ratio, b) for a fixed expansion ratio, increasing the Reynolds number, increases the number of attachment positions for an asymmetric jet, and c) for a fixed Reynolds number, an approximately linear relationship exists between the expansion ratio and the downstream location of the primary reattachment points. The inverse relationship between the Re_c and the ER was confirmed by performing both numerical and bifurcation tests for a wide range of expansion ratios. Suggestively, the numerical results showed that the critical Reynolds number lies between $150 < Re_c < 155$ and $57 < Re_c < 58$ for $ER = 2$ and $ER = 3$, respectively. Similar results were obtained from the bifurcation calculations where the $Re_c = 143.6$ and $Re_c = 53.8$ for the same expansion ratios.

Rusak and Hawa ([97], 1999) conducted a weakly nonlinear analysis based on multiple scale and singular perturbation methods to study the flow behavior around the Re_c. They demonstrated that when $Re < Re_c$ the symmetric flow state is stable. On the other hand, when $Re \geq Re_c$ the symmetric state loses its stability and a steady asymmetric state evolves.

The side wall effects on the structure of a laminar flow over a symmetric sudden expansion were numerically examined by Chiang et al. ([19], 2000). It was found that for a fixed expansion ratio $ER = 3$, the flow remains symmetric in channels whose aspect ratios are less than 3.5. Furthermore, for aspect ratios larger than 12, the flow becomes nominally two-dimensional. According to the authors, the asymmetric nature of the flow emanates from discretisation errors in the solution process of the basic equations of fluid flows as well as from the REAL-number representation in computers.

A weakly nonlinear stability analysis was proposed by Mizushima et al. ([86], 2000) to investigate the structural instability of the bifurcation in symmetric channel with a sudden expansion. It was found that for a fixed expansion ratio $ER = 3$, the critical Reynolds number above which the flow becomes asymmetric is approximately 40.23 based on the half upstream height. The results are in good agreement with those of Fearn et al. [40], Drikakis [26] and Alleborn et al. [4] who predicted that for the same geometrical characteristics the $Re_c \simeq 40.45$, $Re_c = 40$ and $Re_c = 40$, respectively.

The first numerical study of bifurcation in three-dimensional sudden expansions were

performed by Schreck and Schafer ([99], 2000). For that purpose, a multigrid finite volume method was used to carry out simulations in a symmetric channel with a fixed expansion ratio of 3 and two different aspect ratios of 2 and 5. For $AR = 2$ the critical Reynolds number found to be equal to 113.2, while for $AR = 5$ the flow loses its stability at $Re_c = 91$. They also found that when the flow is considered as two-dimensional, the symmetry-breaking bifurcation occurs at $Re_c = 81.2$. It was finally stated that for very small aspect ratios ($AR \rightarrow 0$) the flow is stabilised such that the bifurcation point moves to higher Reynolds numbers.

Hawa et al. ([55], 2001) performed bifurcation analysis, linear stability study and direct numerical simulations of a two-dimensional, incompressible, laminar flow in a symmetric channel with a sudden expansion of $ER = 3$. They found that $Re_c = 53.8$, showing that below and above of this value the decay of the perturbation $\sqrt{Re - Re_c(D/d)}$ is very slow, while at $Re_c = 53.8$ the decay or growth of perturbation is almost zero.

Numerical investigation of bifurcation in a $1:2$ expansion using convection discretisation schemes along with multigrid algorithm was undertaken by Kadja et al. ([62], 2002). They also confirmed the presence of two recirculation zones of unequal lengths evolving in the upper and lower wall above Reynolds number of 200. It was found that further increase of Reynolds number leads to the development of a third separation region located at the same side as the small bubble.

The effect of different types of inlet velocity profiles on the critical Reynolds number was extensively investigated by Wahba ([128], 2007), who performed numerical simulations of an incompressible laminar flow in a sudden expansion duct of ratio $1:4$. When parabolic inflow profile was used, the $Re_c = 36$, which is in good agreement with the bifurcation calculations of Battaglia et al. [11]. However, when a uniform inlet profile was applied, a stable symmetric solution was maintained up to a Reynolds number of 64. Additionally, for Re between 80 and 100, a third recirculation region was detected only when a parabolic inflow was used.

Three-dimensional numerical simulations by means of a finite volume method were performed by Tsui et al. ([122], 2008), to study the influence of different values of aspect ratio on the bifurcation of the flow through a symmetric sudden expansion of $ER = 3$. It was found that for $AR = \frac{1}{3}$ the flow remains symmetric for all Reynolds numbers under consideration. For $AR = 1$ the symmetry-breaking bifurcation occurs at $Re_c \simeq 92$, for $AR = 4$ at $Re_c \simeq 61$ and for $AR = 8$ its value reduces further more to about 58.5. The general statement made by the authors was that the appearance of a side wall, by reducing

the aspect ratio, has a stabilising effect on the flow. This observation agrees well with the numerical results found by Schreck et al. [99].

1.5 Turbulent Studies on PSE

Turbulent flows through plane sudden expansion (PSE) have been considerably less investigated either experimentally or even more numerically. The most important reason is that as the Reynolds number increases further, the flow exhibits high level of complexity and variation. The flow becomes three-dimensional, time-dependent and finally chaotic where complex structures evolve, which makes it difficult for any kind of numerical scheme and turbulence model to sufficiently capture the features of the flow. It is also evident that direct numerical simulations with the current computational power are prohibited for flows with large values of Reynolds number.

The first investigation of turbulent flow over a PSE was undertaken by Abbott and Kline ([1], 1962). They performed hot-film velocity measurements in a plane symmetric channel where the expansion ratio varied from 1.125 to 5 and the aspect ratio from 2.5 to 5. They demonstrated that the flow at large expansions contains an asymmetry but approaches a single-step configuration for aspect ratios less than 1.5. For a fully turbulent inlet profile no effect was found on the reattachment length or the flow pattern for Reynolds numbers ranging from $4 \cdot 10^4$ to 10^5 (Re based on the inlet bulk velocity and the upstream height of the channel). The flow visualisations showed three stall regions with different flow features downstream of the step, the lengths of which were increasing with the expansion ratio and becoming unequal on the two side walls for $ER > 1.5$.

Restivo and Whitelaw ([95], 1978) carried out LDA velocity measurements in a symmetric PSE of $ER = 3$ and $AR = 27.5$. Mean velocity calculations and r.m.s. (root mean square) values were obtained for a wide range of Reynolds numbers between 494 and 2995. It was found that the shape of the mean velocity profiles is linked with the shape of the r.m.s profiles, particularly at 3.5 and 11 step heights downstream. Two maxima were found for the r.m.s. profiles and the minimum value in between was, in all cases, coincident with the maximum mean velocity. Moreover, the authors performed energy spectrum analysis which revealed that at all Reynolds numbers except the highest one, preferred frequencies are present. On top of that, the relationship between the Reynolds number and the preferred frequency found to be linear.

Experimental investigation of turbulent flow with separation and reattachment over a

double backward-facing step was conducted by Smyth ([108], 1979). LDA measurements were performed in a plane symmetric channel of $ER = 1.5$ and $AR = 30.4$, at Reynolds number of 30 210 based on the downstream duct height D and the inlet bulk velocity U_B. Mean axial, transverse and spanwise measurements of the velocity fluctuations were demonstrated, along with turbulence intensities, Reynolds stresses and turbulence kinetic energy calculations. The peak values of both turbulence kinetic energy and Reynolds shear stress were found at the edge of the primary recirculation zone. The maximum streamwise, transverse and cross-stream turbulence intensities found to be approximately 19.5%, 13.5% and 13% of U_B in the recirculation region, respectively. Flow asymmetry downstream of the double step was not detected and the flow regained a profile similar to that upstream of the step at $x/L = 12$.

Mehta ([82], 1981) performed an experimental study of a turbulent flow over a flat PSE at various Reynolds numbers and two different expansion ratios (1 : 2 and 1 : 3), by means of a Pitot tube and a hot-wire anemometer technique. The results revealed a highly asymmetric and unsteady flow pattern for large expansions with two unequal separation regions on the top and bottom wall of length 12 and 3.3, respectively. It was also found that the mean flow pattern becomes uniform and steady more rapidly with increased expansion ratio. Furthermore, in the range of $5 \cdot 10^4 < Re < 10^5$ a weak influence of the Reynolds number on the flow structure was detected. Three-dimensional effects were not mentioned despite the small value of aspect ratio which was significantly less than 1 ($AR = 0.25, 0.5$).

Szymocha ([114], 1984) conducted an experimental analysis of a turbulent flow downstream of a symmetric PSE of $ER = 1.5$ and $AR = 10.67$ using the LDA technique. Mean and fluctuating velocity data was reported at a Reynolds number of 42 000 based on the inlet bulk velocity (a uniform inlet velocity was employed) and the upstream channel height. Symmetric flow patterns were found downstream of the step with two recirculation zones of equal length ($x_R = 5.5 - 6$). The value of the reattachment length was found to be slightly lower compared with that reported in Smyth's work [108], where a fully developed inlet velocity profile was used.

The first numerical simulation of a turbulent flow over a two-dimensional PSE was carried out by Gagnon et al. ([44], 1993). The random vortex method was used to simulate a flow over a double backward-facing step. The geometric features of the channel and the Reynolds number ($Re = 10^5$) were chosen to be the same as those used in Mehta's experimental study. Mean velocity measurements were in good agreement with experiments.

However, the turbulence intensities were not comparable and this is mainly attributed to the three-dimensional nature of the flow in the experiments conducted by Mehta (1981). It was reported that the largest length scales of the flow are of the order of half-width of the channel and are found downstream of the separation regions. These regions are also characterised by the lowest frequencies. On the other hand, the smallest length scales of the flow were found inside the shear layers near the expansion and inside the recirculation regions. The section of the expansion is characterised by the highest frequencies.

Aloui and Souhar ([5], 2000) performed an experimental study of turbulent asymmetric flow in a flat channel with a symmetric sudden expansion of aspect ratio 0.18 and expansion ratio 2.27. Hot-film anemometer measurements were conducted at a Reynolds number of 32 000 based on the inlet bulk velocity and the upstream height of the duct. Mean axial velocity measurements along with mean and fluctuating pressure values were reported based on a fully developed turbulent velocity inlet profile. The results showed that the flow is asymmetric downstream of the step, as in a two-dimensional case, exhibiting two unequal in size recirculation zones in both sides of the expansion. In addition, it was found that the distribution of the average pressure is not symmetrical about the axis of the sudden expansion. The maximum values of the r.m.s velocity were obtained in the regions of the recirculation flow, whereas the minimum values in the core region of the flow. Finally, the authors highlighted that the regions of the recirculating flow are constituted by five vortices of different size lengths.

LDA measurements and numerical simulations of PSE were conducted by De Zilwa et al. ([22], 2000). A near-uniform inlet velocity profile was used in a plane symmetric channel with expansion ratio 2.86 and aspect ratio 12.31 at Reynolds number 26 500 based on the upstream height. Spanwise measurements downstream of the expansion revealed that the mean velocity is uniform over more than 80% of the span. Moreover, the mean velocity profiles found to be asymmetric about the midplane, with two unequal reattachment lengths on the top and bottom wall. Comparisons between numerical and experimental results showed a poor agreement in terms of the recirculation lengths and the velocity measurements inside the separation zones. Specifically, the length of the longer reattachment region was underestimated while the length of the shorter one overestimated for the $k-\varepsilon$ calculations. The predicted reattachment lengths were equal to 3.85 and 10.7 step heights, in contrast to experimental values of 3.4 and 17. Those significant discrepancies were mainly attributed to the limitations of the $k-\varepsilon$ turbulence model, particularly in the presence of anisotropic turbulence and reversed flow regions.

A comprehensive study of a turbulent flow through a PSE of expansion ratio 4 and aspect ratio 5.33 was undertaken by Escudier et al. ([39], 2002). LDA measurements and numerical calculations using a $k-\varepsilon$ model were reported at a Reynolds number of 55 500. Mean and fluctuating axial velocities along with Reynolds stresses and wall-pressure variations were measured both experimentally and numerically. The experiments revealed that the flow is asymmetric and three-dimensional about the XY midplane. On the other hand, the $k-\varepsilon$ calculations failed to capture the spanwise asymmetry due to the limitations of the turbulence model. In the upper recirculation region the flow found to be strongly anisotropic. The maximum value of the streamwise fluctuating velocity was as high as 26% of the inlet bulk velocity, whereas the peak value of the transverse turbulence intensity was approximately 14%. In the lower recirculation region, the flow found to be almost isotropic with the axial and transverse turbulence intensities having values around 20%. The authors also demonstrated that the flow, at $x/d = 21$, had still not recovered from the effect of the inlet expansion and remained asymmetric about the XZ center plane.

Canbazoglu et al. ([16], 2004) performed an experimental investigation of a turbulent asymmetric flow in a PSE with small aspect ratio, which was mainly focused on the analysis of pressure distribution. The expansion ratios examined were equal to 2, 2.5 and 3 while the aspect ratios equal to 0.4, 0.26 and 0.2. The Reynolds number was 22 000, based on the hydraulic diameter D_h of the channel ($Re_{D_h} = 22000$ and $D_h = 2hw/(w+h)$). The results showed that the expansion, aspect and area ratios significantly affect the flow field. For lower expansion ratio and larger aspect and area ratio, the flow becomes less asymmetric and the flow structure downstream of the expansion has a more symmetric appearance. It was also found that for the same values of Reynolds numbers, pressure coefficient increases when the expansion ratio decreases, while both the aspect and area ratio of the expansion increase.

More recently, Casarsa et al. ([17], 2008) carried out an extensive experimental study of a turbulent flow downstream of a planar symmetric sudden expansion of large expansion ($ER = 3$) and aspect ratios ($AR = 10$), by means of a 2D particle image velocimetry (PIV) technique. Mean and r.m.s. velocity measurements, as well as Reynolds stress measurements of the flow field were performed in several mutually perpendicular planes. Two different Reynolds numbers were used $Re = 10^4$ and $Re = 4 \cdot 10^4$ to investigate their effect on the flow structure. The authors found that $Re = 10^4$ is not high enough to support the statement that any further increase in Reynolds number does not have an effect

on the flow structure. For $Re = 10^4$ the values of the short and long reattachment lengths were equal to 3.68 and 14.38 and for $Re = 4 \cdot 10^4$ equal to 3.93 and 14.17, respectively. Two additional secondary recirculation regions were also detected at the upper and lower corners of the channel with lengths of 1.06 and 0.84. Finally, a three-dimensional model of the mean flow structure in the separation bubbles was proposed.

1.6 Summary

The plane sudden expansion, as previously mentioned, is relevant to a number of important engineering applications, such as fluidic devices, heat exchangers and mixing equipment. It is, however, surprising the fact that the number of studies of turbulent flows through plane sudden expansions are very limited. It is noteworthy to underline that LES numerical studies on these kind of flows are not addressed in the past. The main reason is that PSE flows are very complex flows with flow separation from fixed points and reattachment of the shear layers, which makes any attempt to model those flows extremely demanding and computationally very expensive.

Previous numerical investigations on turbulence in flows with a sudden expansion were limited and in many (if not all) cases the results were very far from the experimental data (in terms of both the time-averaged velocity components and the reattachment lengths of the primary and secondary vortices). The first numerical study was conducted by Gagnon et al. [44] by means of a random vortex method. The results were not satisfactory compared to the experimental results demonstrated by Mehta. This discrepancy was mainly attributed to the strong three-dimensional effects of a very flat channel (i.e., the aspect ratio used by Mehta was very small). De Zilwa et al. [22] carried out experimental-numerical calculations of a turbulent flow downstream of a PSE. The RANS-based two equation model ($\kappa - \varepsilon$) used to represent the turbulent properties of the flow was incapable of capturing the characteristics of the flow in regions with large adverse pressure gradients (this is an inherent limitation of RANS-based methods). The last experimental-numerical investigation of a turbulent flow through a PSE was undertaken by Escudier et al. [39]. The same RANS-based turbulence modelling was used to compare the experimental findings with the numerical data. The authors stated that the $\kappa - \varepsilon$ model is not capable of capturing the three-dimensionality of the flow in the spanwise direction due to the limits of the model. The predicted flow turned out to be symmetric in the $x - y$ plane of the channel.

It is, therefore, evident that turbulent flows through a PSE geometry have not been numerically investigated in the past. On top of that, the limited numerical studies on these kind of flows were inadequate of resolving the turbulent structures present in the flow field. The aim of the present study is to bridge the gap between the limited numerical investigations and the experimental data demonstrated the last fifty years on PSE flows. For this purpose, the ILES turbulence modelling method in conjunction with very high-order, high-resolution methods is employed, to shed some lights on the physics of flows with a sudden expansion.

1.7 Aim and Objectives

The aim of this PhD is to perform high-resolution and very high-order CFD simulations, in order to elucidate open questions about the physics of turbulent flows in suddenly-expanded flows. The basic characteristics of this thesis are twofold: (a) to test the capability of ILES to capture the complex flow features (separation, reattachment, recirculation) encountered in suddenly-expanded flows and (b) to investigate the fluid flow behaviour by employing a wide range of Reynolds and Mach numbers spanning from 10^4 to $4 \cdot 10^4$ and 0.1 to 0.8, respectively.

The objectives and the basic steps used to achieve the above aim can be summarised as follows:

- To implement very high-order methods along with efficient inflow boundary conditions in the simulation of suddenly-expanded flows.
- To assess the accuracy of high-resolution methods in the context of ILES, by validating the CFD results against experimental data, wherever possible.
- To perform CFD simulations at different Reynolds numbers and Mach numbers (subsonic and transonic regime), testing in such a way to what extent ILES can capture a wide range of fluid flow features.
- To investigate the flow physics in such flows by calculating crucial turbulent flow parameters, such as the turbulent kinetic energy budget and the turbulent kinetic energy spectrum, seeking to shed some light on one of the most important unsolved problem of classical physics, turbulence.

1.8 Publications

During the period of the PhD project a book chapter, a journal paper, and a conference paper have been written.

- Book chapters
  - D. Mantzalis, K. Karantonis, N. Asproulis, L. Konozy and D. Drikakis, "Computational Modelling of Aquatic Environments", Book Chapter on "Detections of Pathogens Using Micro- and Nano- Technology", IWA Publishing, 2011.
- Journal papers
  - K. Karantonis, B. Thornber and D. Drikakis, "Turbulent Flow Physics in Suddenly Expanded Flows", J. Fluid Mech., 2011 (submitted).
- Conference papers
  - K. Karantonis, B. Thornber and D. Drikakis, "Implicit Large Eddy Simulation of Turbulence in Suddenly Expanded Flows", *9th International ERCOFTAC Symposium on Engineering Turbulence Modelling and Measurements*, Thessaloniki, Greece, June 2012.

1.9 Thesis Structure

The thesis is organised into three major parts. Part I contains the introduction (Chap.1) of the thesis, where the literature survey on ILES and Suddenly-Expanded Flows is presented. The general philosophy of this study, along with the aim and objectives are also highlighted.

Part II contains 2 Chapters. The first (Chap. 2), deals with the most important aspects of transition and turbulence. Basic characteristics of bifurcation analysis and chaos theory are covered, which are responsible for the transition of the flow from a laminar state to a turbulent one. Furthermore, in this chapter several features of turbulence are presented, emphasising mostly on the Kolmogorov length scales and the Kolmogorov $-5/3$ law. The second (Chap.3), contains the fundamental aspects of the conservation laws governing the three quantities: mass, momentum and energy. The finite volume method, along

with state-of-the-art high-resolution and high-order methods for the spatial and temporal discretisation of the governing equations are also presented. Several approaches of modelling turbulent flows (RANS, LES, ILES) can also be found.

Part III is completely dedicated to Suddenly-Expanded Flows and to the most important findings of this study. This Part is organised into 3 Chapters. In the first 2 Chapters the results obtained are based on simulations conducted at the subsonic flow regime, whereas in the third Chapter the investigation is extended to transonic flows. The first (Chapt. 4), contains the flow description, the initial and boundary conditions, the grid convergence study and the validation of the CFD results against experimental data. The second (Chapt. 5), focuses more on the quantitative features of turbulence in such flows. More specific, measurements of turbulent kinetic energy budget, energy spectra and turbulence statistics beyond first and second statistical moments (skewness, flatness) are demonstrated. The third (Chap. 6), deals with the compressibility effects in Suddenly-Expanded Flows. The flow is inhomogeneous, turbulent and in some regions transonic, as the Mach number in the high-velocity core flow area reaches values at about 0.8. The flow physics at this flow regime are also presented.

Finally, the analysis of the key findings, the main observations, some future considerations and recommendations on Suddenly-Expanded Flows are all discussed in the last Chapter (Chap. 7).

Theory

2

Characteristics and Modelling of Turbulence

The majority of flows in our everyday surroundings are turbulent. These flows are prevalent in most of the practical engineering applications, while in many cases represent the dominant physics in all macroscopic scales. Its presence extends from the interior of biological cells, to respiratory and circulatory systems of living organisms, to a large number of household appliances and technological devices of modern world, to geophysical and astrophysical phenomena, including oceans, atmospheres and stellar physics and finally to galactic and even supergalactic scales. It is a paradox that despite the widespread occurrence and the ubiquity of turbulence, the "problem of turbulence" still remains the last unsolved problem of classical mechanics. The answer may lie on the complexity and variability that characterise turbulent flows and make the development of an integrated theory of turbulence to sound impossible.

A turbulent flow can be expected to exhibit all of the following features:

1. random, irregular and seemingly chaotic behaviour,
2. nonrepeatability (sensitivity to initial flow conditions),

3. a large number of different length and time scales,
4. strong diffusivity (turbulent mixing) and enhanced dissipation (both of which are mediated by viscosity at molecular scales),
5. three dimensionality, time-dependence and rotationality, and
6. intermittency in both space and time (the term intermittency refers to the percentage of time, in which a particular flow exhibits irregular temporal behavior at any spatial location).

Before getting through the fundamentals of turbulence, it is essential to describe the routes leading a flow from a laminar state to a turbulent one. The key element along this route is the non-linear term, $(u \cdot \nabla)u$, which appears at the Navier-Stokes Equations and lies at the root of fluid chaos. It has been found that as the relative magnitude of the non-linear term is increased, the solutions become increasingly complex, passing through a sequence of bifurcations (sudden changes), each bifurcation leading to a more complex flow state. Transition to chaos and turbulence is a general property of many non-linear systems. Landau's theory shed some light into these complicated phenomena, by predicting the route of a laminar flow through a sequence of bifurcations, leading to increasingly complex states as Reynolds number is increased, until a fully turbulent regime is established. In the next subsection, the basic properties which characterise transition to turbulence will be demonstrated.

2.1 Transition to Turbulence

Transition is the process by which a laminar flow changes to a turbulent one. It is widely known that the instability of a laminar flow does not immediately lead to turbulence. After the initial breakdown of laminar flow, a series of changes are gradually taking place, resulting in the non-linear and chaotic stage, known as turbulence (see Figure 2.1). The point in space and time in which transition appears, depends on several effects. Particularly, for channel flows these properties may include the wall roughness, the fluctuations at the inlet stream and the shape of the inlet channel. However, the most important parameter that determines if a flow is laminar, transitional or turbulent is the Reynolds number Re.

FIGURE 2.1: A schematic representation of a cigarette plume (after Jefferey [60]).

Osborne Reynolds was the first to systematically investigate the transition to turbulence by injecting a dye streak into flow through a pipe having smooth transparent and parallel walls. His observations led to the identification of a single dimensionless parameter, which as already mentioned is called Reynolds number and is defined by:

$$Re = \frac{\rho U L}{\mu} \tag{2.1}$$

This parameter was found to characterise the flow behavior in every situation. The fluid properties ρ and μ represent the density and the dynamic viscosity of the fluid flow, respectively. U is a typical value of velocity (i.e., bulk velocity or maximum velocity), while L is a typical length scale (i.e. the radius of a pipe through which fluid is flowing). Re expresses the relative importance of inertial and viscous forces.

Reynolds' experiments undertaken inside a pipe showed that the flow is laminar for Reynolds numbers less than $2,300$. At this region the fluid velocity does not change in time and all the streamlines are parallel to the axis of the pipe. On the other hand, if Re is greater than $4,000$, the instantaneous streamlines change direction erratically, and the injected dye is mixed significantly with water. At this stage the flow is considered to be turbulent. It is essential the fact that the transition to turbulence occurs over a wide range of Reynolds numbers. This range depends particularly on the details of the experiment.

Figure 2.2 schematically represents the regimes of a flow over a semi-infinite flat plate. It is shown that as the critical Reynolds number, Re_{cr}, increases the first instabilities start to appear in the downstream direction. Subsequently, a band of waves gets amplified and interacts non-linearly through advective acceleration. Finally, as the Re increases more,

the flow takes a chaotic and irregular shape further downstream. Besides, experiments carried out by Taylor and Bénard[1] revealed that the flow passes through a number of states of increasing complexity as the dynamic viscosity μ is decreased.

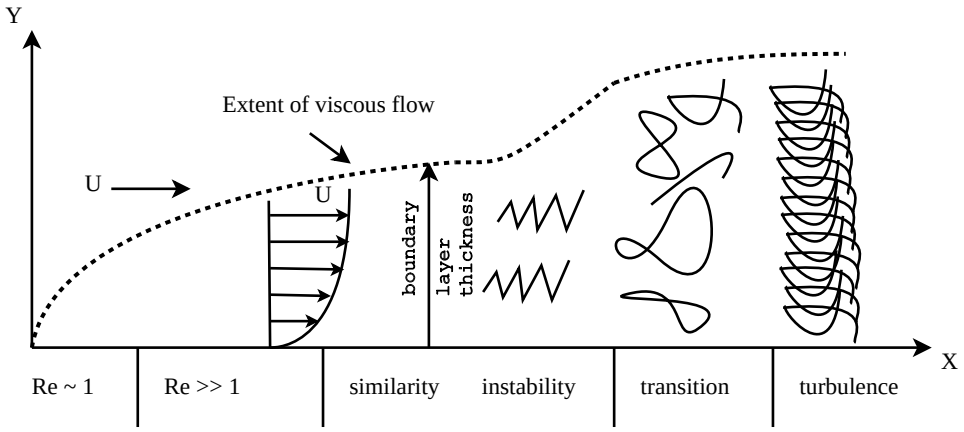

FIGURE 2.2: Schematic depiction of a flow through a semi-infinite flat plate.

The common types of change (bifurcation) of flow regimes are presented in the following lines by means of illustrative Ordinary Differential Equations (ODEs). What is common in all of these types is that changes of flow regime along the "route to turbulence", take place as the *Re* increases. Note that bifurcation, by default, is the change in the number, or in the qualitative character of the set of possible steady or unsteady flows as *Re* varies, and is often linked with the onset of instability.

- **Turning Point:** Consider a simple model problem expressed by the following quadratic equation

$$a - l(U - U_0^2) = 0 \tag{2.2}$$

where

$$a = k(Re - Re_{cr}) \quad for \quad k > 0 \quad , \quad l \neq 0$$

and U_0, Re_{cr} are constants. U represents a given velocity component of the fluid at some given point of a steady flow, as a function of the *Re*. Rearranging Equation (2.2) and solving it for the variable U, we take:

[1]Taylor investigated the behavior of a flow between concentric cylinders and showed that as the rotation rate of the inner cylinder increases, the flow becomes progressively more complex until eventually turbulence sets in. Bénard carried out experiments of a flow held between two parallel, flat plates, where the lower plate was heated. At low temperature values ΔT the fluid is at rest and as ΔT is increased, natural convection in the form of regular convection sets in at a starting stage, taking finally a form of turbulent flow [20].

$$U = U_0 \pm [k(Re - Re_{cr})/l]^{\frac{1}{2}} \tag{2.3}$$

The solutions arising from the above equation are:

1. two solutions when $k(Re - Re_{cr})/l > 0$,
2. one solution for the case $Re = Re_{cr}$ and
3. none when $k(Re - Re_{cr})/l < 0$.

In Figure 2.3 the bifurcation diagram of velocity component U against Re is shown for the case where $k, l > 0$. A simple turning point, or saddle-node bifurcation at $Re = Re_{cr}$ is present. That particular point, in which $U = U_0$, is also called a bifurcation point, as the number and character of the solutions change in that location.

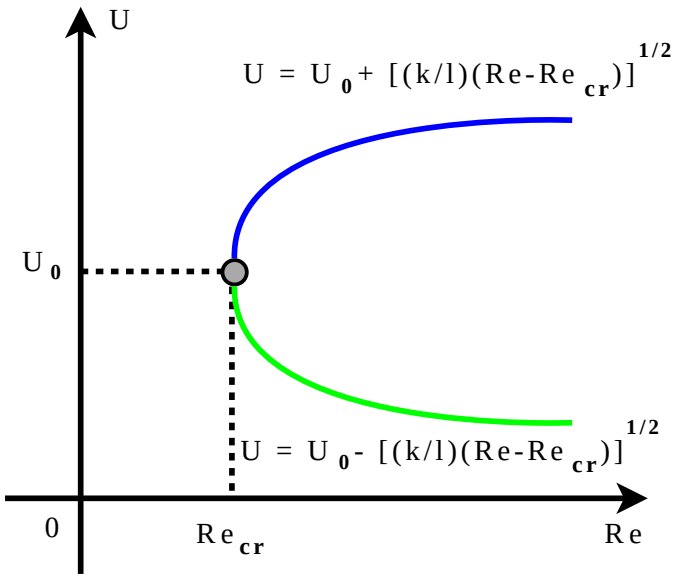

FIGURE 2.3: Bifurcation diagram for the turning point in the (Re, U) - plane for the case where $k, l > 0$.

- **Transcritical Bifurcation:** Consider again a simple model problem of bifurcation encompassing steady solutions of the NSE, expressed by the following quadratic equation:

$$aU - lU^2 = 0 \tag{2.4}$$

For all $Re \neq Re_{cr}$, there are two solutions in the above equation.

$$U = 0 \quad or \quad U = a/l = k(Re - Re_{cr})/l$$

The bifurcation at $Re = Re_{cr}$, $U = 0$ is an example of what is called a transcritical point (see Figure 2.4).

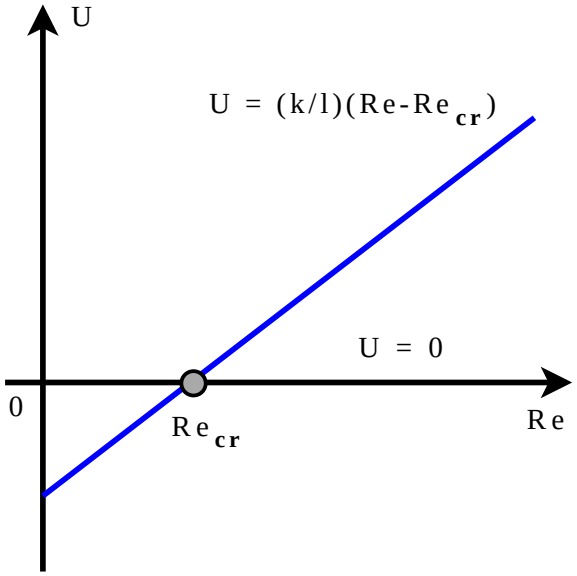

FIGURE 2.4: Bifurcation diagram for the transcritical point in the (Re, U) - plane for the case where $k, l > 0$.

- **Pitchfork Bifurcation:** The model equation used to address a different type of bifurcation is:

$$aU - lU^3 = 0 \tag{2.5}$$

which is typical for the first bifurcation of flows with symmetry in $\pm U$. Rearranging Equation (2.5) and solving it for the variable U, we take:

$$(U^2 = \tfrac{a}{l}) \quad \longrightarrow \quad U = \pm\sqrt{\tfrac{k(Re-Re_{cr})}{l}} \tag{2.6}$$

1. For $Re = Re_{cr} \quad \longrightarrow \quad U = 0$
2. For $k(Re - Re_{cr})/l > 0 \quad \longrightarrow \quad U = \pm[k(Re - Re_{cr})/l]^{1/2}$

There is said to be a pitchfork bifurcation at $Re = Re_{cr}$, $U = U_0$. A symmetry breaking at $Re = Re_{cr}$ takes place, in the sense that if $k, l > 0$, there is a unique symmetric solution for $Re < Re_{cr}$, but there is also a pair of asymmetric solutions for $Re > Re_{cr}$, as that can be shown in Figure 2.5.

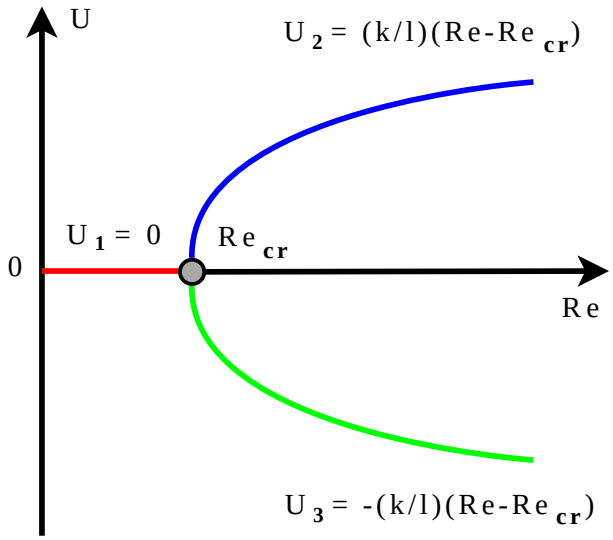

FIGURE 2.5: Schematic representation of a pitchfork bifurcation diagram in the (Re, U) - plane for the case where $k, l > 0$.

This specific type of bifurcation is encountered in suddenly-expanded flows at particularly low Reynolds numbers. The critical Reynolds number in such flows depends on the geometrical characteristics of the channel (such as the expansion ratio, the aspect ratio, etc.). Numerical simulations also showed that the Re_{cr} can be affected by small numerical instabilities arising from the numerical scheme used, the initial and boundary conditions applied, the time step, as well as the time interval for which the calculation proceeds.

The symmetry breaking of all flows in diverging channels is an example of what is widely known as Coanda effect. Laboratory and numerical experiments in that flow types revealed the occurrence of a supercritical pitchfork bifurcation and symmetry breaking. The classic prototype of symmetry breaking can be typically expressed by Landau's equation (model of hydrodynamic stability by Landau in 1944, [72]):

$$\frac{du}{dt} = au - lu^3 \tag{2.7}$$

Two different cases can be distinguished according to the sign of the Landau constant l.

1. a subcritical stability for $l < 0$, and

2. a supercritical stability for $l > 0$.

Particularly, for the case where l is greater than zero, two stable solutions for $Re > Re_{cr}$ and one unstable solution $u = 0$ are forming. Note that:

$$if \quad Re > Re_{cr}, \quad u(t) \rightarrow sign[u(0)][k(Re - Re_{cr})/l]^{1/2} \quad as \quad t \rightarrow \infty$$

whereas

$$if \quad Re \leq Re_{cr}, \quad u(t) \rightarrow 0 \quad as \quad t \rightarrow \infty$$

In the former case the final state depends only on the sign of the initial value $u(t_0)$ of U, and in the latter case the final state is the same for all initial values. The bifurcation diagram of a supercritical stability obtained from the Landau equation for $l > 0$ is depicted in Figure 2.6.

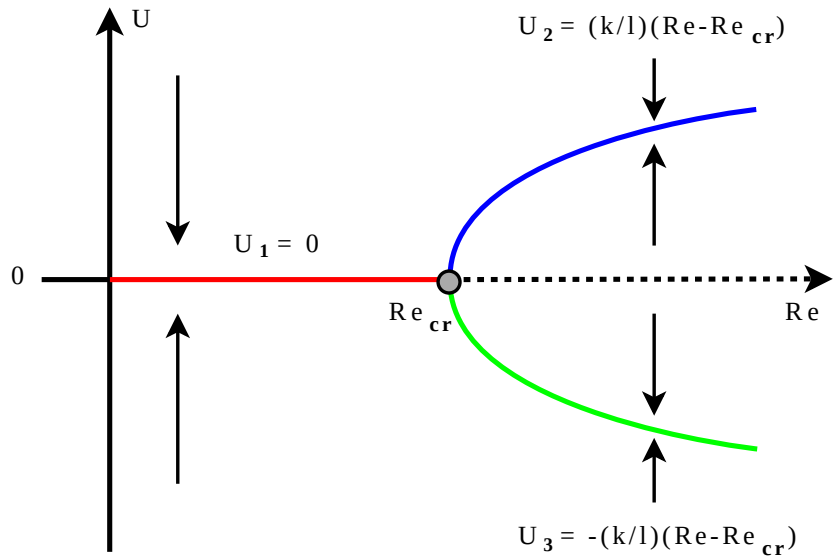

FIGURE 2.6: Bifurcation diagram of a supercritical stability by setting Landau's constant $l > 0$.

Below a brief summary of routes to turbulence, or at least to chaotic flow are presented. Note that there are only a few routes that lead to turbulence. Based on this observation, an attempt will be made to put them in order [25].

1. **Subcritical Instability:** On this route a stable, steady, periodic or quasi-periodic flow becomes unstable as Re increases gradually through a critical value, and the flow then "jumps" rapidly to a turbulent one. This type of turbulence development

has been variously called “abrupt”, “fast” and “savage”. Poiseuille flow in a pipe, plane Poiseuille flow, as well as plane Couette flow are some typical examples of flows where this abrupt onset of turbulence has been found. For such flows this is often called bypass transition.

2. **Ruelle-Takens-Newshouse route:** This route was first discovered by Ruelle & Takens (1971, [96]) and later redefined by Newshouse et al. (1978, [89]) by use of the theory of dynamical systems. Along this route, there is a succession of bifurcations as *Re* increases in which a steady flow may directly, or via other steady flows become time periodic, then quasi-periodic with two or even more frequencies, until a chaotic flow sets in. This route is commonly found in Couette flow between rotating cylinders and Rayleigh-Bénard convection flow.

3. **Periodic Doubling:** In some cases turbulence, or even chaos, takes place after a procession of periodic doubling bifurcations, as Reynolds number increases. Here a sequence of time-periodic flows occur at bifurcations, in which the period of one flow is twice the period of the previous one.

4. **Amplification due to Flow Instability and Perturbation**

2.2 Turbulent Flow Physics

As already mentioned in a preceding section, turbulent flows can be characterised as three-dimensional, which means that the instantaneous field fluctuates rapidly in all three dimensions. They are highly time dependent and are dominated by a broad range of time and length scales. Furthermore, turbulent flows contain vorticity, as it is known that vortex stretching leads to the growth of turbulence intensity. They increase heat transfer and skin friction and promote enhanced mixing of fluids. Turbulence in some cases leads to the delay of flow separation.

It is worth emphasising more in the wide range of length and time scales encountered in turbulent flows. In fact, this is the most important reason for “turbulent problem” to be unsolved for so many years. This is also the reason that Direct Numerical Simulations are precluded from modelling turbulent flows (extremely expensive in terms of the computational cost).

The formation of eddies of so many different length scales makes it requisite to distinguish the large-scale from the small-scale motions. The large-scale motion is influenced

by the geometry of the flow, whereas the behavior of the small-scale motion is determined by two factors: a) the rate at which the flow receives energy from the large scales and b) by the viscosity.

It is important to mention that most of the kinetic energy of turbulent motion is contained in the large-scale structures. The energy then "cascades" from these large structures to smaller one by an inertial and essentially inviscid mechanism. This process continues, creating smaller and smaller structures which produces an hierarchy of eddies as shown in Figure 2.7. Eventually, this process creates structures that are small enough such that molecular diffusion becomes important and viscous dissipation of energy occurs. The scale at which this last process takes place is commonly known as the Kolmogorov length scale.

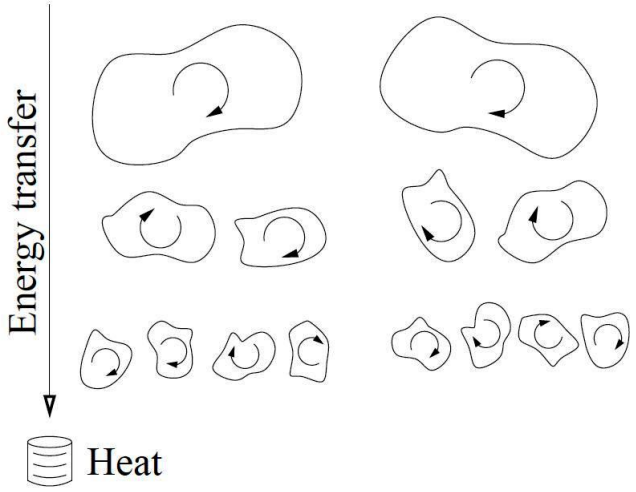

FIGURE 2.7: A schematic representation of the multistage process of energy cascade (after Davidson [20]).

There are four main sets of scales in a turbulent flow; these are the following:

1. the large scale, which is based on the problem domain geometry. The bulk of energy is mainly contained in these large eddies (i.e., the so-called energy containing eddies),

2. the integral scale, which is an $\mathcal{O}(1)$ fraction (usually taken the value of ~ 0.2) of the large scale,

3. the Taylor microscale, which is an intermediate scale, particularly corresponding to Kolmogorov's inertial subrange, and

4. the Kolmogorov (or "dissipation") scale which constitutes the smallest of turbulent scales.

Before continuing with the description of each of the aforementioned turbulent scales, it is worth comparing the scales in terms of their spatial wavenumbers. The spectrum of eddies can be divided up into three ranges. The energy containing range, the inertial sub-range and the universal equilibrium range. Assuming that the magnitude of Reynolds number is high enough for the inertial subrange to be relatively large, as shown in Figure 2.8, the following observations can be made:

1. at low *Re* there is essentially no inertial range, and as *Re* increases the length of this range increases. Note that the inertial range, or sub-range, is the range of length scales (or wavenumbers) in which viscous effects, as well as the effects of the large scales are negligible.

2. the range of wavenumbers appearing in the large and integral scale is slightly affected by increasing *Re*.

3. the range of dissipation scales is strongly influenced by *Re*.

4. the wavenumber range covered by inertial scales increases with increasing *Re*.

5. according to Kolmogorov's hypothesis, the slope in the spectrum of the inertial sub-range is $-5/3$ (see Figure 2.8), and

6. the highest energy is associated with larger scales of motion.

Starting with the description of the largest scales, it is important to define a characteristic length L (for example, for channel flows this could be the height of the duct, or the diameter or radius for a flow through pipes), and a characteristic velocity U (this could also be the mean, or possibly the centerline velocity in a pipe, or the freestream velocity over an airfoil). The corresponding Reynolds number could then become:

$$Re_L = \frac{UL}{\nu} \tag{2.8}$$

where ν is the kinematic viscosity. A "convective" time scale can also be derived from the above length and velocity scales by:

$$t_c = \frac{L}{U} \tag{2.9}$$

A "diffusive" time scale can also be obtained from the given physical quantities, particularly considering the units of the kinematic viscosity, L^2/T. Then it follows that

$$\nu = L^2/T \rightarrow t_d = \frac{L^2}{\nu} \tag{2.10}$$

Comparing the rate at which flow properties are transferred by molecular diffusion, to those transferred by macroscopic convection we have:

$$\frac{t_d}{t_c} = \frac{L^2/\nu}{L/U} = Re_L \tag{2.11}$$

This is another way of defining the ratio of inertial to viscous forces by using the ratio of the time (diffusive and convective) scales.

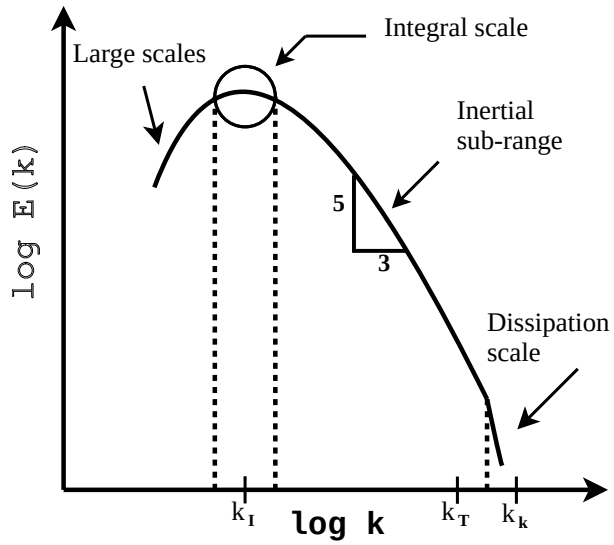

FIGURE 2.8: Schematic representation of turbulence energy wavenumber spectrum.

As far as the integral scales are concerned, the length scales can be obtained from the following expression:

$$l = \frac{1}{\|u'\|_{L^2}^2} \int_{-\infty}^{\infty} u'(x,t)u'(x+r,t)dr \tag{2.12}$$

where u' denotes a turbulent fluctuating component of velocity and $\|\cdot\|_{L^2}^2$ is taken with respect to the spatial domain $\mathscr{V}$. The integral scale Reynolds number (often called "turbulence" Reynolds number) can be interpreted by:

$$Re_l = \frac{\left|u'\right| l}{\nu} \tag{2.13}$$

where

$$\left|u'\right| = \sqrt{\frac{1}{N}\sum_{i=1}^{N}(u_{instant} - \langle U_N \rangle)^2}$$

is usually taken to be the square root of the turbulent kinetic energy per unit mass, i.e., $\left|u'\right| = k^{1/2}$ with $k = \frac{1}{2}(u'^2 + v'^2 + w'^2)$. The time scales at this wavenumber range can be obtained from:

$$T = \int_0^\infty c_a(\tau) d\tau \tag{2.14}$$

where c_a is the autocorrelation coefficient defined as:

$$c_a(x,t) \equiv \frac{\langle u(x,t), u(x,t+\tau) \rangle}{\|u'\|_{L^2}^2} \quad , \quad -1 \leq c_a(x,t) \leq 1$$

The integral time scale is a measure of how long turbulent fluctuations remain correlated. Note that the term denoted by $\langle \cdot \rangle$ is the so-called ensemble average which is a result of averaging a physical quantity over a large number of realisations.

The third length scale is the Taylor microscale which is characteristic of the mean spatial extension of the velocity gradients, and is defined by [115]:

$$\lambda^2 = \frac{\left\langle \left| \vec{u}' \right|^2 \right\rangle}{\left\langle (\vec{\nabla} \times \vec{u})^2 \right\rangle} \tag{2.15}$$

The turbulence energy dissipation rate ε, usually given by

$$\varepsilon = 2\nu \left| (\vec{\nabla} \times \vec{u})^2 \right|$$

can be used in conjunction with Equation (2.15) yielding to the following length scale

$$\lambda = \left[\frac{\nu \left\langle \left| \vec{u}' \right|^2 \right\rangle}{\varepsilon} \right]^{1/2} \tag{2.16}$$

The Taylor microscale Reynolds number is calculated as follows:

$$Re_\lambda = \frac{\left| \vec{u}' \right| \lambda}{\nu} \tag{2.17}$$

The corresponding time scale can be easily calculated by using the length scale of Equation (2.16) along with the velocity $\left| \vec{u}' \right|$. Note that Taylor microscale length is about consistent with the Kolmogorov inertial sub-range scale.

The last characteristic length scale to be defined is the Kolmogorov scale. According to Kolmogorov's hypothesis, in every turbulent flow at high *Re* the statistics of the small-scale motions have a universal form, which is uniquely determined by the kinematic viscosity ν and the average rate of energy dissipation ε. The Kolmogorov length scales can be obtained using dimensional analysis of the aforementioned quantities. Note that the generalised units of kinematic viscosity are L^2/T, and those for energy dissipation rate are:

$$\varepsilon = \frac{u^3}{l} = \frac{L^3}{T^3 L} = \frac{L^2}{T^3}$$

It follows that a length scale can be obtained by eliminating time between these two sets of units. The resulting Kolmogorov scale is given by:

$$\eta = \left(\frac{\nu^3}{\varepsilon} \right)^{1/4} \tag{2.18}$$

In similar manner (employing dimensional analysis), a Kolmogorov time scale can be constructed as:

$$\tau = \left(\frac{\nu}{\varepsilon} \right)^{1/2} \tag{2.19}$$

The Kolmogorov velocity scale is obtained by taking the ratio of two last quantities leading to:

$$\upsilon = (\nu\varepsilon)^{1/4} \tag{2.20}$$

If we try to define the Reynolds number using 2.18 and 2.20 we are ending up with the following expression:

$$Re_{Kolm} = \frac{\upsilon\eta}{\varepsilon} = \frac{\left(\frac{\nu^3}{\varepsilon}\varepsilon\nu\right)^{1/4}}{\nu} = \frac{\left(\nu^4\right)^{1/4}}{\nu} = 1 \tag{2.21}$$

which is expected on scales where viscous dissipation dominates all other phenomena.

Kolmogorov's theory [70, 71] of a universal equilibrium range is one of the most remarkable, if not the most notable, theories in the history of turbulence. The reason why this theory is so important is that its prediction (the so-called two-thirds law) turns out to be quite robust for a large number of turbulent flows. Thus, Kolmogorov's first and second similarity hypotheses are widely used when modelling turbulent flows.

According to the first similarity hypothesis, for the locally isotropic turbulence, assuming that Re is large enough, the statistical properties of the structure function $[\Delta V(r)]$ have a universal form which depends only on ε, r and ν. The structure function $[\Delta V]^2$ is of the order of all the energy contained in eddies of size r or less and is given by the following relation [20]:

$$\left\langle [\Delta V(r)]^2 \right\rangle = \upsilon^2 F(r/\eta) \tag{2.22}$$

where υ and η the Kolmogorov microscales of velocity and length, respectively. Since the large scales have only an indirect influence on the small scales and considering the fact that the global geometry has an impact only on the large scales (low wavenumber regime), $F(r/\eta)$ is expected to be a universal function, valid for all forms of turbulence. Several turbulent flow models that have been experimentally investigated in the past, indicate that F does indeed appear to be universal.

Now consider a sub-domain of the universal equilibrium range, as that is shown in Figure 2.9. The so-called inertial sub-range, which satisfies the relation $\eta << r << l$, followed by the Kolmogorov's second similarity hypothesis, is not expected to include ν as a relevant parameter and that leads to the following Kolmogorov's allegation.

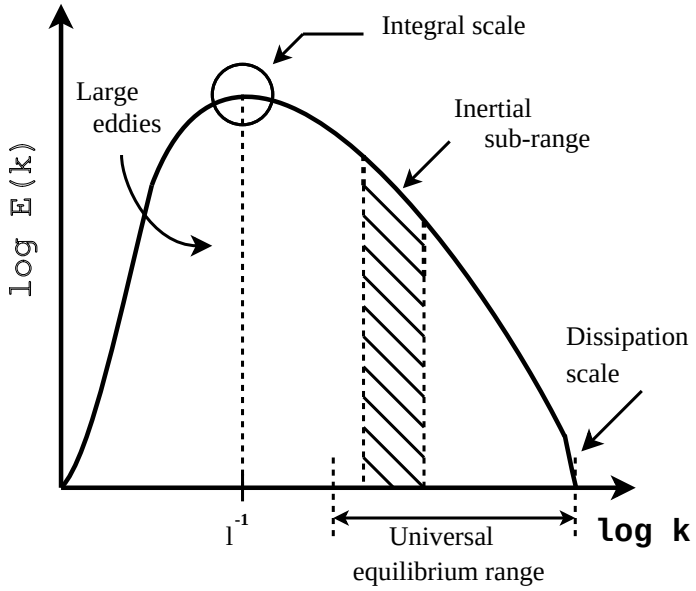

FIGURE 2.9: The energy cascade in terms of kinetic energy versus wavenumber in log log scale, showing the universal equilibrium range.

In the range $\eta << r << l$, assuming that Re is high enough, the statistical properties of $[\Delta V(r)]$ have a universal form which is uniquely determined by the quantities ε and r and do not depend on ν. The only way of eliminating the quantity ν from Equation (2.22) is if $F(x) \sim x^{2/3}$. So taking this last prerequisite into account, the structure function of the inertial sub-range will take the form:

$$\left\langle [\Delta V(r)]^2 \right\rangle = \beta \varepsilon^{2/3} r^{2/3} \tag{2.23}$$

where β is a universal constant, found to have a value of ~ 2 [94]. This is also known as Kolmogorov's two-thirds law. In terms of energy spectrum Equation (2.23) takes the form:

$$E(k) = C\varepsilon^{2/3} k^{-5/3} \tag{2.24}$$

Equation (2.24) is known as Kolmogorov's five-thirds law, in which C is a universal Kolmogorov constant. Experimental data support the value of $C = 1.5$ [94]. The table below shows the properties of the turbulent scales in terms of their range r and form of structure function.

TABLE 2.1: Range of r and approximate form of the structure function $[\Delta V(r)]^2$ at high Re.

Name	Range	Form of $[\Delta V(r)]^2$
Energy Containing Range	$r \sim l$	$\left\langle [\Delta V(r)]^2 \right\rangle = u^2 F(r/l)$
Inertial Sub-range	$\eta << r << l$	$\left\langle [\Delta V(r)]^2 \right\rangle = \beta \varepsilon^{2/3} r^{2/3}$
Universal Equilibrium Range	$r << l$	$\left\langle [\Delta V(r)]^2 \right\rangle = \nu^2 F(r/\eta)$

Very high values of Re are necessary for the appearance of the inertial sub-range. Particularly, if we are to obtain a range of r in which $\eta << r << l$, then the following relation should be observed [20]:

$$Re^{3/8} >> 1$$

2.3 Modelling of Turbulent Flows

2.3.1 Explicit LES

Large Eddy Simulation (LES) is a common technique for simulating turbulent flows. This technique is based on the fact that the large eddies of the flow are dependent on the geometry while the smaller scales, according to Kolmogorov's theory, are more universal. This is the reason why the large eddies are explicitly solved, while the small eddies are represented statistically, by using a subgrid-scale (SGS) model. Separating the velocity field into a resolved (for the large eddies) and sub-grid (for the small eddies) part and using a spatial filtering operation of a variable $f(x,t)$, we obtain the following [75, 93, 98]:

$$\widetilde{f(x,t)} = \int_{-\infty}^{+\infty} \int G_s(x-x') f(x',t) dx' dy' dz' \tag{2.25}$$

where $G_s(x)$ are the spatial components of the filter, associated with the cutoff scales in space. The most widely used filters are the box or top hat filter, the Gaussian filter and the spectral or sharp cutoff filter. Note that the fluctuating component, $f^{'}$, is defined by $f^{'} = f - \tilde{f}$ and that in LES the mean value of a fluctuating flow component is not zero ($f^{'} \neq 0$). The filtering operation process then, implemented into the Navier-Stokes equations for a compressible flow can be written as:

$$\left.\begin{aligned} \frac{\partial \overline{\rho}}{\partial t} + \frac{\partial \overline{\rho}\tilde{u}_j}{\partial x_j} &= 0 \\ \frac{\partial \overline{\rho}\tilde{u}_i}{\partial t} + \frac{\partial \overline{\rho}\tilde{u}_i\tilde{u}_j}{\partial x_j} &= -\frac{\partial \tilde{p}}{\partial x_i} + \frac{\partial \hat{\sigma}_{ij}}{\partial x_j} - \frac{\partial \overline{\rho}\tau_{ij}^{SGS}}{\partial x_j} \end{aligned}\right\} \tag{2.26}$$

where $\tilde{u}_i$ and $\tilde{p}$ are the filtered velocities and pressure, respectively, and τ_{ij}^{SGS} are the subgrid-scale (SGS) stresses given by:

$$\tau_{ij}^{SGS} = \widetilde{u_i u_j} - \tilde{u}_i \tilde{u}_j \tag{2.27}$$

Consider that the velocity component u_i in every turbulent flow equals the sum of its mean $\overline{u}_i$ and its fluctuating part $u_i^{'}$.

$$u_i = \overline{u}_i + u_i^{'}$$

Using the above equation, the term $\widetilde{u_i u_j}$ takes the following form:

$$\widetilde{u_i u_j} = (\widetilde{\overline{u}_i + u_i^{'}})(\widetilde{\overline{u}_j + u_j^{'}}) = \widetilde{\overline{u}_i \overline{u}_j} + \widetilde{\overline{u}_i u_j^{'}} + \widetilde{u_i^{'} \overline{u}_j} + \widetilde{u_i^{'} u_j^{'}} \tag{2.28}$$

Note that the overbar denotes a filter operation, which commutes with the partial derivatives $\frac{\partial}{\partial t}$ and $\frac{\partial}{\partial x_j}$. The second filter, represented by a tilde, refers to the Favre filter operation. On the other hand, the 'hat' symbol does not refer to a filter operation, but shows that the quantity is based on filtered variables.

The final form of the subgrid-scale stresses after substituting Equation (2.28) into Equation (2.27) becomes:

$$\tau_{ij}^{SGS} = (\widetilde{\overline{u}_i \overline{u}_j} - \bar{u}_i \bar{u}_j) + (\widetilde{\overline{u}_i u_j^{'}} + \widetilde{u_i^{'} \overline{u}_j}) + \widetilde{u_i^{'} u_j^{'}} \tag{2.29}$$

The first term in brackets at the RHS of the above equation represents the so-called Leonard stresses (interaction between resolved scales), the second term in brackets the cross stress tensor (interaction between resolved and unresolved scales) and the third term represents interactions between unresolved scales.

2.3.2 Implicit LES

The explicit subgrid-scale models presented in the previous subsection, come up in the high-resolution schemes as the combined result of flux-form differencing (i.e., direct consequence of averaging the inertial terms over a grid cell) and the fundamentally nonlinear nature of the non-oscillatory approximations. Besides, in the case of modern high-resolution methods, the numerical method provides an effective differential equation that has many explicit LES models embedded implicitly in the solution technique. In other words, high-resolution methods contain a "built-in" or embedded subgrid-scale (SGS) model. Ghosal (1996,[48]) pointed out that the truncation terms have the same order of magnitude as the SGS terms in explicit LES.

Drikakis and Rider [32] used the modified equation analysis to investigate the form of truncation error arising from various non-oscillatory finite volume methods and its similarity with the conventional subgrid-scale models (see Smagorinsky, dynamic Smagorinsky and Leonard model). As a starting point, they considered the one-dimensional high-resolution algorithm that has the following form:

$$U_j^{n+1} = U_j^n - \frac{\Delta t}{\Delta x}\left[E(U_{j+1/2}) - E(U_{j-1/2})\right] \tag{2.30}$$

Using a high-resolution Godunov method based on reconstruction and employing nonlinear limiter slopes, $S_j(U)$, two edge values in each grid cell is produced such that:

$$U_{j\pm 1/2;L/R} = U_j \pm \frac{1}{2} S_j \tag{2.31}$$

These two values at the left and right face of each cell can be resolved by a linearised Riemann solver, as follows:

$$E(U_{j+1/2}) = \frac{1}{2}\left[E_{j+1/2;R} + E_{j+1/2;L}\right] - \frac{\left|E^{'}\right|}{2}\left[U_{j+1/2;R} - U_{j-1/2;L}\right] \tag{2.32}$$

with

$$E^{'}(U) = \frac{\partial E}{\partial U} \tag{2.33}$$

being the flux Jacobian (exact details of the Jacobian of the flux vectors can be found in Appendix A). The truncation error produced for this general form of modified equation is

of order Δ^2 and is given by:

$$\mathscr{T}(U) = C_1 E^{'}(U)\frac{\partial^2 U}{\partial x^2} + C_2 E^{''}(U)\left(\frac{\partial U}{\partial x}\right)^2 \tag{2.34}$$

The effective subgrid stress $\mathscr{T}(U)$ is a second order approximation with C_1 and C_2 depending on the particular differencing (NFV) scheme. The second term on the RHS of Equation (2.34) is identical to the effect of a self-similar model encountered in conventional LES. Note also that this specific term, $E^{''}(U)\left(\frac{\partial U}{\partial x}\right)^2$ is a consequence of the conservation form of the equations, arising from the finite volume approximation along with high-resolution non-oscillatory schemes (such as ENO, WENO, TVD and TVB schemes).

MEA analysis has been carried out by Drikakis and Rider [32] for a third-order and a fifth-order WENO scheme. For the third-order WENO the effective subgrid stress found to have the same form as van Leer and van Albada limiters with the physical dissipation being of order Δ^3, whereas for the fifth-order WENO the physical dissipation has an order of Δ^5, as that can be seen in the following relation:

$$\mathscr{T}(U) = C\Delta^5 \left|E^{'}(U)\right| \left(\frac{\partial^3 U}{\partial x^3}\right)^2 \left(\frac{\partial U}{\partial x}\right)^{-1} \tag{2.35}$$

High-resolution methods can all be characterised as dissipative. However, all models are not equivalent, in the sense that they all have different dissipation properties. Margolin and Rider [80] showed that the physical dissipation of a numerical scheme should be of order Δ^2. It is, hence, important to further investigate the capability of high-order, nonlinear schemes of resembling the physical dissipation of a turbulent flow in the correct level.

To summarise, ILES can be considered as a useful research tool for numerically simulating turbulent flows. Grinstein, Margolin and Rider [52] stated that ILES works because it solves the equations that most accurately represent the dynamics of finite volumes in a fluid - i.e, governing the behaviour of physical measurable quantities on the computational cells.

3

Governing Equations and Numerical Modelling

3.1 Governing Equations

The derivation of the basic equations of fluid motion is based on three fundamental physical principles.

1. The mass of fluid is conserved
2. The rate of change of momentum equals the sum of the forces on a fluid particle (Newton's second law, $\sum F = m \cdot \frac{dv}{dt}$) and
3. The rate of change of energy is equal to the sum of the rate of work done on a fluid particle and the rate of heat addition to the fluid particle (First law of thermodynamics)

These physical principles are applied to a suitable model of the flow which can be either a finite control volume $\mathscr{V}$ or an infinitesimally small fluid element with a differential

fluid $d\mathscr{V}$. The corresponding fluid-flow equations can be expressed in either integral or partial differential form. The equations obtained from a finite control volume fixed in space, in either integral or partial differential form, are called the conservation form of the governing equations. On the other hand, the equations obtained from a finite control volume moving with the fluid, in either integral or partial differential form, are called the non-conservation form of the governing equations. Note also that one form can be obtained from the other, after applying some simple manipulation. There are cases in CFD where it is very important which form is used.

3.1.1 Conservation of Mass

The continuity equation is based on the physical principle that the mass is conserved which means that the net mass flow out of a control volume (CV) through surface S, equals the time rate of decrease of mass inside the CV.

Consider the flow model shown in Figure 3.1. The net mass flow of a moving fluid across any fixed space is equal to the product of (density) $\times$ (velocity component perpendicular to the surface) $\times$ (area of surface). Thus the elemental mass flow across the area dS is:

$$\rho V_n dS = \rho \mathbf{V} \cdot \mathbf{dS} \tag{3.1}$$

where $\mathbf{V} = ui + \upsilon j + wk$ is the velocity vector.

The net mass flow out of the entire CV through surface S is the summation over S of the elemental mass flow, expressed in Equation (3.1). In the limit, this becomes a surface integral where

$$\rho \mathbf{V} \cdot \mathbf{dS} \rightarrow \iint_S \rho \mathbf{V} \cdot \mathbf{dS} \tag{3.2}$$

Note that when $\mathbf{V}$ points out of the control volume, the product $\rho \mathbf{V} \cdot \mathbf{dS}$ is positive and the flow state can be considered as an *outflow.* On the other hand, when $\mathbf{V}$ points into the control volume, the product $\rho \mathbf{V} \cdot \mathbf{dS}$ is negative and the flow state can be considered as an *inflow.*

The time rate of decrease or increase of mass inside the CV is given by:

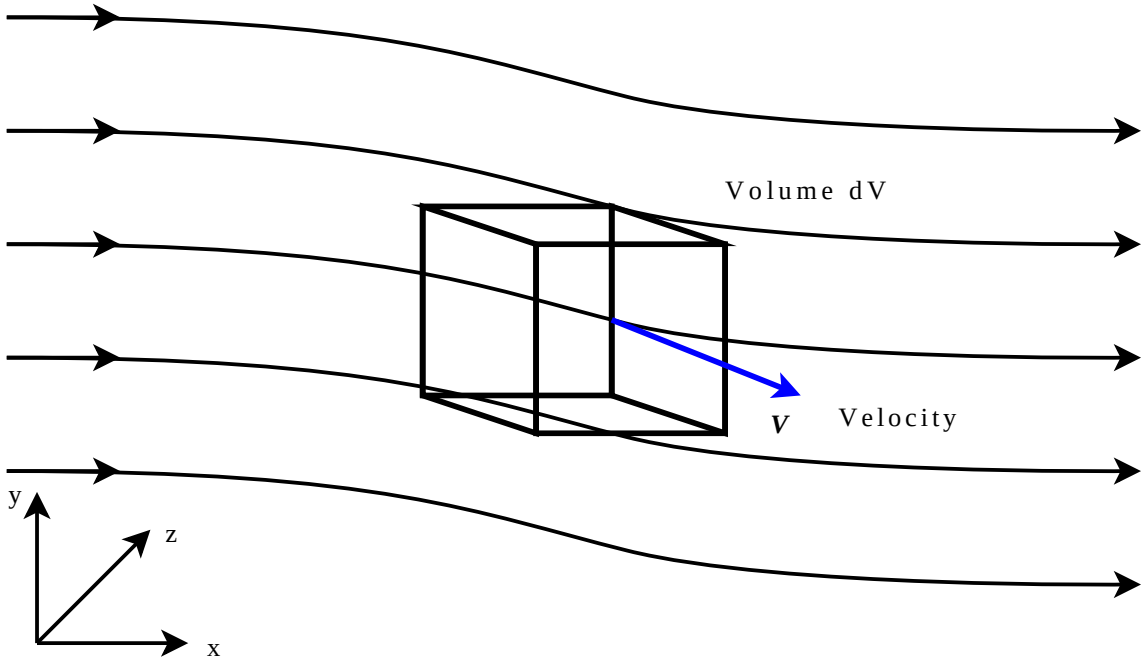

FIGURE 3.1: Infinitesimal control volume fixed in space with the fluid moving through it.

$$\frac{\partial}{\partial t}\iiint_{\mathscr{V}} \rho d\mathscr{V} \tag{3.3}$$

Thus, the final expression of the integral form of the continuity equation in conservation form is:

$$\frac{\partial}{\partial t}\iiint_{\mathscr{V}} \rho d\mathscr{V} + \iint_{S} \rho \mathbf{V} \cdot \mathbf{dS} = 0 \tag{3.4}$$

3.1.2 Conservation of Momentum

The momentum equation is based on the physical principle of Newton's second law which states that:

> "The force exerted on a body is equal to the time rate of change of momentum."

The time rate of change of momentum as it moves through the fixed CV is the sum of two terms:

- Time rate of change of momentum due to unsteady fluctuations of flow properties inside the CV, and
- Net flow of momentum through the CV across surfaces of area S.

The momentum of an infinitesimally small portion ($d\mathscr{V}$ of the CV of volume $\mathscr{V}$) is simply given by

$$\rho \mathbf{V} d\mathscr{V} \tag{3.5}$$

where $\rho \mathbf{V} = [\rho u, \rho v, \rho w]^{Transpose}$.

Thus, the variation in time of momentum inside a CV can be expressed in integral form as:

$$\frac{\partial}{\partial t} \iiint_{\mathscr{V}} \rho \mathbf{V} d\mathscr{V} \tag{3.6}$$

The second term comprises the convective flux tensor which describes the transfer of momentum across the boundary of the CV and in the Cartesian coordinate system consists of three components:

$$\left\{ \begin{array}{l} x-component : \rho u \mathbf{V} \\ y-component : \rho v \mathbf{V} \\ z-component : \rho w \mathbf{V} \end{array} \right\} \tag{3.7}$$

Thus, the contribution of the convective flux tensor to the conservation of momentum is given by:

$$\iint_{S} \rho \mathbf{V} (\mathbf{V} \cdot \mathbf{dS}) \tag{3.8}$$

The forces that the fluid elements are exposed to are of two types. The first category includes the body forces, i.e. inertial forces, gravitational forces, electromagnetic forces, which act directly on the volumetric mass of the fluid element. The contribution of the body forces per unit volume, $\rho \mathbf{f}_b$, to the momentum conservation is:

$$\iiint_{\mathscr{V}} \rho \mathbf{f}_b d\mathscr{V} \tag{3.9}$$

The second category includes the surface forces, which act directly on the surface of the CV and are due to two sources:

1. the pressure distribution, which in turn acts on the surface of the fluid element and is imposed by the outside fluid surrounding the volume, and
2. the normal and shear stresses

Thus, the contribution of the surface forces to the momentum conservation is given by:

$$-\iint_S p\mathbf{dS} \tag{3.10}$$

for the pressure distribution, where p stands for the pressure, and also by:

$$\iint_S \bar{\bar{\tau}}\mathbf{dS} \tag{3.11}$$

for the normal and shear stress components, where $\bar{\bar{\tau}}$ is the stress tensor.

Adding all the above contributions to the general conservation law, the momentum conservation inside an arbitrary control volume $\mathscr{V}$ that is fixed in space can be expressed as:

$$\frac{\partial}{\partial t}\iiint_{\mathscr{V}} \rho\mathbf{V}d\mathscr{V} + \iint_S \rho\mathbf{V}(\mathbf{V}\cdot\mathbf{dS}) = \iiint_{\mathscr{V}} \rho\mathbf{f}_b d\mathscr{V} - \iint_S p\mathbf{dS} + \iint_S \bar{\bar{\tau}}\mathbf{dS} \tag{3.12}$$

3.1.3 Conservation of Energy

The energy equation is based on the principle of the first law of thermodynamics which states that:

> "The energy in an isolated system can be neither created nor destroyed, but only can change forms."

In other words, the rate of change of energy inside a fluid element is equal to the net flux of heat into element plus the rate of work done on element thanks to body and surface forces. The total energy per unit mass, E, of a fluid is obtained by adding its internal

energy per unit mass, e, to its kinetic energy per unit mass, $|\mathbf{V}|^2/2$. Hence, the total energy per unit mass can be expressed as:

$$E = e + \frac{|\mathbf{V}|^2}{2} = e + \frac{u^2 + v^2 + w^2}{2} \tag{3.13}$$

In this case the conserved quantity is the total energy per unit volume, ρE, and its variation in time within the volume $\mathscr{V}$ is given by:

$$\frac{\partial}{\partial t} \iiint_{\mathscr{V}} \rho E d\mathscr{V} \tag{3.14}$$

The contribution of the convective flux to the energy conservation equation is:

$$- \iint_{S} \rho E \mathbf{V} \mathbf{dS} \tag{3.15}$$

Additionally, the net heat flux consists of two parts. The first is the heat flux due to volumetric rate of heat addition per unit mass or due to chemical reactions and is denoted by $\dot{q}_h$. The second part is the net heat flux due to temperature gradients and according to Fourier's law of heat conduction, the local heat flux is equal to the product of the thermal conductivity coefficient k and the negative local temperature gradient, $-\nabla T$. Thus, the contribution of the diffusive (heat) flux to the conservation of energy can be split into two parts as follows:

$$\begin{gathered} \iiint_{\mathscr{V}} \dot{q}_h d\mathscr{V} \\ \iint_{S} k \nabla T \mathbf{dS} \end{gathered} \tag{3.16}$$

The rate of the total work done over the complete CV, due to body forces, is given by the following integral:

$$\iiint_{\mathscr{V}} (\rho \mathbf{f}_b \cdot \mathbf{V}) d\mathscr{V} \tag{3.17}$$

Finally, the surface forces, $\mathbf{f}_s$, which correspond to the time rate of work done by pressure, as well as by normal and shear stresses on the fluid element are given by:

$$\mathbf{f}_s = -p\mathbf{V} + \bar{\bar{\tau}} \cdot \mathbf{V} \tag{3.18}$$

The total time rate of work over the surface S of the CV $\mathscr{V}$ is obtained by:

$$\iint_S \mathbf{f}_s dS = \iint_S -p\mathbf{V}\mathbf{dS} + \iint_S (\bar{\bar{\tau}} \cdot \mathbf{V})\mathbf{dS} \tag{3.19}$$

Summing up all the above terms, the following formula for the energy conservation equation is derived:

$$\begin{aligned} \frac{\partial}{\partial t}\iiint_{\mathscr{V}} \rho E d\mathscr{V} + \iint_S \rho E \mathbf{V}\mathbf{dS} \;=\; & \iiint_{\mathscr{V}} \dot{q}_h d\mathscr{V} + \iint_S k\nabla\mathbf{T}\mathbf{dS} + \\ & \iiint_{\mathscr{V}} (\rho \mathbf{f}_b \cdot \mathbf{V}) d\mathscr{V} - \iint_S p\mathbf{V}\mathbf{dS} + \iint_S (\bar{\bar{\tau}} \cdot \mathbf{V})\mathbf{dS} \end{aligned} \tag{3.20}$$

3.1.4 Viscous Stresses

The normal and shear stresses originate from the friction between the surface of an element and the fluid. The time rate of change of the shearing deformation of the fluid element is related to the shear stress, τ_{xy}, as shown in Figure 3.2(b), whereas the time rate of volume change of the fluid element is related to the normal stress, τ_{xx}, as sketched in Figure 3.2(a).

In Cartesian coordinates, the general form of the stress tensor $\bar{\bar{\tau}}$ is given by:

$$\bar{\bar{\tau}} = \begin{bmatrix} \tau_{xx} & \tau_{xy} & \tau_{xz} \\ \tau_{yx} & \tau_{yy} & \tau_{yz} \\ \tau_{zx} & \tau_{zy} & \tau_{zz} \end{bmatrix} \tag{3.21}$$

where τ_{xx}, τ_{yy} and τ_{zz} are the normal stresses, while the remaining six components represent the shear stresses. By convention, the notation τ_{ij} denotes a stress component that affects a plane perpendicular to the i-axis, in the direction of the j-axis (see Figure 3.2). For a Newtonian fluid, where the shear stress is proportional to the velocity gradient, the viscous stresses can be evaluated as:

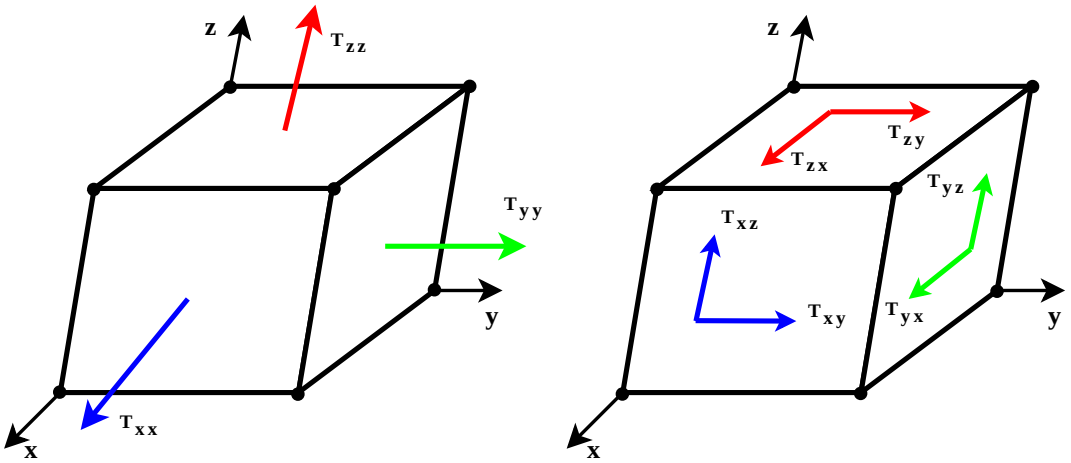

(a) Normal Stresses acting on a fluid element (b) Shear Stresses acting on a fluid element

FIGURE 3.2: Illustration of (a) normal and (b) shear stresses exerted on a fluid element

$$\tau_{xx} = \lambda(\frac{\partial u}{\partial x} + \frac{\partial v}{\partial y} + \frac{\partial w}{\partial z}) + 2\mu\frac{\partial u}{\partial x}$$

$$\tau_{yy} = \lambda(\frac{\partial u}{\partial x} + \frac{\partial v}{\partial y} + \frac{\partial w}{\partial z}) + 2\mu\frac{\partial v}{\partial y} \tag{3.22}$$

$$\tau_{zz} = \lambda(\frac{\partial u}{\partial x} + \frac{\partial v}{\partial y} + \frac{\partial w}{\partial z}) + 2\mu\frac{\partial w}{\partial z}$$

where λ represents the second viscosity coefficient and μ denotes the dynamic viscosity coefficient.

$$\tau_{xy} = \tau_{yx} = \mu(\frac{\partial u}{\partial y} + \frac{\partial v}{\partial x})$$

$$\tau_{xz} = \tau_{zx} = \mu(\frac{\partial u}{\partial z} + \frac{\partial w}{\partial x}) \tag{3.23}$$

$$\tau_{yz} = \tau_{zy} = \mu(\frac{\partial v}{\partial z} + \frac{\partial w}{\partial y})$$

According to Stokes hypothesis, the second viscosity coefficient $\lambda = -\frac{2}{3}\mu$, or $\lambda + \frac{2}{3}\mu = 0$. The latter relation is also termed the bulk viscosity and its property is particularly responsible for the energy dissipation in a fluid of uniform temperature, when a change in volume at finite rate occurs. From the above relations, the normal stress components after some small modification becomes:

$$\begin{aligned}
\tau_{xx} &= 2\mu[\tfrac{\partial u}{\partial x} - \tfrac{1}{3}(\underbrace{\frac{\partial u}{\partial x} + \frac{\partial \upsilon}{\partial y} + \frac{\partial w}{\partial z}}_{div\vec{u}})] \\
\tau_{yy} &= 2\mu(\tfrac{\partial \upsilon}{\partial y} - \tfrac{1}{3} div\vec{u}) \\
\tau_{zz} &= 2\mu(\tfrac{\partial w}{\partial z} - \tfrac{1}{3} div\vec{u})
\end{aligned} \tag{3.24}$$

3.1.5 Complete System of the Navier-Stokes Equations

The various terms appeared in the conservation laws of mass, momentum and energy can be collected into one system of equations by using the general conservation law for a vector quantity as follows.

$$\frac{\partial}{\partial t}\iiint_{\mathscr{V}} \vec{C} d\mathscr{V} + \iint_{S} (\vec{F}_c - \vec{F}_\upsilon) dS = \iiint_{\mathscr{V}} \vec{Q} d\mathscr{V} \tag{3.25}$$

In three dimensions the vector of the conservative variables $\vec{C}$ consists of the following five components.

$$\vec{C} = \begin{bmatrix} \rho \\ \rho u \\ \rho \upsilon \\ \rho w \\ \rho E \end{bmatrix} \tag{3.26}$$

The column vector $\vec{C}$ is also known as the solution vector because its elements (ρ, ρu, $\rho \upsilon$, ρw and ρE) are the dependent variables obtained numerically in steps of time. The vector of convective fluxes, $\vec{F}_c$, can be written as:

$$\vec{F}_c = \begin{bmatrix} \rho V \\ \rho u V + n_x p \\ \rho \upsilon V + n_y p \\ \rho w V + n_z p \\ \rho H V \end{bmatrix} \tag{3.27}$$

where V the contravariant velocity defined as the scalar product of the velocity vector and the unit normal vector, i.e, $V \equiv \vec{u} \cdot \vec{n} = n_x u + n_y \upsilon + n_z w$. The total enthalpy H is related to the total energy and the pressure by the following expression.

$$H = E + \frac{p}{\rho} \tag{3.28}$$

Additionally, the vector of viscous fluxes, $\vec{F}_\upsilon$, can be written as:

$$\vec{F}_\upsilon = \begin{bmatrix} 0 \\ n_x\tau_{xx} + n_y\tau_{xy} + n_z\tau_{xz} \\ n_x\tau_{yx} + n_y\tau_{yy} + n_z\tau_{yz} \\ n_x\tau_{zx} + n_y\tau_{zy} + n_z\tau_{zz} \\ n_x\Theta_x + n_y\Theta_y + n_z\Theta_z \end{bmatrix} \tag{3.29}$$

where the term Θ describes the work of viscous stresses and heat conduction in the fluid and reads

$$\begin{cases} \Theta_x = u\tau_{xx} + \upsilon\tau_{xy} + w\tau_{xz} + k\frac{\partial T}{\partial x} \\ \Theta_y = u\tau_{yx} + \upsilon\tau_{yy} + w\tau_{yz} + k\frac{\partial T}{\partial y} \\ \Theta_z = u\tau_{zx} + \upsilon\tau_{zy} + w\tau_{zz} + k\frac{\partial T}{\partial z} \end{cases} \tag{3.30}$$

Finally, the column vector Q, as shown below, represents a source term which is zero if the body forces and volumetric heating are negligible in the calculations.

$$\vec{Q} = \begin{bmatrix} 0 \\ \rho f_{b,x} \\ \rho f_{b,y} \\ \rho f_{b,z} \\ \rho(u f_x + \upsilon f_y + w f_z) + \dot{q}_h \end{bmatrix} \tag{3.31}$$

Note that the first elements of the C,F_c, F_υ, and Q column vectors, when added together, reproduce the continuity equation 3.4. The next three elements of the C,F_c, F_υ, and Q vectors, when added together, reproduce the x-, y- and z-momentum equation 3.12, respectively. The energy equation, 3.20, can be derived, when the last elements of the column vectors are added together.

For all simulations in the present study, the three-dimensional Navier-Stokes (NS) equations for a Newtonian, viscous fluid flow has been employed. The 3D compressible NS equations can be written in conservative variables and Cartesian co-ordinates as follows:

$$\frac{\partial \mathbf{U}}{\partial t}+\frac{\partial \mathbf{F}}{\partial x}+\frac{\partial \mathbf{G}}{\partial y}+\frac{\partial \mathbf{H}}{\partial z}=\frac{\partial \mathbf{P}}{\partial x}+\frac{\partial \mathbf{Q}}{\partial y}+\frac{\partial \mathbf{R}}{\partial z} \tag{3.32}$$

where $\mathbf{U}$ represents a vector of conservative variables (ρ,ρu, $\rho \upsilon$, ρw, e), $\mathbf{F}$, $\mathbf{G}$, $\mathbf{H}$ are vectors of the inviscid fluxes, and $\mathbf{P}$, $\mathbf{Q}$, $\mathbf{R}$ are vectors of the viscous fluxes in x, y and z direction, respectively.

$$\mathbf{U}=[\rho,\rho u,\rho \upsilon,\rho w,e]^T$$

$$\mathbf{F}=[\rho u,\rho u^2+p,\rho u\upsilon,\rho uw,(e+p)u]^T$$

$$\mathbf{G}=[\rho \upsilon,\rho u\upsilon,\rho \upsilon^2+p,\rho \upsilon w,(e+p)\upsilon]^T$$

$$\mathbf{H}=[\rho w,\rho uw,\rho \upsilon w,\rho w^2+p,(e+p)w]^T$$

$$e=\rho i+\frac{1}{2}\rho(u^2+\upsilon^2+w^2)$$

where ρ is the fluid density, u, υ, w are the Cartesian velocity components, i is the specific internal energy per unit volume and p is the pressure. The viscous flux vector is given by:

$$\mathbf{P}=[0,\tau_{xx},\tau_{xy},\tau_{xz},u\tau_{xx}+\upsilon\tau_{xy}+w\tau_{xz}+\dot{q}_x]^T$$

$$\mathbf{Q}=[0,\tau_{yx},\tau_{yy},\tau_{yz},u\tau_{yx}+\upsilon\tau_{yy}+w\tau_{yz}+\dot{q}_y]^T$$

$$\mathbf{R}=[0,\tau_{zx},\tau_{zy},\tau_{zz},u\tau_{zx}+\upsilon\tau_{zy}+w\tau_{zz}+\dot{q}_z]^T$$

where τ_{ij} is the stress tensor and $\dot{q}_i$ is the rate of heat transfer. Finally, the system of equations is closed by specifying an equation of state for an ideal gas as:

$$p = \rho RT = \rho i(\gamma - 1)$$

with T representing the temperature and γ the ratio of the specific heats.

3.2 Finite Volume Methods

3.2.1 Introduction

The spatial discretisation of the NSE, where the convective and viscous fluxes, as well as the source terms are numerically approximated, can be achieved by using one of the following three methods: finite difference (FDM), finite element (FEM) and finite volume methods (FVM). All of these methods can provide accurate approximations under certain circumstances. These circumstances are mainly related to the nature of the problem to be solved and the complexity of the numerical scheme used to solve the problem. In this section the FVM will be extensively presented, as this discretisation approach has been used throughout this study to approximate the PDE of the NSE both in space and time.

FVM use the integral form of the NSE as its starting point. The solution domain is subdivided into a finite number of adjacent CVs and the conservation equations are applied to each CV.

The cell-centred scheme has been chosen for the definition of the position and shape of the CV with respect to the grid, where the flow variables are stored at the centroids of the grid cells, as shown in Figure 3.3. In that case, the CVs are identical to the grid cells.

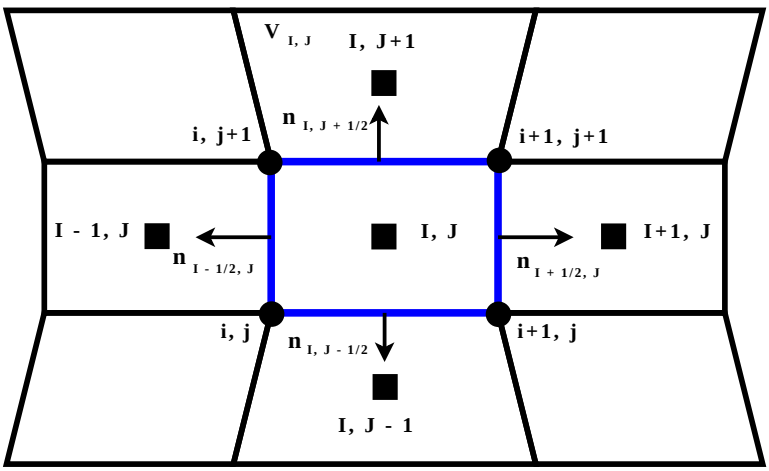

FIGURE 3.3: CV of a cell-centred scheme in two dimensions (i, j)

Consider a PDE in conservation form as follows:

$$\frac{\partial u}{\partial t} + \nabla \cdot f(u) = 0$$

where u is a vector variable and $f(u)$ is the corresponding flux vector with $f(u) = [f_1(u), f_2(u), \ldots, f_d(u)]$ in vector space $\mathbb{R}^d$. Taking the volume integral over the total volume V_i of a particular cell i, the following expression can be obtained:

$$\int_{V_i} \frac{\partial u}{\partial t} dV + \int_{V_i} \nabla \cdot f(u) dV = 0$$

Integrating the first term to get the volume average and applying the divergence theorem (converting that way the volume integral to a surface integral over the surface ΔV) to the second term, the starting point for the finite volume method is generated.

$$\frac{d\overline{u}_i}{dt} + \frac{1}{V_i} \oint_{S_i} f(u) \cdot n ds = 0$$

where S_i represents the surface area of the particular cell i and n represents the unit normal vector to the surface that points outward.

In the next subsection the geometrical quantities of a CV will be discussed, before moving on with the spatial and temporal discretisation of the conservative equations.

3.2.2 Geometrical Characteristics of a Control Volume

The calculation of the geometrical quantities of a CV $V_{I,J,K}$ - its volume ΔV, unit normal vector $\vec{n}_m$ and surface area $\triangle S_m$ of a face m - is presented in the next lines. The three-dimensional case is considered, where the four vertices of the face m of a CV may not lie in one plane. This implies that the normal vector is no longer constant on the face as that can be seen in Figure 3.4.

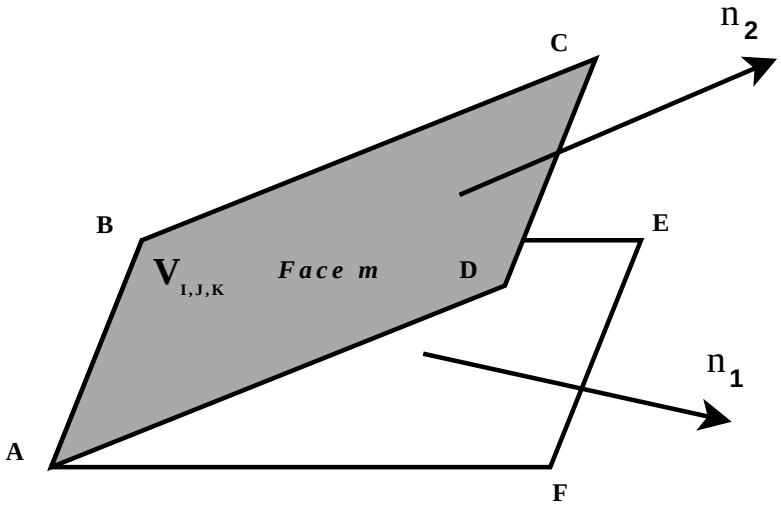

FIGURE 3.4: Face m of a CV $V_{I,J,K}$ with varying normal unit vector in three dimensions.

To overcome this difficulty, a simplified treatment of the quadrilateral faces has been employed, based on an averaged normal vector. The first term that has to be determined is the unit normal vector $\vec{n}_m$, which is given by:

$$\vec{n}_m = \frac{\vec{S}_m}{\triangle S_m} \tag{3.33}$$

As far as the surface area of a quadrilateral is concerned (see Figure 3.5), the Shoelace formula (also known as Gauss' area formula) has been used in two dimensions for the derivation of the face vectors $\vec{S}_m$. The formula can be expressed as:

$$A = \frac{1}{2}|(x_1 - x_3)(y_2 - y_4) + (x_4 - x_2)(y_1 - y_3)|$$

where A is the area of the quadrilateral and (x_i, y_i), $i = 0, 1, \cdots, n-1, n$ are the vertices (or corners) of the quadrilateral with n the number of its sides.

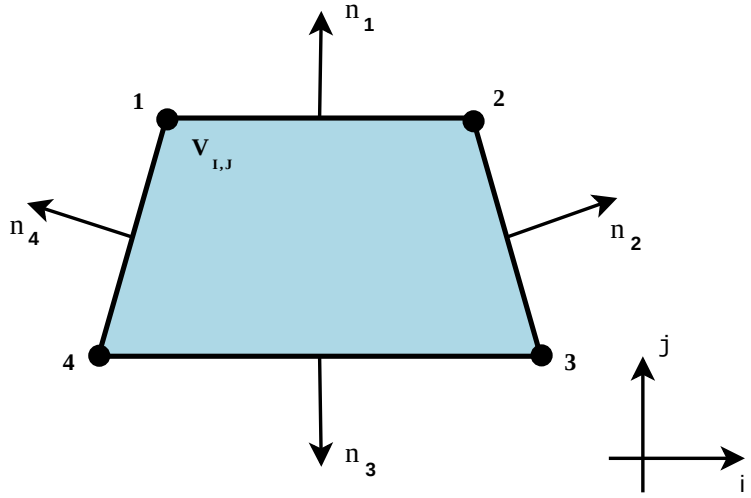

FIGURE 3.5: A two-dimensional CV $V_{I,J}$ and its associated face unit normal vectors n_m.

The same formula can be used for the calculation of the surface area of an hexahedral CV. For a CV like that displayed in Figure 3.6 and for its face $m = 1$ (points 1, 5, 8 and 4), the following differences can be defined:

$$\begin{cases} \Delta X_A = x_8 - x_1 \quad , \quad \Delta X_B = x_5 - x_4 \\ \Delta Y_A = y_8 - y_1 \quad , \quad \Delta Y_B = y_5 - y_4 \\ \Delta Z_A = z_8 - z_1 \quad , \quad \Delta Z_B = z_5 - z_4 \end{cases}$$

Note that in Figure 3.6 the unit vectors $\vec{n}_1$ and $\vec{n}_2$ are associated with the i-coordinate, $\vec{n}_5$ and $\vec{n}_6$ with j-coordinate, whereas $\vec{n}_3$ and $\vec{n}_4$ with the k-coordinate, respectively.

The face vector $\vec{S}_1$ of an hexahedral CV after applying the Gauss' area formula is then given by:

$$\begin{aligned} \vec{S}_1 \quad = \quad & \tfrac{1}{2}\,|[(y_8 - y_1)(z_4 - z_5) + (y_4 - y_5)(z_8 - z_1) + \\ & + (z_8 - z_1)(x_4 - x_5) + (z_4 - z_5)(x_8 - x_1) + \\ & + (x_8 - x_1)(y_4 - y_5) + (x_4 - x_5)(y_8 - y_1)]| \end{aligned}$$

The above formula can also be written in a matrix form as:

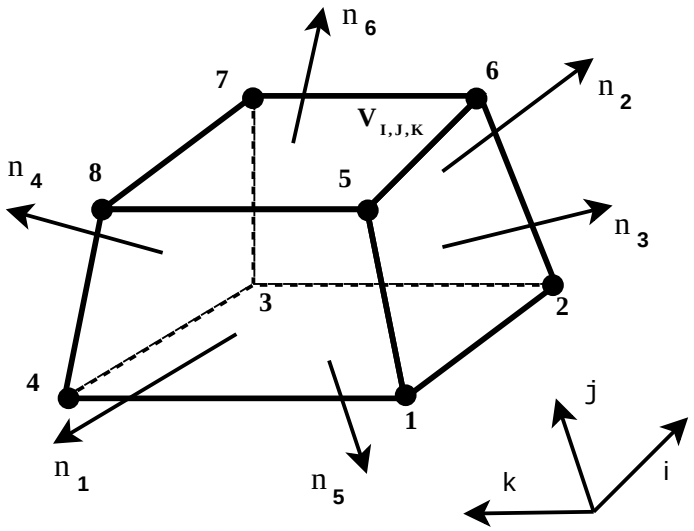

FIGURE 3.6: A three-dimensional CV $V_{I,J,K}$ and its associated face unit normal vectors n_m.

$$\vec{S}_1 = \frac{1}{2}\begin{bmatrix} \Delta Y_A \Delta Z_B + \Delta Y_B \Delta Z_A \\ \Delta Z_A \Delta X_B + \Delta Z_B \Delta X_A \\ \Delta X_A \Delta Y_B + \Delta X_B \Delta Y_A \end{bmatrix}$$

The five remaining face vectors are calculated in similar manner. Note that it is more convenient to store only the three face vectors (e.g., $\vec{S}_1$, $\vec{S}_3$, $\vec{S}_5$) for each CV $V_{I,J,K}$. The remaining three face vectors $\vec{S}_2$, $\vec{S}_4$ and $\vec{S}_6$ can be obtained from the appropriate neighbouring CVs by taking the reversed signs to become outward facing. The unit normal vector can then be calculated by Equation (3.33), where the surface area $\triangle S_m$ is given by:

$$\triangle S_m = \sqrt{S_{x,m}^2 + S_{y,m}^2 + S_{z,m}^2}$$

The last quantity to be computed is the volume for each cell. The vector cross product, usually referred as the scalar triple product, is used to compute the area of the volume of the grid cell. The formulation for the calculation of the volume area, in vector notation, is given by:

$$\triangle V = \left| \vec{q} \cdot (\vec{r} \times \vec{s}) \right|$$

In matrix form the above formula can be written as:

$$\Delta V = \begin{vmatrix} \Delta X_{\vec{q}} & \Delta Y_{\vec{q}} & \Delta Z_{\vec{q}} \\ \Delta X_{\vec{r}} & \Delta Y_{\vec{r}} & \Delta Z_{\vec{r}} \\ \Delta X_{\vec{s}} & \Delta Y_{\vec{s}} & \Delta Z_{\vec{s}} \end{vmatrix}$$

where the components of the matrix on the RHS of the above equation can be computed by:

$$\left\{ \begin{array}{lcl} \Delta X_{\vec{q}} & = & \frac{X_{i+1,j,k}+X_{i+1,j+1,k}+X_{i+1,j+1,k+1}+X_{i+1,j,k+1}}{4} - \\ & & - \frac{X_{i,j,k}+X_{i,j+1,k}+X_{i,j+1,k+1}+X_{i,j,k+1}}{4} \\ \Delta X_{\vec{r}} & = & \frac{X_{i,j,k}+X_{i,j,k+1}+X_{i+1,j,k+1}+X_{i+1,j,k}}{4} - \\ & & - \frac{X_{i,j+1,k}+X_{i,j+1,k+1}+X_{i+1,j+1,k+1}+X_{i+1,j+1,k}}{4} \\ \Delta X_{\vec{s}} & = & \frac{X_{i,j,k+1}+X_{i,j+1,k+1}+X_{i+1,j+1,k+1}+X_{i+1,j,k+1}}{4} - \\ & & - \frac{X_{i,j,k}+X_{i,j+1,k}+X_{i+1,j+1,k}+X_{i+1,j,k}}{4} \end{array} \right\}$$

where $X = \{x, y, z\}$.

3.2.3 Spatial Discretisation

The majority of the numerical schemes used for the solution of the Euler and Navier-Stokes equations employ the method of lines. According to this technique, a separate discretisation process of space and time can be followed. By consequence, numerical approximations of different accuracy for the spatial and temporal derivatives are allowed to be used, as it may be required by the problem itself. Thus, this method leads to more flexible and various forms of different discretisation schemes for both space and time.

As previously mentioned, a general structured, finite volume scheme is naturally based on the conservation laws of the governing equations (mass, momentum and energy), which in turn are expressed by the NSE. In a pre-processing step, the physical space is subdivided into a number of grid cells - quadrilateral in 2D, hexahedra in 3D. The grid/meshing process is done in such a way that [12]:

1. The domain is completely covered by the grid,

2. There is no free space left between the grid cells, and

3. The grid cells do not overlap each other.

The resulting structured grid is uniquely described by the coordinates x, y, z of the grid points (or corners of the grid cells) and by the indices i, j, k in the computational space.

Based on the grid, CVs are defined in order to evaluate the integrals of the convective and viscous fluxes, as well as of the source terms if any exists. For a CV that does not change in time, the time derivative of the conservative variables $\vec{C}$ can be expressed by:

$$\frac{\partial}{\partial t}\iiint_{\mathscr{V}} \vec{C}\, d\mathscr{V} = \mathscr{V}\frac{\partial \vec{C}}{\partial t}$$

Therefore, using the above formula, the complete system of the NSE expressed by Equation (3.25) can take the following form:

$$\frac{\partial \vec{C}}{\partial t} = -\frac{1}{\mathscr{V}}\left[\iint_{S}(\vec{F}_c - \vec{F}_v)dS - \iiint_{\mathscr{V}}\vec{Q}\, d\mathscr{V}\right] \tag{3.34}$$

The surface integral on the RHS of Equation (3.34) is approximated by a sum of the fluxes crossing the faces of the CV. This approximation is widely known as spatial discretisation. The source term, Q, is generally assumed to be constant inside the control volume.

Consider a control volume $V_{I,J,K}$, as that depicted in Figure 3.3. Applying the above formula on that particular volume, one can obtain:

$$\frac{\partial \vec{C}_{I,J,K}}{\partial t} = -\frac{1}{\mathscr{V}_{I,J,K}}\left[\sum_{m=1}^{N_F}(\vec{F}_c - \vec{F}_v)_m \Delta S_m - (\vec{Q}\mathscr{V})_{I,J,K}\right]$$

The indices in capital letters (I, J, K) are ascribed to a particular CV $V_{I,J,K}$, since in general a CV does not necessarily coincide with the grid points. N_F denotes the number of faces m in the CV ($N_F = 4$ in 2D and $N_F = 6$ in 3D). If the above equation is applied to all the CVs, a system of ordinary differential equations is created. The most important characteristic of those equations is that they are hyperbolic in time, which means that they have to be advanced in time starting from a known initial solution. It is also important to note that after the discretisation technique, all the flow variables, i.e. the conservative variables (ρ, ρu, ρv, ρw and ρE) and the dependent variables (P, T, etc.), are stored at the same

location at the cell center. In other words, the pressure and velocity components are stored at the same location in the center of each cell.

A wide range of choices exists as far as the evaluation of the convective fluxes is concerned. The basic problem arising from the discretisation process is that the values of the flow variables at all N_F faces to be defined, may not be directly available there. In this case, an interpolation either of the fluxes or of the flow variables at each face of a CV should take place. This approximation can be in principle done in two ways [12]:

1. by arithmetic averaging (like in central discretisation schemes), and
2. by some biased interpolation, which take care of the characteristics of the flow equations (like in upwind discretisation schemes).

Note that for the dicretisation of the viscous fluxes, different methodologies are used mainly due to the different nature of the flow equations involved. The equations representing both the viscous (Sutherland's law) and the convective fluxes are non-linear.

3.2.4 Godunov Method

One of the most important high-resolution methods are the Godunov-type methods which are based on the work of S.K. Godunov [49] and the extensions of van Leer [125]. The main feature of these methods is their basis in interpolation of the dependent variables in a control volume and resolution of the resulting edge values through an exact or approximate Riemann solver. The method particularly consists of two steps, with the first being interpolation, which is also known as "reconstruction" and the second being the Riemann solution which produces a physically relevant flux from the dependent variables used in the first stage.

Consider the one-dimensional system of hyperbolic conservation laws

$$\frac{\partial U}{\partial t} + \frac{\partial F}{\partial x} = 0$$

for a set of the following initial data

$$U(x,0) = \begin{cases} U_L \quad for \quad x < 0 \\ \\ U_R \quad for \quad x > 0 \end{cases}$$

The Godunov method in conservative form [118] can be written as:

$$U_i^{n+1} = U_i^n + \frac{\Delta t}{\Delta x}[F_{i-\frac{1}{2}} - F_{i+\frac{1}{2}}] \tag{3.35}$$

with the inter-cell numerical flux given by:

$$F_{i+\frac{1}{2}} = F(U_{i+\frac{1}{2}}(0)) \tag{3.36}$$

if the time step Δt satisfies the following condition:

$$\triangle t \leqslant \frac{\Delta x}{S_{max}^n} \tag{3.37}$$

where S_{max}^n presents the maximum wave velocity throughout the domain at time t^n.

The order of interpolation determines the order of a Godunov-type method. The first-order method derives from the piecewise constant sub-cell distribution. The second-order method, which is the most commonly associated with the name of Godunov these days, is defined by a linear distribution. The third-order methods are defined through parabolic profiles. Finally, arbitrary order methods are available via WENO/ENO (Weighted/ Essential Non-oscillatory) Schemes.

3.2.5 HLLC Riemann Solver

Godunov-type methods and very high-resolution methods require, as previously mentioned, the solution of the Riemann problem. In the literature, two different ways of solving the aforementioned problem can be found, including the exact Riemann solvers and the approximate Riemann solvers. Exact Riemann solvers require a large computational effort, which sometimes cannot be completely justified and can be dramatically increased either by the complexity of the particular system of equations being solved or the complicated algebraic form of equations of state, or both. Thus the procedure of solving the Riemann problem by using exact Riemann solvers can be in most cases a very expensive process.

Due to the cost of the exact Riemann solvers, approximate Riemann solvers have been developed that can be applied much more cheaply and give robust and accurate results when used in the context of Godunov-type or high-resolution methods. Furthermore, approximate Riemann solvers are more suitable for general occasions (equations of state, complicated physics) encountered in most applications, where the exact solution can be

very expensive [10].

Harten, Lax and van Leer [54] presented an approach for solving the Riemann problem approximately. The resulting solvers have become known as HLL Riemann solvers. The main idea is to assume a wave configuration for the solution, which consists of two waves separating three constant states. They defined an approximate Riemann solver by:

$$U_{LR} = \begin{cases} U_L & if \quad x/t \leq S_L \\ U^{hll} & if \quad S_L \leq x/t \leq S_R \\ U_R & if \quad x \geq S_R \end{cases} \tag{3.38}$$

where S_L and S_R are the fastest signal velocities at time t and U^{hll} is the velocity in the intermediate state between S_L and S_R.

$$U^{hll} = \frac{S_R U_R - S_L U_L + E_L - E_R}{S_R - S_L} \tag{3.39}$$

where E_L and E_R the left and right flux, respectively.

The main difficulty with HLL scheme, is the assumption of a two-wave configuration. In many cases, this assumption is incorrect and as a consequence the resolution of physical features can be inaccurate.

Toro et al. [119] proposed an efficient modification of the HLL scheme, where the missing contact is restored. In addition to the slowest and fastest signal velocities S_L and S_R , we include a middle wave of speed $S_\star$. The HLLC Riemann solver ("C" stands for the contact wave) is then defined by:

$$U^{hllc} = \begin{cases} U_L & if \quad x/t \leq S_L \\ U_{\star L} & if \quad S_L \leq x/t \leq S_\star \\ U_{\star R} & if \quad S_\star \leq x/t \leq S_R \\ U_R & if \quad x \geq S_R \end{cases} \tag{3.40}$$

3.2.6 Higher Order Accuracy

The development of very high-order methods remains a challenging issue for numerical analysts. It is important to point out that high-order of accuracy and absence of unphysical oscillations are two contradictory requirements in numerical methods. It is widely known that high-order linear methods produce spurious oscillations. On the other hand, the class of monotone methods (monotonicity is the requirement, where cell variable updates are bounded by the neighbor cells) do not produce unphysical oscillations, but are at most first order accurate. One way of resolving the contradiction between linear methods of high-order accuracy and absence of unphysical oscillations, is by creating non-linear schemes.

TVD (Total Variation Diminishing) methods are a prominent class of non-linear methods. TVD schemes are particularly linked to Artificial Viscosity methods. Both schemes attempt to circumvent Godunov's theorem by constructing schemes of accuracy larger than one, in order to eliminate or control the spurious oscillations near high gradients. The scheme is total variation non-increasing (TVNI) or TVD, if for all w,

$$TV(L \cdot U) \leq TV(U) \tag{3.41}$$

where w is a monotone mesh function and L is the finite difference operator. Further description of the TVD schemes can be found in the following papers [78, 118].

MUSCL Scheme

The Monotone Upstream-centered Scheme for Conservation Laws (MUSCL) is another approach of achieving high-order of accuracy. Van Leer [123], introduced the idea of replacing the piecewise constant data in the first order Godunov method by piecewise linear functions. The MUSCL approach allows the construction of very high order methods, fully discrete, semi-discrete and implicit methods as well.

In Figure 3.7, a piecewise linear MUSCL reconstruction is presented, where u_i^n represents an integral average in cell $I_i = [x_{i-\frac{1}{2}}, x_{i+\frac{1}{2}}]$. A piecewise linear reconstruction of u_i^n is:

$$u_i(x) = u_i^n + \frac{(x - x_i)}{\Delta x}\Delta i \tag{3.42}$$

where $\frac{\Delta_i}{\Delta x}$ is a suitably chosen slope of $u_i(x)$ in the cell I_i. The local co-ordinates in the center of the cell x_i are $x = \frac{1}{2}\Delta x$ and $u_i(x_i) = u_i^n$. A fundamental role in the reconstruction of the data play the values of $u_i(x)$ at the extreme points. The values at these points are given by:

$$\begin{cases} u_i^L = u_i^n - \frac{1}{2}\Delta_i \\ \\ u_i^R = u_i^n + \frac{1}{2}\Delta_i \end{cases} \tag{3.43}$$

The slopes Δ_i can be defined by the following equation:

$$\Delta_i = \frac{1}{2}(1+\omega)\Delta u_{i-\frac{1}{2}} + \frac{1}{2}(1-\omega)\Delta u_{i+\frac{1}{2}} \tag{3.44}$$

where ω is a free parameter in the real interval $[-1,1]$.

An alternative approach of MUSCL type high-order methods is the piecewise quadratic reconstruction, which is more accurate than the piecewise linear reconstruction. A piecewise quadratic reconstruction is given by:

$$u_i^x = u_i^n + \frac{(x - x_i)}{\Delta x}\Delta_i^{(1)} + \frac{3k}{2(\Delta x)^2}[(x - x_i)^2 - \frac{(\Delta x)^2}{12}]\Delta_i^{(2)} \tag{3.45}$$

where $\Delta_i^{(1)} = \Delta_i$. Note that Δ_i is related to the estimation of the second space derivative in the cell I_i and k is a parameter that controls different MUSCL realisations. Thornber et al. [116] showed that the accuracy of the second-order limiters is independent of the

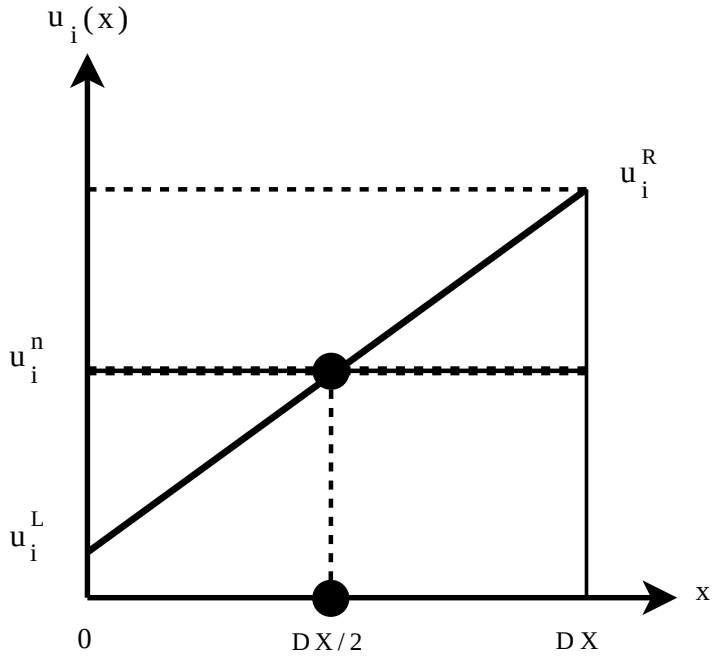

FIGURE 3.7: A piecewise linear MUSCL reconstruction of data in a single cell I_i with boundary extrapolated values u_i^R and u_i^L.

parameter k, as the limiters turn out to be symmetric. This was shown to be true for the van Leer, Minmod, van Albada and other second-order limiters.

Apart from the 2^{nd} and 3^{rd} order MUSCL limiter, Kim Kim [67, 68] have proposed the fifth-order interpolation with TVD limiting. For equal spaced grid points, the primitive variable vector at the cell interface $\Phi_{\frac{1}{2}} = \left(\rho_{\frac{1}{2}}, u_{\frac{1}{2}}, v_{\frac{1}{2}}, p_{\frac{1}{2}}\right)$ can be written as:

$$\Phi_{i+\frac{1}{2}} = \Phi_i + 0.5\beta(r_{i-1}, r_i, r_{i+1})\Delta\Phi_{i-\frac{1}{2}} \tag{3.46}$$

where Φ_i denotes a cell averaged value of the primitive variables and is a TVD limiter which determines the local slope under monotonic condition. The term β is given by:

$$\beta = \frac{-2/r_{i-1} + 11 + 24r_i - 3r_i r_{i+1}}{30}$$

where

$$r_{i-1} = \frac{\Phi_i - \Phi_{i-1}}{\Phi_{i-1} - \Phi_{i-2}} \quad , \quad r_i = \frac{\Phi_{i+1} - \Phi_i}{\Phi_i - \Phi_{i-1}} \quad , \quad r_{i+1} = \frac{\Phi_{i+2} - \Phi_{i+1}}{\Phi_{i+1} - \Phi_i}$$

Note that β of fifth order interpolation is a function of r_{i-1}, r_i and r_{i+1}.

The fifth order interpolation filtered by TVD limiting is given by the following expressions, where L and R are the left and right values of the cell interface, respectively:

$$\Phi_L = \Phi_i + 0.5max(0, min(2, 2r_{L,i}, \beta_L)\Delta\Phi_{i-\frac{1}{2}} \tag{3.47}$$

$$\Phi_R = \Phi_{i+1} - 0.5max(0, min(2, 2r_{R,i+1}, \beta_R)\Delta\Phi_{i+\frac{3}{2}} \tag{3.48}$$

In the above equations, β_L and β_R are:

$$\beta_L = \frac{-2/r_{L,i-1} + 11 + 24r_{L,i} - 3r_{L,i}r_{L,i+1}}{30}, \beta_R = \frac{-2/r_{R,i-1} + 11 + 24r_{R,i} - 3r_{R,i}r_{R,i+1}}{30} \tag{3.49}$$

where

$$\begin{cases} r_{L,i-1} = \frac{\Phi_i - \Phi_{i-1}}{\Phi_{i-1} - \Phi_{i-2}} \quad , \quad r_{L,i} = \frac{\Phi_{i+1} - \Phi_i}{\Phi_i - \Phi_{i-1}} \quad , \quad r_{L,i+1} = \frac{\Phi_{i+2} - \Phi_{i+1}}{\Phi_{i+1} - \Phi_i} \\ r_{R,i+2} = \frac{\Phi_{i+2} - \Phi_{i+1}}{\Phi_{i+3} - \Phi_{i+2}} \quad , \quad r_{R,i+1} = \frac{\Phi_{i+1} - \Phi_i}{\Phi_{i+2} - \Phi_{i+1}} \quad , \quad r_{R,i-1} = \frac{\Phi_i - \Phi_{i-1}}{\Phi_{i+1} - \Phi_i} \end{cases}$$

ENO/WENO Schemes

Another class of high-order schemes, which was first developed by Harten et al. [53], are the ENO (Essentially Non-Oscillatory) schemes. Particularly, these schemes are developed, in order to produce high-order schemes in smooth regions and achieve high accuracy up to discontinuities, through the use of adaptive stencils. Furthermore, they aim to provide high-order solutions that are free of unphysical oscillations. The schemes provide solutions for systems of hyperbolic conservation laws.

Consider the hyperbolic conservation law for the scalar case:

$$\frac{\partial U}{\partial t} + \frac{\partial E(U)}{\partial x} = 0 \tag{3.50}$$

The above equation can be discretised as:

$$\bar{U}^{n+1} = \bar{U}^n - \frac{\Delta t}{\Delta x}(\bar{E}_{i+1/2} - \bar{E}_{i-1/2}) \tag{3.51}$$

where $\bar{E}$ is the numerical flux and $\bar{U}$ is the numerical approximation of U.

After splitting the numerical flux $\bar{E}$ into positive and negative fluxes $\bar{E}_{i+1/2} = \bar{E}^{+}_{i+1/2} + \bar{E}^{-}_{i+1/2}$ and using a Taylor series expansion, we can define the numerical flux as follows:

$$\bar{E}^{\pm}_{i+1/2} = E^{\pm}_{i+1/2} + \sum_{k=1}^{m-1} a_{2k} \Delta x^{2k} \left(\frac{\partial^{2k}}{\partial x^{2k}} E^{\pm} \right)_{i+1/2} + \mathscr{O}(\Delta x^{2m+1}) \tag{3.52}$$

A different approach was developed by Shu and Osher [103], where polynomial interpolants $p^{\pm}_{i+1/2}$ were used such that:

$$p^{\pm}_{i+1/2}(x) = E^{\pm}(U(x)) + \mathscr{O}(\Delta x^{2m+1})$$

The numerical flux can then be written as:

$$\bar{E}^{\pm}_{i+1/2} = p^{\pm}_{i+1/2} + \sum_{k=1}^{m-1} a_{2k} \Delta x^{2k} \left(\frac{\partial^{2k}}{\partial x^{2k}} p^{\pm}_{i+1/2} \right)_{i+1/2} \tag{3.53}$$

The WENO (Weighted Essential Non-Oscillatory) schemes, which were first proposed by Liu et al. [78], use a convex combination of all the interpolating polynomials on the stencil, so as to compute an approximate polynomial for each cell. The main advantage of WENO against ENO schemes is that the unphysical oscillations near discontinuities are avoided, due to the fact that the interpolating polynomials on the discontinuous stencil do not contribute to the convex combination. Furthermore, the order of accuracy improves by one, as the convex combination of all the corresponding interpolating polynomials, leads to the cancellation of the truncation error ($\mathscr{O}(\Delta x^{2m+1})$). The weighted ENO schemes uses up to eleventh-order spatial discretisation in conjunction with Runge-Kutta methods for time advancement.

The main steps of implementing the third-order WENO reconstruction, for example, are:

1. Define the stencils for the cell with intervals $[x_{i-1/2}, x_{i+1/2}]$, as follows

$$\begin{cases} S_i = (x_{i-3/2}, x_{i-1/2}, x_{i+1/2}) \\ \\ S_{i+1} = (x_{i-3/2}, x_{i-1/2}, x_{i+1/2}) \end{cases} \tag{3.54}$$

2. Perform a linear polynomial interpolation for each grid cell

$$\begin{cases} p_i(x) = \bar{U}_i + \frac{\bar{U}_i - \bar{U}_{i-1}}{\Delta x}(x - x_i) \\ p_{i+1}(x) = \bar{U}_i + \frac{\bar{U}_{i+1} - \bar{U}_i}{\Delta x}(x - x_{i)} \end{cases} \tag{3.55}$$

3. Define the convex combination of the interpolating polynomials

$$P_i = \frac{\alpha_0^i}{\alpha_0^i + \alpha_1^i} p_i(x) + \frac{\alpha_1^i}{\alpha_0^i + \alpha_1^i} p_{i+1}(x) \tag{3.56}$$

- For $\frac{\partial E(U)}{\partial U} > 0$,

$$\left.\begin{array}{l} \alpha_0^i = \frac{1}{2(\varepsilon + (IS)_i)^2} \\ \alpha_1^i = \frac{1}{(\varepsilon + (IS)_{i+1})^2} \end{array}\right\} \tag{3.57}$$

- For $\frac{\partial E(U)}{\partial U} < 0$,

$$\left.\begin{array}{l} \alpha_0^i = \frac{1}{(\varepsilon + (IS)_i)^2} \\ \alpha_1^i = \frac{1}{2(\varepsilon + (IS)_{i+1})^2} \end{array}\right\} \tag{3.58}$$

where $(IS)_i$ is the smoothness indicator, which is estimated by the summation of all averages of square values. Thus $(IS)_i = (\bar{U}_i - \bar{U}_{i-1})^2$ and $(IS)_i = (\bar{U}_{i+1} - \bar{U}_i)^2$.

WENO schemes are more expensive than ENO schemes for the same order of accuracy, in both serial and parallel computations. However, WENO schemes lead to a smoother flux than that of ENO schemes.

3.2.7 Low Mach Number Treatment

The reconstruction method described in the preceding subsection has been modified [117] in such a way that the dissipation rate of the kinetic energy is uniformly changing in the limit of zero Mach number. It has been shown that the leading order kinetic energy

dissipation ε^{VL} (for the van Leer limiter) is proportional to the velocity normal to the cell interface u and speed of sound a such that:

$$\varepsilon^{VL} = \frac{\Delta x^2}{12} u u_x u_{xx} + \frac{\Delta x^3 a}{24}(3u_{xx}^2 + (2C-3)u_x u_{xxx}) \tag{3.59}$$

where C is the Courant-Friedrich-Levy (CFL) number and Δx is the length of the cell. The problem which arises from the above relation is that for low Mach number flows the kinetic energy dissipation increases. Thus the low Mach number features are extremely dampened by the numerical scheme. In [117] a different approach of the reconstruction method has been proposed, which effectively removes the Mach number dependence of the leading order kinetic energy dissipation. The Low Mach Number Treatment (**LMNT**) constitutes a method where the left and right values of the reconstruction are treated in such a way that, as the Mach number inclines to zero, no further dissipation is introduced. This is achieved by the following expression:

$$u^R_{i+\frac{1}{2}} = \frac{u^L + u^R}{2} + z\frac{u^L - u^R}{2}$$

$$u^L_{i+\frac{1}{2}} = \frac{u^L + u^R}{2} + z\frac{u^L - u^R}{2}$$

where the parameter z is given by:

$$z = min(M_{total}, 1) \quad , \quad M_{total} = max(M_L, M_R)$$

M_L and M_R are the local Mach numbers at the left and right of the cell face, respectively. Note that the left and right values of the density and pressure are not changed, which would cause excessive diffusion in stationary contact surfaces. It is also important to underline that the modified reconstruction method is based on the local properties of the flow field, thus the same governing equations are solved throughout the computational domain.

The modified fifth order MUSCL scheme introduced by [117] was selected throughout the simulations. It is also important to note that it successfully meets the requirements of monotonicity preserving. The elimination of oscillations near discontinuities have been also achieved by means of a slope limiter function used in the formulation of the MUSCL scheme.

3.3 Time Stepping Schemes

Time Integration Method and CFL number

There are various approaches in order to achieve time accurate solutions for the compressible flows. The most common time integration methods are the following:

- Linear Multi-Step Methods (LMM)
- Lax-Wendroff-type Method (LW)
- Implicit Methods
- Runge-Kutta (R-K), as well as total variation diminishing (TVD) R-K.

Time integration is related with the differentiation index of partial differential-algebraic equations. That means that the index of the system of equations characterizes the difficulty of solving that system.

The global time step (applied to all the grid cells) is computed based on the Courant-Friedrichs-Lewy number (CFL). The CFL number is defined as the ratio of the distance covered by a wave to the size of the computational grid cell. The global time step is defined as:

$$\Delta t = min\left(J \frac{CFL}{max\left(\left|\lambda_0^{\xi}\right|, \left|\lambda_1^{\xi}\right|, \left|\lambda_2^{\xi}\right|, \left|\lambda_0^{\eta}\right|, \left|\lambda_1^{\eta}\right|, \left|\lambda_2^{\eta}\right|, \left|\lambda_0^{\zeta}\right|, \left|\lambda_1^{\zeta}\right|, \left|\lambda_2^{\zeta}\right| \right)} \right) \tag{3.60}$$

where J denotes the Jacobian determinant and λ_i^{ξ}, λ_i^{η}, λ_i^{ζ} $(l = 0,1,2)$ are the eigenvalues of the advective fluxes $\overline{F}, \overline{G}, \overline{H}$, respectively.

Time integration is obtained by an explicit three-stage second-order accurate scheme, known as the Strong Stability Preserving Runge-Kutta (SSPRK) method after Spiteri and Ruuth [112] who first introduced it. The SSPRK time advancement scheme produces larger stability (CFL) limits with the cost of more function evaluations, in that it extends the stability of the method up to a CFL number of 2. The formulation of the above scheme can be written as folllows:

$$\left.\begin{aligned} U_i^1 &= U_i^n + \tfrac{1}{2}\tfrac{\Delta t}{\Delta x}[f(U_i^n)], \\ U_i^2 &= U_i^n + \tfrac{1}{2}\tfrac{\Delta t}{\Delta x}[f(U_i^1)], \\ U_i^{n+1} &= \tfrac{1}{3}\left(2U_i^2 + U_i^n + \tfrac{\Delta t}{\Delta x}[f(U_i^2) + f(U_i^1)]\right) \end{aligned}\right\} \tag{3.61}$$

Suddenly-Expanded Flows

4

Validation of the Numerical Schemes

4.1 Introduction

Numerical investigations of turbulence in planar sudden expansion flows are very few in literature and as demonstrated in previous sections most of the attempts made to simulate these kind of flows were not adequate. The most important reason is that PSE, despite its simple geometry, exhibits very complex flow phenomena that mainly are related with flow separation from fixed points and reattachment of shear layers. Besides, the flow above a critical Reynolds number, which in turn depends on the geometrical characteristics of the PSE configuration, becomes asymmetric with two recirculation zones of unequal size lengths. This is due to a pitchfork bifurcation of the three-dimensional Navier-Stokes equations that takes place in the flow field. The higher the Reynolds number, the more complex fluid flow phenomena are present.

In this Chapter, the results obtained from the ILES of an incompressible, turbulent flow downstream of a planar sudden expansion are presented. The calculations were carried out on the Cranfield's University 7 Teraflop High Performance Computing Facility (ASTRAL). The computational study is based on the CFD code **CNS3D** [27, 28, 34]

(Compressible Navier Stokes Solver in 3D). The code uses the finite volume (upwind) Godunov method in conjunction with several approximate Riemann solvers, including flux vector splitting methods, a characteristic-based method [32], and the HLLC (Harten-Lax-van Leer-Contact) solver [118], written in Fortran 90/95. It includes high-resolution methods extending from 2^{nd} to 9^{th} order in space, and up to 3^{rd} order accuracy in time. In the present study, the HLLC solver was used in conjunction with three high-resolution schemes, including the MUSCL 3^{rd} (M3) and MUSCL 5^{th} (M5) order schemes of Kim and Kim [67, 68], and the WENO 5^{th}-order method (W5) addressed in [7, 118]. As far as the time integration of the solution is concerned, this is obtained by an explicit three-stage 2^{nd}-order accurate SSPRK scheme proposed by Spiteri and Ruuth [112], which extends the stability of the method up to a CFL number of 2.

Two different Reynolds numbers were used in the calculations having values of 10000 and 40000, both based on the inlet bulk velocity, U_b, and the step height of the channel, h. Besides, three different grid meshes were generated using the commercial mesh generator software **Gridgen-Pointwise**®. Instantaneous and time-averaged quantities of the flow field are provided, along with comparisons of the numerical results against the experimental data of Casarsa et al. [17]. Comparisons have also been carried out between the two Reynolds numbers under investigation, examining any potential difference in the flow field, which could indicate that $Re = 10^4$ is not high enough to allow the influence of an increase in Reynolds number to be completely disregarded.

4.2 Flow Configuration and Flow Field Initialisation

Figure 4.1 shows a schematic view of the sudden expansion domain, which consists of two channels having different heights. The flow domain, hence, consists of an inlet channel of height h and a main channel of height $3h$. The characteristic length of the channel is the step height, h, with value 1. The total length of the domain is $84h$, where the inlet channel has a length of $4h$ and the main channel a length of $80h$. These particular geometrical properties were chosen in order to ensure that the flow a) is fully developed turbulent before reaching the step and b) has fully recovered further downstream of the expansion forming a laminar profile before exiting. The expansion ratio, i.e. the ratio of the main channel height to the inlet channel height ($ER = L_2/L_1$), which is of great importance when simulating suddenly-expanded flows, equals to 3 : 1, having the same value with that of Casarsa et al. [17]. The aspect ratio, i.e. the ratio of the channel width, w, to the

step height ($AR = w/h$), is $5:1$. Note that simulations were also performed for a series of different inlet streamwise and spanwise lengths (i.e., with an inlet channel length of $12h$ and a spanwise distance of $1h$) before selecting the more appropriate values. The primary results were not as well as expected. By gradually increasing the spanwise length and reducing the length of the inlet channel, the resulting mean flow characteristics and turbulence intensities were getting closer to the experimental values.

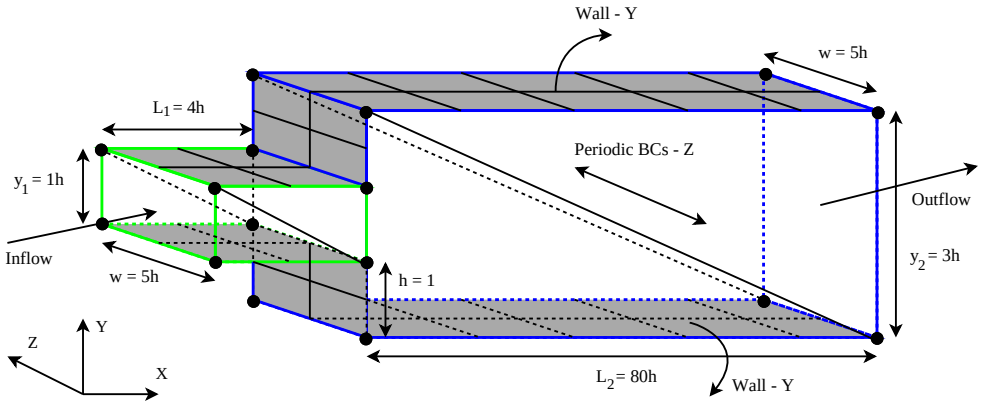

FIGURE 4.1: Schematic diagram of the sudden expansion configuration - lengths and boundary conditions.

Initial conditions must be stipulated for the density, pressure and velocity at the start of the time-marching calculations. Thus, at time $t = 0$ all the above variables must be set up. Note that in theory the initialisation of the problem can be purely arbitrary. However, in practice there is one important reason that those initial conditions must be selected intelligently. The reason is that the closer the initial conditions are to the final steady-state answer, the faster will take for the time advancement procedure to converge, thus the shorter will be the computer run time. According to the above statement, the initial conditions chosen for the simulation of turbulence in flows with a sudden expansion is as follows.

The flow to be simulated belongs to the incompressible regime with $Ma = 0.1$, hence, a constant initial value has been given to the flow density throughout the computational domain. The streamwise velocity was set equal to 1 along the x-axis between $y/h = 0$ and $y/h = 1$ and 0 anywhere else (see Figure 4.2). The wall-normal as well as the spanwise velocities were set equal to 0. The initial flow relations at $t_0 = 0$ are addressed below:

$$U_0(x,y,z,t_0) = 1 \quad for \quad 0 < y/h < 1$$

$$V_0(x,y,z,t_0) = 0$$

$$W_0(x,y,z,t_0) = 0$$

$$\rho_0(x,y,z,t_0) = 1$$

The energy has been initialised using the following formula:

$$E_0(x,y,z,t_0) = \frac{P_{ref}(\gamma-1)^{-1}}{\rho_0 U_{ref}^2} + \frac{1}{2}(U_0^2 + V_0^2 + W_0^2)$$

where P_{ref} and γ are the reference pressure used to non-dimensionalise the energy equation and the ratio of specific heats, respectively.

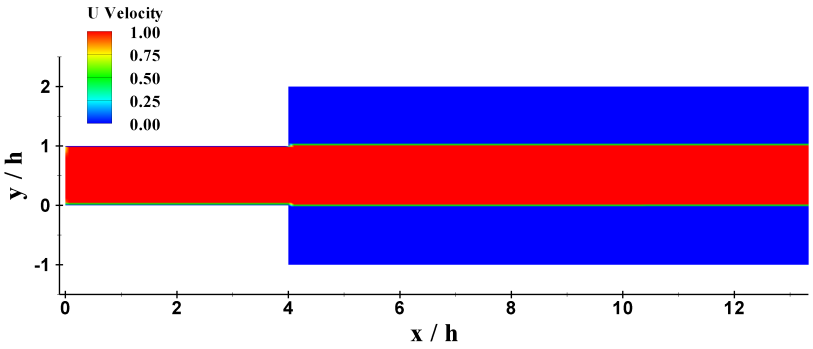

FIGURE 4.2: Initialisation of U Velocity at $t_0 = 0$ upstream and downstream (part of the domain) of the expansion.

$$P_{ref} = 10^5 \ (Pascal)$$

$$\gamma = 1.4$$

The reference velocity U_{ref} is given by:

$$U_{ref} = Ma\sqrt{\frac{\gamma P_{ref}}{\rho_0}} = 0.1\sqrt{\frac{1.4\times 10^5}{1}} = 37.417\,\frac{m}{s}$$

4.3 Boundary Conditions

The numerical solution of the compressible Navier-Stokes equations requires the use of appropriate boundary conditions. In CNS3D, several ghost cells (cells that do not belong to the real computational domain) are being used in three directions I, J and K, analogous to the order of magnitude of the numerical scheme applied each time.

In the next subsections the initial and boundary conditions used in the simulations of a turbulent flow over a sudden expansion configuration will be presented. In the wall-normal direction (y coordinate), a no-slip (wall) condition along the surfaces of the two parallel plates is applied, whereas in the spanwise direction (z coordinate) a set of periodic boundary conditions has been used, which facilitates the simulation of a smaller part of the computational domain that is far from its edge. The main feature of the periodic boundary conditions is that the information that exits one face reappears on the opposite face with the same information (e.g. in the code the first ghost cell at the left face takes its value from the first ghost cell at the right face and so on). Symmetry conditions were also applied in the spanwise direction to investigate any possible difference in the behaviour of the flow. Calculations of mean streamwise velocities and turbulence intensities showed large discrepancies between the numerical and experimental results. The results obtained from the latter boundary conditions will not be presented. At the inflow, fixed density with extrapolated pressure have been applied, while turbulent-based inlet velocity conditions have been developed and implemented into the CNS3D code. At the outflow, the pressure was kept constant, whereas the density and velocity were both extrapolated.

Finally, a 1-D domain was added at the outlet, downstream of the main channel consisting of 200 cells. The extended domain allows waves to pass through it without any artificial reflections. In other words, the pressure wave reaches the end of the main channel, enters the 1-D domain and travels through it without significant reflections. The 200 cell boundary condition overcomes the difficulty arising when modelling internal flows with a compressible solver where pressure waves may become "trapped" and resonate.

4.3.1 Inflow and Outflow Boundary Conditions

Synthetic turbulent boundary conditions were implemented and used throughout the simulations, which are based on the digital filter (DF) generator technique proposed by Touber and Sandham [120]. The DF approach is used to produce a velocity signal in three directions by matching ad hoc first- and second-order statistical moments, length and time

scales as well as energy spectra. Several studies on DF technique have been made in the past. However, the approach for the generation of artificial inflow data developed by Touber and Sandham have been chosen among others, as the filtering operation is applied only in 2D (rather than in 3D), making the whole process much faster.

The velocity signal expression contains two parts (see Equation (4.1)). The first part is the prescribed mean velocity profile $\overline{u}_i$ obtained mainly from previous experimental data. The second part contains the two-dimensional signal $\rho^{u_i}(y,z)$ generated for each velocity component and the prescribed correlation tensor R_{ij} known from experimental data.

$$u_i = \overline{u}_i + a_{ij}\rho^{u_i}(y,z) \tag{4.1}$$

where a_{ij} the prescribed Reynolds stress tensor given by the following matrix:

$$a_{ij} = \begin{bmatrix} \sqrt{R_{11}} & 0 & 0 \\ R_{21}/\sqrt{R_{11}} & \sqrt{R_{22} - (R_{21}/\sqrt{R_{11}})^2} & 0 \\ 0 & 0 & \sqrt{R_{33}} \end{bmatrix} \tag{4.2}$$

The 2-D signal $\rho^{u_i}(y,z)$ suggested by Xie and Castro [131] is given by:

$$\rho^{u_i}(y,z) = \upsilon_k^{old} exp(-\frac{\pi\Delta t}{2\tau_l}) + \upsilon_k \sqrt{1 - exp(-\frac{\pi\Delta t}{\tau_l})} \tag{4.3}$$

where Δt is the time step and τ_l is the Lagrangian time scale ($\tau_l = I_i/\overline{u}_i$ in the calculations, where I_i is the prescribed integral length scale with $i = \{x,y,z\}$). The above formula contains also the velocity field correlations of the digital linear non-recursive filters υ_k and υ_k^{old}. The newly computed field υ_k is correlated with the previous one υ_k^{old} at each time step, except of course when performing the very first time step Δt_1. The discrete filter operator υ_k can be defined as:

$$\upsilon_k = \sum_{j=-N}^{N} b_j r_{k+j} \tag{4.4}$$

where N_{F_X} is the filter size defined by $N_{F_X} = 3n_{I_x}$, with $n_{I_x} = I_i/\Delta x$ (n_{I_x} the equivalent number of grid points, given the computational grid spacing Δx and the integral length

scale I_i). The filter coefficient b_j is approximated by the following relation:

$$b_j \approx \frac{\tilde{b}_k}{\left(\sum_{j=-N_{F_X}}^{N_{F_X}} \tilde{b}_j^2 \right)} \tag{4.5}$$

where the filter coefficient $\tilde{b}_k$ arises from an exponential auto-correlation function proposed by Xie and Castro [131] and takes the form:

$$\tilde{b}_k = \exp\left(-\frac{\pi k}{n_{I_x}}\right) \tag{4.6}$$

The term r_k with $1 \leq k \leq p$, refers to a set of p random numbers with zero-mean ($\bar{r}_k = \sum_{k=1}^{p} \frac{r_k}{p} = 0$) and unit-variance ($\overline{r_k r_k} = \sum_{k=1}^{p} \frac{r_k^2}{p} = 1$). The generation of the random numbers was based on the Box-Muller theorem, which states that: if a and b are two independent numbers uniformly distributed in $(0,1]$, combining them such that

$$\left\{ \begin{array}{c} c = \sqrt{-2\ln(a)}\cos(2\pi b) \\ \\ \textit{and} \\ \\ d = \sqrt{-2\ln(a)}\sin(2\pi b) \end{array} \right\} \tag{4.7}$$

will make c and d be two independent numbers from a normal distribution of unit-standard deviation.

In three dimensions the final single-point correlation formula can now be specified by the following expression:

$$\begin{bmatrix} u(0,y,z,t) \\ \\ v(0,y,z,t) \\ \\ w(0,y,z,t) \end{bmatrix} = \begin{bmatrix} < u(0,y,z) > \\ \\ < v(0,y,z) > \\ \\ < w(0,y,z) > \end{bmatrix} + a_{ij} \begin{bmatrix} \rho^u(y,z) \\ \\ \rho^v(y,z) \\ \\ \rho^w(y,z) \end{bmatrix} \tag{4.8}$$

The first term on the RHS of the above equation defines the prescribed mean velocity profile, while the second term determines the fluctuating velocity for each time step in

the calculations. Note that the aforementioned synthetic inflow boundary conditions are time-dependent and this technique can also be extended to compressible flows after some simple modifications. For further details of the method, the author recommends the following studies ([24, 69, 79, 120, 127, 131])

As already mentioned in the previous subsection, a one dimensional buffer domain consisting of 200 grid cells has been added at the end of the computational domain, allowing pressure waves to pass through it, preventing that way any artificial reflections from taking place in the flow field. Fixed values have been given to the pressure, while an extrapolation has been applied for the three velocity components and density at the outflow.

Snapshot profiles of the three velocity components u, v and w, along with the total energy E and the turbulent kinetic energy K obtained at the inlet plane of the channel along the y-axis are depicted in Figure 4.3, after applying the inflow synthetic boundary conditions described above.

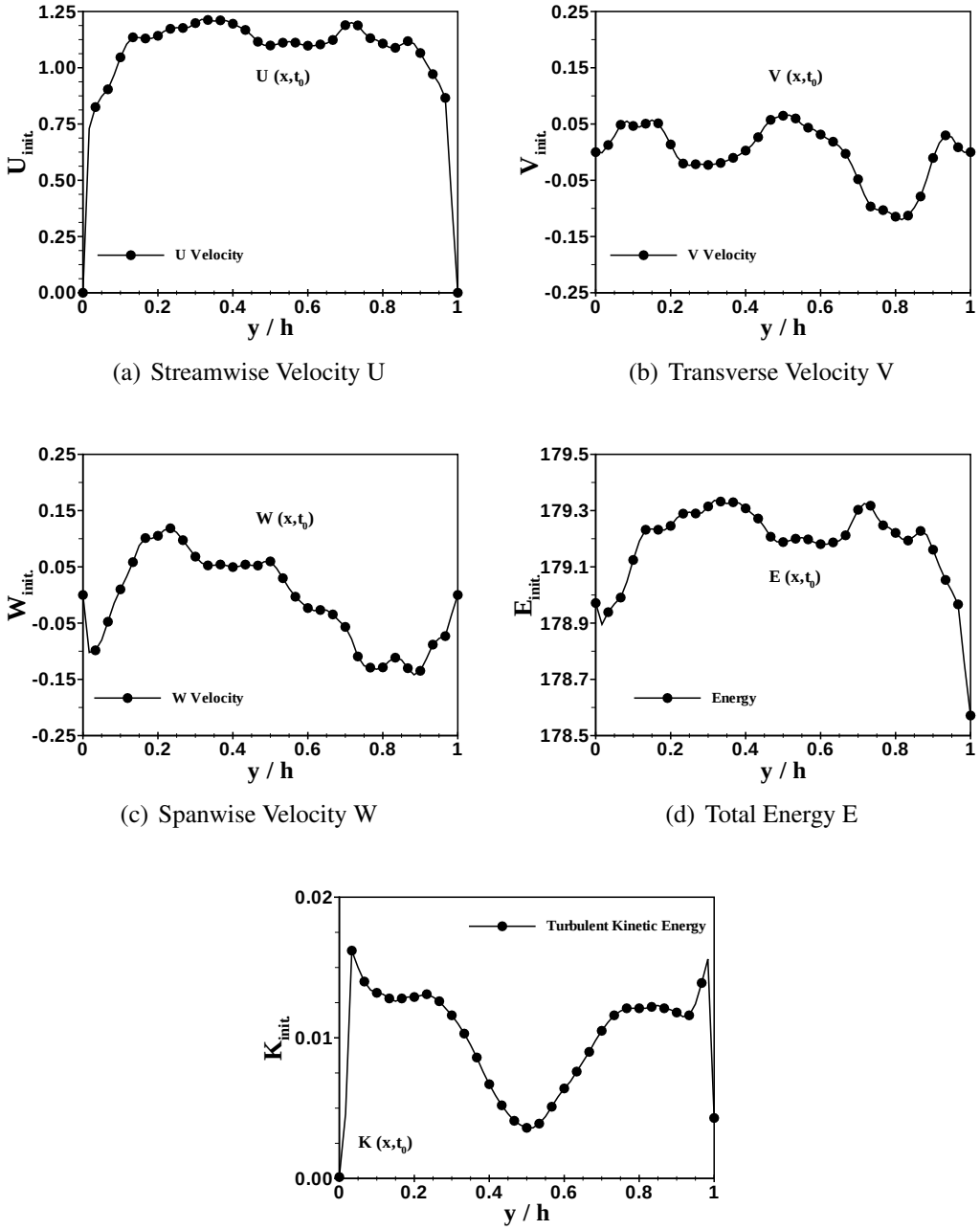

(a) Streamwise Velocity U

(b) Transverse Velocity V

(c) Spanwise Velocity W

(d) Total Energy E

(e) Turbulent Kinetic Energy K

FIGURE 4.3: Snapshot profiles of the three velocity components, total energy, and turbulent kinetic energy (TKE) at $x-y$ inlet plane, at $z/h = 2.5$.

Note that all the velocity profiles have been non-dimensionalised by the inlet bulk velocity (U_{init}/U_b, V_{init}/U_b and W_{init}/U_b), the energy profile by the quantity $p/\rho u^2$, whereas

the turbulent kinetic energy by the inlet bulk velocity squared (K_{init}/U_b^2). Furthermore, the profile of the density has not been plotted, since its initial value is constant and equals to 1 throughout the domain ($\rho/\rho_{ref} = 1$, taking into account that the flow under investigation belongs to the incompressible regime, as $Ma = 0.1$). Further information about the non-dimensionalisation process can be found in Appendix C.

4.4 Inlet Conditions

Figure 4.4 shows the profiles of the mean streamwise velocity component, U, and the corresponding rms turbulent fluctuation, $u^{'}$, measured in the xy-inlet plane at the midplane $z/h = 2.5$ of the channel. Both quantities are normalised by the bulk velocity in the plane, U_b, and compared with the numerical DNS results of Iwamoto et al. [59], who performed numerical simulation of a fully developed two-dimensional flow between parallel, flat plates at $Re = 10049$. There is a very good agreement between ILES results and DNS data, particularly for the mean flow velocity component. At centerline of the inlet channel $y/h = 0.5$, the streamwise turbulent fluctuations found to be approximately 4.7% of U_b ($\sim 5\%$ deviation from the DNS results).

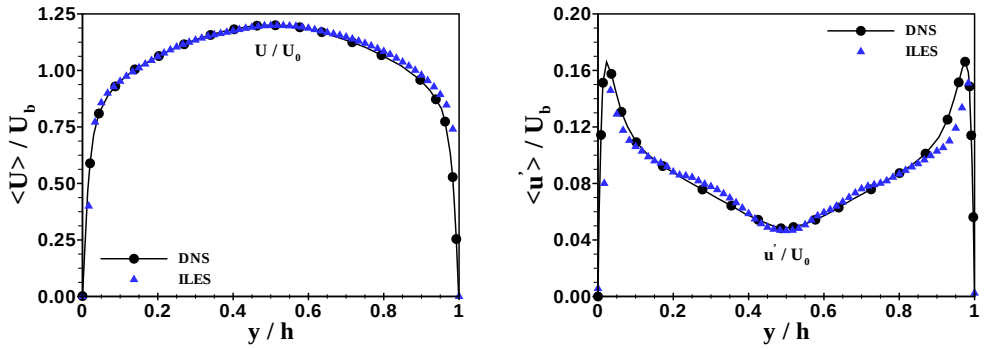

(a) Mean velocity profile at the inlet channel (b) Rms velocity profile at the inlet channel

FIGURE 4.4: Measured (DNS, [59]) and computed mean and rms streamwise velocity components in the xy-inlet plane, after applying the DF generation technique for producing synthetic turbulent inflow boundary conditions.

The maximum values of rms velocity component are observed near the two side walls at $y/h \simeq 0.1$ and $y/h \simeq 0.9$, respectively. At these locations the rms velocity fluctuations reach the value of 15% of U_b ($\sim 9.3\%$ deviation from the DNS results with $u^{'} = 16.4\%$ of U_b). According to the above remarks, the flow can be characterised as fully developed

turbulent in the xy-inlet plane, indicating that the synthetic turbulent boundary conditions applied at the inflow are well-behaved. It is also important to underline that the ILES results are in very good agreement with the PIV measurements of Casarsa et al. [17], (see Figure 4.5).

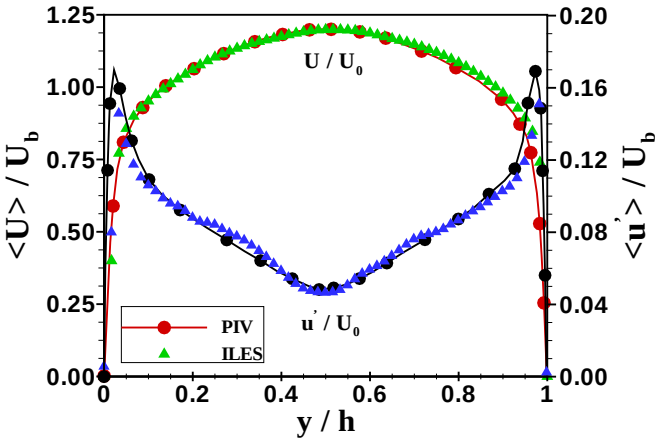

FIGURE 4.5: Measured (PIV, [17]) and computed (ILES) mean and rms streamwise velocity components in the xy-inlet plane.

Note that the maximum value of the measured fluctuating velocity near the side walls of the channel is slightly higher in the PIV experiment compared to the DNS results, reaching the level of 17% of U_b.

4.5 Grid Convergence Study

Three different meshes (see Figure 4.6) have been employed in the calculations of the sudden expansion flow, with the finer grids having approximately the double grid size of the coarser ones. Thus, a total number of about 0.66×10^6, 1.57×10^6, and 3.13×10^6 grid points have been used, representing the coarse, medium and fine grid, respectively. Stretching was employed in the streamwise direction in order to adequately resolve the turbulence scales in the shear layers appearing in both sides of the downstream channel and the backflow in the recirculation regions near the upper and lower walls. On the other hand, a uniform grid mesh was used in the wall-normal and spanwise direction. Clustering has not been applied to those two directions, as the turbulence flow behaviour downstream of the expansion, the separation as well as the reattachment of the shear layers

depend mainly on the geometrical characteristics of the sudden expansion configuration (sudden change of the channel height), and not on the boundary layer of the walls.

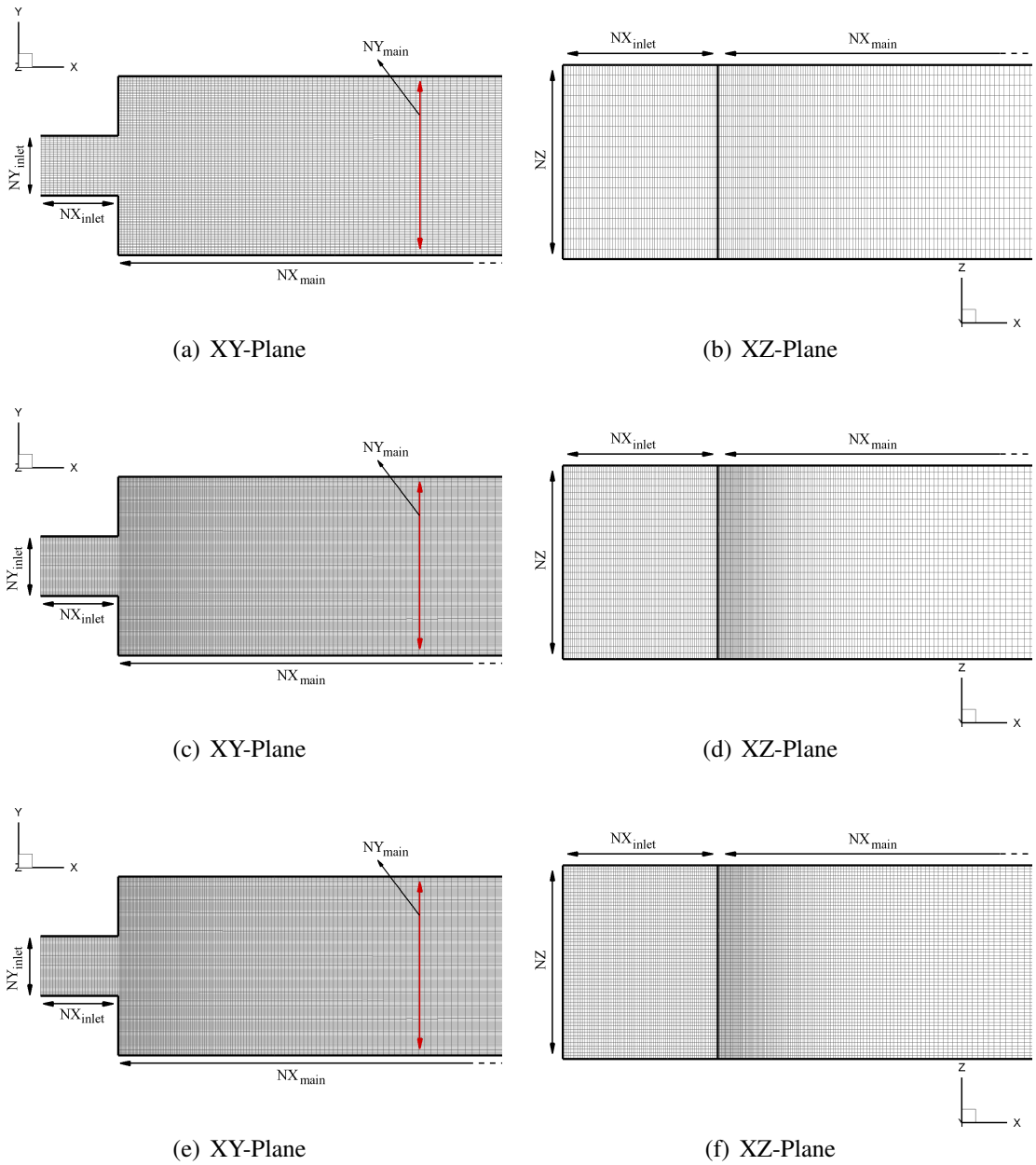

(a) XY-Plane (b) XZ-Plane

(c) XY-Plane (d) XZ-Plane

(e) XY-Plane (f) XZ-Plane

FIGURE 4.6: Illustration of three different grid meshes used for the simulation of the sudden expansion flow. (a),(b) Coarse Grid, (c),(d) Medium Grid, and (e),(f) Fine Grid at xy- and xz-planes.

The detailed computational parameters are provided in Table 4.1. The last column

contains the values of the non-dimensional wall distance term, y^+, for the three different grid meshes. The y^+ is given by the following formula:

$$y^+ = \frac{u_\tau y}{\nu}$$

where u_τ is the friction velocity, y is the distance to the nearest wall and ν is the local kinematic viscosity of the fluid. Given the grid spacing in the wall-normal direction and considering the fact that the Δy has the same value in the medium and fine grid, it is important to point out that for $Re = 10^4$, two grid points lie in the buffer layer (region between viscous sublayer and log-law region, where $5 < y^+ < 30$), four points in the viscous wall region (region where the viscous contribution to the shear stress is significant, $y^+ < 50$) and six points in the inner layer (region where the mean velocities are independent of the inlet bulk velocity, U_b, and the step height, h, with $y/h < 0.1$). On the other hand, for $Re = 4 \cdot 10^4$, only one point lies in the viscous wall region, six points in the inner layer and no point in the buffer layer. Note also that for this specific grid resolution, no point stands in the viscous sublayer (region where the Reynolds stresses are negligible compared with the viscous stress, with $y^+ < 5$).

TABLE 4.1: Computational parameters used for the simulation of the sudden expansion flow in the framework of ILES. The superscript + denotes scaling with the viscous length scale ν/u_τ.

Grid	$N_x(In.+Ch.)$	N_{y1},N_{y2}	N_z	Total $(In.+Ch.)$ $(\times 10^5)$	Δy	y^+
Coarse	$310(60+250)$	$40, 120$	20	$6.6(0.48+6.12)$	0.025	17.6
Medium	$340(80+260)$	$60, 180$	30	$15.7(1.5+14.2)$	0.017	11.7
Fine	$340(80+260)$	$60, 180$	60	$31.3(2.9+28.4)$	0.017	11.7

Table 4.2 shows the computational parameters used to define the inflow synthetic boundary conditions and, particularly, the filter size of the discrete filter operator υ_k addressed in Section 4.3.1. The filter size, based on the numerical investigation of Klein et al. [69], is given by the following relation:

$$NF_i = 3n_{I_i}$$

where n_{I_i} is the equivalent number of grid points, given the grid spacing in the computational domain, and can be written as:

$$n_{I_i} = \frac{I_i}{\Delta X_i} \tag{4.9}$$

In Equation (4.9) the numerator, I_i, stands for the integral length scale of the flow, whereas the denominator, ΔX_i, denotes the grid spacing.

$$\Delta X_i = \frac{L_i}{NX_i - 1}$$

where L_i is the length of the channel and NX_i is the total number of points in each direction, with $i = \{x, y, z\}$. Note that as the number of the equivalent grid points increases, the computational cost increases further. It is also important to pinpoint that the filter size should be $NF_i \geq 2n_{I_i}$.

TABLE 4.2: Computational parameters used in the digital filter generation technique for three different grid resolutions.

Grid	I_x	I_y	I_z	n_{I_y}	n_{I_z}	NF_y	NF_Z	τ_l
Coarse	0.5	0.2	0.2	7.8	3.8	23	11	0.0134
Medium	0.5	0.2	0.2	11.8	5.8	35	17	0.0134
Fine	0.5	0.2	0.2	11.8	11.6	35	35	0.0134

4.5.1 Reynolds Number 10000

In this subsection a grid convergence study is carried out using the MUSCL 5^{th}- order scheme. For this purpose the three grids described above has been employed. The Re number, based on the step height of the channel and the inlet bulk velocity, is 10^4. The CFL number used in the calculations has the value of 1, achieving a good compromise between numerical stability and computational cost.

The simulations have been run for a reasonable time ensuring that way that the flow has reached its statistically steady state. The number of samples used for the averaging was approximately between $500-600$ depending on the numerical method and the grid mesh used each time. Note that the samples were saved every 2000 time steps, and taking into account that the mean Δt was about $4 \cdot 10^5$ (for the medium grid), that leads to a corresponding non-dimensional time of $t \simeq 0.08$ per sample.

Mean and instantaneous velocity profiles, turbulence statistics and Reynolds stresses

are provided along the streamwise direction of the downstream channel in three different wall-normal locations at the xy-plane as shown in Figure 4.7. The first line (blue), which is located near the side of the lower wall at $y/h = -0.5$, crosses the larger recirculation zone, while the second line (red) is positioned in the centerplane at $y/h = 0.5$, where the core flow is present. Finally, the third line (green) is located near the side of the upper wall at $y/h = 1.5$, crossing the shorter recirculation zone. We have assumed that the flow bends upward and "hits" the side of the upper wall (the flow in all the investigated cases found to bend upwards apart from the case where the WENO $5th$-order scheme was used). Note that each of the lines extends from $x_d/h = 4$ to $x_d/h = 24$ step heights downstream of the expansion covering a total streamwise length of 20 step heights. x_d is the streamwise distance corresponding to the actual computational domain.

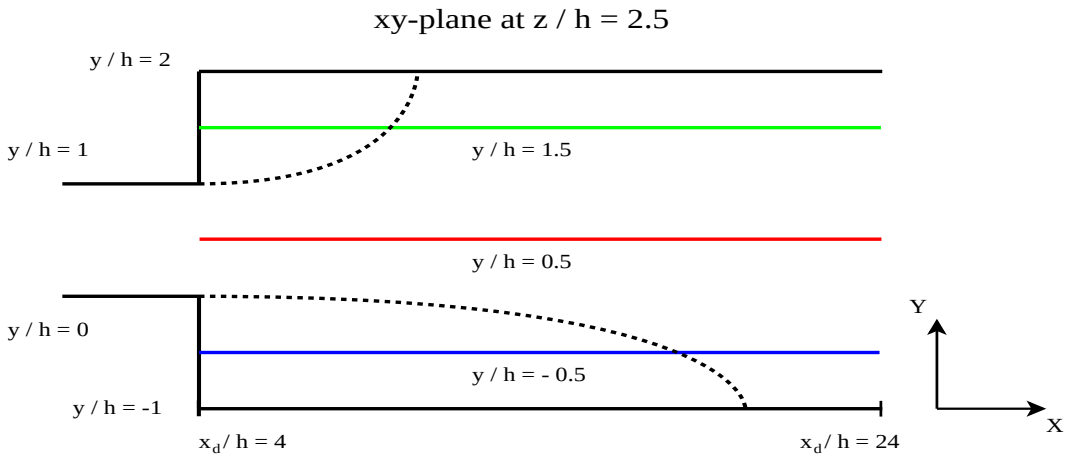

FIGURE 4.7: Three different locations along the x direction in the xy-plane where measurements are performed.

The results obtained from the numerical simulations are compared against the experimental data of Casarsa et al. [17], who investigated a turbulent flow downstream of a planar sudden expansion by means of a 2D PIV technique. Note that for the sake of consistency with the numerical results, the experimental data were mirrored appropriately such that comparisons between the two different data sources can easily be made. In Figure 4.8 the time-averaged flow paths in the midplane of the channel, visualised by means of stream tracers for all the grid meshes, are shown. It is evident that the two-dimensional symmetric flow encountered in the inlet channel emerges in the expansion, creating an asymmetric flow deviated towards the upper side wall. The high velocity core is separated from two recirculation bubbles of considerably unequal length by two shear layers

located at the expansion edges of the upstream channel. The shorter recirculation zone is encountered at the side of the upper wall where the flow primarily impinges, while the larger recirculation zone right at the opposite wall (lower wall). It is noteworthy that two secondary vortices near the corners of the side walls directly after the expansion have been found. These small-size vortices were also reported in [17], however no further investigation on their origins and contribution to the primary large flow structure was undertaken.

The primary reattachment and secondary separation lengths, determined by evaluating the locations where the mean streamwise velocity components change sign, are shown in Table 4.3. To be consistent with the experimental data, two decimal points of accuracy are used to present the numerical findings (as far as the reattachment lengths of the primary and secondary vortices are concerned). The lengths of the shorter recirculation bubble (L_1 and L_3) as well as those of the larger recirculation bubble (L_2 and L_4) are normalised by the step height of the channel, h. The PIV data, which are also provided in Table 4.3, agree well with the numerical results found in all the three grid meshes. Particularly, the reattachment length of the larger recirculation increases with increasing grid resolution and approaches the experimental value. This latter is reasonable as the length of the large recirculation zone is mainly controlled by the turbulent diffusion. On the other hand, the reattachment length of the shorter recirculation slightly decreases with increasing grid resolution, indicating that this zone is much less influenced by the turbulent diffusion of the shear layers. Abbott and Kline [1] claimed that the shorter reattachment length depends on the geometrical characteristics of the sudden expansion configuration, i.e. the expansion and aspect ratios.

As far as the lengths of the secondary vortices are concerned, both are of the same order of the step height. The same feature was addressed in [110], where the unsteady behaviour of a flow over a backward-facing step was investigated. They found that the length of the secondary vortex is of the order of one step height. However, L_3, particularly for the two finer meshes, is much smaller than that reported in the PIV experiments.

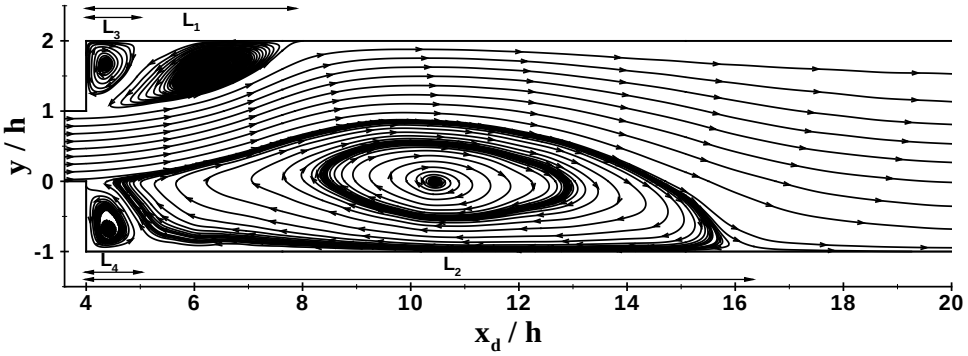

(a) Coarse Grid

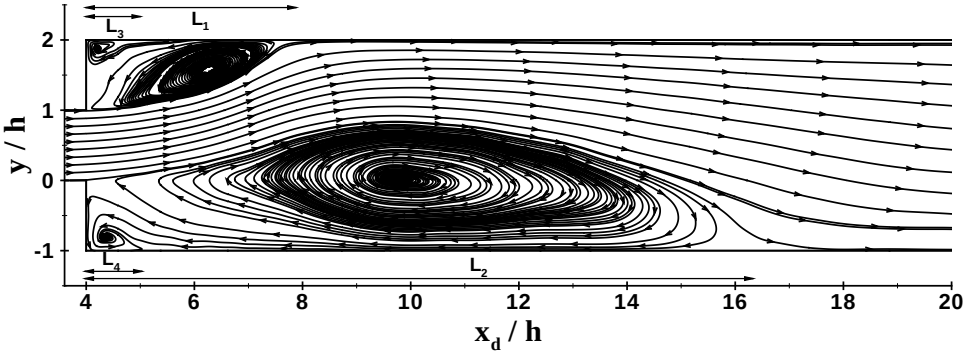

(b) Medium Grid

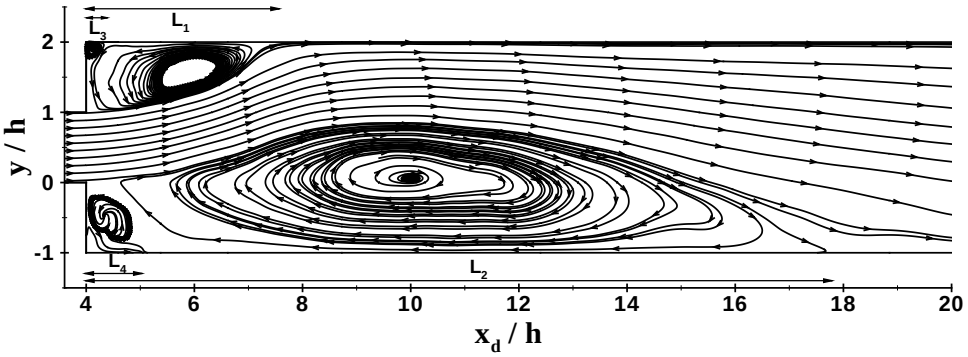

(c) Fine Grid

FIGURE 4.8: Streamlines of the mean flow at the center plane of the channel ($z/h = 2.5$) for three different grid meshes at $Re = 10^4$.

TABLE 4.3: Reattachment lengths of three different grid meshes at $Re = 10000$ for the 5^{th}-order MUSCL scheme compared against those found in [17].

Grid	L_1/h	L_2/h	L_3/h	L_4/h
Coarse	3.72	12.45	0.89	0.81
Medium	3.51	13.63	0.63	0.91
Fine	3.42	13.85	0.51	0.93
PIV 10^4	3.68	14.38	0.84	1.06

Precise comparison with previous experimental and numerical data in terms of the reattachment lengths is almost impossible because of the extremely different geometries and inflow conditions used in these studies. However, it is worth addressing some of the differences with the previous results while at the same time analysing the influence of the flow parameters on the reattachment lengths. In their pioneering work, Abbott and Kline [1] stated that the reattachment lengths of the recirculation zones are strongly related with the expansion ratio. For the case of $ER = 3$, they obtained the following ranges: $L_1/h = 11-15$ and $L_3/h = 3.5-4$, which agree well with the ILES results. They used a fully developed inlet velocity profile with the Reynolds number ranging between 20000 and 50000. Mehta [82] for $R = 3$ and a fully developed inlet velocity profile at $Re = 1.25 \times 10^5$ measured the reattachment lengths $L_1 = 15$ and $L_2 = 4.5$, which are slightly higher than that found in the present study. This can be attributed to the very low aspect ratio used for his channel ($AR = 0.25$). The reattachment lengths found by Aloui and Souhar [5] for a fully developed inlet velocity profile ($L_1 = 10.8$ and $L_2 = 5.4$) are not in good agreement with the results presented in Table 4.3. The relative small expansion ratio ($ER = 2.27$) and the extremely low aspect ratio ($AR = 0.18$) are the main reasons of this discrepancy. De Zilwa et al. [22] obtained $L_2 = 3.4$ for the small recirculation area, which agrees well with the ILES findings, especially with the results of the finest grid mesh. However, the reattachment length of the larger recirculation zone $L_1 = 17$ found to be much larger in their experiments (LDA technique). It is important to underline that a uniform inlet velocity profile was used in their experiments along with $ER = 2.86$ and $AR = 12.31$, which can in part explain the difference between the experimental and numerical results. Finally, the reattachment lengths demonstrated in [39] ($L_1 = 11.5$ and $L_2 = 3.13$) are slightly lower compared with the ILES results. However, care should

be paid in the comparisons due to the different expansion ratio and initial conditions used in their LDA experiments ($ER = 4$ with a uniform inlet velocity profile at $Re = 5.55 \times 10^4$). The reattachment lengths (x_R) found in the literature of PSE flows along with the corresponding geometrical properties are all summarised and presented in Table 4.4.

TABLE 4.4: Literature review on the primary reattachment lengths of a turbulent planar sudden expansion flow.

Author(s)	$Re(\times 10^4)$	ER	AR	U_{inlet} Profile	x_R (x/h)
[1]	2-5	1.125-5	2-16	Fully developed	3.5-4, 11-15
[82]	12.5	3	0.25	Fully developed	4.5, 15
[5]	3.2	2.27	0.18	Fully developed	5.4, 10.8
[22]	2.65	2.86	12.31	Uniform	3.4, 17
[39]	5.55	4	5.33	Uniform	3.13, 11.5
[17]	1	3	10	Fully developed	3.68, 14.38
Current Study	1	3	5	Fully developed	3.72, 13.85

The time-averaged streamwise and transverse velocity profiles are depicted in Figure 4.9 using the three grid meshes mentioned in Section 4.5. Both velocities are normalised by the inlet bulk velocity and the numerical results are compared with the experimental data provided in [17]. Note that measurements were conducted at three different locations in the x-y plane at the midplane of the channel as shown in Figure 4.7. For the calculations of the time-averaged velocity components, the following formula has been used:

$$X = \langle x \rangle \equiv \frac{1}{N} \sum_{n=1}^{N} x_n$$

where $\langle x \rangle$ is the ensemble average of the variable x (obtained at every point in the computational mesh) and N is the total number of realisations in time (i.e, the total number of saved samples). The mean flow measurements were conducted in the region where the flow is considered as statistically steady, avoiding that way of obtaining large oscillations in the mean flow values. Note that in the results presented below, the flow has crossed the whole domain in the streamwise direction, between 5 and 10 times depending on the grid

size.

Furthermore, it is also important to underline that as far as the coarse grid (henceforth grid 1) is concerned, the domain was decomposed into 13 blocks, while the simulations required 1242 CPU-hours of computational time in order to complete 20 non-dimensional timeframe (note that the flow needs $\simeq 2.2449$ non-dimensional time to cross the whole channel once). As for the medium grid (henceforth grid 2), it required 4849 CPU-hours of computational time to complete the same timeframe but having decomposed the domain into 30 blocks. Finally, the finest grid (henceforth grid 3) required 10035 CPU-hours of computational time to complete the same timeframe having decomposed the domain into 60 blocks.

The same CFL number was used in all of the three grid meshes ($\mathscr{C} = 1$), leading to the following mean time steps: $\Delta t_c = 6.17 \times 10^{-5}$, $\Delta t_m = 4.05 \times 10^{-5}$ and $\Delta t_f = 3.66 \times 10^{-5}$ for the coarse, medium and fine grid, respectively. Note, however, that in all the three different grid resolutions used, Δt was not uniform. It was closely related to the updated solution of the problem at each time step and centred around the above mean values.

In the region of the shorter reattachment ($y/h = 1.5$), all grids found to resolve the mean flow field well up to $x/h \simeq 5$, where $x = x_d - x_{step}$. However, further downstream grid 1 is not capable of resolving the mean values correctly, exhibiting a very large discrepancy compared to both the PIV data and the other two finer meshes. The clustering in the streamwise direction leads to a much coarser grid further downstream of the step, making that more prominent for the grid 1, resulting in a large discrepancy compared to both the PIV data and the other two grids. The underprediction of the streamwise velocity profile is evident for grids 2 and 3 in the same region up to $x/h = 16$, in a much lower level though. The mean transverse velocity is well predicted in the region of the shorter reattachment, with the grids 2 and 3 being almost identical along the streamwise axis.

In the region of the core flow ($y/h = 0.5$), both velocities appear to be somewhat shifted upstream up to $x/h \simeq 5$ and $x/h \simeq 3$ for the streamwise and transverse velocity, correspondingly. The grid 3 seems to be in a very good agreement with the PIV data and closer to grid 2. Between $x/h \simeq 6$ and $x/h \simeq 13$, the transverse velocity magnitude of grid 1 is slightly larger compared to its counterparts. This is mainly attributed to the coarser grid structure present in this region. The transverse velocity is almost everywhere positive from the enlargement up to $x/h \simeq 8$, reaching its maximum value about the axial location of the shorter reattachment, where $V/U_b \simeq 0.2$. Further downstream it turns out to be negative as the core flow tends to recover from the initial deviation.

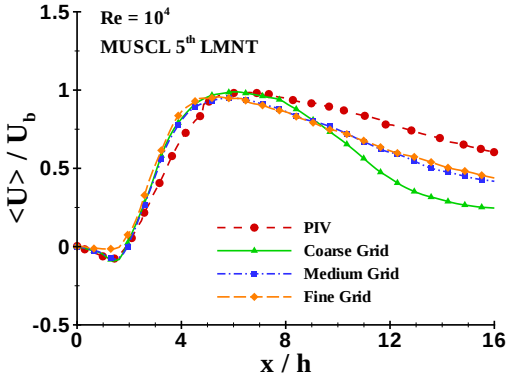

(a) U Velocity profile at Y = 1.5h

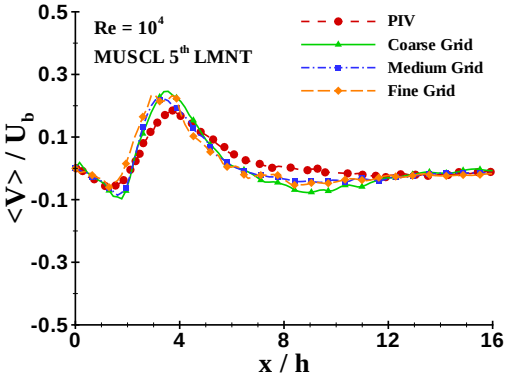

(b) V Velocity profile at Y = 1.5h

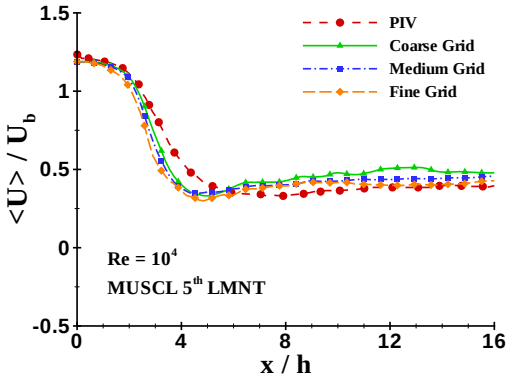

(c) U Velocity profile at Y = 0.5h

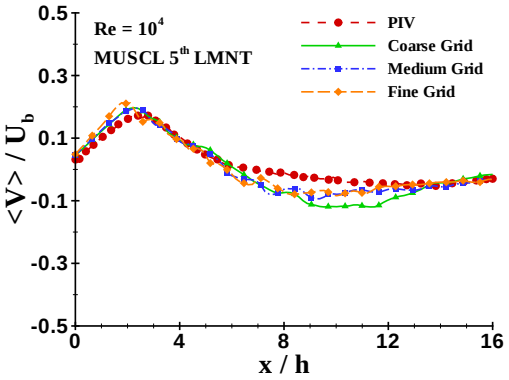

(d) V Velocity profile at Y = 0.5h

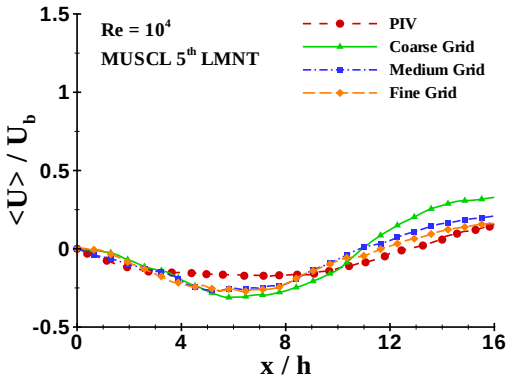

(e) U Velocity profile at Y = -0.5h

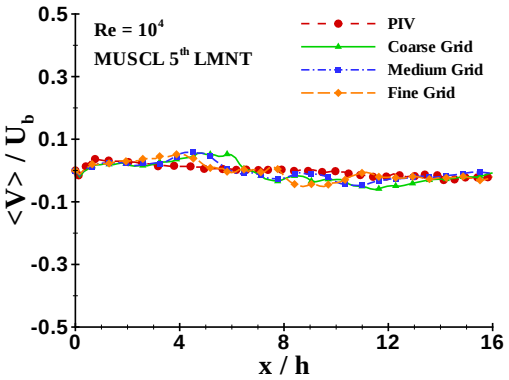

(f) V Velocity profile at Y = -0.5h

FIGURE 4.9: Time-averaged streamwise and transverse velocities along the x-axis at Re 10000.

The time-averaged streamwise velocity is negative up to $x/h \simeq 12$, in the region of the larger recirculation zone ($y/h = -0.5$) with grid 2 being closer to grid 3, indicating

that the solution has been successfully converged in that specific flow area. Besides, as the grid resolution increases, the mean velocity components get closer to the experimental data. The maximum absolute value of the streamwise velocity is observed at $x/h \simeq 6.3$ with $U/U_b = 0.27$, which is considerably higher than the experimental one. However, the mass transfer in the other two flow regions is lower than the measured one, explaining the difference in magnitude observed in this latter region in terms of the streamwise velocity. The mean wall-normal velocity found to be positive in this region almost up to 16 step heights downstream of the expansion.

Turbulence statistics are also provided in terms of r.m.s. (root mean square) velocities in both x and y direction. For that purpose, the square root of the ensemble average of the velocity fluctuations squared (also known as standard deviation) has been calculated using the following equation:

$$X_{r.m.s.} = \sqrt{\langle (x')^2 \rangle} = \sqrt{\sum_{n=1}^{N} \frac{1}{N}(x_n - \bar{x})^2}$$

where $\bar{x}$ is the mean value of variable x and $x^{'}$ stands for the fluctuations around the mean ($x^{'} = x - \bar{x}$). Note that the calculation of the r.m.s. quantity is of great importance when dealing with turbulent flows, as it defines the magnitude of fluctuations, thus the strength of turbulence in the flow field. The time-averaged velocity components, shown in Figure 4.11, are plotted against distance x/h and normalised by U_b^2. For the sake of consistency with the PIV data, the resultant quantity has been multiplied by 10^2.

In the region of the shorter recirculation zone ($y/h = 1.5$), the flow found to be rather isotropic at $x/h = 0-4$ with both r.m.s. velocity components reaching a maximum value of 25% of U_b at $x/h \simeq 3.3$. On the other hand, further downstream the flow turns out to be anisotropic, with the streamwise fluctuating velocity being slightly higher than its counterpart. The overshoot observed at the backflow area between $x/h = 1$ and $x/h = 4.5$ is as a result of both r.m.s velocities being of a higher magnitude to that of PIV. Beyond that point, the turbulent fluctuations seem to match reasonably well with the PIV data (except for grid 1), with the grid 2 being closer to grid 3. Above $x/h = 12$ all grids found to underestimate the value of the fluctuating velocities reported in the experiment. This feature has been observed in all the three regions examined in the present study, which can be explained by the fact that the grid resolution at several step heights downstream of the narrowing is poor even for the finest grid.

The turbulent field turns out to be anisotropic, the streamwise turbulence intensity being in general higher than the transverse one both in the core flow region and in the region of the larger reattachment. The maximum magnitude of the longitudinal r.m.s. velocity that has been detected is at $x/h \simeq 3$, where $U_{r.m.s.} \sim 25\%U_b$. Note that in this particular location, at the centerplane of the channel ($y/h = 0.5$), the corresponding experimental value is $\sim 20\%U_b$ resulting in a 20% difference between the ILES and experimental results. These deviations cannot be ascribed to the measurement uncertainty addressed in the experiments, which is about 5% for the stresses. These differences are mainly attributed to 1) the periodic boundary conditions applied in the spanwise direction of the channel, 2) the different aspect ratio used in the simulations and 3) the grid limitations. The presence of walls in the z-direction in conjunction with larger aspect ratio would tend to regularise the flow, by stabilising it in such a way that the intensity of turbulent fluctuations would decrease. It is important to underline that the higher turbulence intensities, observed in the larger separation region, lead to a higher turbulent diffusion which in turn leads to a shorter recirculation length.

Figure 4.10 shows the streamwise velocity and fluctuation profiles extracted at different locations downstream of the expansion channel. The results are compared against those demonstrated in [17], who provided data up to $x/h = 4$, while several more profiles are presented up to $x/h = 9$ showing the distribution of the mean and fluctuating streamwise velocity at the cross-section of the channel. The ILES results agree reasonably well with the PIV data, exhibiting only a small difference in terms of the location of the maximum streamwise velocity at $x/h = 3$ and 4. The velocity profile seems to be shifted slightly upwards, impinging the upper wall earlier compared to the experimental profile. This leads to a shorter reattachment length of the upper recirculation zone, as previously reported. As far as the fluctuating velocity is concerned, despite the fact that the turbulence intensity in the core flow region at $x/h = 0$ is lower in magnitude, further downstream seems to agree well with the PIV data, particularly in the region of the larger recirculation vortex. However, the magnitude of the time-averaged r.m.s. velocity in the region of the shorter reattachment found to be overestimated, mainly at the shear layer region close to the top wall (at $x/h = 3$).

The small noise observed in the results of the mean fluctuating velocity component is mainly due to the high levels of turbulence throughout the flow field and, particularly, near the shear layer flow regions. Note that a sufficient number of different time samples was used to investigate further the above observation. However, the results with even a

larger sample than that presented here did not change significantly (i.e., this small noise in the turbulence intensity was observed in all the time samples under investigation).

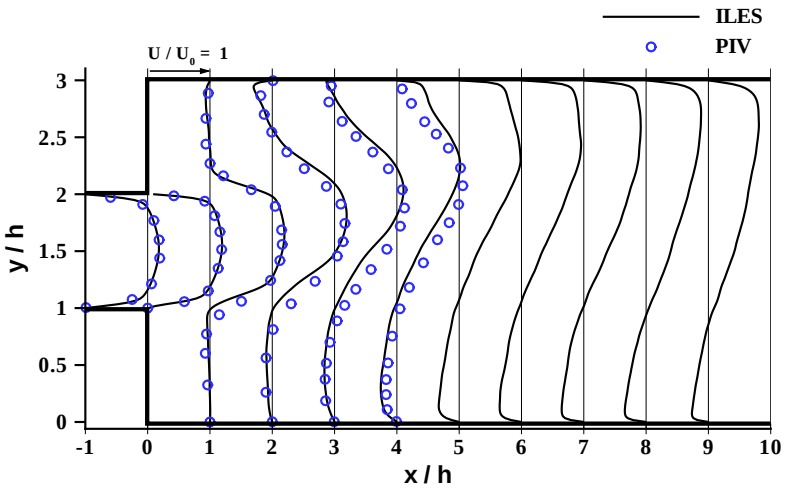

(a) Mean streamwise velocity

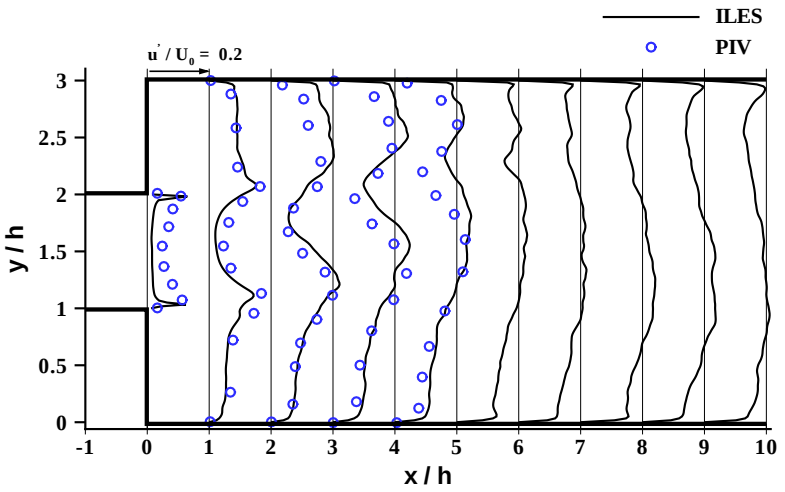

(b) Mean fluctuating velocity of U

FIGURE 4.10: Time-averaged streamwise velocity $\langle U \rangle / U_b$ and turbulence intensity u'_{rms}/U_b at $z/h = 2.5$.

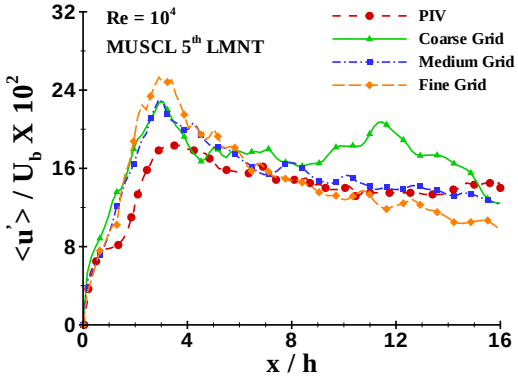

(a) U r.m.s. Velocity profile at Y = 1.5h

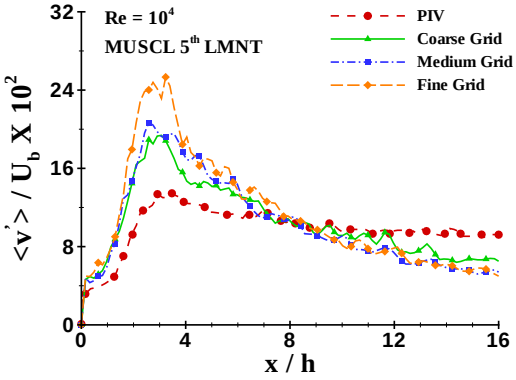

(b) V r.m.s. Velocity profile at Y = 1.5h

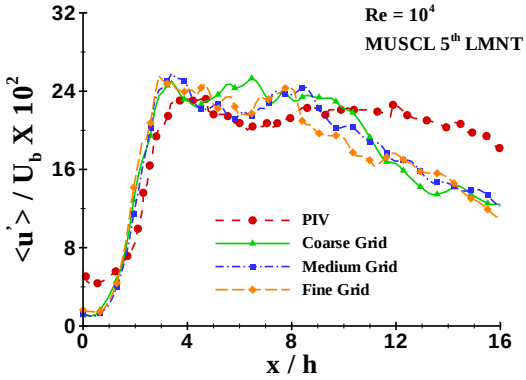

(c) U r.m.s. Velocity profile at Y = 0.5h

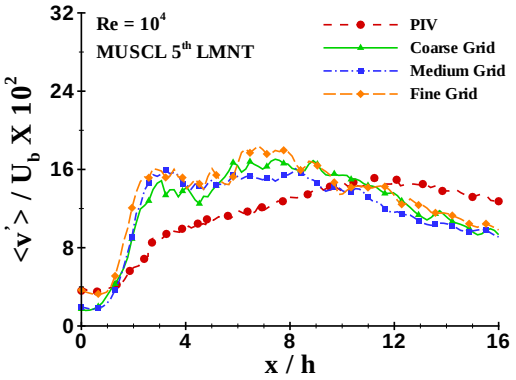

(d) V r.m.s. Velocity profile at Y = 0.5h

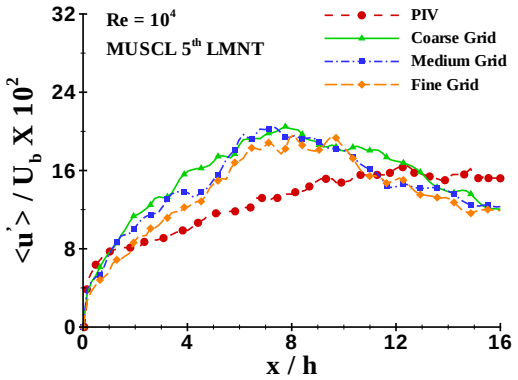

(e) U r.m.s. Velocity profile at Y = -0.5h

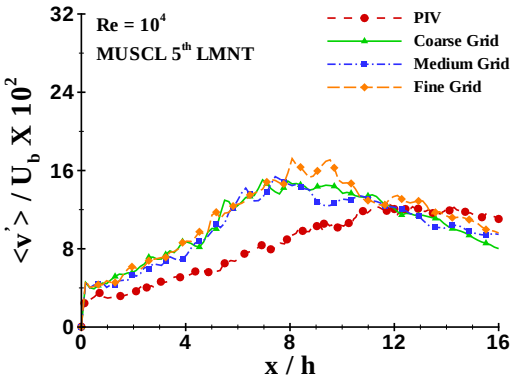

(f) V r.m.s. Velocity profile at Y = -0.5h

FIGURE 4.11: Time-averaged streamwise and transverse r.m.s. velocities along the x-axis at Re 10000.

The Reynolds shear stress, $-\overline{u'v'}$, and the turbulent kinetic energy, k, have been also

calculated along the three different axial locations at the channel midplane. Experimental data are provided for the former quantity and compared against the numerical results, whereas for the latter quantity only the results found in the present study are presented (no experimental data available). For the Reynolds shear stress calculations, the following expression has been used:

$$\left\langle u' v' \right\rangle \equiv \frac{1}{N} \sum_{n=1}^{N} [(u_n - \overline{u})(\upsilon_n - \overline{\upsilon})]$$

where u_n and υ_n represent the streamwise and transverse instantaneous velocities, respectively. The average turbulent kinetic energy per unit mass is given by:

$$k = \frac{1}{2}\left\langle q^2 \right\rangle = \frac{1}{N} \sum_{n=1}^{N} \frac{1}{2}[(u_n - \overline{u})^2 + (\upsilon_n - \overline{\upsilon})^2 + (w_n - \overline{w})^2]$$

where $q^2 \equiv u_i u_i$ and w_n is the instantaneous spanwise velocity. Note that both quantities are normalised by the mean-square inlet velocity, U_b^2.

The distributions of the normalised Reynolds shear stress are shown in Figure 4.12. The shear stress is consistent with the mean flow path of the streamwise velocity, since the inversion of the stress takes place at points of maximum U velocity. In the region of the shorter reattachment ($y/h = 1.5$) at $x/h \simeq 2-5$ the shear stress is negative with its maximum value ($\overline{u'v'} \simeq 3$) being considerably larger compared to the experimental one in all the three grids examined. However, further downstream as the flow recovers from the initial deviation and its velocity decreases, the shear stress found to be approximately zero. At this axial location the numerical results are in excellent agreement with the PIV data. It is also important the fact that grid 3 managed to accurately predict the location where the maximum value of the shear stress takes place. In this region the turbulent kinetic energy increases rapidly up to $x/h \simeq 3.2$ reaching a peak value of $k = 7$ (for grid 3), whereas beyond that point it "dies out" gradually, as expected.

In the region of the high core velocity, the shear stresses are almost zero up to a point where the measurement line crosses the shear layer of the upper wall while that moves towards the opposite wall. In that particular location the shear stress tends to increase, however the change of its magnitude is imperceptible. All grids agree well with

the experimental results with some small imperfections downstream of the flow reattachment. Taking into account that the statistical quantity under investigation is the second moment of variable U_i, that can explain the differences observed between numerical and experimental findings. The turbulent kinetic energy increases immediately after the step reaching its peak value at the same location where the maximum value of the streamwise r.m.s. velocity is detected, while maintaining its peak values up to $x/h \simeq 8$ before starting to decrease in magnitude.

In the region of the larger recirculation zone ($y/h = -0.5$), all grids found to be in excellent agreement with the PIV data at $x/h \leq 5$ and $x/h \geq 10$. In-between, the magnitude of the shear stresses is slightly higher in the present study, indicating that turbulence is present at the core of the larger recirculation vortex. The same feature was addressed in [113], with the shear stress being approximately 0.15 or 15% of U_b at $x/h \simeq 8$, which agrees well with the numerical results found at the same axial location. As far as the turbulent kinetic energy is concerned, its peak value is considerably lower than that detected in the region of the shorter bubble, with $k_{max} \simeq 5$ at $x/h = 8$, situated at the periphery of the core flow of the large recirculation area.

In all plots presented in this section, the improvement of the results from grid 1 to grid 2 is significant whereas from grid 2 to grid 3 is less prominent. That indicates that the numerical solution has been successfully converged throughout the sudden expansion domain. Furthermore, taking into account that for the completion of the same non-dimensional timeframe, the computational cost of grid 3 is about two times more than that of grid 2, all calculations in the remainder part of the thesis are undertaken using grid 2.

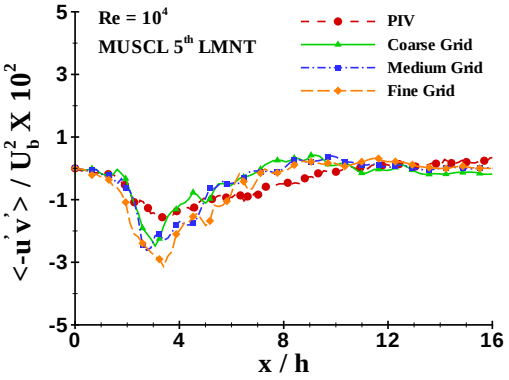

(a) Reynolds stress profile of u'v' at Y = 1.5h

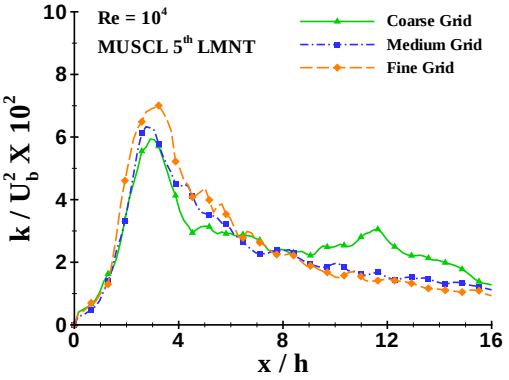

(b) Turbulent kinetic energy profile at Y = 1.5h

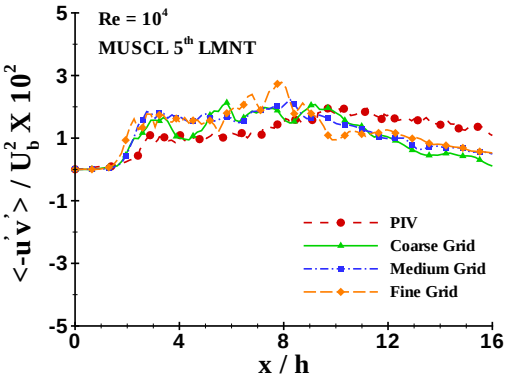

(c) Reynolds stress profile of u'v' at Y = 0.5h

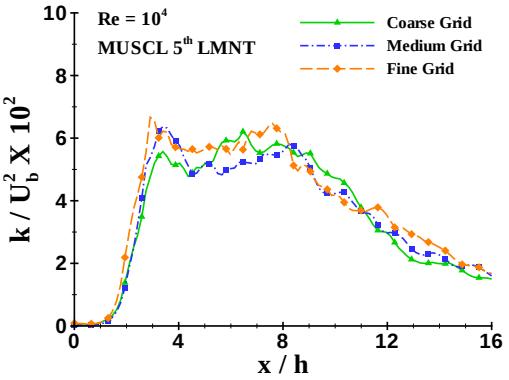

(d) Turbulent kinetic energy profile at Y = 0.5h

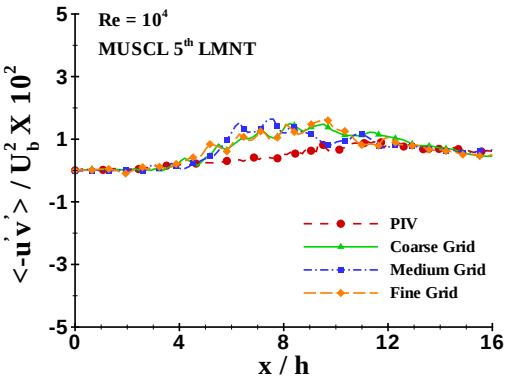

(e) Reynolds stress profile of u'v' at Y = -0.5h

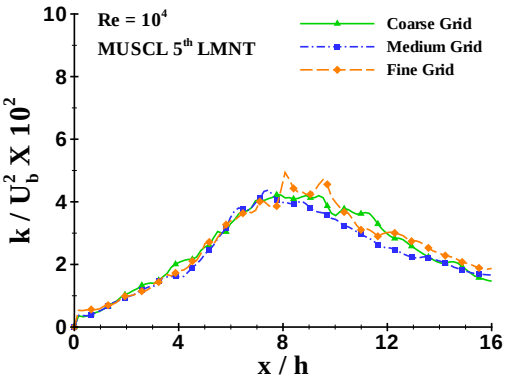

(f) Turbulent kinetic energy profile at Y = -0.5h

FIGURE 4.12: Time-averaged Reynolds stresses and turbulent kinetic energy along the x-axis at Re 10000.

4.5.2 Reynolds Number 40000

The same procedure as that presented in the preceding section will be followed here, in order to examine the grid convergence of the solution using a larger Reynolds number at $Re = 4 \times 10^4$. The number and size of the grid meshes, the computational parameters, as well as the CFL number employed in the present simulations are exactly the same with that used for $Re = 10^4$. The 5^{th}-order MUSCL scheme was also used for the numerical calculations and the results obtained are compared against the experimental data of Casarsa et al. [17].

In Figure 4.13 the time-averaged flow paths at the center plane of the channel, visualised by means of stream tracers and contour plots, are shown. Similar asymmetric flow pattern as that reported for $Re = 10^4$ is observed downstream of the step, with two recirculation zones of unequal size being formed in the two sides of the channel. The flow in all grids found to bend upward with the shorter vortex being formed at the top wall, whereas the larger one at the bottom wall. The streamwise mean velocity field is also presented - after being normalised by the inlet bulk velocity - confirming further the previous statement. Besides, the contour levels used in all the three grid resolutions are the same and range from -0.2 to 1.15, as shown in Figure 4.13. Two secondary vortices at the corners of the wall are formed having a size of about one step height. Surprisingly, these secondary vortices have been successfully captured even by the coarse grid used in the simulations.

The core flow stemmed from the inlet channel, emerges in the expansion and keeps its high momentum up to approximately 12 step heights downstream of the step. The position of the high-velocity core flow, however, is highly affected by the formation of the large recirculation vortex, which suppresses the flow field and, subsequently, changes its direction. Beyond that point, the mean streamwise velocity gradually decreases, reaching a value of $\sim 40\%$ of the maximum centerline velocity at the step. Further downstream the flow pattern does not exhibit any particular behaviour, with the streamlines being almost parallel to each other and the mean streamwise velocity keeping its low magnitude.

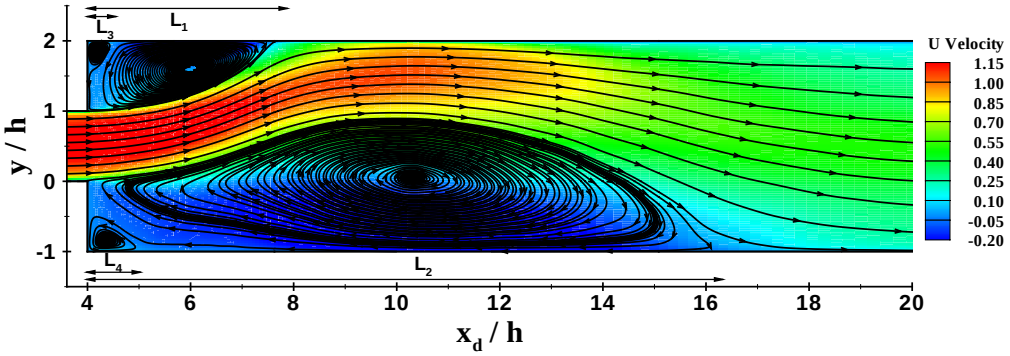

(a) Coarse Grid

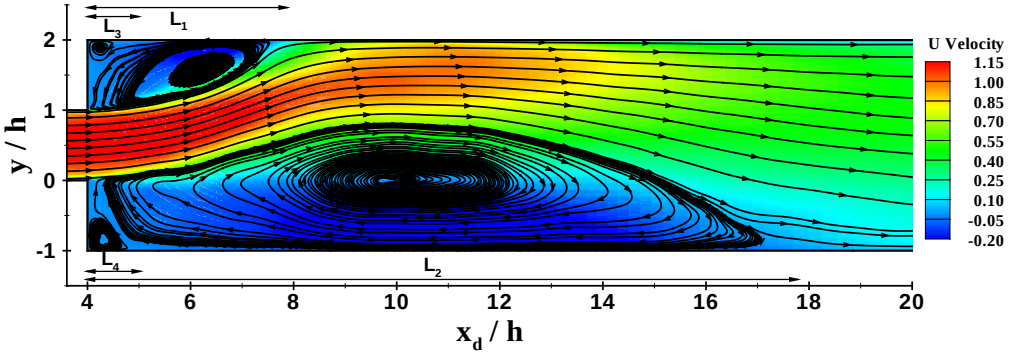

(b) Medium Grid

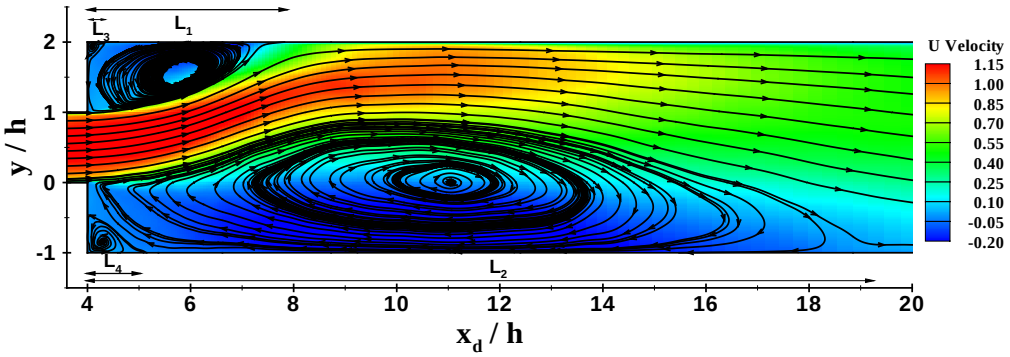

(c) Fine Grid

FIGURE 4.13: Contour streamlines of the mean flow at the center plane of the channel ($z/h = 2.5$) for three different grid meshes at $Re = 4 \cdot 10^4$.

In Table 4.6, the reattachment lengths of the primary and secondary recirculation zones of the three grids used in the numerical calculations are demonstrated. For the sake of comparison with the numerical results found in the present study, the experimental data addressed in [17] are also presented. Note also that the method followed to estimate the lengths of the vortices is the same in both cases, and is accomplished by evaluating the locations in the flow field where the streamwise velocity component changes sign.

As far as the length of the shorter reattachment is concerned, this was found to barely decrease with increasing grid resolution. It is evident that L_1 compared to the PIV data is slightly underestimated with a percentage difference lying between 7.9 and 9.7 per cent. This can be mainly ascribed to the different boundary conditions applied on the spanwise direction, as well as to the smaller aspect ratio used in the present study. Furthermore, it can be said that the higher r.m.s. velocity profiles detected close to the region of the shorter recirculation area, result in the increase of the turbulent diffusion which in turn leads to a lower reattachment length. It is important to underline that this last observation has been also made for the lower Re under investigation, as that was addressed in the previous section.

The primary separation lengths of the longer reattachment seem to have exactly the opposite behaviour compared to that found for the shorter reattachment. That is, the separation length increases with increasing mesh resolution. Grids 2 and 3 agree reasonably well with each other, as well as with the PIV data. On the contrary, grid 1 found to deviate a lot from the experimental value. The lengths of the secondary vortices in all the three grids under investigation are in a very good agreement with the experimental ones. However, grid 3 seems to give the best results in terms of the lengths of the secondary separations, with the values of L_3 and L_4 matching surprisingly well with the experimental data.

TABLE 4.5: Reattachment lengths of three different grid meshes at $Re = 40000$ for the 5^{th}-order MUSCL scheme compared against those found in [17].

Grid	L_1/h	L_2/h	L_3/h	L_4/h
Coarse	3.62	12.56	0.84	0.81
Medium	3.61	14.17	0.85	0.71
Fine	3.54	14.65	0.56	1.12
PIV $4 \cdot 10^4$	3.93	14.17	0.54	1.06

The time-averaged streamwise and wall-normal velocity components are shown in Figure 4.14. Both components have been normalised with respect to the inlet bulk velocity, U_b. Note that the same measurement lines, along the main channel of the computational domain, were used to compare the ILES results with the experimental data provided by Casarsa et al. [17] (see Figure 4.7). It can be clearly seen that in the region of the shorter recirculation zone, as well as in the high-velocity core flow region, the mean streamwise and transverse velocity components are shifted upwards compared to the experimental data. However, further downstream and up to $x/h = 16$ both curves agree reasonably well with the PIV data, with grid 2 being closer to grid 3. The maximum negative value of the mean streamwise velocity found to be overestimated in the region of the larger reattachment, with its magnitude being approximately four times larger than that in the experiment. In this latter region, the mean transverse velocity curve matches reasonably well with the experimental one, exhibiting almost everywhere a positive value. Note also that the maximum value of the wall-normal velocity is reached in the core flow region, and about the axial location of the shorter reattachment at $x/h \simeq 3.6$. The earlier maximum value in the region of the shorter recirculation area (see Figure 4.14(b)) is associated with earlier reattachment, as that was established in the measurements of the reattachment lengths shown in Table 4.6.

The normalised r.m.s. axial and transverse turbulence intensities u' and v' are shown in Figure 4.15. The flow asymmetry that takes place after the step leads to the fluctuating velocities having different maximum values towards the two sides of the main channel. It is also evident that these maximum values are located at different streamwise locations. Thus, in the lower recirculation area the positions of maxima follow the trajectory of the

mean streamwise velocity towards the lower wall, whereas in the region of the longer reattachment the high turbulence intensity increases with the shear layer growth, reaching its peak value at $x/h \simeq 9$ and $x/h \simeq 10$ for the axial and transverse r.m.s. velocity component, respectively ($u^{'} \simeq 18\%U_b$ and $v^{'} \simeq 16\%U_b$). The flow anisotropy is more pronounced in the high-velocity core flow region and in the location of the larger recirculation zone. On the other hand, the flow seems to be almost isotropic in the region of the shorter reattachment, with the streamwise r.m.s. velocity being almost identical to its counterpart (i.e., the maximum time-averaged values in that particular location are: $u^{'}_{max} \simeq v^{'}_{max} = 22\%U_b$).

After the reattachment both flow quantities, $\left\langle u^{'}_{max} \right\rangle / U_b$ and $\left\langle v^{'}_{max} \right\rangle / U_b$, decrease rapidly with streamwise distance. This last feature was also demonstrated in the experimental study of Eaton and Johnston [37] for a turbulent flow over a backward-facing step. Besides, Escudier et al. [39] found that several step heights after the reattachment location, $u_{r.m.s.}$ and $v_{r.m.s.}$ profiles are almost uniform across the duct, with their magnitudes being approximately 50% lower than those detected in the region prior to reattachment. In regions close to the top and bottom wall, grid 2 is much closer to grid 3 than to grid 1. This last observation is more pronounced in the calculations of the axial r.m.s. velocity, $u^{'}$. It is also important to underline that the turbulence intensities found here are, in general, higher than those demonstrated in the experimental study of Casarsa et al. [17].

The time-averaged Reynolds shear stress, $-\overline{u^{'}v^{'}}$, along with the mean turbulent kinetic energy, k, are shown in Figure 4.16. Both flow quantities were normalised by the inlet bulk velocity squared, U_b^2. A direct comparison with experimental data was not possible for $Re = 4 \cdot 10^4$, because of the lack of information on the shear stress and turbulent kinetic energy. Nevertheless, measurements of turbulence statistics are considered to be of very high importance, especially when a grid convergence study is carried out. It is widely known that accurate measurements of high-order statistics require sufficiently large number of realisations in time. Thus, the aim here is twofold: (a) to show that the number of the total time steps, hence, the time window of the simulations is sufficient enough for the flow to reach a fully steady state, and (b) to use this time window in order to further investigate whether the numerical solution has been successfully converged.

In the lower recirculation region all the three curves found to have a similar shape, with grid 2 being in excellent agreement with the finest grid employed in the simulations. The Reynolds stress takes its peak value, $\overline{u^{'}v^{'}}_{max} = 0.027U_b^2$, about the location of the maximum r.m.s. streamwise velocity at $x/h \simeq 3$. Escudier et al. [39] demonstrated a maximum shear stress of $\overline{u^{'}v^{'}}_{max} = 0.023U_b^2$, which agrees well with the present results.

Besides, they also observed that the peak shear stress occurs at the same streamwise location as the maximum axial turbulence intensity. The turbulent kinetic energy profile is similar to that of the streamwise r.m.s. velocity in that particular region, with its maximum value being detected at $x/h \simeq 3$. The turbulent kinetic energy magnitude decreases with downstream distance, as expected.

In the region of the larger recirculation zone the maximum shear stress is almost half of that in the lower recirculation area, reaching a peak value of $\sim 0.012U_b^2$ at $x/h = 7$. The magnitude of shear stress remains high for up to several step heights downstream of the step until 11 step heights downstream of the step where it starts gradually to decrease. Escudier et al. [39] found that in this latter region the maximum shear stress has a value of $0.011U_b^2$, which agrees well with the present results. However, they addressed that the location of the peak shear stress is immediately after the expansion, which is not consistent with the present results. It is also evident that grid 2 is in excellent agreement with grid 3, while grid 1 slightly deviates from its counterparts in the region of the maximum shear stress. The turbulent kinetic energy profile is similar to the r.m.s axial and transverse velocity profiles presented above.

With regard to the grids used to investigate the time-averaged flow behaviour at $Re = 4 \cdot 10^4$, it is noteworthy that all the three grids gave, in general, similar results. The differences observed are more pronounced between grid 1 and grid 2, whereas they are less prominent between grid 2 and grid 3. There is, thus, a strong indication that the numerical solution has well converged. Over and above taking into account that (a) grid 3 is almost two times more computationally expensive than grid 2, and (b) the differences between these two finer grids are not very significant with each other, grid 2 will be used in the remainder part of the thesis in order to investigate further the influence of different Reynolds numbers on the flow behaviour in the sudden expansion configuration.

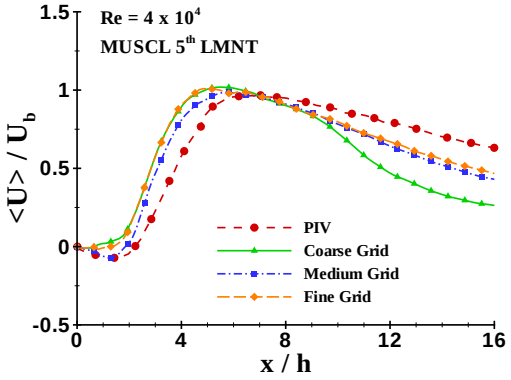

(a) U Velocity profile at Y = 1.5h

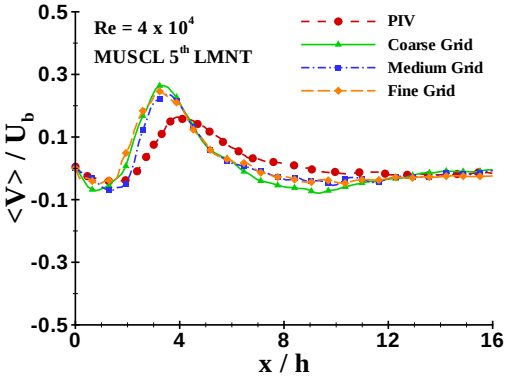

(b) V Velocity profile at Y = 1.5h

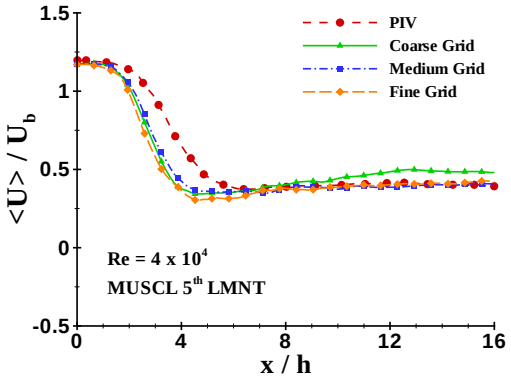

(c) U Velocity profile at Y = 0.5h

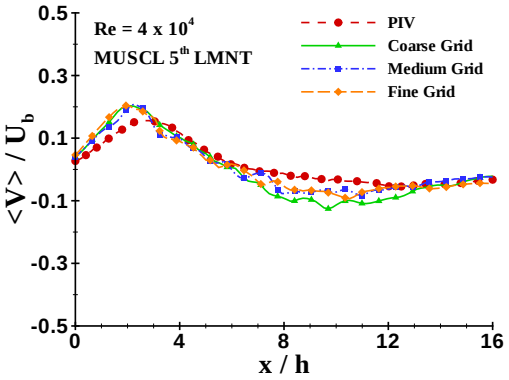

(d) V Velocity profile at Y = 0.5h

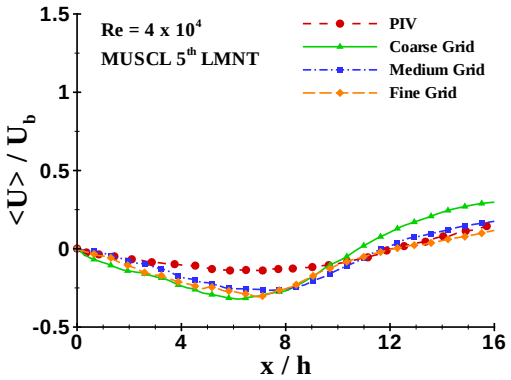

(e) U Velocity profile at Y = -0.5h

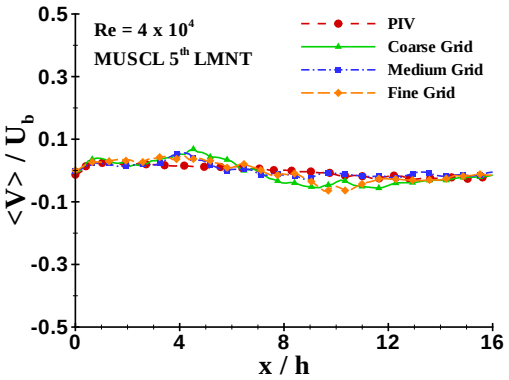

(f) V Velocity profile at Y = -0.5h

FIGURE 4.14: Time-averaged streamwise and transverse velocities along the x-axis (xy-plane) at Re 40000.

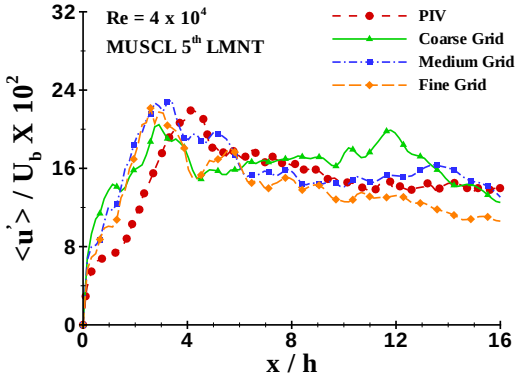

(a) U r.m.s. Velocity profile at Y = 1.5h

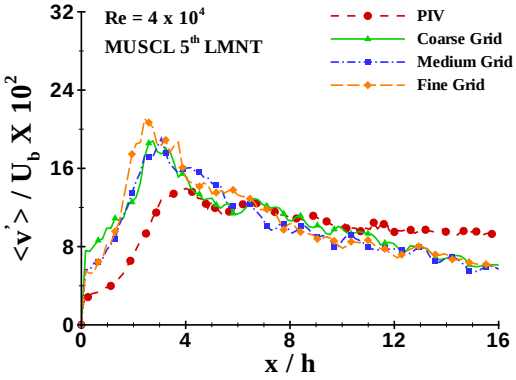

(b) V r.m.s. Velocity profile at Y = 1.5h

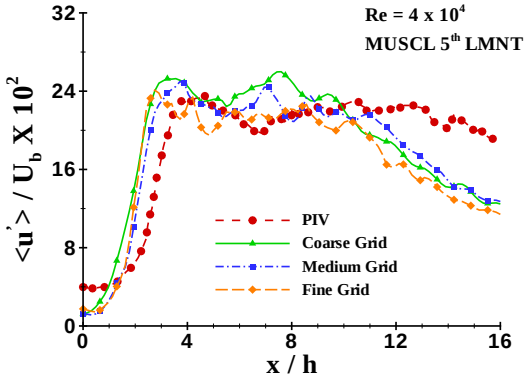

(c) U r.m.s. Velocity profile at Y = 0.5h

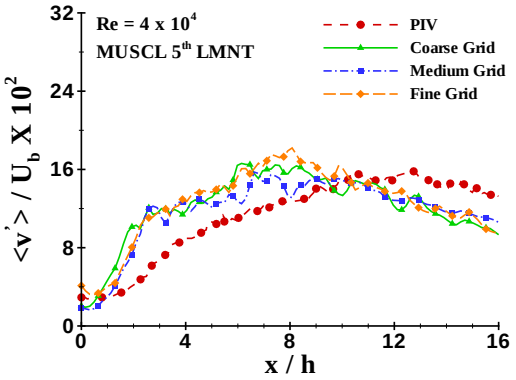

(d) V r.m.s. Velocity profile at Y = 0.5h

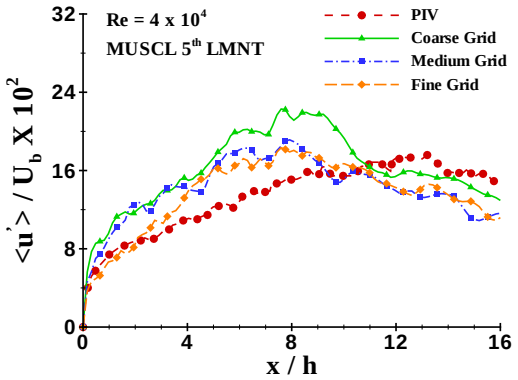

(e) U r.m.s. Velocity profile at Y = -0.5h

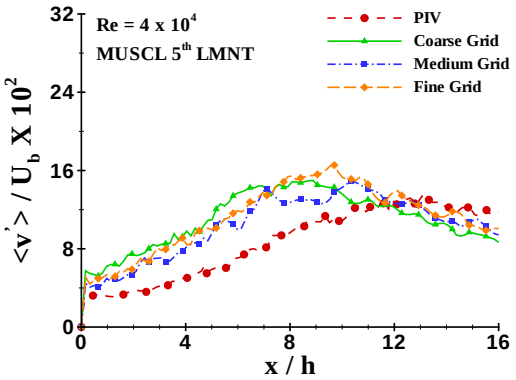

(f) V r.m.s. Velocity profile at Y = -0.5h

FIGURE 4.15: Time-averaged streamwise and transverse r.m.s. velocities along the x-axis (xy-plane) at Re 40000.

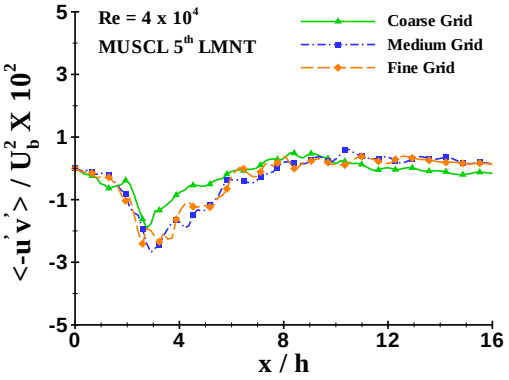

(a) Reynolds stress profile of u'v' at Y = 1.5h

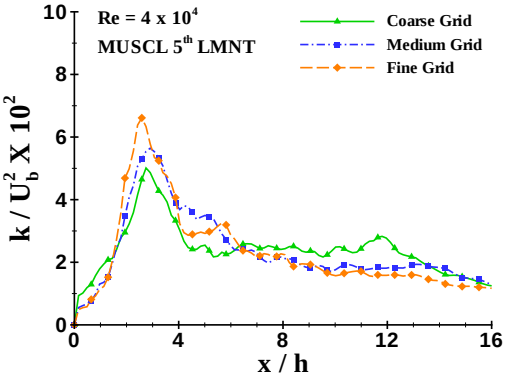

(b) Turbulent kinetic energy profile at Y = 1.5h

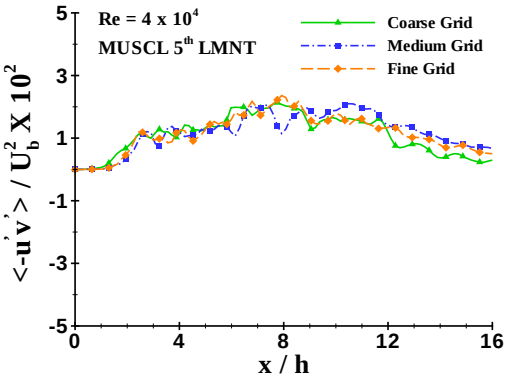

(c) Reynolds stress profile of u'v' at Y = 0.5h

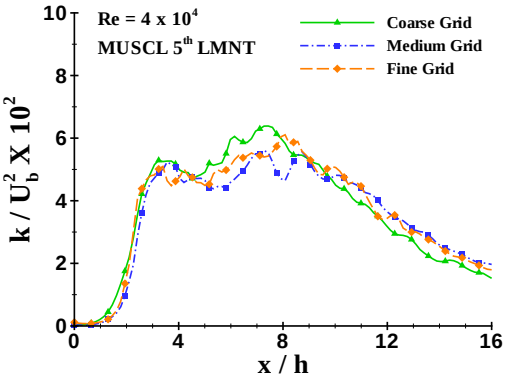

(d) Turbulent kinetic energy profile at Y = 0.5h

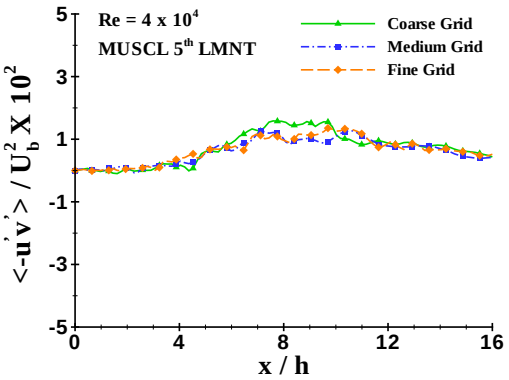

(e) Reynolds stress profile of u'v' at Y = -0.5h

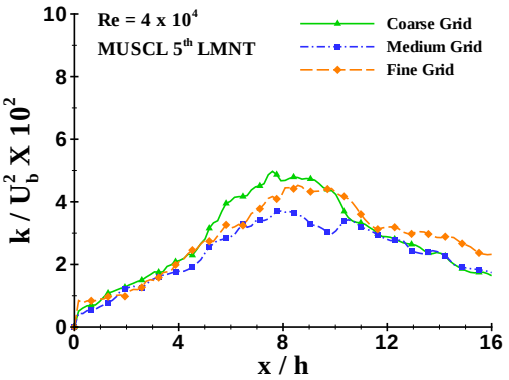

(f) Turbulent kinetic energy profile at Y = -0.5h

FIGURE 4.16: Time-averaged Reynolds stresses and turbulent kinetic energy along the x-axis (xy-plane) at Re 40000.

4.6 Validation

4.6.1 Numerical Methods

In this section the influence of the numerical schemes on the mean flow values is examined. For that purpose three different high-resolution schemes are used in the simulations of a turbulent flow over a sudden expansion configuration at $Re = 10^4$, based on the inlet bulk velocity and the step height of the channel. As previously mentioned, these high-resolution, high-order schemes include the MUSCL 3^{rd} and 5^{th} (M3, M5) order schemes proposed by Kim and Kim [67, 68], as well as the WENO 5^{th} order method (W5) introduced by Jiang and Shu [61]. For further information on WENO schemes and their properties (stability, accuracy, convergence) see [7, 102, 118]. Besides, considering that the simulations are performed at a low Mach number (the flow belongs to the incompressible regime), on each scheme a Low Mach Number Treatment (LMNT) is imposed, which aims to increase turbulence intensity, and at the same time reduce the numerical dissipation.

In Figure 4.17 the mean flow structures for the three different numerical schemes are represented by means of stream tracers. The flow emanating from the inlet channel upstream of the expansion bends upwards, before impinging on the upper wall of the main channel. At this particular side wall, a primary recirculation zone is formed extending several step heights downstream, while at the same time a secondary vortex appears immediately after the step at the corner of the channel.

Furthermore, a second recirculation zone in the near-wall region of the lower-half of the channel is created, with its reattachment length being several step heights larger than the shorter one at the opposite side. Further downstream the flow recovers from the strong instability, as finally the streamlines become almost parallel to each other. A secondary vortex at the location of the larger reattachment is also formed, having almost the same length with the secondary vortex found on the opposite wall.

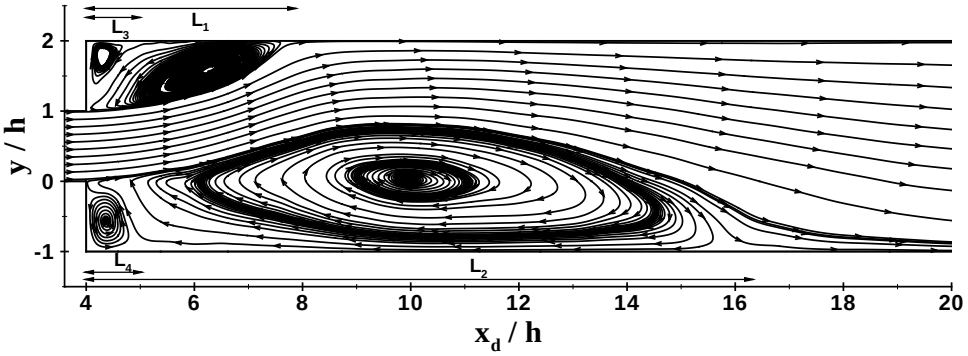

(a) third-order MUSCL scheme

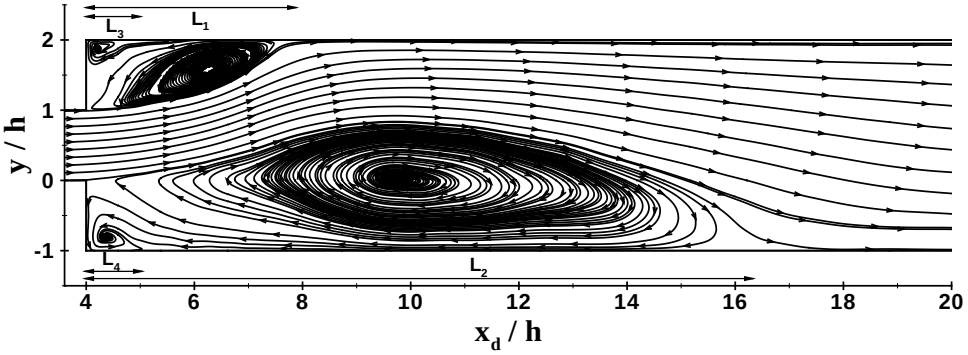

(b) fifth-order MUSCL scheme

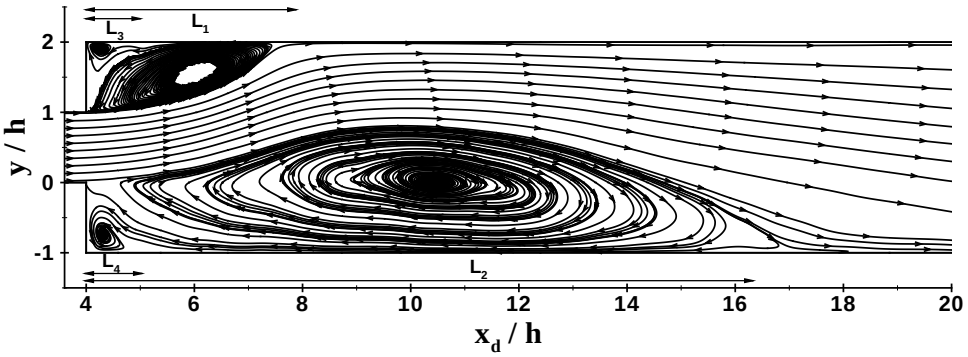

(c) fifth-order WENO method

FIGURE 4.17: Streamlines of the mean flow at the center plane of the channel ($z/h = 2.5$) for three different high-resolution schemes.

TABLE 4.6: Reattachment lengths of three different numerical schemes at $Re = 10^4$ compared against those found in [17].

Numerical Scheme	L_1/h	L_2/h	L_3/h	L_4/h
M3	3.61	12.91	0.94	0.81
M5	3.51	13.63	0.91	0.71
W5	3.61	14.11	0.86	0.92
PIV 10^4	3.68	14.38	0.84	1.06

The reattachment lengths are moderately influenced by the numerical scheme applied to approximate the advective fluxes of the NSE. This can be clearly seen in Table 4.6, where the sizes of primary and secondary recirculation zones are addressed. The length of the primary recirculation in the larger bubble appears to be larger for the case of W5, and at the same time much closer to the the experimental data demonstrated in [17] than its counterparts. The development of the longer recirculation region is mostly controlled by the turbulent diffusion which is rather larger for W5. The percentage differences in terms of the primary recirculation zone of the larger vortex are approximately 1.9%, 5.2% and 10.2% for W5, M5 and M3, respectively.

The shorter reattachment, on the other hand, is much less influenced by the numerical scheme, with its length having about the same magnitude for all the three numerical schemes examined. Besides, the lengths of the secondary recirculation zones found to be in a very good agreement with the experimental data. It can be concluded that as far as the lengths of the recirculation zones are concerned, these found to be closer to the PIV data for the case of W5. This superiority of W5 over M3 and M5 is also appearing in the calculations of the time-averaged velocities and turbulence intensities.

The streamwise and transverse velocity profiles calculated at three different wall-normal positions, are shown in Figure 4.18. The transverse velocity profiles show slight difference in the region of the high-velocity core flow at $y/h = 0.5$. At this particular position, W5 appears to be closer to the experimental profile for several step heights downstream of the expansion, until the location (approximately $x/h = 8$) where it deviates from the PIV data and collapses with the M3 and M5 profiles. The streamwise velocity distributions do not exhibit any significant variation, with a slight difference being only observed at about the location of the larger reattachment between $x/h = 9.5 - 16$.

The turbulent statistics (r.m.s. velocity profiles) for the three different numerical schemes are shown in Figure 4.19. It turns out that the mean fluctuating velocity profiles are almost identical for M3 ad M5. On the other hand, the profiles corresponding to W5 seem to considerably deviate from its counterparts, being however much closer to the experimental data. Particularly, in the region of the shorter reattachment ($y/h = 1.5$) the streamwise r.m.s. velocity profile for W5 turns out to be almost identical to the PIV profile along the x-direction. Its maximum value is approximately $u^{'}/U_b \sim 17\%$ which is in excellent agreement with the findings of Casarsa et al. in that particular location. The transverse fluctuating profiles found to be closer to the experimental results for the case of W5. However, it is evident that its peak value is overestimated for all the numerical methods examined. It has been also observed that the flow is almost everywhere anisotropic with the streamwise turbulence intensity being slightly higher, and in some cases, considerably higher than the transverse one. The fluctuations show local maxima about the shorter reattachment ($x/h \simeq 4$) and three to four step heights upstream of the longer one ($x/h \simeq 9$).

The Reynolds shear stress, $-\overline{u'v'}$, along with the turbulent kinetic energy, k, calculated at three measurement locations along the streamwise direction of the xy- plane, are plotted in Figure 4.20. Two large areas of positive and negative $-\overline{u'v'}$ can be shown in the lower and upper part of the channel, respectively. The field of shear stresses is consistent with the mean flow pattern found for the streamwise velocity component, since the inversion of the stress direction takes place in points of maximum streamwise velocity U/U_b. In the region of the shorter recirculation zone, the shear stress profile corresponding to W5 appears to be in excellent agreement with the experimental evidence. It can be clearly seen that for W5, the Reynolds shear stress profile at $y/h = 1.5$ agrees reasonably well with the experimental one in terms of its maximum absolute value and location (i.e., the position of the maximum absolute shear stress value is placed at approximately four step heights downstream of the step, at about the reattachment location of the shorter bubble). The peak values observed for M3 and M5 seem to be considerably higher in both flow regions where strong backflow is formed.

As far as the turbulent kinetic energy (TKE) is concerned, it can be said that the highest level of turbulence is observed in the region of the shorter reattachment at about $x/h \simeq 4$. Furthermore, the peak values for M3 and M5 appeared to be significantly larger compared to those found for W5. This is consistent with the peak r.m.s. velocity values found for M3, M5 and W5 (i.e., in the case of M3 and M5 all the fluctuating velocity profiles found

to be largely overestimated). From the above observation it can be extracted that W5 combined with the LMNT approach yields to lower levels of TKE compared to the M3 and M5 reconstruction methods. This last means that W5 is not so underdissipative as its counterparts. As no experimental data is provided for the turbulent kinetic energy, further comparisons cannot be made. However, it can be said that the level of turbulence intensity when the W5 is used, is probably closer to the real TKE levels (based on the results on the fluctuating velocity components presented in Figure 4.19).

To sum up, it is important to point out that all the three numerical schemes examined, found to adequately resolve the mean flow. Results on turbulence intensities and Reynolds stresses revealed that W5 outperforms M3 and M5 significantly. It seems that MUSCL schemes in conjunction with LMNT leads to much less numerical dissipation, which in turn results in larger levels of turbulence, particularly in the strong reversed flow regions. It is therefore essential to further investigate the performance of high-resolution high-order schemes in suddenly-expanded flows, when LMNT is imposed.

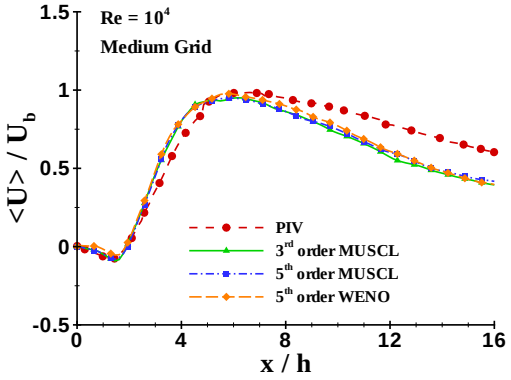

(a) U Velocity profile at Y = 1.5h

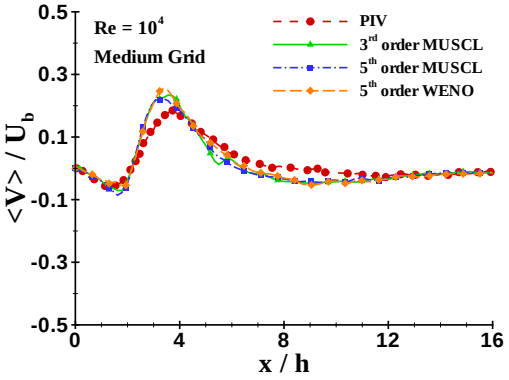

(b) V Velocity profile at Y = 1.5h

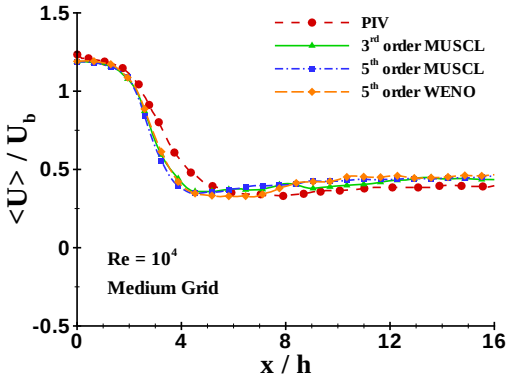

(c) U Velocity profile at Y = 0.5h

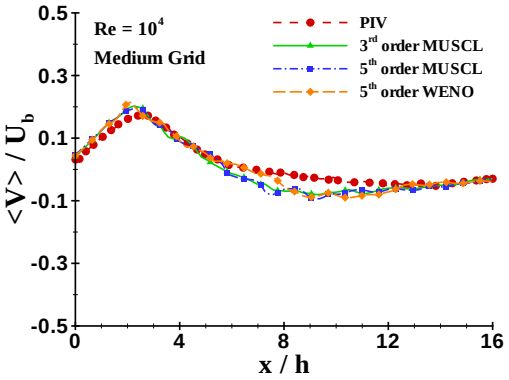

(d) V Velocity profile at Y = 0.5h

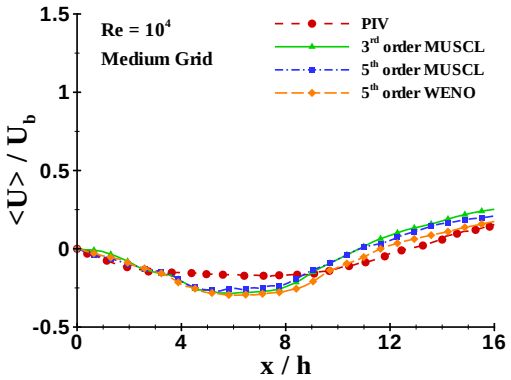

(e) U Velocity profile at Y = -0.5h

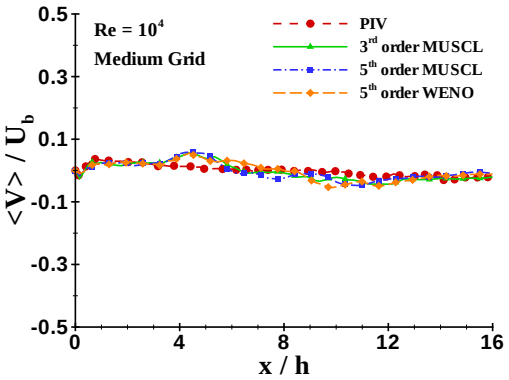

(f) V Velocity profile at Y = -0.5h

FIGURE 4.18: Time-averaged streamwise and transverse velocities along the x-axis (xy-plane) at $Re = 10^4$.

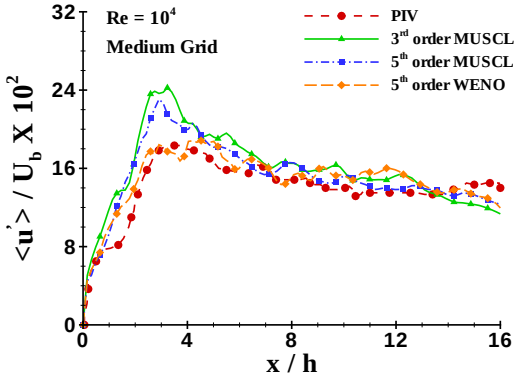

(a) U r.m.s. Velocity profile at Y = 1.5h

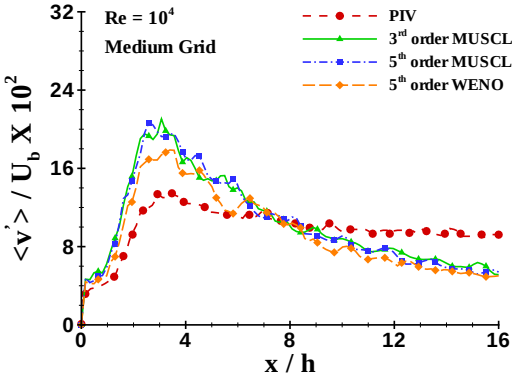

(b) V r.m.s. Velocity profile at Y = 1.5h

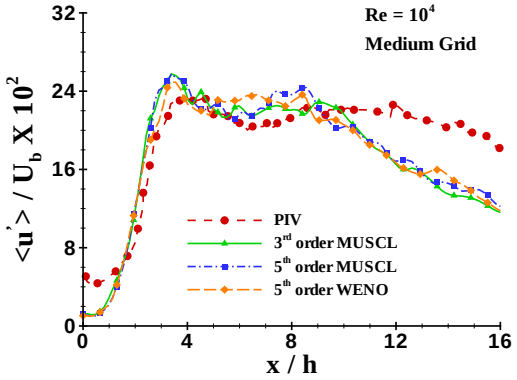

(c) U r.m.s. Velocity profile at Y = 0.5h

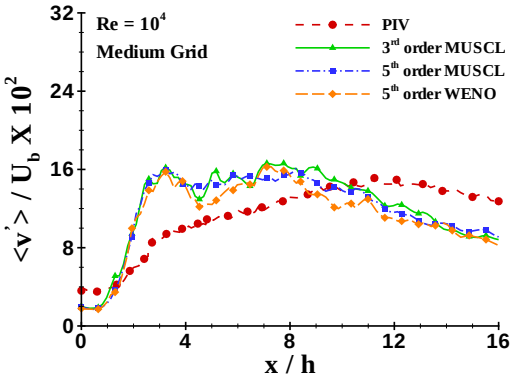

(d) V r.m.s. Velocity profile at Y = 0.5h

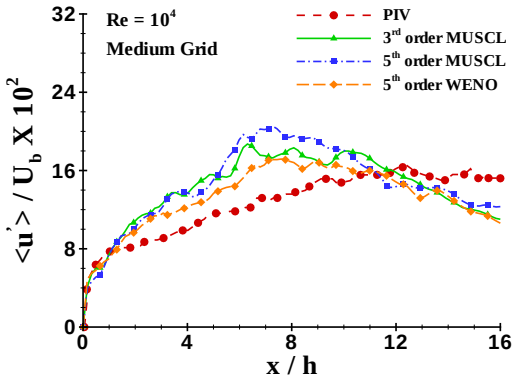

(e) U r.m.s. Velocity profile at Y = -0.5h

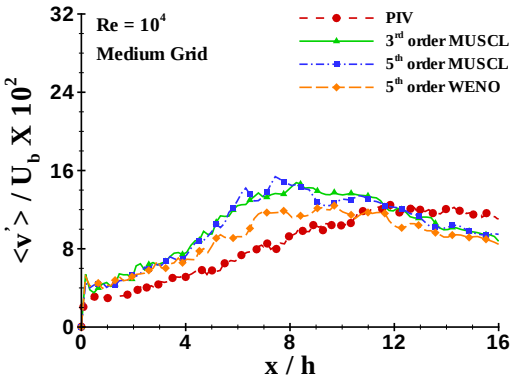

(f) V r.m.s. Velocity profile at Y = -0.5h

FIGURE 4.19: Time-averaged streamwise and transverse r.m.s. velocities along the x-axis (xy-plane) at $Re = 10^4$.

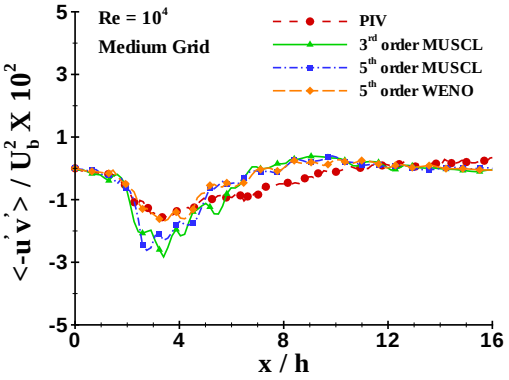

(a) Reynolds stress profile of u'v' at Y = 1.5h

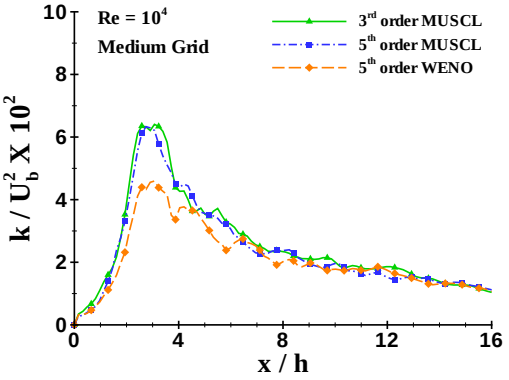

(b) Turbulent kinetic energy profile at Y = 1.5h

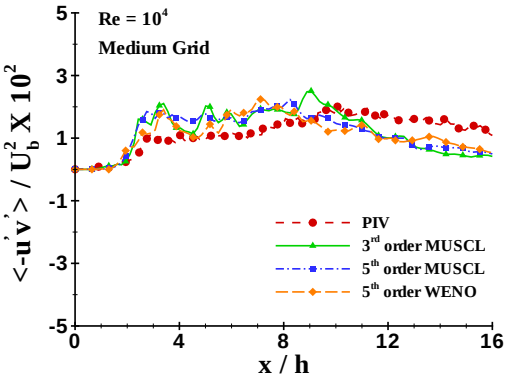

(c) Reynolds stress profile of u'v' at Y = 0.5h

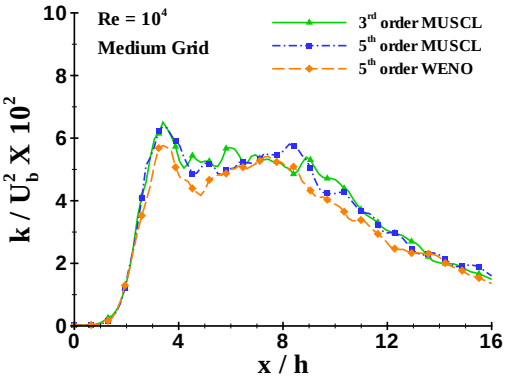

(d) Turbulent kinetic energy profile at Y = 0.5h

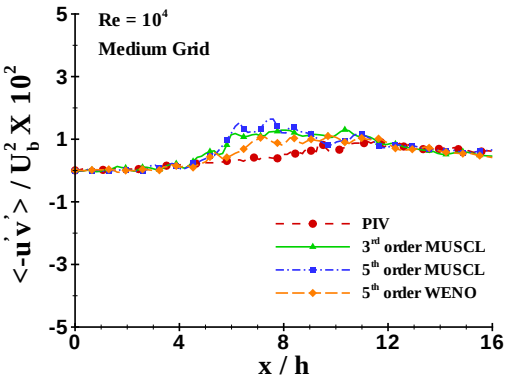

(e) Reynolds stress profile of u'v' at Y = -0.5h

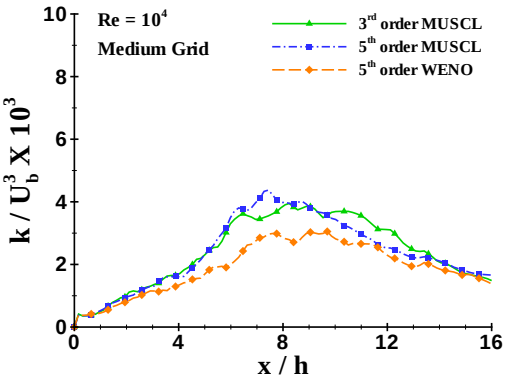

(f) Turbulent kinetic energy profile at Y = -0.5h

FIGURE 4.20: Time-averaged Reynolds stresses and turbulent kinetic energy along the x-axis (xy-plane) at $Re = 10^4$.

Wall Pressure and Skin-Friction Coefficients

The wall pressure distribution, as well as the wall skin-friction coefficient are shown in Figure 4.22. Both flow quantities were measured along the xy center plane of the channel for both upper and lower walls. Note that measurements were carried out up to 30 step heights downstream of the step in the streamwise direction, as further downstream the flow did not exhibit any particular behaviour. Three different high-resolution schemes were used in order to investigate the numerical scheme effects on the pressure and skin-friction profiles. The local wall pressure coefficient distribution is defined by the following equation:

$$C_P = \frac{2\,(P_w - P_{in})}{\rho U_{in}^2} \tag{4.10}$$

where P_w is the pressure on the wall, and P_{in} is a reference pressure taken as the upstream centerline pressure at the inlet, which corresponds to the maximum inlet velocity, U_{in}. The U_{in} and P_{in} were averaged over a sufficient number of time realisations extending up to 1 million timesteps, corresponding to approximately $t = 20$ non-dimensional time. Note that the flow needs $\simeq 2.25$ non-dimensional time to pass through the whole channel once. This latter means that the flow has passed through the whole channel (i.e., with the inlet channel included) approximately 9 times. The flow has reached, therefore, its statistically steady state before taking the averages of the flow variables (velocity components, pressure, energy).

The results indicate the formation of an asymmetric flow field downstream of the expansion, with the variation of the wall pressure distribution inside the smallest recirculation bubble being much lower in magnitude than that in the larger. To be more specific, the distribution of the wall pressure coefficient on the lower wall is similar to that found in backward-facing step flows. It slightly decreases up to $x/h \simeq 6$ and thereafter monotonically increases toward a constant value. Barri et al. [9] calculated the wall pressure coefficient for a turbulent flow over a backward-facing step. They found that C_P takes its minimum value in the region of the primary recirculation vortex, and about the position of the maximum backflow. Further downstream and up to $x/h \simeq 20$ the pressure coefficient found to monotonically increase until the recovery region where it almost reached a constant level in both walls.

Along the upper wall, C_P exhibits a local minimum immediately after the step at $x/h \simeq 1.8$, which is close to the position of the maximum backflow. Moreover, a local

maximum and a second local minimum are observed at the streamwise locations of $x/h \simeq 3.8$ and $x/h \simeq 6.7$, respectively. It should be noted that the local pressure maximum almost coincides with the reattachment point of the flow on the upper side of the wall (the reattachment lengths found to be in the region of $3.51 \lesssim x_R \lesssim 3.61$ for the three different numerical schemes under investigation). This last observation is in excellent agreement with the pressure coefficient results presented by El Khoury et al. [38] for a flow through a channel with a single thin-plate obstruction. De Zilwa et al. [22] performed RANS calculations of a turbulent flow through a planar sudden expansion calculating, among others, the wall pressure coefficient. The resulting shape of the wall-pressure curve along the upper wall is very similar to the variation of C_P along the wall with the smallest recirculation vortex shown in Figure 4.22. Measurements of the wall-pressure coefficient have been also reported by Escudier et al. [39] for a turbulent flow over a planar sudden expansion. For their experiments, the researchers have used a Reynolds number of 5.55×10^4 and an expansion ratio of 4. Comparisons between ILES results and experimental data (LDA technique) are presented in Figure 4.21.

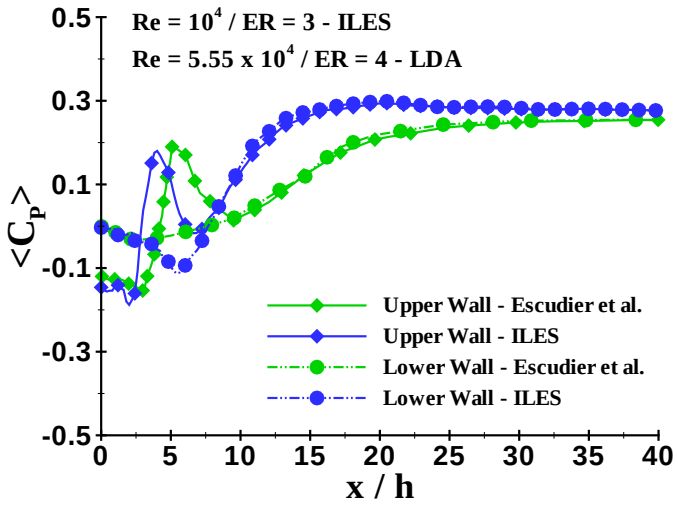

FIGURE 4.21: Wall-pressure variation along the upper and lower wall of the channel up to $x/h = 40$ downstream of the step. The ILES results are compared against those of Escudier et al. [39].

To be conformal with the experimental data provided by the authors, the calculations were carried out up to 40 step heights downstream of the expansion. The shape of the wall-pressure variation for the current study seems to be in a very good agreement with the

experimental one. However, it is evident that its magnitude along the upper and lower wall of the channel differs from each other, which is normal to happen as both Re and ER are different between the two studies. In the experimental case the curve of the wall-pressure coefficient is shifted downwards with the local minimum and local maximum values being taken at $x/h \simeq 2.8$ and $x/h \simeq 5$, respectively. This last observation is consistent with the reattachment lengths reported by the authors. The length of the shorter recirculation vortex found to be larger in their experiments and equal to $x_R = 4.7$. In the recovery region pressure on the upper wall of the channel becomes identical to that on the opposite wall at $x/h \simeq 18$ and $x/h \simeq 20$ for the numerical and experimental case, respectively.

As previously stated, the secondary pressure minimum in the region of the shorter reattachment is located at $x/h \simeq 6.7$ downstream of the constriction. This local minimum is associated with the largest recirculation bubble which is more pronounced in this cross-section area, forcing the flow to speed-up along the region of the upper wall with an accompanying pressure drop. Moreover, this pressure drop can be also related to the impingement of the high-velocity core flow on the wall at that particular location.

The skin friction coefficient was calculated using the following relation:

$$C_F = \frac{2\tau_w}{\rho U_i^2} \tag{4.11}$$

where ρ is the fluid density and U_i is the free stream velocity at the inlet. τ_w represents the wall shear stress that is due entirely to the viscous distribution, as all the Reynolds stresses close to the wall are zero. This last quantity is given by:

$$\tau_w = \mu \left(\frac{\partial u}{\partial y} \right)_{y=0}$$

where μ is the dynamic viscosity, u is the flow velocity parallel to the top and bottom wall, and y is the distance to the wall. Drikakis [26] addressed that at low Reynolds numbers ($Re < 80$ for an expansion ratio of 3), where the flow is symmetric with separation regions of equal size, the pressure and skin friction coefficients on the top and bottom wall are the same. This, however, is not the case for a turbulent flow over a planar sudden expansion, where flow asymmetries are more pronounced. As with the results of the pressure variation along the two parallel walls, the skin friction coefficient similarly exhibits different variations along the upper and lower wall of the channel, as shown in Figure 4.22. It can be said that immediately downstream of the expansion an alternating behaviour of C_F is apparent, which confirms the existence of the secondary vortices at the corners of the

walls (see Figure 4.17). The two curves further downstream turn out to be almost parallel, with the one representing the skin friction coefficient along the upper wall being negative, while the one in the opposite direction being positive. The parallel curves indicate that the wall shear stress is constant on each wall.

It is also important to underline that the results obtained from the three different high-resolution schemes are in excellent agreement with each other. There is only a slight difference of the skin friction coefficient for the M5 scheme, and particular of its maximum negative magnitude and its streamwise location along the lower wall of the channel. The separation and reattachment positions of the flow can be clearly seen from the skin friction distributions in the locations where the skin friction coefficient changes sign. It can be, thus, extracted that the reattachment positions of the shorter recirculation zone (upper wall) are approximately 3.65, 3.58 and 3.72 for the M3, M5 and W5, respectively. These values are not far from those found by evaluating the locations where the mean streamwise velocity components change sign (see length L_1 in Table 4.6). Furthermore, in all three cases examined, the secondary pressure minimum - about 6.5 step heights downstream of the step - almost coincides with the largest negative C_F on the opposite side of the channel. This last feature has been also observed by El Khoury et al. [38] for a turbulent flow over a long plane channel with a single thin-plate obstruction.

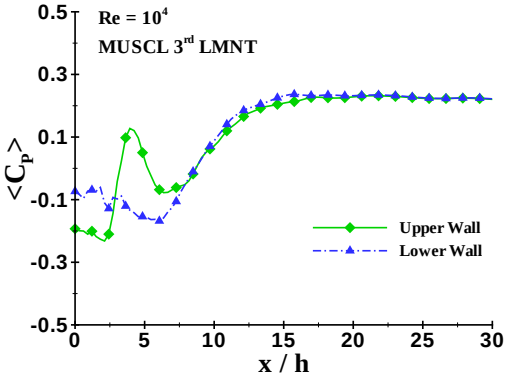

(a) Pressure Coefficient for M3

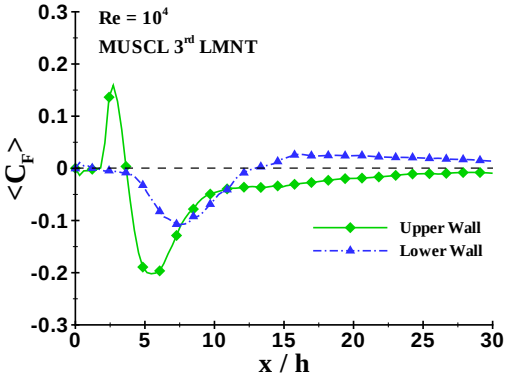

(b) Wall skin-friction coefficient for M3

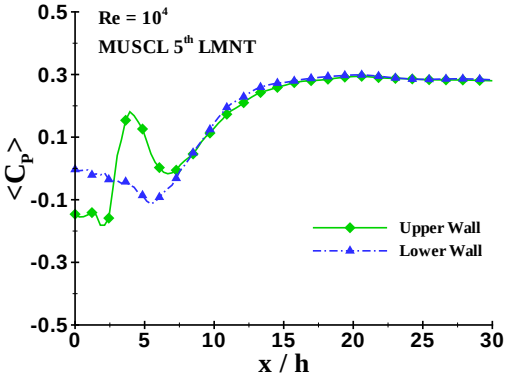

(c) Pressure Coefficient for M5

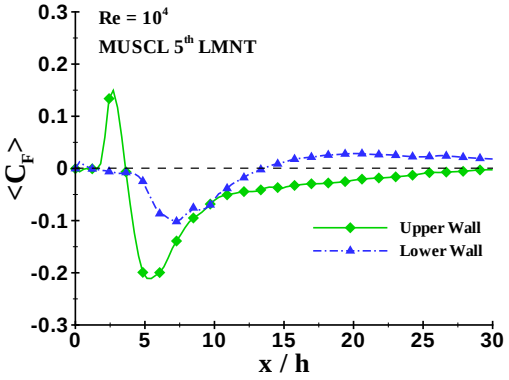

(d) Wall skin-friction coefficient for M5

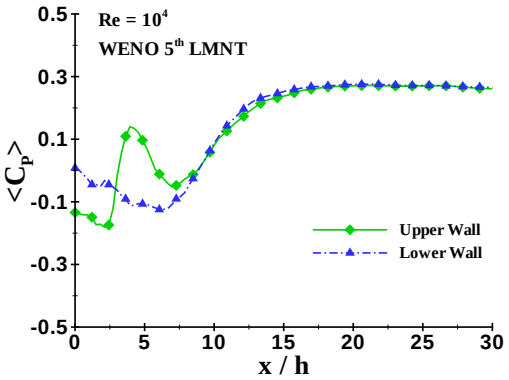

(e) Pressure Coefficient for W5

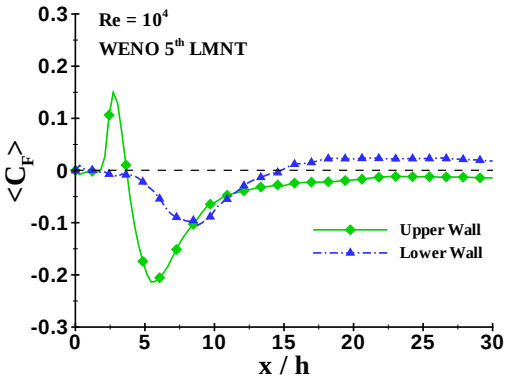

(f) Wall skin-friction coefficient for W5

FIGURE 4.22: Time-averaged pressure and wall skin-friction coefficients along the upper and lower channel wall at $Re = 10^4$.

4.6.2 Reynolds Numbers

In this section, two different Reynolds numbers are used in order to examine further the flow behaviour in the sudden-expansion channel. It is of great importance to investigate the influence of Re on the reattachment lengths of the recirculation vortices on the top and bottom wall of the channel, as well as on the time-averaged flow quantities (i.e., mean velocity components, Reynolds stresses and turbulent kinetic energy). In their pioneering study, Abbott and Kline [1] demonstrated that in the range $Re = 4 \cdot 10^4 - 10^5$, the reattachment lengths along with the mean flow structures (time-averaged velocities and turbulence intensities) do not change dramatically. Moreover, Mehta [82] found that at even higher Reynolds numbers the flow does not exhibit any particular behaviour, as the primary and secondary reattachment lengths remain the same. However, the influence of Re on the flow pattern is more pronounced at lower Re, where the reattachment points along with the mean flow quantities change with Re. Casarsa et al. [17] found that at $Re = 4 \cdot 10^4$ the reattachment length of the shorter separation is significantly larger than that at $Re = 10^4$. On the other hand, the reattachment length of the larger recirculation zone was much less influenced by the increase of the Reynolds number. The authors supported this last finding by stating that the development of the large recirculation vortex is mostly affected by the turbulent diffusion rather than by the inertial effects.

In Figure 4.23, the time-averaged flow paths in the xy plane of the channel at two different Re are presented. The measurements are limited up to $x_d/h = 20$, as the flow field downstream of the shorter and longer recirculation areas does not exhibit any special feature, with the streamlines being almost parallel through the rest of the computational domain. Note also that the results presented in this section were obtained by using the M5 with LMNT. It can be clearly seen that the flow downstream of the step exhibits an asymmetric behaviour, characterised by two separation zones with unequal size. In both cases, two primary and two secondary vortices are formed close to the top and bottom wall of the channel. However, it is evident that the reattachment lengths for the two Re under investigation are not the same. Specifically, as far as the lengths of the primary separation bubbles are concerned, these found to increase with increasing Re.

In Table 4.7, the measured reattachment lengths along with the experimental data demonstrated in [17], are presented. It is clear that at $Re = 10^4$, L_1 is smaller in magnitude compared to that at $Re = 4 \cdot 10^4$. This last observation can be explained by the fact that at higher Re, the deviation of the high-velocity core flow from the channel axis is less pronounced, mainly due to stronger inertial effects. However, both lengths seem to be

slightly underestimated in the present study, with percent differences of about 4.6% and 8.1% for the lower and higher *Re* case, respectively.

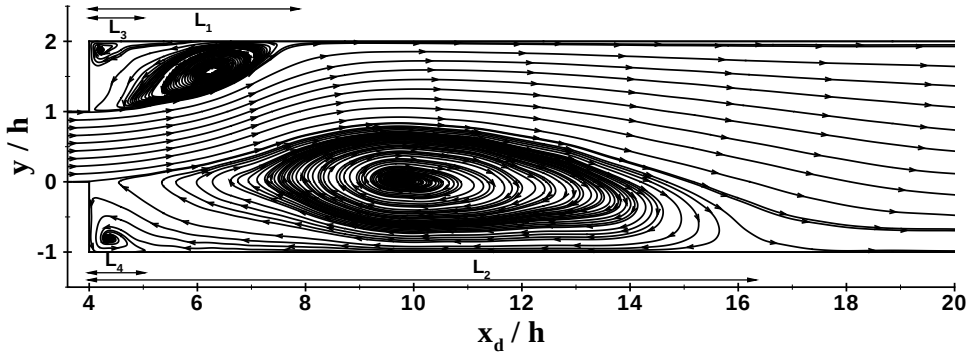

(a) Re = 10000

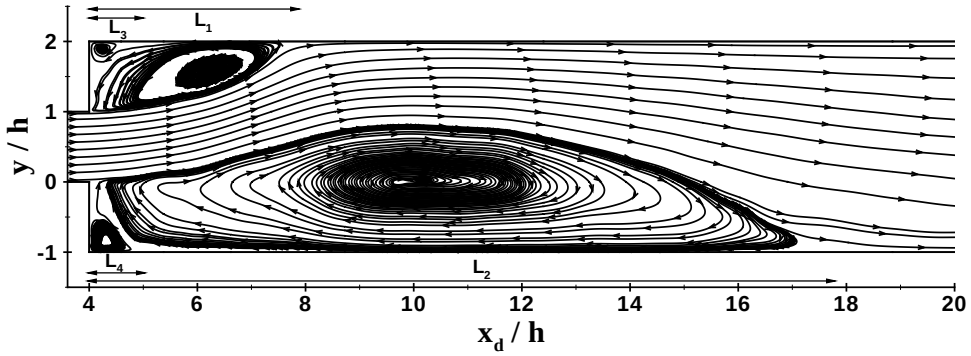

(b) Re = 40000

FIGURE 4.23: Streamlines of the mean flow at the center plane of the channel ($z/h = 2.5$) for two different Reynolds numbers using the 5^{th}-order MUSCL scheme.

The separation length of the larger reattachment increases with increasing *Re*, as shown in Table 4.7. This is, however, opposite to the observation of Casarsa et al., who addressed that the reattachment length of the larger recirculation vortex decreases with increasing *Re*. The ILES results at $Re = 4 \cdot 10^4$ are in excellent agreement with the experimental data. On the other hand, the length at the lower *Re* found to be slightly underestimated by approximately 5.2%. Abbott and Kline [1] studied the influence of the geometrical characteristics of the sudden expansion configuration on the primary and secondary reattachment lengths. They demonstrated that for the case $ER = 3$ (i.e., same

expansion ratio as that used in the present study), the ranges of the two primary lengths were $L_1/h = 3.5-4$ and $L_2/h = 11-15$, which agree well with the present results.

TABLE 4.7: Reattachment lengths of two different Reynolds numbers using the 5^{th}-order MUSCL scheme. The PIV data of Casarsa et al. [17] for both Reynolds numbers are also presented and compared with the numerical results.

Reynolds number	L_1/h	L_2/h	L_3/h	L_4/h
$Re = 10000$	3.51	13.63	0.91	0.53
PIV 10^4	3.68	14.38	0.84	1.06
$Re = 40000$	3.61	14.17	0.52	0.85
PIV $4 \cdot 10^4$	3.93	14.17	0.54	1.06

The time-averaged velocity and fluctuating profiles extracted at three different wall-normal locations, at $y/h = 1.5, 0.5, -0.5$, are shown in Figure 4.24 and Figure 4.25. Both flow fields were normalised with respect to the inlet bulk velocity, U_b. The curves of the mean streamwise and transverse velocity components match reasonably well with each other, exhibiting some small differences in the region of the larger recirculation zone, as well as at the location of the high-velocity core flow. In these specific regions and in the case $Re = 4 \cdot 10^4$, the velocity and fluctuating profiles seem to be somehow shifted downstream. Besides, at $x/h < 4-5$ smaller values of u'/U_b and v'/U_b for the larger Re are detected. This last finding is in excellent agreement with the results outlined in [17]. Beyond that position and up to $x/h = 16$, the fluctuating velocity magnitude appeared to be larger at $Re = 4 \cdot 10^4$. That flow characteristic is more pronounced in the transverse fluctuating velocity profile at all measurement points examined, as shown in Figures 4.25(b),4.25(d),4.25(f). In the region of the shorter separation vortex, and particularly at $x/h < 4$ and $y/h = 1.5$, the maximum deviations (in percentage terms) of the mean fluctuating velocity profiles at the two Reynolds numbers are approximately 9% and 18% for u'/U_b and v'/U_b, respectively. It is, therefore, evident that despite the fact that the averaged first-order flow quantities does not exhibit any particular difference for the two Re, the turbulence intensities seem to produce some moderate differences in the flow field.

In order to investigate further the above observation, comparisons of the mean streamwise velocity, U, and turbulence statistics, $\sqrt{u'^2}$ and $\sqrt{v'^2}$, for the flow inside the sudden

expansion channel are made, as shown in Figure 4.26. The mean streamwise velocity profiles appeared to be almost identical with each other, with some small variation in the region of the larger recirculation zone between $x/h = 4-9$. Furthermore, a slight difference is detected after the reattachment point of the shorter recirculation vortex, close to the upper wall of the channel. In that particular location the maximum streamwise velocity seems to be larger in magnitude for $Re = 4 \cdot 10^4$. The fluctuating velocity profiles exhibit some moderate differences in the region of the two shear layers emanating from the step. In general, both the streamwise and the cross-stream turbulence intensities found to be smaller in magnitude for the larger Re. However, it seems that beyond $x/h = 7$ the two profiles are superposed on one another, as shown in Figures 4.26(b)- 4.26(c). The same trend was also observed in [17], as far as the fluctuating velocity components $u^{'}$ and $v^{'}$ are concerned. Particularly, close to the channel step the above quantities were slightly larger for the lower Re, whereas further downstream $u^{'}$ and $v^{'}$ were higher for the larger Re. Besides, the flow is almost everywhere anisotropic, with the streamwise turbulence intensity being considerably larger than its counterpart.

Calculations of the Reynolds shear stress and turbulent kinetic energy revealed that the flow does not exhibit any particular variation between the two Re under investigation (see Figure 4.27. A small difference is only detected in the high-velocity core flow region, where the peak values of the shear stress and turbulent kinetic energy appear to be larger for the lower Re.

It can be concluded that $Re = 10^4$ and $Re = 4 \cdot 10^4$ exhibit some small variations in terms of the reattachment lengths and the mean flow quantities. It was found that the length of the primary reattachment of the shorter bubble is not significantly influenced by the increase in Re. However, the length of the larger recirculation found to be substantially larger for the higher Re. Furthermore, it was found that the peak values of the mean turbulence intensities (i.e., particularly the maximum transverse fluctuating velocity) slightly decrease with increasing Re. The same trend was also observed for the turbulent kinetic energy. It is therefore evident that $Re = 10^4$ cannot be considered high enough for the effects of an increase in the Re to be utterly neglected.

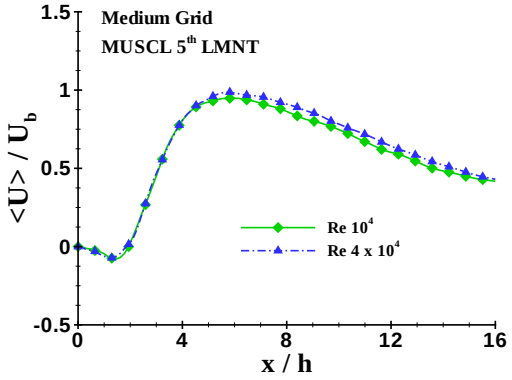

(a) U Velocity profile at Y = 1.5h

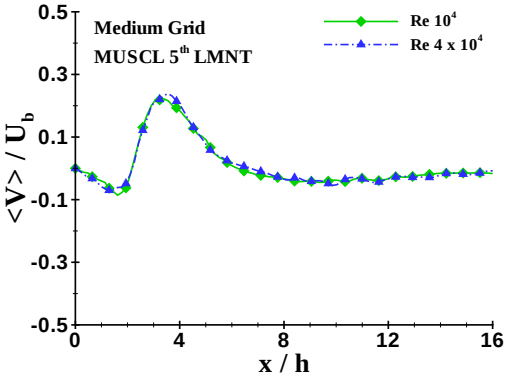

(b) V Velocity profile at Y = 1.5h

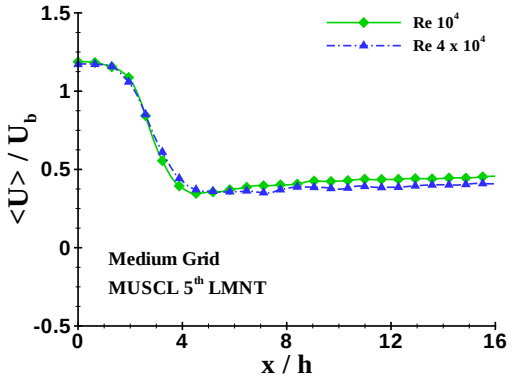

(c) U Velocity profile at Y = 0.5h

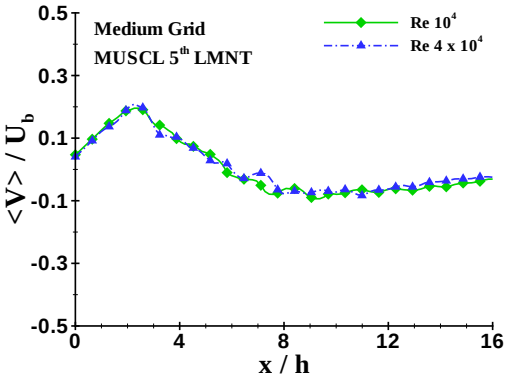

(d) V Velocity profile at Y = 0.5h

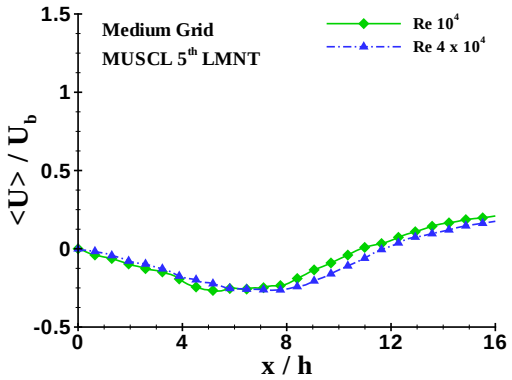

(e) U Velocity profile at Y = -0.5h

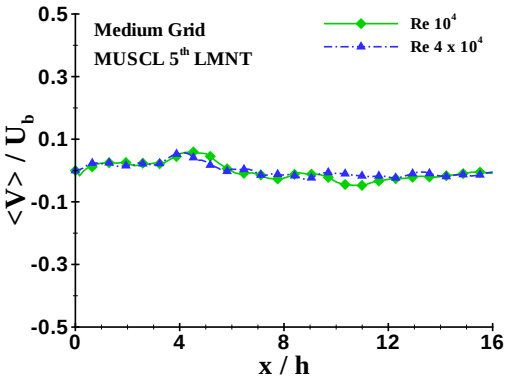

(f) V Velocity profile at Y = -0.5h

FIGURE 4.24: Time-averaged streamwise and transverse velocities along the x-axis (xy-plane) at Re 10000 and 40000.

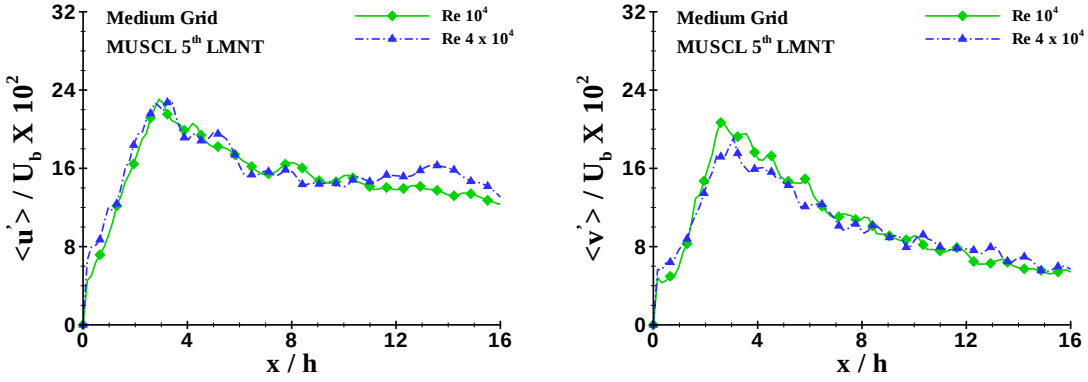

(a) U r.m.s. Velocity profile at Y = 1.5h

(b) V r.m.s. Velocity profile at Y = 1.5h

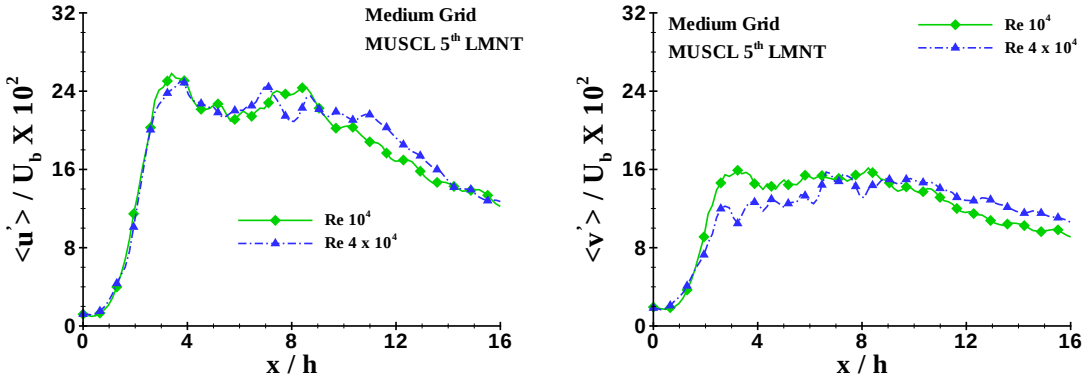

(c) U r.m.s. Velocity profile at Y = 0.5h

(d) V r.m.s. Velocity profile at Y = 0.5h

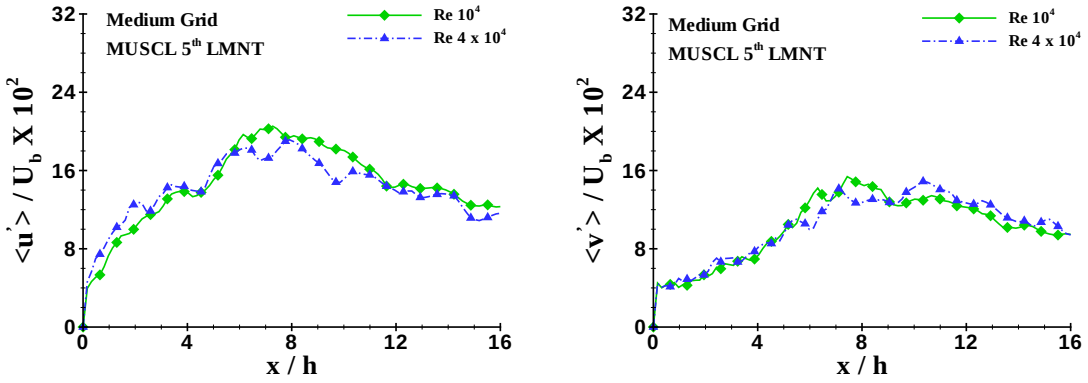

(e) U r.m.s. Velocity profile at Y = -0.5h

(f) V r.m.s. Velocity profile at Y = -0.5h

FIGURE 4.25: Time-averaged streamwise and transverse r.m.s. velocities along the x-axis (xy-plane) at Re 10000 and 40000.

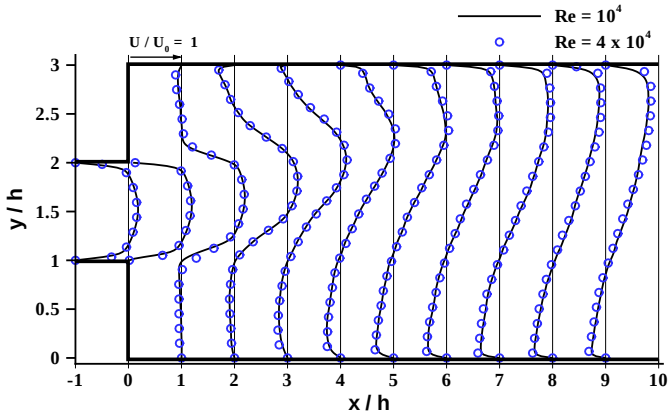

(a) Streamwise velocity

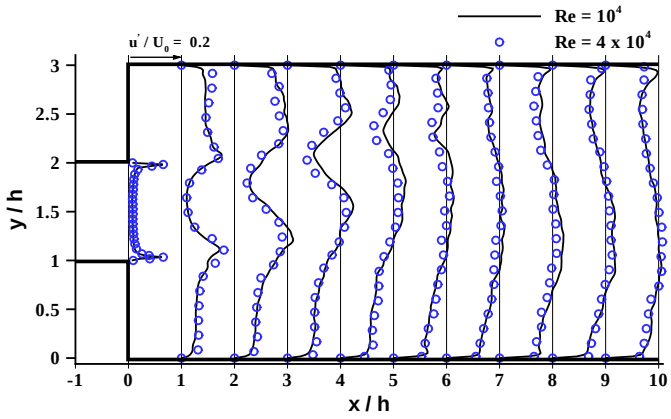

(b) Fluctuating streamwise velocity

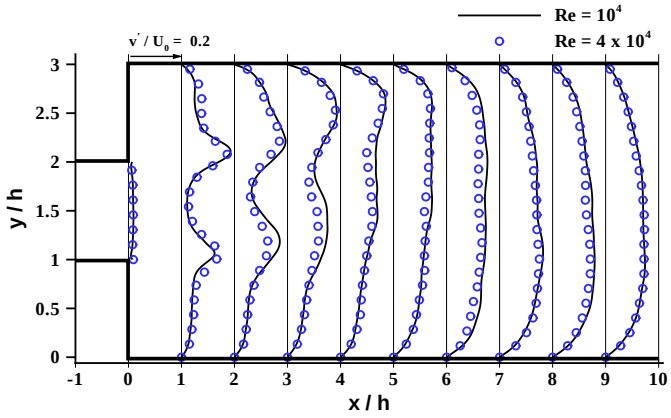

(c) Fluctuating wall-normal velocity

FIGURE 4.26: Time-averaged streamwise velocity $\langle U \rangle$, and mean turbulence intensities $\left\langle u'_{rms} \right\rangle$, $\left\langle v'_{rms} \right\rangle$ at $z/h = 2.5$ for two different Reynolds numbers, at $Re = 10^4$ and $Re = 4 \cdot 10^4$.

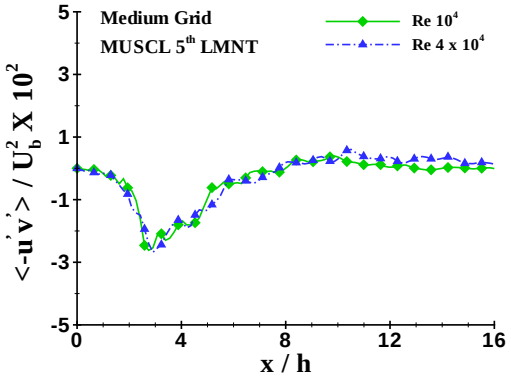

(a) Reynolds stress profile of u'v' at Y = 1.5h

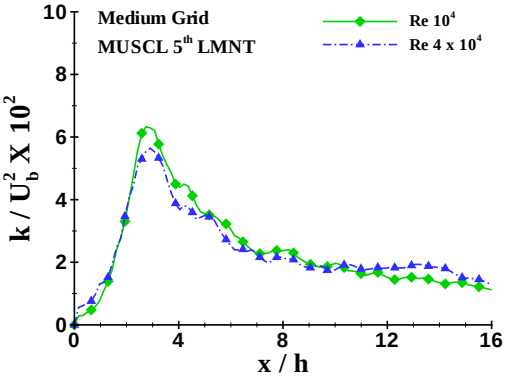

(b) Turbulent kinetic energy profile at Y = 1.5h

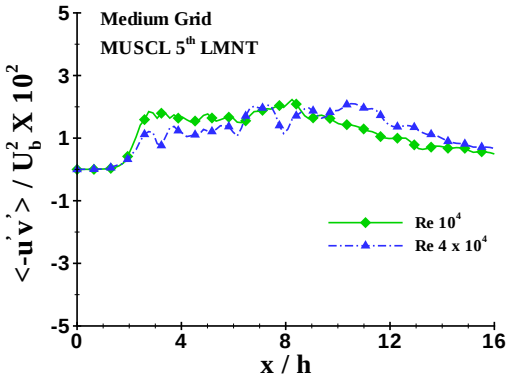

(c) Reynolds stress profile of u'v' at Y = 0.5h

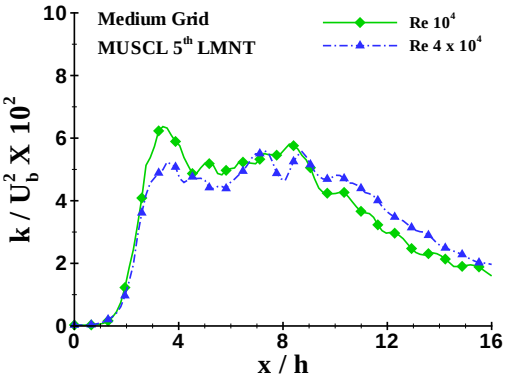

(d) Turbulent kinetic energy profile at Y = 0.5h

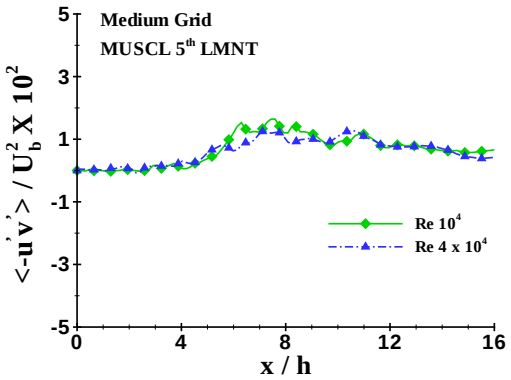

(e) Reynolds stress profile of u'v' at Y = -0.5h

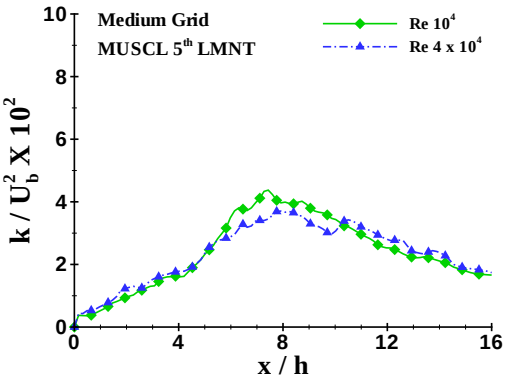

(f) Turbulent kinetic energy profile at Y = -0.5h

FIGURE 4.27: Time-averaged Reynolds stresses and turbulent kinetic energy along the x-axis (xy-plane) at Re 10000 and 40000.

5

Quantitative Analysis of Turbulence Statistics

5.1 Introduction

In this Chapter, a more comprehensive analysis of the turbulence statistics will be carried out, in order to shed some insight into the turbulent structures in suddenly-expanded flows. For that purpose, turbulent kinetic energy budget measurements are made in a sudden expansion geometry with $ER = 3$ and $AR = 5$. The Reynolds number based on the step height h of the channel and the inlet bulk velocity U_b is 10000. Each of the components of the energy budget (convection, production, turbulent diffusion, pressure diffusion, viscous diffusion and energy dissipation) are thoroughly examined, in order to determine which of the aforementioned terms contribute to the energy budget and which can be completely neglected.

Furthermore, the influence of different high-resolution/high-order schemes, as well as of different Re on the turbulent kinetic energy budget is studied. The results revealed that the influence of the applied numerical schemes to the energy budget is significant,

particularly in the regions of the shear layers where high turbulence production and energy dissipation is observed. On the other hand, the influence of Re (i.e., $Re = 10^4$ and $Re = 4 \cdot 10^4$) on the energy budget is not substantial, while at the same time it cannot be considered as negligible. The Chapter is organised as follows: (a) the triple correlation terms calculated at different streamwise locations are introduced in Section 5.2, (b) the numerical results related to the turbulent kinetic energy budget terms are addressed in Section 5.3.

5.2 Triple Correlation Terms

In this section, the most significant components of the triple velocity correlations calculated at three different streamwise locations are presented. Note that their spatial derivatives appear as turbulent diffusion terms in the transport equations (i.e. turbulent diffusion, pressure diffusion and viscous diffusion terms comprise the transport terms in the energy budget) of Reynolds stresses. It is important, therefore, to investigate their behaviour throughout the flow field, and especially along the recirculation zones of the channel, as well as inside the shear-layer regions.

The triple velocity correlation terms were calculated using the following formula:

$$\left\langle u_i' u_i' u_j' \right\rangle = \frac{1}{N} \sum_{i,j=1}^{N} \left[(u_i - \overline{u}) (u_i - \overline{u}) \left(u_j - \overline{u} \right) \right] \tag{5.1}$$

where N is the total number of time realisations in a given window.

The distributions of four components, $\overline{u'^3}$, $\overline{u v'^2}$, $\overline{v'^3}$ and $\overline{v u'^2}$ are shown in Figures 5.1-5.4. Note that measurements were performed at three different wall-normal locations (at $y/h = 1.5$, $y/h = 0.5$ and $y/h = -0.5$), which include the region of the shorter reattachment, the high-velocity core flow region, and the area of the larger recirculation vortex, respectively. It can be said that despite the fact that some of the triple correlation terms have opposite signs, they exhibit very similar distributions in all the measured lines along the streamwise direction. That is, there is a peak value at the region of the shorter recirculation zone about the location where the flow reattaches (at $x/h \simeq 4$). Besides, in the high-velocity flow region at the centerline of the channel, triple correlation terms exhibit a local minimum and a local maximum. The local minimum is formed due to the low turbulence intensity observed immediately after the step, whereas the local maximum due to

the shear layer (turbulence intensity is very high inside the free-shear layer) crossing the measurement line in that particular region. Finally, at $y/h = -0.5$ all the triple correlation profiles found to exhibit small peak values, with their magnitudes being considerably lower than those at $y/h = 0.5$ and $y/h = 1.5$.

It can be clearly seen that the triple velocity correlations exhibit strong variations along the wall-normal direction, whereas the change of the correlations in the streamwise direction is rather moderate. This last observation indicates that mainly the wall-normal turbulent diffusion should be appreciable. This is consistent with the findings of the turbulent diffusion calculations for the streamwise, lateral and spanwise components presented in the ensuing section. It was found that the most dominant term among the turbulent diffusion components is the lateral one. Nevertheless, the streamwise turbulent diffusion should not be totally neglected, as the triple velocity correlations decrease quite rapidly over the reattachment region.

As far as the influence of the high-resolution schemes on the triple velocity correlations is concerned, it can be said that all the profiles match reasonably well with each other, with M3 being in a very good agreement with M5. On the other hand, the profiles corresponding to W5 seem to be quite underestimated, particularly in the recirculation areas, with their peak values being slightly lower compared to M3 and M5. As there is no experimental or numerical evidence to compare with, verification of which numerical scheme gives the best results cannot be made. It can be said, however, that M3 and M5 are, in general, less dissipative than W5 when combined with LMNT. This last argument can be further supported by the fact that turbulence intensities found to be higher for the MUSCL schemes compared to W5 (see Chapter 4).

The influence of Re on the triple correlation components is rather moderate. It can be clearly seen that both curves at $Re = 10^4$ and $Re = 4 \cdot 10^4$ match reasonably well with each other, as far as the distribution profiles of $\overline{u\upsilon'^2}$, $\overline{\upsilon'^3}$ and $\overline{\upsilon u'^2}$ are concerned. On the other hand, it is evident that for the triple streamwise velocity correlation $\overline{u'^3}$ the two Re give considerably different results, particularly close to the region of the shorter recirculation vortex. Furthermore, large variations have been observed in the high-velocity core flow region at $x/h \simeq 4$ and $x/h \simeq 8$, as that can be seen in Figure 5.1(d).

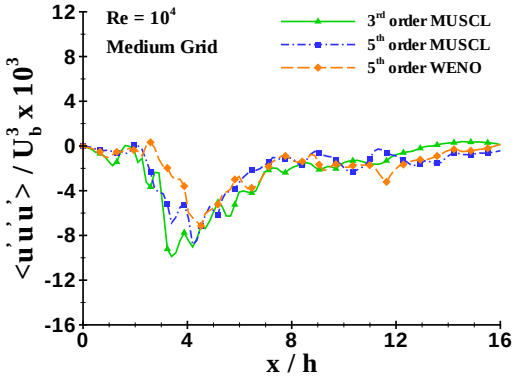

(a) Triple velocity correlation at Y = 1.5h for M3, M5 and W5.

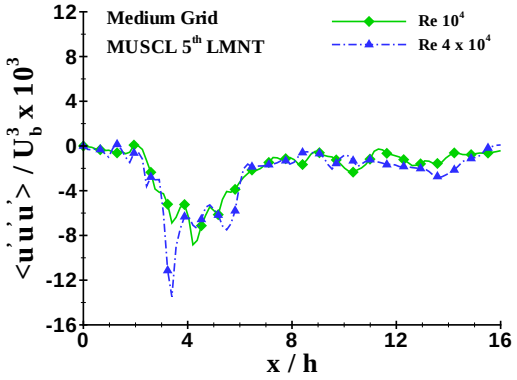

(b) Triple velocity correlation at Y = 1.5h for Re 10000 and 40000.

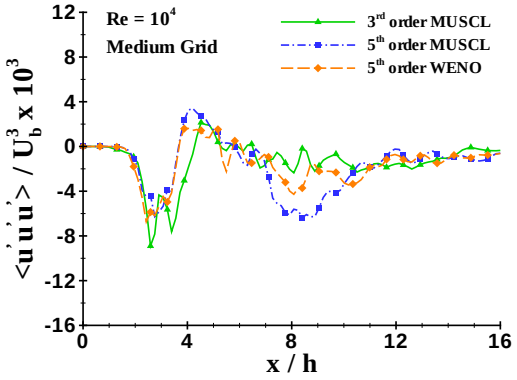

(c) Triple velocity correlation at Y = 0.5h for M3, M5 and W5.

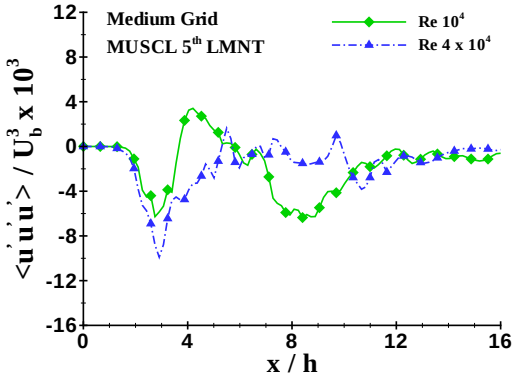

(d) Triple velocity correlation at Y = 0.5h for Re 10000 and 40000.

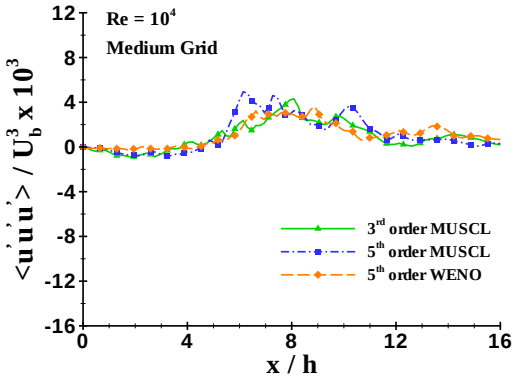

(e) Triple velocity correlation at Y = -0.5h for M3, M5 and W5.

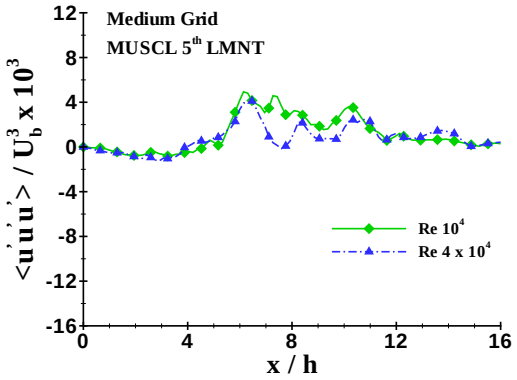

(f) Triple velocity correlation at Y = -0.5h for Re 10000 and 40000.

FIGURE 5.1: Triple velocity correlation of $\overline{u'u'u'}$ for three different numerical schemes and two Reynolds numbers at (a),(b) $Y = 1.5h$, (c),(d) $Y = 0.5h$ and (e),(f) $Y = -0.5h$ along the x- axis.

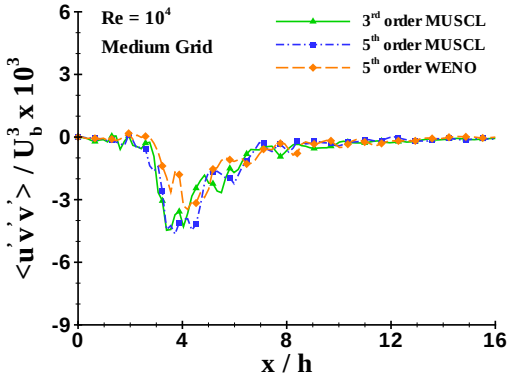

(a) Triple velocity correlation at Y = 1.5h for M3, M5 and W5.

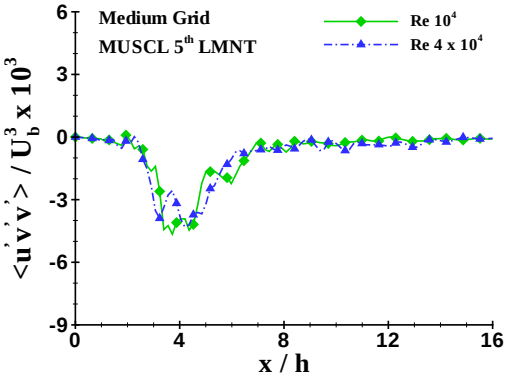

(b) Triple velocity correlation at Y = 1.5h for Re 10000 and 40000.

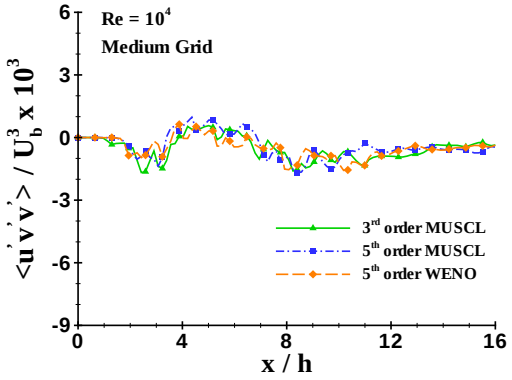

(c) Triple velocity correlation at Y = 0.5h for M3, M5 and W5.

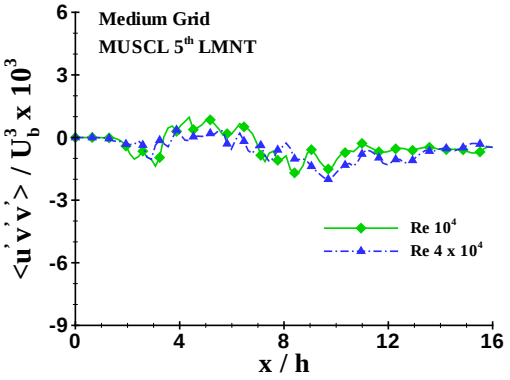

(d) Triple velocity correlation at Y = 0.5h for Re 10000 and 40000.

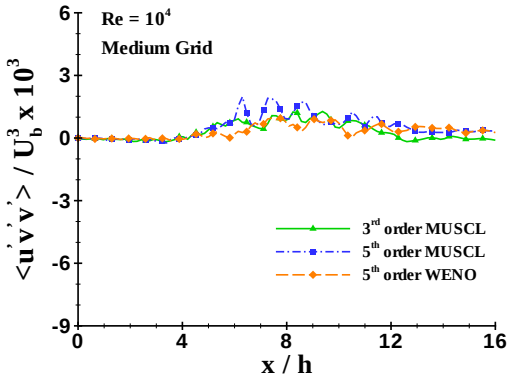

(e) Triple velocity correlation at Y = -0.5h for M3, M5 and W5.

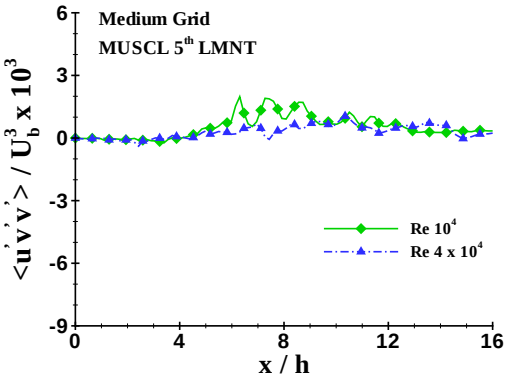

(f) Triple velocity correlation at Y = -0.5h for Re 10000 and 40000.

FIGURE 5.2: Triple velocity correlation of $\overline{u'v'v'}$ for three different numerical schemes and two Reynolds numbers at (a),(b) $Y = 1.5h$, (c),(d) $Y = 0.5h$ and (e),(f) $Y = -0.5h$ along the x- axis.

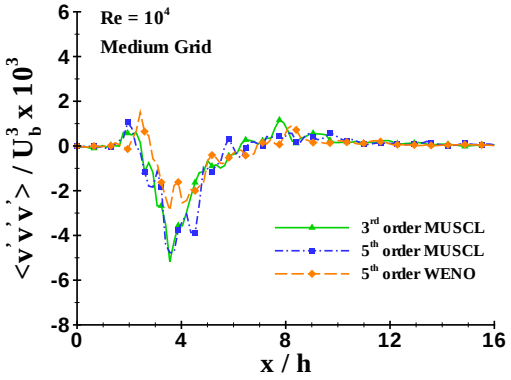

(a) Triple velocity correlation at Y = 1.5h for M3, M5 and W5.

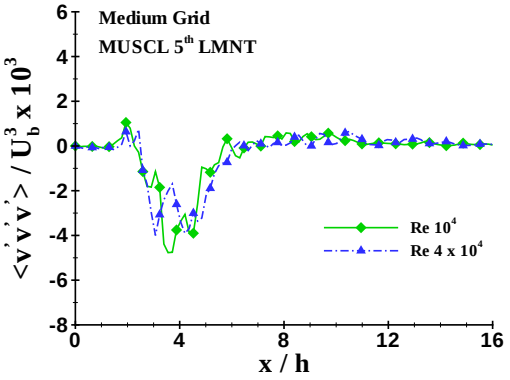

(b) Triple velocity correlation at Y = 1.5h for Re 10000 and 40000.

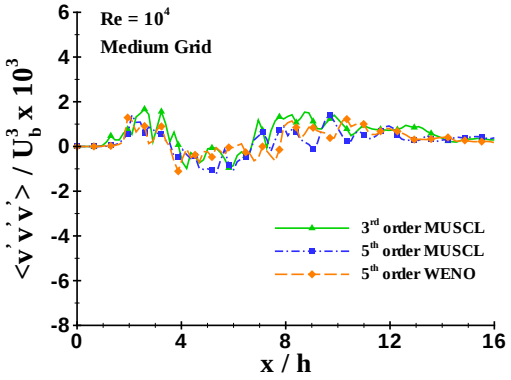

(c) Triple velocity correlation at Y = 0.5h for M3, M5 and W5.

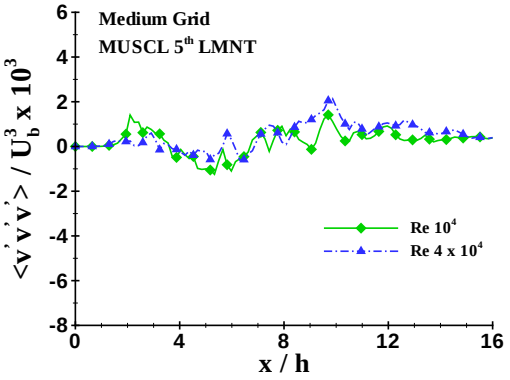

(d) Triple velocity correlation at Y = 0.5h for Re 10000 and 40000.

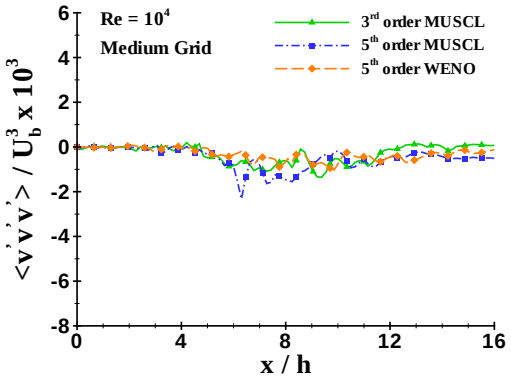

(e) Triple velocity correlation at Y = -0.5h for M3, M5 and W5.

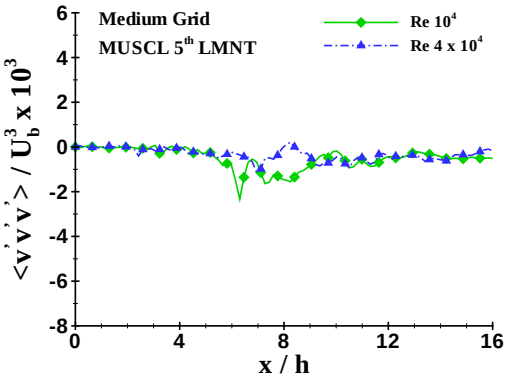

(f) Triple velocity correlation at Y = -0.5h for Re 10000 and 40000.

FIGURE 5.3: Triple velocity correlation of $\overline{v'v'v'}$ for three different numerical schemes and two Reynolds numbers at (a),(b) $Y = 1.5h$, (c),(d) $Y = 0.5h$ and (e),(f) $Y = -0.5h$ along the x- axis.

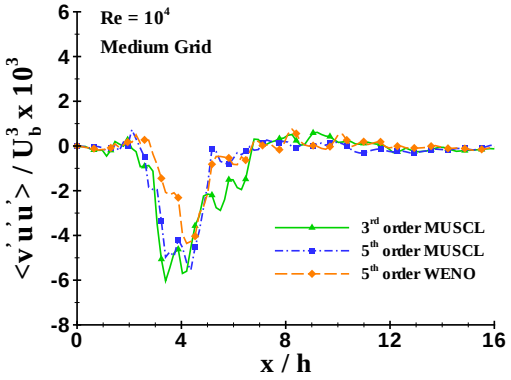

(a) Triple velocity correlation at Y = 1.5h for M3, M5 and W5.

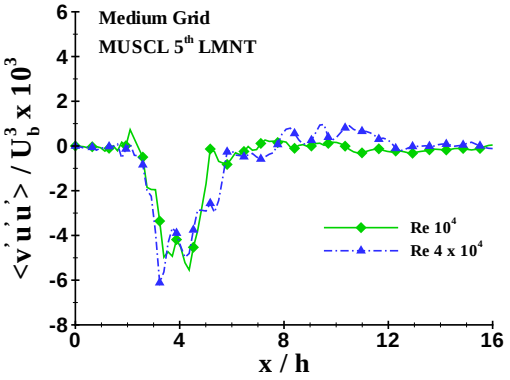

(b) Triple velocity correlation at Y = 1.5h for Re 10000 and 40000.

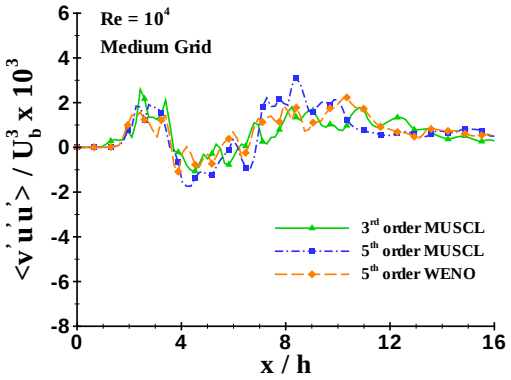

(c) Triple velocity correlation at Y = 0.5h for M3, M5 and W5.

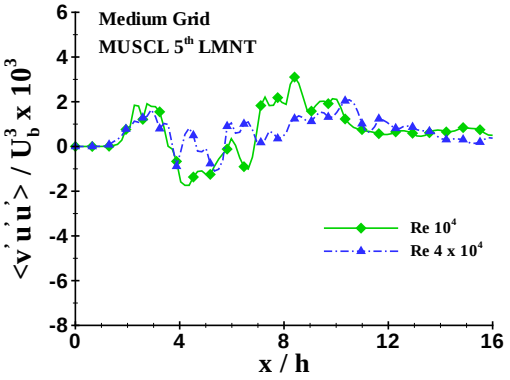

(d) Triple velocity correlation at Y = 0.5h for Re 10000 and 40000.

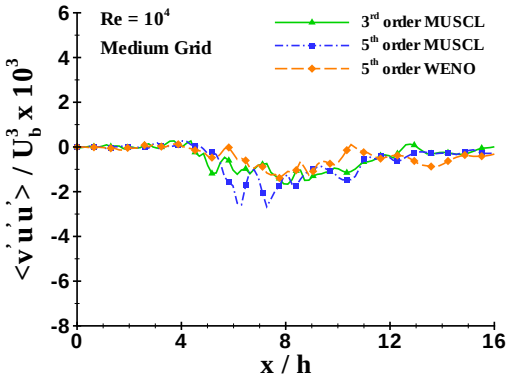

(e) Triple velocity correlation at Y = -0.5h for M3, M5 and W5.

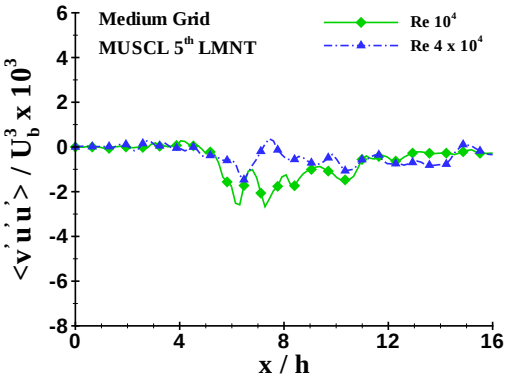

(f) Triple velocity correlation at Y = -0.5h for Re 10000 and 40000.

FIGURE 5.4: Triple velocity correlation of $\overline{v'u'u'}$ for three different numerical schemes and two Reynolds numbers at (a),(b) $Y = 1.5h$, (c),(d) $Y = 0.5h$ and (e),(f) $Y = -0.5h$ along the x- axis.

5.3 Turbulent Kinetic Energy Budget

In this section, the budgets of the turbulent kinetic energy are evaluated, assuming a steady, incompressible flow. The influence of the channel step on the budgets is thoroughly examined, while at the same time the transport mechanism of the turbulent kinetic energy is provided. Comparisons among different high-resolution numerical schemes, as well as between different Reynolds numbers have been carried out, intending to shed some light on the physics of turbulence in suddenly-expanded flows (i.e., flows that exhibit separation, reattachment and flow asymmetry downstream of the channel step). To the author's knowledge, similar study on the turbulent kinetic energy budget in a PSE geometry has not been addressed in the past. Note that in the present study an incompressible turbulent kinetic energy budget equation was used, despite the fact that the CFD calculations were conducted by means of a compressible solver. The reason is that the flow under consideration belongs to the incompressible regime in that the Mach number is taken equal to 0.1. This value is much lower than the critical Mach number value of 0.3, above which the flow can be considered as compressible with significant variations in density (approximately 5% at $M = 0.3$). The variation in density at $M = 0.1$ found to be less than 1%. Therefore, according to Hinze [56], the turbulent kinetic energy transport equation for an incompressible flow can be written in the following form:

$$\frac{\partial k}{\partial t} = -\overline{U}_k \frac{\partial k}{\partial X_k} - \overline{u_l' u_k'} \frac{\partial \overline{U}_l}{\partial X_k} - \frac{\partial \overline{k' u_k'}}{\partial X_k} - \nu \overline{\frac{\partial u_l'}{\partial X_k} \frac{\partial u_l'}{\partial X_k}} - \frac{\partial \overline{p' u_l'}}{\partial X_l} + \nu \frac{\partial^2 k}{\partial X_k^2} \tag{5.2}$$

where $k = \frac{1}{2}\overline{u_l' u_l'}$ is the turbulent kinetic energy per unit mass and $k' = \frac{1}{2} u_l' u_l'$ is the fluctuating turbulent kinetic energy per unit mass. The LHS of Equation (5.2) represents the material derivative of turbulent kinetic energy, while the terms on the RHS are, respectively, the convection, the turbulence production, the turbulence diffusion, the turbulence dissipation to heat, the pressure-velocity correlations and the viscous diffusion. Although the mean spanwise velocity component, $\overline{W}$, and the corresponding velocity gradient, $\frac{\partial \overline{\phi}}{\partial z}$, are much lower in magnitude compared to their streamwise and lateral counterparts, all three velocity components have been calculated. The derivatives were approximated by a second-order central difference scheme applied throughout the sudden expansion domain apart from the boundaries. Along normal boundaries, as well as in overlapping regions (regions where two or more faces of different blocks overlap each other), a first-order difference scheme has been used. Both schemes are presented below with $U = \{u, \upsilon, w\}$,

$X = \{x, y, z\}$ and $I = \{i, j, k\}$:

$$\frac{\partial U}{\partial X} = \frac{U_{I+1} - U_I}{\Delta X} + \mathscr{O}(\Delta X)$$

$$\frac{\partial U}{\partial X} = \frac{U_{I+1} - U_{I-1}}{2\Delta X} + \mathscr{O}(\Delta X)^2$$

representing the first- and second-order difference scheme, respectively.

As far as the convection term is concerned, this can be expanded to a sum of a streamwise, lateral and spanwise convection as:

$$CK_{tot} = CK_{str} + CK_{lat} + CK_{span}$$

where

$$\begin{aligned} CK_{str} &= -\tfrac{1}{2}\overline{U}\left(\frac{\partial \overline{u'u'}}{\partial x} + \frac{\overline{v'v'}}{\partial x} + \frac{\overline{w'w'}}{\partial x}\right) \\ CK_{lat} &= -\tfrac{1}{2}\overline{V}\left(\frac{\partial \overline{u'u'}}{\partial y} + \frac{\overline{v'v'}}{\partial y} + \frac{\overline{w'w'}}{\partial y}\right) \\ CK_{span} &= -\tfrac{1}{2}\overline{W}\left(\frac{\partial \overline{u'u'}}{\partial z} + \frac{\overline{v'v'}}{\partial z} + \frac{\overline{w'w'}}{\partial z}\right) \end{aligned} \tag{5.3}$$

The streamwise and lateral convection terms found to be the most dominant in the flow field, while the spanwise convection was almost zero throughout the sudden expansion domain. Nevertheless, it has been included to the calculations. The three normal Reynolds stress components constituting the turbulent kinetic energy were measured along with their gradients, at each of the three directions.

The production term of the turbulent kinetic energy budget is composed of the normal and shear production, as follows:

$$PK_{tot} = PK_N + PK_S$$

where

$$\begin{aligned} PK_N &= -\overline{u'^2}\frac{\partial \overline{U}}{\partial x} - \overline{v'^2}\frac{\partial \overline{V}}{\partial y} - \overline{w'^2}\frac{\partial \overline{W}}{\partial z} \\ PK_S &= -\overline{u'v'}\left(\frac{\partial \overline{U}}{\partial y} + \frac{\partial \overline{V}}{\partial x}\right) - \overline{u'w'}\left(\frac{\partial \overline{U}}{\partial z} + \frac{\partial \overline{W}}{\partial x}\right) - \overline{v'w'}\left(\frac{\partial \overline{V}}{\partial z} + \frac{\partial \overline{W}}{\partial y}\right) \end{aligned} \tag{5.4}$$

The production term is interpreted as the rate at which kinetic energy is lost from the mean flow and transferred to the turbulent eddies. In most cases, PK is positive, representing a transfer of kinetic energy from the mean flow to the turbulence one. However, under special flow conditions, the production term can be locally negative in certain regions. In the present study, the normal production of Equation (5.4) was neglected from the turbulence production term, since the flow downstream of the channel step is considered as a free shear flow, where the shear production is expected to be the dominant one. Liu and Tomas [77] conducted measurements of the turbulent kinetic energy budget for a symmetric turbulent planar wake flow. They claimed that despite the streamwise pressure gradients imposed, the wake was shear dominated since $PK_N \ll PK_S$. However, they included the normal production term in the TKE budget.

The dissipation term consists of three parts, the streamwise, the lateral and the spanwise dissipation.

$$EK_{tot} = EK_{str} + EK_{lat} + EK_{span}$$

Assuming homogeneous and locally isotropic turbulence, the dissipation term can be written by the following simplified formula ([15]):

$$EK_{tot} = 15\nu\overline{\left(\frac{\partial u'}{\partial x}\right)^2} \tag{5.5}$$

where ν is the kinematic viscosity of the fluid. However, as already mentioned in a previous chapter, the flow is highly anisotropic with the streamwise intensity being higher than the transverse one, almost everywhere in the flow field. Thus, this assumption cannot be made in the present study and subsequently Equation (5.5) cannot be used for the calculation of the dissipation term. The dissipation term of the turbulent kinetic energy transport equation, then, can be measured by the following formula:

$$\begin{aligned}
EK_{str} &= -\nu\left[\overline{\left(\frac{\partial u'}{\partial x}\right)^2} + \overline{\left(\frac{\partial v'}{\partial x}\right)^2} + \overline{\left(\frac{\partial w'}{\partial x}\right)^2}\right] \\
EK_{lat} &= -\nu\left[\overline{\left(\frac{\partial u'}{\partial y}\right)^2} + \overline{\left(\frac{\partial v'}{\partial y}\right)^2} + \overline{\left(\frac{\partial w'}{\partial y}\right)^2}\right] \\
EK_{span} &= -\nu\left[\overline{\left(\frac{\partial u'}{\partial z}\right)^2} + \overline{\left(\frac{\partial v'}{\partial z}\right)^2} + \overline{\left(\frac{\partial w'}{\partial z}\right)^2}\right]
\end{aligned} \tag{5.6}$$

The above equation is the proper form for the dissipation only if the turbulent flow is homogeneous. Taking into account the magnitude of the Reynolds numbers under investigation ($Re = 10^4$ and $Re = 4 \times 10^4$), then the use of the nine-term homogeneous approximation is sensible, given the fact that at these Re numbers the turbulent flows tend to approach homogeneity at the smallest scales, which in turn are characteristic of the dissipation range.

The viscous diffusion term can be similarly expanded to a sum of streamwise, lateral and spanwise terms:

$$DK_{tot} = DK_{str} + DK_{lat} + DK_{span}$$

where

$$\begin{aligned} DK_{str} &= \nu \left[\frac{\partial^2 \overline{u'u'}}{\partial x^2} + \frac{\partial^2 \overline{v'v'}}{\partial x^2} + \frac{\partial^2 \overline{w'w'}}{\partial x^2} \right] \\ DK_{lat} &= \nu \left[\frac{\partial^2 \overline{u'u'}}{\partial y^2} + \frac{\partial^2 \overline{v'v'}}{\partial y^2} + \frac{\partial^2 \overline{w'w'}}{\partial y^2} \right] \\ DK_{span} &= \nu \left[\frac{\partial^2 \overline{u'u'}}{\partial z^2} + \frac{\partial^2 \overline{v'v'}}{\partial z^2} + \frac{\partial^2 \overline{w'w'}}{\partial z^2} \right] \end{aligned} \tag{5.7}$$

The second derivatives that appear in the viscous diffusion term were numerically approximated in a similar way as the first derivatives, described above (taking into account that a second derivative of a function f is the derivative of the derivative of f). Thus, the first- and second-order difference schemes were applied here two times, taking that way the advantage of applying a first-order difference scheme in the boundary and overlapping regions of the computational domain (the approximation of the second derivative in any other way should make it necessary to use a second-order central second difference with respect to x, y, and z along the boundaries and overlapping regions, resulting in an increased computational cost). It should be noted that in all past investigations on the turbulent kinetic energy budget, the viscous diffusion term was neglected. Panchapakesan and Lumley [91] , suggest that in free turbulent flows, in regions away from the walls, viscous diffusion is small compared to the turbulent diffusion. Furthermore, Liu and Tomas [77] reached the same conclusion after calculating the local turbulent viscosity. They found that the contribution of the viscous diffusion to the transport terms is negligible compared to the turbulent contribution. In the present study, viscous diffusion

is included in the energy budget in order to affirm the results of the previous works. As it will be shown later, the viscous diffusion away from the channel walls found to be much smaller than the turbulent diffusion, whereas close to the walls its contribution cannot be considered as negligible.

The turbulent diffusion term is expressed as a sum of its streamwise, lateral and spanwise components, as follows:

$$TK_{tot} = TK_{str} + TK_{lat} + TK_{span}$$

where

$$\begin{aligned} TK_{str} &= -\frac{1}{2}\left(\overline{\frac{\partial u'^3}{\partial x}} + \overline{\frac{\partial u v'^2}{\partial x}} + \overline{\frac{\partial u w'^2}{\partial x}}\right) \\ TK_{lat} &= -\frac{1}{2}\left(\overline{\frac{\partial v u'^2}{\partial y}} + \overline{\frac{\partial v'^3}{\partial y}} + \overline{\frac{\partial v w'^2}{\partial y}}\right) \\ TK_{span} &= -\frac{1}{2}\left(\overline{\frac{\partial w u'^2}{\partial z}} + \overline{\frac{\partial w v'^2}{\partial z}} + \overline{\frac{\partial w'^3}{\partial z}}\right) \end{aligned} \tag{5.8}$$

The turbulent transport term is so-called because it redistributes energy in space without creating or destroying it. Using the divergence theorem, the integral of this term over a control volume equals the flux through the surface of the volume. This latter can be expressed by the following equation.

$$\int_{\mathscr{V}} \partial_j \overline{u_j u_i u_i} d\mathscr{V} = \int_S \hat{n}_j \overline{u_j u_i u_i} dS$$

The physical effect of transport terms, such as turbulent diffusion and pressure-diffusion terms, is to spread the Reynolds stresses in space. It is generally assumed that they manage to balance the flow field in terms of its stresses, by driving the spatial distribution toward uniformity, similarly to gradient diffusion by molecular procedures.

Panchapakesan [91] and Hussein et al. [58] assumed that the normal transverse flux of $\overline{v'^2}$ equals to the normal spanwise flux $\overline{w'^2}$, resulting in $\overline{v w'^2} = \overline{v'^3}$. The error introduced by this assumption found to be less than 10%. Sideridis et al. [105] found that the absence of that product did not alter the total turbulent diffusion term more than 10%, thus conducting all the calculations without using this term, assuming a total error approximately 10%. The reason for making this assumption was that the experimental techniques used in all the aforementioned studies were not capable of measuring directly the product $\overline{v w'^2}$.

In the present calculations, the above assumption was not made and the triple correlation term $\overline{v w'^2}$ was estimated in the same way as the other eight terms.

Finally, the pressure diffusion term can be also expanded to a sum of streamwise, lateral and spanwise velocity-pressure gradients.

$$\Pi K_{tot} = \Pi K_{str} + \Pi K_{lat} + \Pi K_{span}$$

where

$$\Pi K_{str} = -\left(\overline{\frac{\partial u' p'/\rho}{\partial x}}\right) \quad , \quad \Pi K_{lat} = -\left(\overline{\frac{\partial v' p'/\rho}{\partial y}}\right) \quad , \quad \Pi K_{span} = -\left(\overline{\frac{\partial w' p'/\rho}{\partial z}}\right) \tag{5.9}$$

Most of the previous researchers have either neglected the pressure diffusion term (see [91]) or extracted it by difference (see [14, 58, 77, 105, 121]), having initially calculated the rest of the TKE transport equation terms. However, in the ILES calculations the pressure-velocity correlation, $\overline{pu'_j}$, has been directly measured using the equation below.

$$\Pi K = -\frac{1}{\rho}\left(\overline{\frac{\partial u' p'}{\partial x}} + \overline{\frac{\partial v' p'}{\partial y}} + \overline{\frac{\partial w' p'}{\partial z}}\right) \tag{5.10}$$

The pressure correlation term shows how the turbulent kinetic energy is spatially redistributed by pressure perturbations. However, the terminology of the so-called "pressure-diffusion" term is rather peculiar, as the pressure effects are by convention nonlocal and instantaneous in incompressible flows, while diffusion evolves gradually and slowly in the flow field. Fortunately, most of the times the pressure diffusion is small compared to the other terms in Equation (5.2), having a small contribution to the total energy budget.

All the six terms described above were measured for three different high-resolution schemes and presented in Figure 5.5. The measurement location is placed immediately downstream of the step, and particularly in the region of the separated shear layers, at $x/h = 1$. In this region, the peak production rate is approximately two times larger than the dissipation and the convection term. These two latter terms found to contribute negatively to the turbulent kinetic energy budget. The viscous dissipation becomes also significant in the near-wall region, where it is balanced by the viscous diffusion term. Moreover, the turbulent diffusion term along with the pressure-velocity correlations redistribute energy from the free shear layer to the outer regions toward the upper and lower wall, as well as in the centerline area of the channel. This budget structure has been also observed in the region of the shorter recirculation zone further downstream of the expansion, though

all the aforementioned properties and effects are fairly attenuated with distance. It is noteworthy to mention that the six terms in the kinetic energy equation do not balance exactly. Thus adding all the six terms together the resulting balance is either negative or positive (depending on the streamwise location where the turbulent kinetic energy budget is measured). The terms do not balance due to the numerical dissipation produced by the high-order terms (H.O.T.) of the high-resolution high-order reconstruction schemes used in conjunction with the ILES turbulence modelling approach. Thus, the truncation error of each of the three different numerical methods used (M3, M5 and W5), added to the current energy balance shown in Figure 5.5, leads to a balanced kinetic energy equation.

It is also important to underline that M3 appears to overestimate the turbulent production rate compared to M5 and W5. This is more apparent in the region of the shorter reattachment, where generally the production term is larger than that in the opposite direction. All the six terms of the energy budget will be discussed in details in the next section.

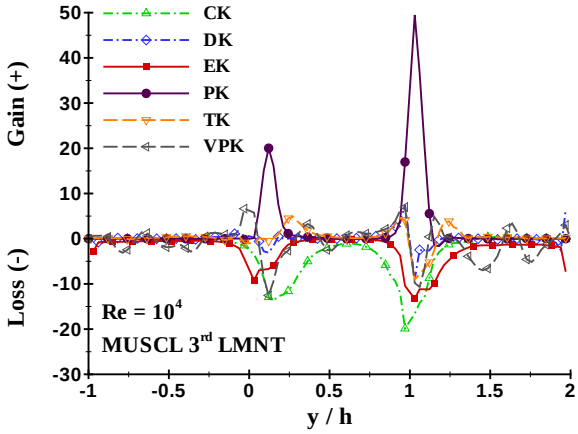

(a) M3

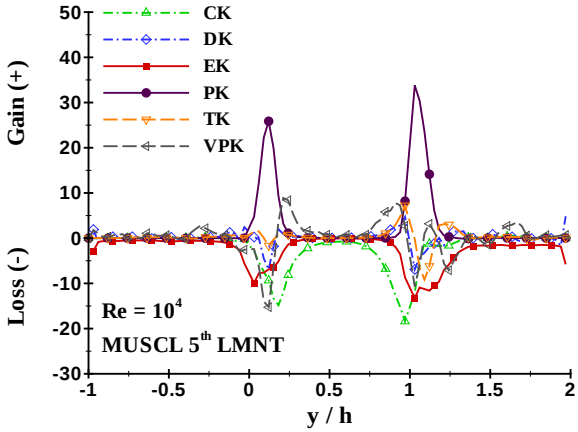

(b) M5

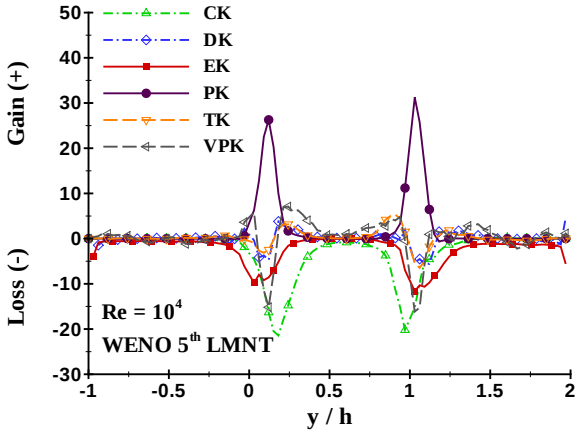

(c) W5

FIGURE 5.5: Turbulent kinetic energy budget terms across the wall-normal direction for three different numerical schemes, normalised by U_b^3/h at $x/h = 1$.

In Figures 5.7 - 5.14 the results downstream of the channel expansion are represented, where three typical wall-normal distributions are shown. The first measurement location is placed immediately after the step at $x/h = 1$, where the separation of the two shear layers in the upper and lower step edge takes place. The second measurement line, at $x/h = 2$, crosses the middle point of the shorter recirculation zone, while the final cross-section line passes approximately through the middle point of the larger recirculation vortex, at $x/h = 5$. Note that this last measurement line is outside the region of the shorter reattachment, as that can be seen in Figure 5.6.

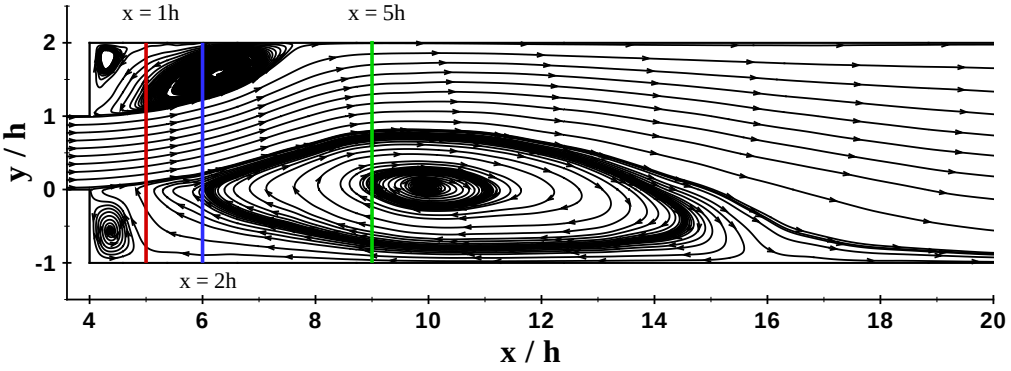

FIGURE 5.6: Positions of the measurement lines taken along the lateral direction at the xy midplane of the channel ($z/h = 2.5$).

For the calculation of the turbulent kinetic energy budget, three different high-resolution schemes were used including the M3, M5 and W5, investigating such a way the influence of the numerical schemes on the energy budget. Besides, the influence of the Re on the energy budget has also been examined by employing two different Reynolds numbers at $Re = 10^4$ and $Re = 4 \times 10^4$. All budget terms of turbulent kinetic energy are normalised by U_b^3/h and then multiplied by 10^3.

Convection Term

The convection term appears to be generally negative throughout the sudden expansion domain (see Figure 5.7). Note that negative values indicate energy loss, which means that energy is subtracted from the mean flow and is conduced to the shear layer spreading. Convection peaks on the high-speed sides of the two free shear lines about the upper and lower wall and decreases to zero on the walls. Furthermore, convection appears to be of nearly equal magnitude in the shear layer regions, with the one closer to the shorter recirculation zone being slightly higher than that located in the opposite wall. The spanwise convection component found to be at least one order of magnitude lesser than the streamwise and lateral convection terms. The same observation has been also addressed in [105] and [77], where in both studies the spanwise component of the convection term was not included in the calculations due to its small magnitude. The streamwise convection,CK_{str}, dominates the flow field in the region of the shorter reattachment, mainly due to the sustaining streamwise velocity contribution. On the other hand, the lateral convection term is the dominant one about the region of the larger recirculation zone where the transverse velocity gradient is more pronounced.

As far as the influence of the numerical schemes on the convection term is concerned, the magnitude of the convection term at the region of the shorter reattachment, at $x/h = 1$, found to be similar among the high-resolution schemes, reaching its maximum negative value of 19.8, 18.4 and 20.2 for the M3, M5 and W5, respectively. Its contribution to the energy budget is more dominant for the W5, particularly at the shear layer region near the upper wall of the channel. At this particular location, the ratio of the convection term to the production term found to be larger for the W5 ($CK/PK = 0.64$), indicating that convection is a significant contributor to the turbulent kinetic energy budget. At $x/h = 2$ the magnitude of the convection term has been considerably decreased for all the numerical schemes under investigation. However, the term CK/PK still remains quite high, approaching the values of 0.5 to 0.8 and 0.4 to 0.7 in the upper and lower shear layer region, respectively. Further downstream at $x/h = 5$ the streamwise convection seems to take positive values, transferring that way energy to the high-speed side of the free shear line along the wall-normal direction. This last observation is mainly noticeable only for the MUSCL schemes. The convection term in that specific location appeared to be almost constant and close to zero for the W5.

The influence of the Reynolds numbers on the convection term is represented in Figures (5.7(a),5.7(c),5.7(e)) for three different streamwise locations along the cross-section

of the duct. At $x/h = 1$ the plots from the two different Reynolds numbers seem to be nearly identical one another, exhibiting a small disparity in the region of the larger reattachment at $y/h \simeq 0.2$. Although the magnitude of the convection term for $Re = 4 \times 10^4$ is lower in that flow region, the ratio of the convection to the the production term is almost the same for the two Re numbers ($CK/PK \simeq 0.56$). At $x/h = 2$ the shear layers have been shifted upwards, as the flow moves in this specific direction forming a short recirculation zone at the top wall and a large one at the bottom wall, respectively. The magnitude of the convection term in these two flow regions have been considerably decreased, especially for $Re = 4 \times 10^4$, where both shear layers found to have the same peak value. On the other hand, the peak on the high-speed side of the shear line at the region of the larger reattachment remained the same for $Re = 10^4$ with that found at the previous streamwise location at $x/h = 1$. All the above properties seem to attenuate with distance downstream. From $x/h = 5$ onwards, the contribution of the convection term to the total energy budget is negligible. It is also important to underline that the positive values observed at $x/h = 5$ for the three different numerical methods at $Re = 10^4$, have been also appeared at $Re = 4 \times 10^4$ as shown in Figure 5.7(f).

Kasagi et al. [65] performed turbulent kinetic energy budget measurements in a flow over a backward-facing step at $Re = 5540$, based on the channel step height and the upstream centerline velocity. They found that at $x/h = 1$ downstream of the expansion the convection term played a significant role, contributing negatively to the kinetic energy budget. The general shape of the convection term is in a very good agreement with the ILES findings. However, the ratio of the convection to the production term demonstrated in their experimental study, found to be much smaller than that presented above ($CK/PK \simeq 0.28$). This discrepancy can be attributed mainly to the different Reynolds number used and obviously to the different channel configuration. TKEB measurements in a sudden expansion flow have not been previously reported either experimentally or numerically.

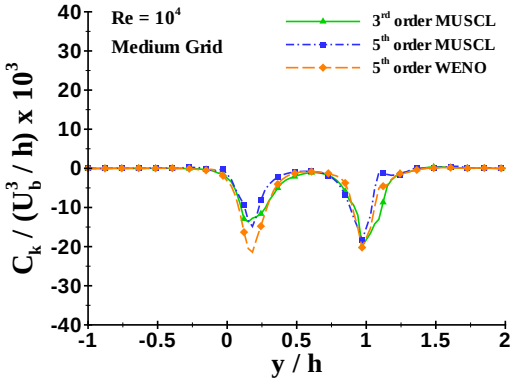

(a) Convection term at X = 1h for M3, M5 and W5.

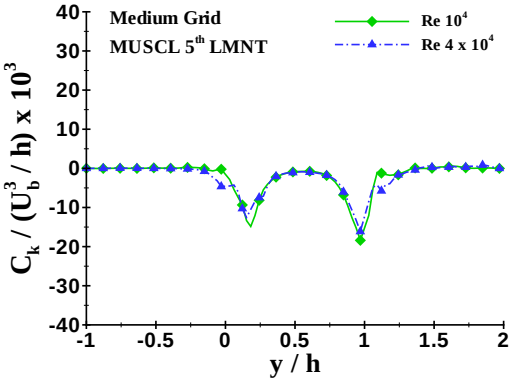

(b) Convection term at X = 1h for Re 10000 and 40000.

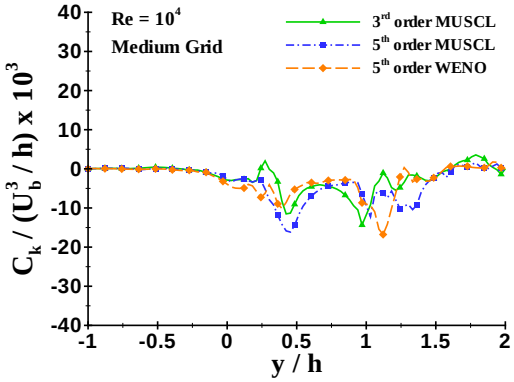

(c) Convection term at X = 2h for M3, M5 and W5.

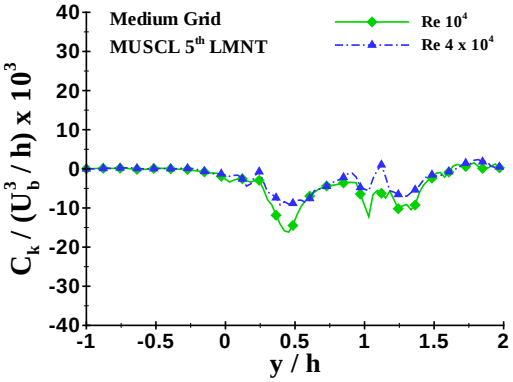

(d) Convection term at X = 2h for Re 10000 and 40000.

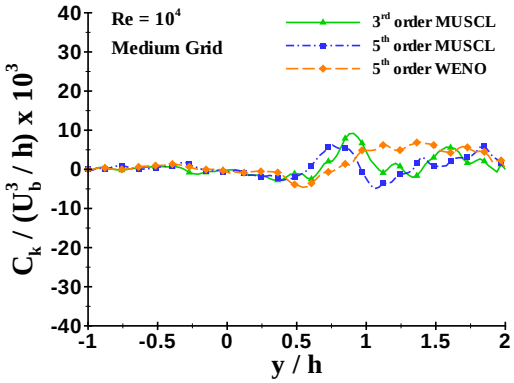

(e) Convection term at X = 5h for M3, M5 and W5.

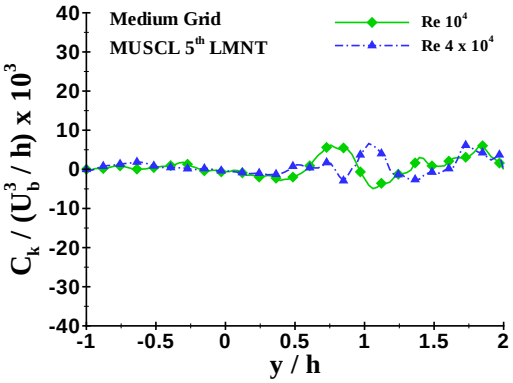

(f) Convection term at X = 5h for Re 10000 and 40000.

FIGURE 5.7: The **Convection** term for three different numerical schemes and two Reynolds numbers at (a),(b) $X = 1h$, (c),(d) $X = 2h$ and (e),(f) $X = 5h$ downstream of the expansion along the Y - axis.

Production Term

Contrary to the convection term is the production term, which appears to be generally positive throughout the sudden expansion domain. We can see why this is so, assuming that the mean flow is a parallel shear layer, $U(y)$, in the streamwise direction, x (see Figure 5.8). If the only non-zero mean velocity gradient is $\partial_2 U_1 = \partial_y U$, it follows that $PK = -\overline{u'v'}\frac{\partial \overline{U}}{\partial y}$. Furthermore, if the flow element at $t = t_0$ is located at $y = Y_0$, then at time $t = t_1$ the cross-stream position of this element convected by turbulence velocity will be at $Y(t_1) = Y_0 + \int_0^{t_1} v(t_1^{'})dt_1^{'}$. If we further assume that the velocity remains the same from point 1 to point 2 then the instantaneous velocity at $Y(t_1) = y$ will be the particle's velocity $u_{inst} = U(Y_0)$. Since $Y_0 = y - \int_0^{t_1} v(t_1^{'})dt_1^{'}$, the above velocity is equivalent to $u_{inst} = U(y - \int_0^{t_1} v(t_1^{'})dt_1^{'})$. By convention, the velocity fluctuations are given by: $u^{'} = u_{inst} - U$. Thus, the resulting fluctuating velocity will be:

$$u^{'} = U(y - \int_0^{t_1} v(t_1^{'})dt_1^{'}) - U(y) \approx -\int_0^{t_1} v(t_1^{'})dt_1^{'}\partial_y U \tag{5.11}$$

Multiplying Equation (5.11) by $v(t_1)$ and averaging, the resultant Reynolds shear stress, $\overline{u'v'}$, is formed as follows:

$$\overline{u'v'} = -\int_0^{t_1} \overline{v(t_1)v(t_1^{'})}dt_1^{'}\partial_y U \tag{5.12}$$

If $\partial_y U > 0$ then Equation (5.11) shows that a positive v correlates with a negative u. This is also the reason why in parallel shear flows, $\overline{u'v'}$ tends to have the opposite sign of the mean flow gradient. The general tendency of $\overline{u'v'}$ to be negative (if $\partial_y U > 0$, see Equation (5.12)), explains why the production term, PK, tends to be generally positive.

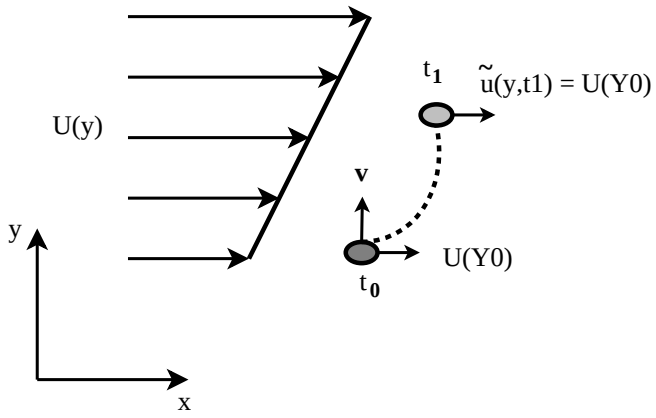

FIGURE 5.8: Schematic of a parallel shear layer flow moving in the streamwise direction.

In the present study, turbulence production found to be the most dominant term exhibiting two peaks on the high-speed sides of the free shear layers about the upper and lower wall of the channel. The same feature has been addressed in several studies on turbulent kinetic energy budget. Liu and Thomas [77] performed an experimental study, in which they measured the turbulent kinetic energy budget of a planar wake flow employing different pressure gradients. They found that the production term is the dominant term in the calculations with the longitudinal shear production $-\overline{u'v'}\left(\frac{\partial \overline{U}}{\partial x}+\frac{\partial \overline{V}}{\partial x}\right)$ being particularly the major contributor to the energy balance (positive values found across the turbulent wake).

Kasagi and Matsunaga [65] carried out three-dimensional PIV measurement of turbulence energy budget in a backward-facing step flow at $Re = 5540$. They showed that turbulence production is almost three times larger than the turbulence convection and approximately two times larger than the dissipation term. They also found that the maximum production rate decreased with increasing distance and the major contributor over the entire flow region was the term $-\overline{u'v'}\frac{\partial \overline{U}}{\partial y}$. These last two observations are in excellent agreement with the results presented in Figure 5.9. It should also be noted that in the present case throughout the sudden expansion domain, $\frac{\partial \overline{V}}{\partial x}$ is negligible compared to $\frac{\partial \overline{U}}{\partial y}$.

Le et al. [73] performed a numerical investigation of a turbulent flow over a backward-facing step at $Re = 5100$, based on the step channel height and the inlet free-stream velocity, by means of direct numerical simulation. They found that production is the most dominant term in the region of the free shear layer immediately downstream of the step, while as approaching the wall it becomes a consuming term due to the negative gradient of the mean reverse flow. They also showed that in the recirculation region, PK is mostly

due to the production of the longitudinal stress, PK_{uu}.

The influence of the numerical schemes on the production term has been examined and represented in Figures (5.9(a),5.9(c),5.9(e)) for three different streamwise locations. At $x/h = 1$ the peak turbulence production occurs in the high-speed side of the two shear layer regions at $y/h \simeq 0.1$ and $y/h \simeq 1.1$, respectively. The peak value of turbulence production in all numerical schemes found to be in the shear layer closer to the shorter recirculation vortex. As mentioned in the previous chapter, in this particular region, the Reynolds stress, $-\overline{u'v'}$, and the turbulent kinetic energy, k, have their maximum values, justifying that way the above observation. It is important to underline that M5 and W5 gave similar results, having almost the same cross-section distribution in all the three streamwise measurement locations. On the other hand, the peak turbulence production at $x/h = 1$ and $x/h = 2$ for M3 found to be underestimated in the free shear layer of the larger reattachment, while it was overestimated in the region of the shorter reattachment. At $x/h = 3$ all the numerical schemes appears to agree with each other reasonably well. Although not shown here, the shear stress, $u'v'$, and the shear turbulent kinetic energy production become almost symmetrical from $x/h = 5$ onwards, about the center point of the two shear layers, while both decreasing with distance downstream.

As far as the influence of the Reynolds number to the turbulence production is concerned, it is evident from Figures 5.9(b) and 5.9(d) that turbulence production is higher for $Re = 10^4$, particularly in the first two streamwise locations examined. This peculiar production structure was observed in both free shear layers, up to $x/h = 3$. That means that the rate at which energy is transferred from the mean flow to turbulent fluctuations is higher at the lower Re. The lower rate of energy transfer at larger Re can be attributed to the lower fluid viscosity, which in turn results in the delay of the loss of energy from the mean flow. Besides, the same trend was also detected in the results of the turbulent kinetic energy, where the highest peak values at the recirculation regions were obtained at the lower Re. Beyond that spot the turbulence production appears to be higher at $Re = 4 \times 10^4$, until the point where both curves match each other precisely, at $x/h = 5$ downstream of the step. In the vicinity of the walls, a rapid decrease of $-\overline{u'v'}$ and $\frac{\partial U}{\partial y}$ is noticeable, resulting in a zero turbulence production for both Re used, as expected.

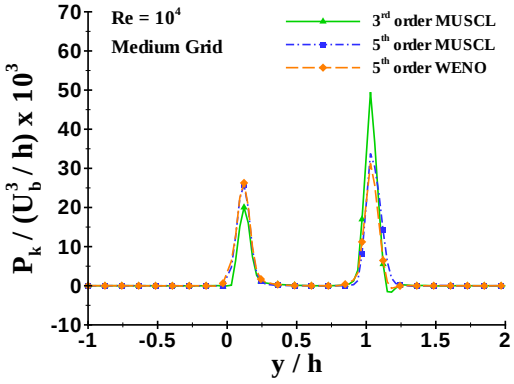

(a) Production term at X = 1h for M3, M5 and W5.

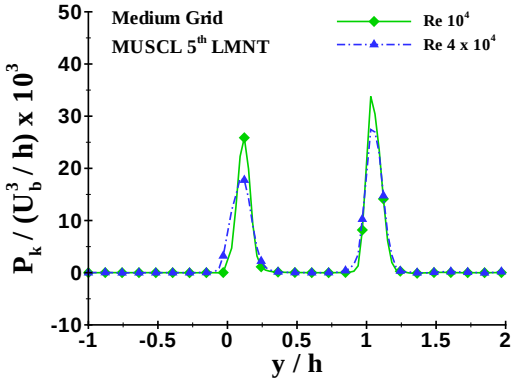

(b) Production term at X = 1h for Re 10000 and 40000.

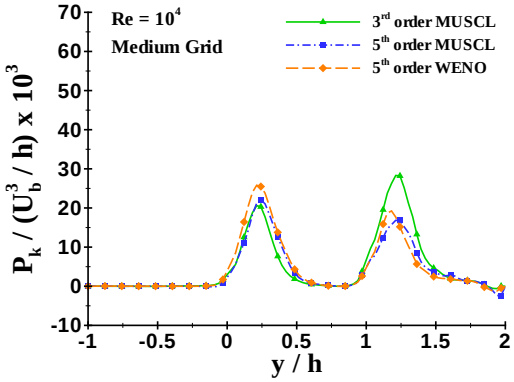

(c) Production term at X = 2h for M3, M5 and W5.

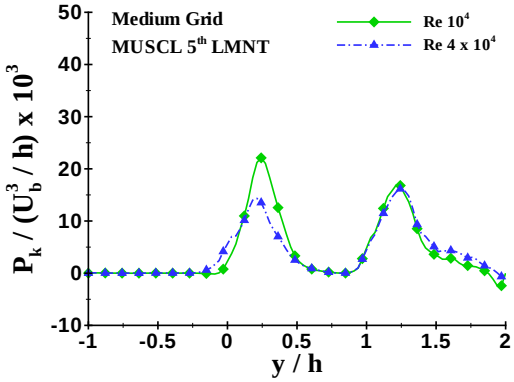

(d) Production term at X = 2h for Re 10000 and 40000.

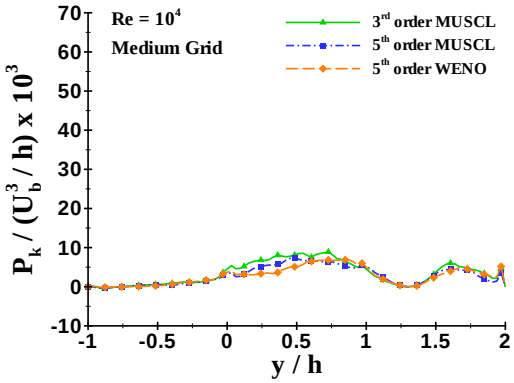

(e) Production term at X = 5h for M3, M5 and W5.

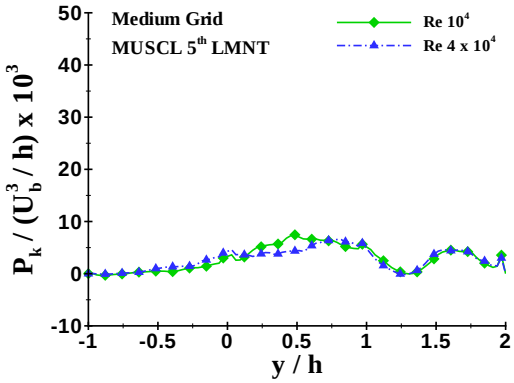

(f) Production term at X = 5h for Re 10000 and 40000.

FIGURE 5.9: The **Production** term for three different numerical schemes and two Reynolds numbers at (a),(b) $X = 1h$, (c),(d) $X = 2h$ and (e),(f) $X = 5h$ downstream of the expansion along the Y - axis.

Dissipation Term

The dissipation term contributes negatively to the turbulent kinetic energy budget, behaving in similar way as the convection term discussed above. It represents decay of turbulence and for that reason is preceded by a negative sign. The dissipation term in the Reynolds transport equation is denoted by:

$$\varepsilon_{ij} = -2\nu\overline{\partial_k u_i \partial_k u_j}$$

The turbulent kinetic energy transport equation is obtained after dividing the Reynolds transport equation by 2 and inserting the variable $k = \frac{1}{2}\left\langle u_i' u_i' \right\rangle$ to the former equation. In that case the quantity $\varepsilon = -\nu\overline{\partial_k u_i \partial_k u_i} = -\nu\overline{|\nabla u|^2}$ is formed, which represents the rate of dissipation of turbulent kinetic energy. It is the rate at which viscous stresses perform deformation work against the fluctuating strain rate. Unlike the dissipation term in the energy equation for the mean flow (which is negligible compared to the other energy budget terms), here it is essential to the dynamics of turbulence and cannot normally be neglected.

Dissipation appears to be more intense in region where turbulence production is higher. Particularly, it peaks on the high-speed sides of the two free shear layers for several step heights downstream of the expansion. These places are off the turbulent wake centerline, as shown in Figure 5.10. Its magnitude seems to decrease with downstream distance, responding well to the decrease of the production term, while at the same it turns out to be a significant consuming term near the top and bottom wall of the channel. In near wall regions, where the total production rate is small, dissipation is the dominant term. In these regions the ratio of dissipation to production (EK/PK) found to be approximately 1.9 at $x/h = 5$ downstream of the step, which is higher than that addressed in previous studies on the backward-facing step flow. This discrepancy is mainly attributed to the low grid resolution achieved near the walls at the lateral direction. In the regions of the two shear layers the contribution of dissipation to the energy budget found to be significant and of about the same magnitude as the convection term. Besides, the lateral dissipation term $-\nu\left(\overline{\left(\frac{\partial u'}{\partial y}\right)^2} + \overline{\left(\frac{\partial v'}{\partial y}\right)^2} + \overline{\left(\frac{\partial w'}{\partial y}\right)^2}\right)$ detected to be the most dominant throughout the sudden expansion domain, with the streamwise and spanwise terms being approximately one order of magnitude lower than the lateral one.

Table 5.1 shows the ratio of dissipation term to production term for three different numerical schemes at two streamwise locations $x/h = 1$ and $x/h = 2$. Note that the results

presented refer to the two free shear lines extended downstream of the step edges. The first one corresponds to the side of the channel where the shorter reattachment is present (upper wall), whereas the second one to the side of the channel with the larger vortex (lower wall).

TABLE 5.1: Ratio of dissipation term to production term at two streamwise locations downstream of the channel expansion calculated for three high-resolution schemes.

$x/h = 1$	M3 (ε, EK/PK)	M5 (ε, EK/PK)	W5 (ε, EK/PK)
Region 1	-13.3, 0.3	-13.2, 0.39	-11.62, 0.39
Region 2	-9.24, 0.48	-9.89, 0.38	-9.19, 0.36
$x/h = 2$	M3 (ε, EK/PK)	M5 (ε, EK/PK)	W5 (ε, EK/PK)
Region 1	-9, 0.32	-11, 0.65	-8.41, 0.45
Region 2	-6.81, 0.35	-7.77, 0.36	-7.36, 0.31

It is evident that the magnitude of the dissipation term is negative in all flow regions examined, with that closer to the shorter recirculation zone being slightly higher than that in the region of the larger reattachment. Furthermore, at $x/h = 1$ the ratio of the dissipation to the production term found to be in the range of 0.3 to 0.4 and 0.36 to 0.48 for region 1 and region 2, respectively. The corresponding ratio at $x/h = 2$ extends from 0.32 to 0.65 and from 0.31 to 0.36 for the same regions under investigation. Further downstream its magnitude appears to be relatively small in the regions of the shear layers as well as in locations near the reattachment. On the other hand, very close to the upper and lower wall the viscous term, EK, grows rapidly, with their value at the wall being approximately 30% higher than the peak production in the shear layers. This last observation is in very good agreement with the DNS results presented in [73], where the dissipation term close to the wall found to be about 40% higher than the maximum value of production in the shear layer of a flow over a backward-facing step.

It should be also noted that the dissipation curves for the three high-resolution schemes match reasonably well with each other, with the maximum absolute value in the region of the shorter reattachment being slightly higher for M5, as shown in Figure 5.10. It turns out that dissipation is a significant term in the energy transport budget. The peak EK is approximately 40% of the production peak, which means that the commonly used assumption leading to eddy viscosity models, that the production is balanced with dissipation, is not likely in separated and suddenly expanded flows (in the recirculation regions

dissipation is much lower than production).

As far as the influence of the Reynolds number to the dissipation term is concerned, it can be said that no significant difference was detected for the two Re. As shown in Figure 5.10, the peak dissipation, in the separated shear layers of the sudden expansion domain, takes place at $y/h \simeq 0.15$ and $y/h \simeq 1.15$ immediately after the step at $x/h = 1$ for both Re. Further downstream (at $x/h = 2$) the peak values were shifted toward the upper wall, following the fluid flow pattern as it bends upward. As the flow moves in the streamwise direction the near wall dissipation becomes larger at higher Re, while its peak values at the shear layers gradually decrease, as expected. Thus, the dissipation seems to be the same throughout the sudden expansion domain for the two Reynolds numbers under investigation, except for the near wall regions where its magnitude appears to be higher for $Re = 4 \times 10^4$.

The most important feature revealed in the study of the dissipation term between $Re = 10^4$ and $Re = 4 \times 10^4$ is the ratio of the production to dissipation term. This found to be closer to experimental and numerical data for the latter Re. In that case, the peak EK is approximately 64% and 62% of the production peak at $x/h = 1$ and $x/h = 2$, respectively. For a backward-facing step flow, Le et al. [73] found that in the recirculation region the peak dissipation is about 60% of the production peak, having their maxima at the same point in the free shear layer. Kasagi et al. [65] showed that the maximum value of dissipation is approximately 61% of the production peak at $x/h = 1$ downstream of the expansion. Prior to reattachment point, at $x/h = 4$, they found that the ratio of the dissipation to the production term increases and approaches the value of $E_k/P_k \simeq 0.7$. It is then obvious that the results obtained at $Re = 4 \times 10^4$ (in terms of the dissipation rate) are in excellent agreement with the aforementioned studies as far as the ratio of EK/PK is concerned. Nevertheless, the contribution of dissipation term to the energy budget found to be substantial for both Reynolds numbers.

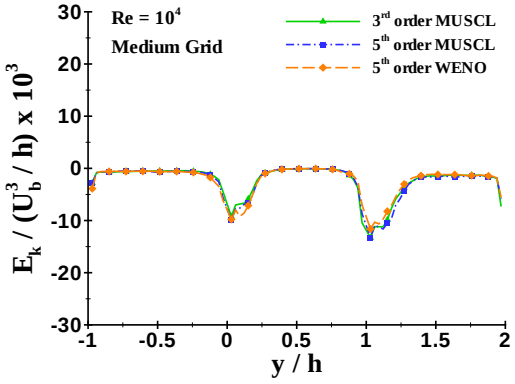

(a) Dissipation term at X = 1h for M3, M5 and W5.

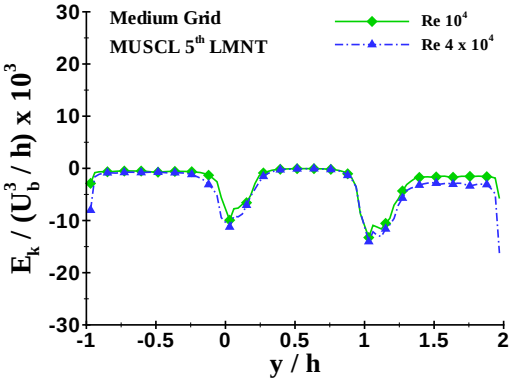

(b) Dissipation term at X = 1h for Re 10000 and 40000.

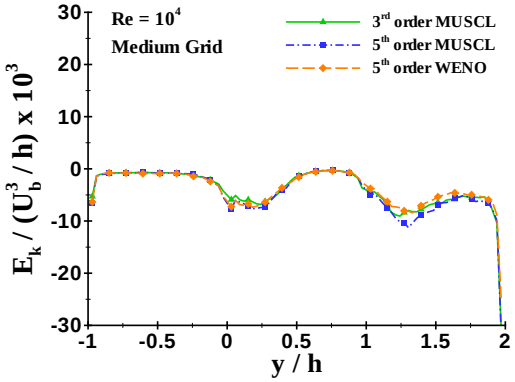

(c) Dissipation term at X = 2h for M3, M5 and W5.

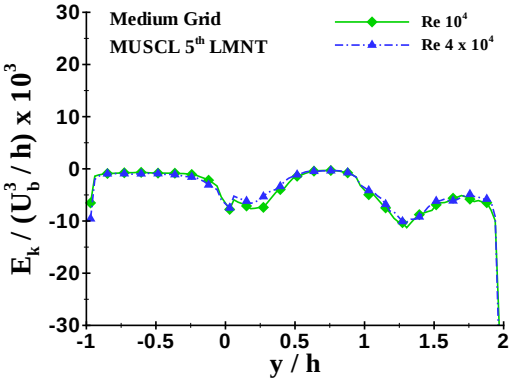

(d) Dissipation term at X = 2h for Re 10000 and 40000.

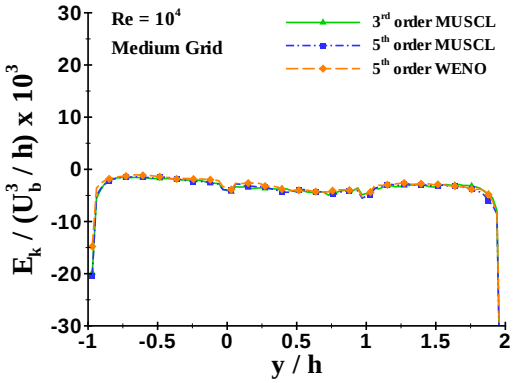

(e) Dissipation term at X = 5h for M3, M5 and W5.

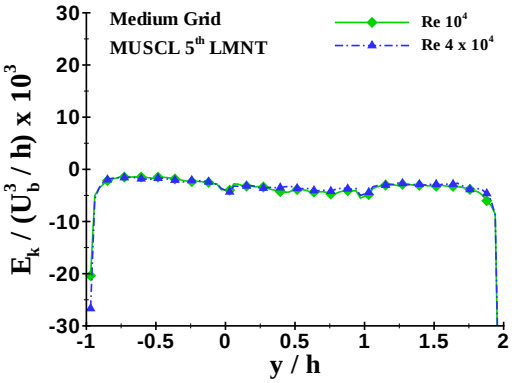

(f) Dissipation term at X = 5h for Re 10000 and 40000.

FIGURE 5.10: The **Dissipation** term for three different numerical schemes and two Reynolds numbers at (a),(b) $X = 1h$, (c),(d) $X = 2h$ and (e),(f) $X = 5h$ downstream of the expansion along the Y - axis.

Pressure Diffusion Term

The velocity-pressure gradient term calculated by Equation (5.10) is represented in Figure 5.11. As previously stated, in most experimental studies found in the literature, pressure diffusion term has either been neglected or extracted by difference, having calculated the rest of the turbulent kinetic energy budget terms. This implies that it is not a directly measurable quantity and it cannot be calculated from hot-wire or PIV data. Thus, comparisons of the ILES results with other experimental data cannot be generally made as the error encountered in such calculations is considered very high. Kasagi et al. [65] did not include pressure diffusion term in their calculations. It was instead assumed as small compared to the other terms and finally the dissipation term was estimated as the residual. The pressure diffusion term was also neglected in the estimation of the dissipation term in the experimental study of Panchapakesan et al. [91].

Contrary to the above studies, in the present case the pressure diffusion found to be comparable to the rest of the turbulent kinetic energy terms as shown in Figure 5.11. This observation agrees well with the results of Sideridis et al. [105] who addressed that although pressure-correlation term is lower than the other terms in the energy budget, its magnitude cannot be considered as negligible. Besides, Le et al. [73] found that the pressure diffusion is very significant in the near wall region where it balances the turbulence transport and dissipation terms. In their experimental measurements Liu et al. [77] though not calculating the pressure diffusion term directly (it was inferred from the forced balance of the turbulent kinetic energy equation), they stated that it is not negligible, as it facilitates energy transfer from the shear layers of the wake to the outer region.

The pressure-velocity gradient found to be significant in the regions $-0.8 \leq y/h \leq 0.5$ and $0.9 \leq y/h \leq 2$. It seems that pressure diffusion redistributes energy, by spreading the Reynolds stresses in space. More specific, it seems to transport turbulence away from the two shear layers (regions with high mean strain), where it is produced, and toward those locations with very low production rate (like the outer edges of the shear layers and the centerline of the high velocity core). Furthermore, pressure diffusion found to predominate near the upper and lower wall of the channel. This last feature of the flow is consistent with its inhomogeneous nature. It should also be noted that pressure diffusion responds to the lateral gradient in turbulent kinetic energy associated with newly-generated turbulence resulting from the production term.

In all streamwise locations M5 seems to agree reasonably well with W5, whereas M3

found to deviate from its counterparts especially in the region of the shorter recirculation zone, at $x/h = 2$. At this specific location the pressure diffusion term takes both positive and negative values near the top and bottom wall, as well as near the free shear layer areas. This feature is prominent in all high-resolution schemes examined in the present study. Further downstream, at $x/h = 5$, pressure diffusion is more dominant at the near wall regions, having almost zero magnitude at the centerline of the channel. This is reasonable, as in the latter region the production term is well balanced by the dissipation and convection terms, whereas at the former regions pressure-velocity gradient balances the dissipation and the viscous diffusion terms (they are different in magnitude).

In the free shear layer close to the bottom wall (at $x/h = 1$) the lower *Re* seems to exhibit larger peak values of pressure diffusion, with its absolute value being almost 2 times higher than that of the higher *Re* under investigation. At $x/h = 2$ pressure-velocity correlation term seems to have a major contribution to the energy budget, especially at the near wall region of the shorter reattachment. Thus, a significant amount of energy is transferred from the shear layer region where turbulence production is high to regions where production rate is relatively lower. This phenomenon has been observed in both Reynolds numbers, indicating that the influence of *Re* number on the pressure diffusion term at this streamwise location is not great (considering the fact that the magnitude of the higher Reynolds number is 4 times larger than that of the lower one, with the corresponding flow viscosity values being 3.74×10^{-3} and 9.35×10^{-4} for $Re = 10^4$ and $Re = 4 \times 10^4$, respectively). At $x/h = 5$, and particularly in the recirculation and shear layer regions, its magnitude found to be comparatively smaller than production and dissipation rate, however closer to the upper wall pressure diffusion is a considerable transport term in the TKE budget.

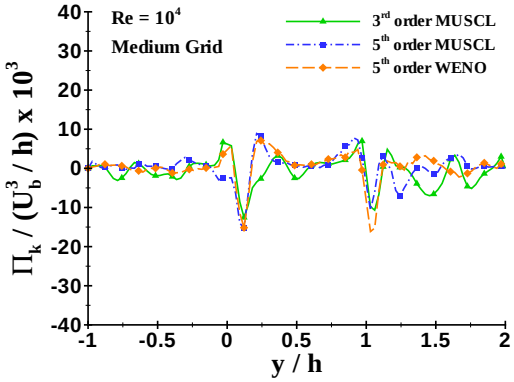

(a) Pressure Diffusion term at X = 1h for M3, M5 and W5.

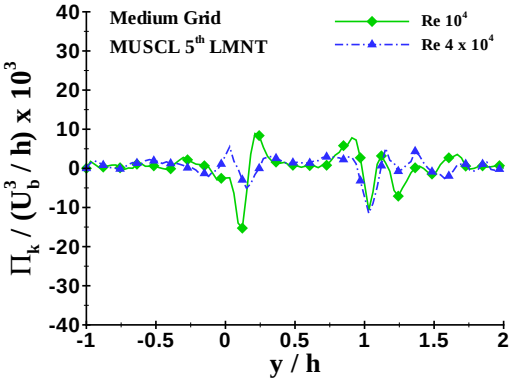

(b) Pressure Diffusion term at X = 1h for Re 10000 and 40000.

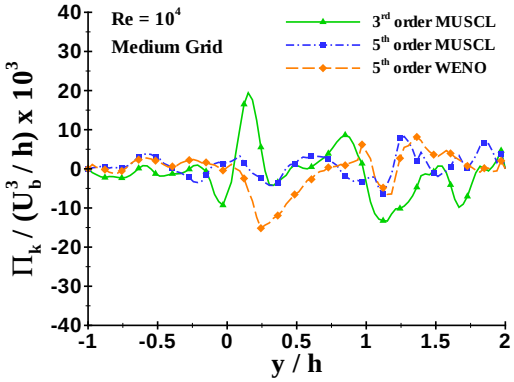

(c) Pressure Diffusion term at X = 2h for M3, M5 and W5.

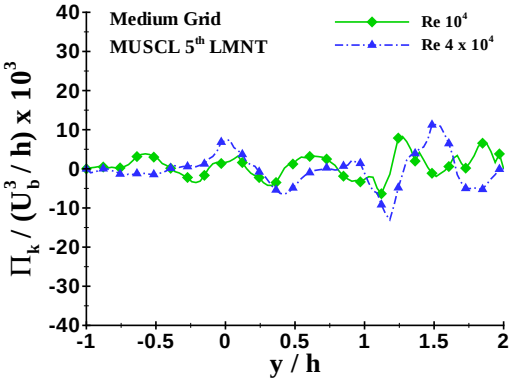

(d) Pressure Diffusion term at X = 2h for Re 10000 and 40000.

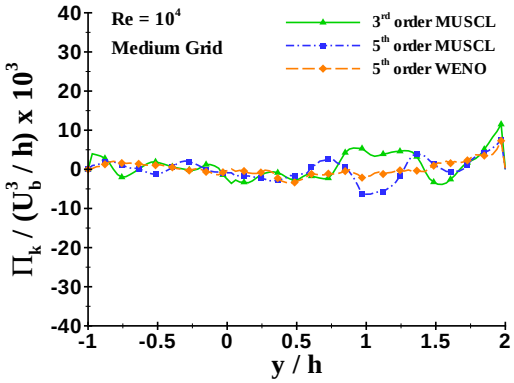

(e) Pressure Diffusion term at X = 5h for M3, M5 and W5.

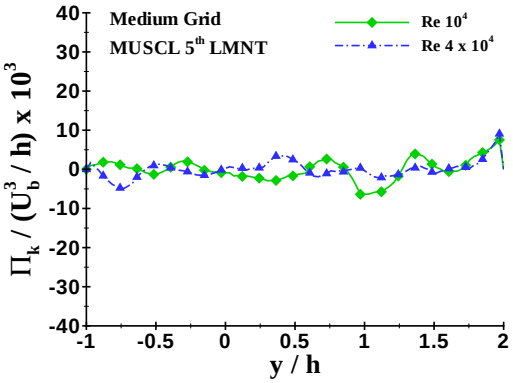

(f) Pressure Diffusion term at X = 5h for Re 10000 and 40000.

FIGURE 5.11: The **Pressure Diffusion** term for three different numerical schemes and two Reynolds numbers at (a),(b) $X = 1h$, (c),(d) $X = 2h$ and (e),(f) $X = 5h$ downstream of the expansion along the Y - axis.

Turbulent Diffusion Term

The profile shape of turbulent diffusion term is similar to that of the pressure-velocity correlation component, as shown in Figure 5.13. Both terms are responsible for transferring energy from higher to lower turbulence regions, and particularly from the free shear layers to the near-wall region, as well as to the centerline of the high velocity core flow. Transport peaks on the high-speed sides of the two free shear lines and decreases to zero on the wall. It is also zero on both sides of the separated shear layers. For example, at $x/h = 2$ turbulent diffusion term seems to decrease to zero at $y/h \simeq 0.01, 0.35$ and at $y/h = 1.01, 1.35$ located close to the longer and shorter reattachment region, respectively. The peaks detected near the upper wall are generally higher than that on the lower wall. Similar flow behaviour was also observed at $x/h = 1$ immediately downstream of the expansion, as well as at $x/h = 5$ at lower intense level though. It is thus evident that turbulent diffusion moves turbulent kinetic energy from high production rate regions towards the wall, the outer region and the centerline of the channel.

The lateral diffusion term $-\frac{\partial}{\partial y}\frac{1}{2}\overline{\left(v'u'^2 + v'^3 + v'w'^2\right)}$ found to be the dominant diffusion mechanism in the calculations, being approximately two times larger than the streamwise turbulent diffusion term $-\frac{\partial}{\partial x}\frac{1}{2}\overline{\left(u'^3 + u'v'^2 + u'w'^2\right)}$ throughout the sudden expansion domain. The spanwise transport component appears to be approximately one order of magnitude lesser than the lateral diffusion term, as shown in Figure 5.12.

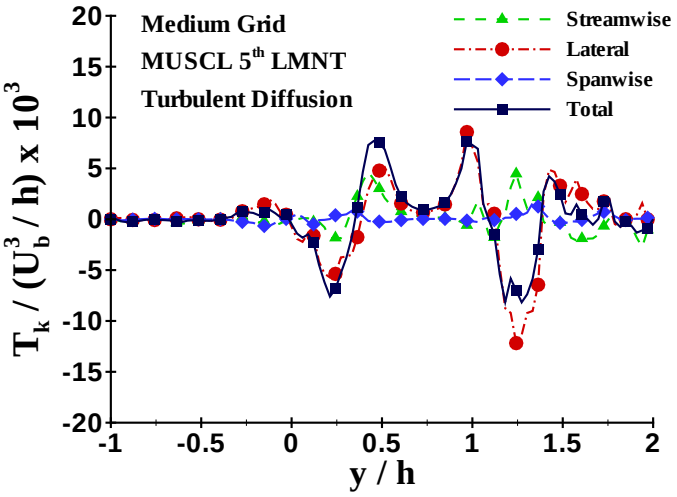

FIGURE 5.12: Streamwise, lateral and spanwise turbulent diffusion terms at $x/h = 2$ for the M5 scheme.

This observation is in excellent agreement with the results presented by Sideridis et al. ([105], 2010). In their study only the streamwise and lateral transport components were experimentally examined, with the lateral diffusion being the most dominant of the two, due to the lateral differentiation of the triple products. Furthermore, Liu and Thomas ([77], 2004) found that for a zero-pressure gradient turbulent wake the dominant diffusion mechanism is the lateral one, demonstrating that the streamwise turbulent diffusion is negligible compared to its counterpart.

Since the streamwise and spanwise transport terms are not so significant, and the major term that contributes to the turbulent diffusion is the lateral component, we expect that the cross-stream integration should give the following:

$$\int_{-\infty}^{\infty} \left[-\frac{\partial}{\partial y} \overline{\frac{1}{2} \left(v' u'^2 + v'^3 + v' w'^2 \right)} \right] dy = 0 \tag{5.13}$$

In order to evaluate the accuracy of the calculation of the lateral diffusion term, a numerical integration of its profile, as well as of the total turbulent diffusion profile shown in Figure 5.12 was carried out across the wall-normal direction, and the result was indeed found to be zero in both cases ($\simeq 10^{-20}$ and $\simeq 2.5 \times 10^{-17}$ for the lateral and total turbulent diffusion term, respectively).

The wall-normal distribution of turbulent diffusion profiles obtained at three streamwise locations downstream of the step channel, are shown in Figure 5.13. All the numerical schemes used, seems to be in a very good agreement with each other. Considering also the fact that the measurement of turbulent diffusion term presupposes the calculation of the triple correlation terms, $\overline{u_l' u_l' u_k'}$, which are very sensitive to small errors might present in the calculation of the fluctuating velocities, this makes the present findings even more remarkable. The transport mechanism found to be more significant in the region of the shorter recirculation zone, at $x/h = 2$, with the ratio of the turbulent diffusion term to the production term, TK/PK, being approximately 0.30, 0.47 and 0.41 for the M3, M5 and W5, correspondingly. It should also be noted that these values are in a very good agreement with those documented in the literature for a backward-facing step flow ([65, 73]).

The influence of the Reynolds number on the turbulent diffusion term is not significant in most parts of the sudden expansion domain. A discernible discord was found at $x/h = 1$, in the region where the free shear layer emanates from the step edge of the lower wall upstream of the expansion. In that specific location, the peak turbulent diffusion profile at $Re = 10^4$ appears to be considerably lower than that at $Re = 4 \times 10^4$. This can be

explained by the fact that both streamwise normal velocity, $\overline{u'u'}$, and its triple correlation term, $\overline{u'u'u'}$, found to exhibit larger magnitudes with increasing Re. Further downstream, at $x/h = 5$, all the above effects and properties seem to weaken, with the transport term having lower peak values in the free shear layer regions.

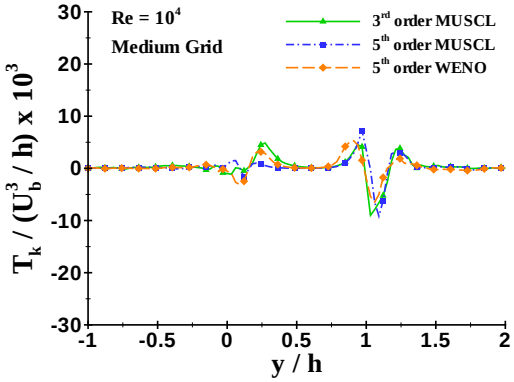

(a) Turbulent Diffusion term at X = 1h for M3, M5 and W5.

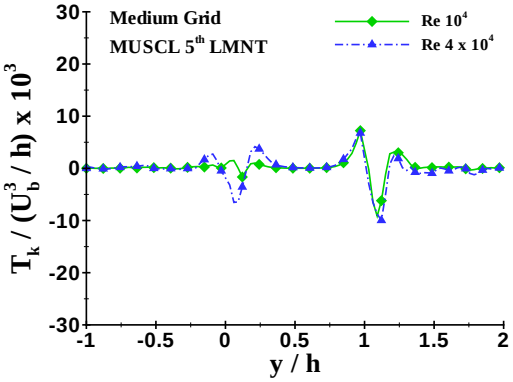

(b) Turbulent Diffusion term at X = 1h for Re 10000 and 40000.

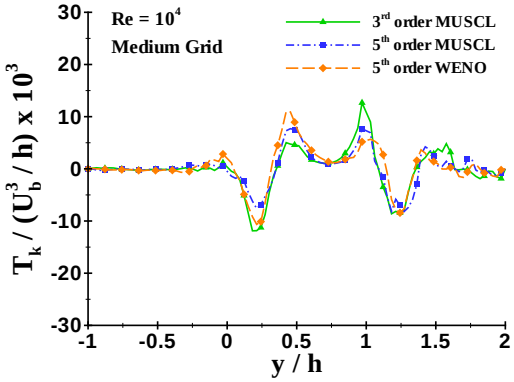

(c) Turbulent Diffusion term at X = 2h for M3, M5 and W5.

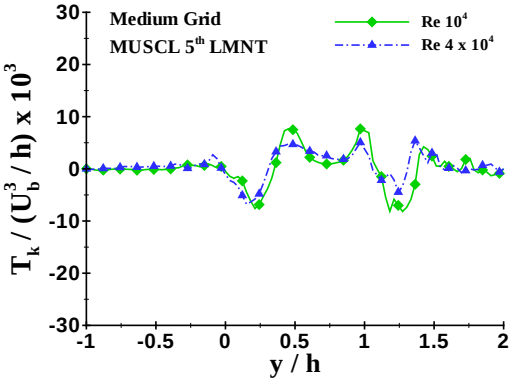

(d) Turbulent Diffusion term at X = 2h for Re 10000 and 40000.

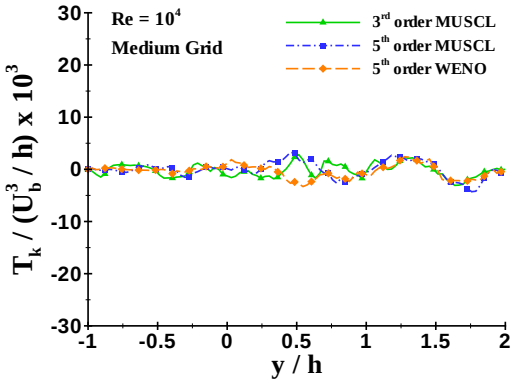

(e) Turbulent Diffusion term at X = 5h for M3, M5 and W5.

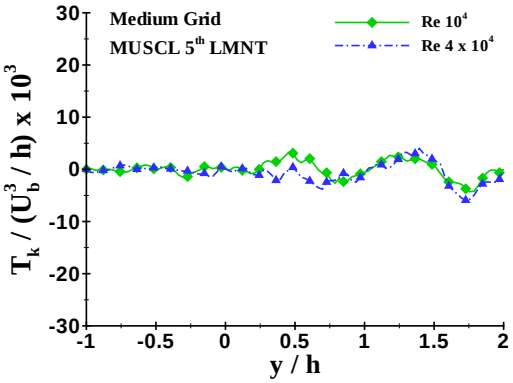

(f) Turbulent Diffusion term at X = 5h for Re 10000 and 40000.

FIGURE 5.13: The **Turbulent Diffusion** term for three different numerical schemes and two Reynolds numbers at (a),(b) $X = 1h$, (c),(d) $X = 2h$ and (e),(f) $X = 5h$ downstream of the expansion along the Y - axis.

Viscous Diffusion Term

The last term in the turbulent kinetic energy transport equation (see Equation (5.2)) accounts for the viscous diffusion. As previously mentioned, viscous diffusion is a dominant term in the near-wall regions, balancing mainly the turbulence dissipation term which in turn contributes negatively to the energy budget. On the other hand, in regions of high turbulence production rate, it becomes considerably small compared to the other energy budget terms. However, as shown in Figure 5.14, at $x/h = 1$ viscous diffusion term cannot be considered as negligible, as its magnitude is much greater than zero. This last indicates that viscous diffusion in conjunction with turbulent and pressure diffusion terms plays a significant role in the redistribution of turbulent kinetic energy in separated and suddenly expanded flows.

Further downstream, at the location where the measurement line crosses the shorter recirculation zone, the viscous diffusion term turns out to be approximately zero in the shear layer regions of the flow. Note that the scatter of the data for the viscous diffusion term at $x/h = 2$ is likely either due to insufficient period for the time-averaging or due to large truncation error stemmed from the finite difference scheme that is used to calculate the second spatial derivative of the stresses $\frac{\partial^2 \overline{u'u'}}{\partial X_k^2}$. Generally, in this streamwise location, and even further beyond that point, molecular diffusion is about an order of magnitude smaller than any other term across the entire layer except near the upper and lower walls of the main channel, where it becomes a significant producing term. It is also important to point out that all terms decay with streamwise distance x except near the wall, where both viscous diffusion and viscous dissipation are rapidly increased, while at the same time balanced each other.

The viscous diffusion profiles across the wall-normal direction for the three high-resolution schemes used, are represented in Figure 5.14. It is evident that all numerical schemes agree reasonably well with each other, with W5 being slightly lower in the near-wall regions than its counterparts. As far as the Reynolds numbers are concerned, it can be said that in the regions of the free shear layers both viscous diffusion profiles seems to match each other satisfactorily. However, close to the top and bottom wall higher peak values found for $Re = 4 \times 10^4$.

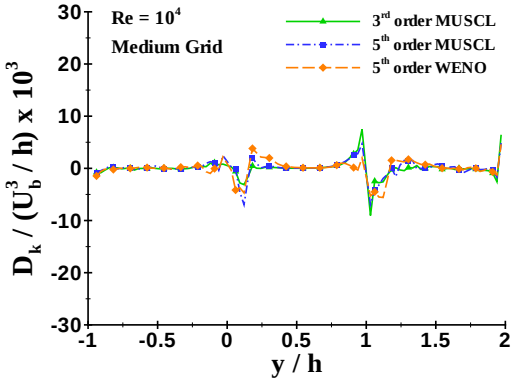

(a) Viscous Diffusion term at X = 1h for M3, M5 and W5.

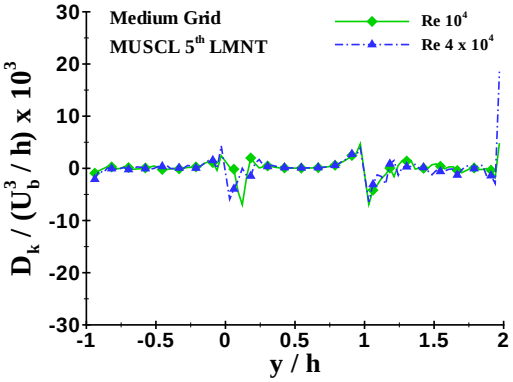

(b) Viscous Diffusion term at X = 1h for Re 10000 and 40000.

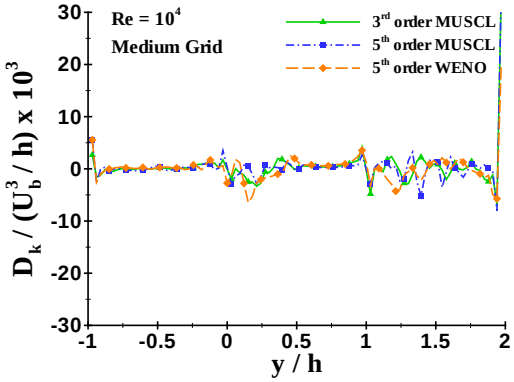

(c) Viscous Diffusion term at X = 2h for M3, M5 and W5.

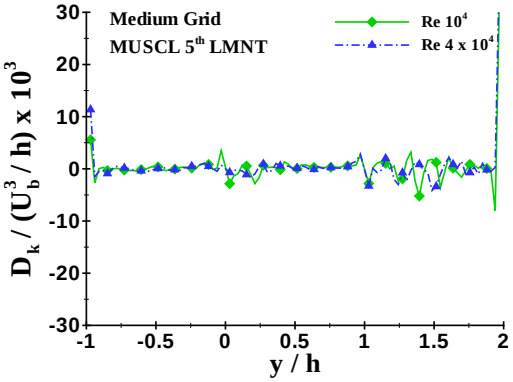

(d) Viscous Diffusion term at X = 2h for Re 10000 and 40000.

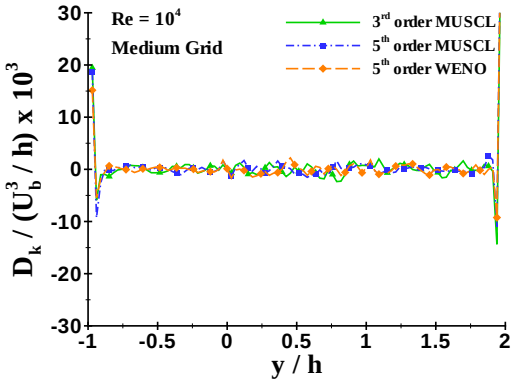

(e) Viscous Diffusion term at X = 5h for M3, M5 and W5.

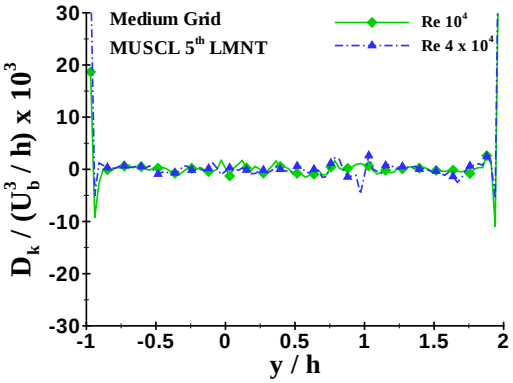

(f) Viscous Diffusion term at X = 5h for Re 10000 and 40000.

FIGURE 5.14: The **Viscous Diffusion** term for three different numerical schemes and two Reynolds numbers at (a),(b) $X = 1h$, (c),(d) $X = 2h$ and (e),(f) $X = 5h$ downstream of the expansion along the Y - axis.

5.4 Summary

In this chapter, a comprehensive study on the budgets of the turbulent kinetic energy for an incompressible flow was conducted. The influence of the channel expansion on the energy budgets was investigated, while two different *Re* and three high-resolution high-order schemes were employed aiming at shedding some light on the physics of turbulence in suddenly-expanded flows. The six terms of the energy budget (i.e., convection, production, dissipation, turbulent diffusion, velocity-pressure correlation, viscous diffusion) were thoroughly examined, and its derivatives were approximated by means of a first- and second-order central difference approach, applied on the entire computational domain.

Results revealed that the production term is the most dominant term at the high-velocity core flow and the shear layer regions. The peak production rate is approximately two times larger than the dissipation and convection term. The normal production term was not included in the calculations of the total turbulence production, as its magnitude was significantly lower than that of the shear production (i.e., the flow is shear dominated). The same feature was addressed in [77] for a symmetric turbulent planar wake flow. It was also found that the derivative of the transverse velocity with respect to the streamwise distance x is negligible compared to the rate of change of the streamwise velocity with respect to y. However, both terms was used for the calculation of the turbulence production.

The dissipation and convection terms contribute negatively to the turbulent kinetic energy budget almost everywhere in the flow field. As far as the convection term is concerned, it can be said that the streamwise convection, CK_{str}, is the most dominant term in the region of the shorter recirculation zone, where the streamwise velocity contribution is significant. The lateral convection, CK_{lat}, dominates along the region of the larger vortex, where the rate of change of the velocity with respect to the wall-normal direction is very high. Dissipation is significant in the flow regions where turbulence production is large (i.e., close to the shear layers formed downstream of the step edges of the channel). Note that the lateral dissipation term is approximately one order of magnitude higher than its counterparts. However, all the dissipation terms were included in the calculations, as the elimination of one or both the other two terms would have introduced significant numerical errors).

The turbulent diffusion term, as well as, the pressure-velocity correlations redistribute energy from the free shear layers to both the outer regions toward the upper and lower wall

and the centerline of the channel. As far as the turbulent diffusion is concerned, transport peaks on the high-speed sides of the two free shear lines and decreases to zero on the wall. The lateral diffusion term is the most dominant diffusion mechanism with its maximum magnitude being about two times larger than the streamwise turbulent diffusion. Note also that the spanwise turbulent diffusion is about one order of magnitude lesser than its lateral counterpart. The velocity-pressure gradient is significant in the shear layer regions. It is important to note that pressure-velocity correlations have a major contribution to the energy budget in the near wall region of the shorter recirculation zone. Thus, a significant amount of energy is transferred from the shear layer regions where turbulence production is very high to regions where production rate is relatively lower. It was also observed that close to the upper wall of the channel, the pressure diffusion is a considerable transport term in the TKE budget.

Viscous diffusion is a dominant term in the near-wall regions, balancing mainly the turbulence dissipation term, which in turn contributes negatively to the energy budget. On the other hand, in regions of high turbulence production rate, it becomes considerably small compared to the other energy budget terms. However, close to the channel step (i.e., at $x/h = 1$) viscous diffusion term cannot be considered as negligible, as its magnitude is much greater than zero. This indicates that viscous diffusion in conjunction with turbulent and pressure diffusion terms plays a significant role in the redistribution of turbulent kinetic energy in separated and suddenly expanded flows.

6 Compressibility Effects

6.1 Introduction

In this chapter, a numerical simulation study is performed in order to investigate the influence of compressibility on a turbulent channel flow with sudden expansion. The ILES method is used for simulating the compressible flow at $Re = 10000$ (based on the reference density ρ_{ref}, the step height of the channel h, and the inlet bulk velocity U_b) over a planar sudden expansion configuration. The simulations were conducted by using a 5^{th}-order MUSCL scheme proposed by Kim and Kim [67], in conjunction with LMNT introduced by Thornber et al. [117]. The role of compressibility in the subsonic/transonic flow regime is studied by simulating the flow at different Mach numbers ($M = 0.1$ and $M = 0.8$). The main aim here is to shed some insight on modifications to separated and reattached flow behaviour. For this purpose, the mean flow, the Reynolds stresses and the turbulent kinetic energy are analysed. Moreover, the wall-pressure and the skin-friction coefficients along the top and bottom wall of the channel are measured, to determine the reattachment lengths of the primary and secondary vortices. Finally, calculations of the turbulent kinetic energy budget are carried out in order to examine the behaviour of the

shear layers (separation, growth rate and reattachment).

To the best of the author's knowledge, neither experimental nor numerical studies for compressible flow over the sudden expansion geometry have been undertaken in the past. Previous studies on separated and suddenly-expanded flows were mainly focused on the incompressible regime. Some of those studies related to the backward-facing step and sudden expansion configuration were addressed in Chapter 1. In the present study the same geometry as that used in preceding sections to investigate the turbulence behaviour of a flow over a planar sudden expansion at low Mach number ($M = 0.1$) is utilised. Note that the ratio of the main channel length to the inlet channel length is 3 ($ER = D/d = 3$), whereas the aspect ratio is 5 ($AR = w/h = 5$). The streamwise length (L) is $84h$ including an inlet section $L_i = 4h$, where the step height h is taken as 1. Moreover, the total height in the y-direction is $3h$, while the spanwise extent is taken to be $5h$. The co-ordinate system along with the geometric characteristics of the sudden expansion geometry are represented in Figure 4.1. This chapter is organised as follows: In Section 6.2, a grid convergence study is performed in order to validate the numerical methodology used in the simulations. The flow physics and the flow topology are discussed in Section 6.3, by calculating the turbulent kinetic energy budget in several streamwise locations downstream of the expansion. Finally, the most important findings of this study are summarised in Section 6.4.

6.2 Convergence Study

The purpose of this section is to validate the numerical method used in the simulations by means of three different grid meshes. The total number of grid points, the spatial increments in the three directions (x, y, z), as well as the grid-clustering approach employed in the present study were discussed in Chapter 4. The total number of blocks used to run the simulations in parallel mode were 13, 30 and 60 for the coarse (grid 1), medium (grid 2) and fine grid (grid 3), respectively.

For all the grid meshes under investigation, the ratio of the distance of a wavelike disturbance that travels in a time step to the grid size (CFL number) is taken equal to 1. This leads to an average time step $\Delta t_1 \simeq 3.42 \cdot 10^{-5}$, $\Delta t_2 \simeq 2.27 \cdot 10^{-5}$ and $\Delta t_3 \simeq 2.24 \cdot 10^{-5}$ for grid 1, grid 2 and grid 3, respectively. Note, however, that in all the simulations conducted in this study the computational time per time step is not uniform (its values are very close to the average time step described above for the three different

grids under study, though). The time required for a fluid particle to pass through the whole computational domain, is given by L/U_∞, where U_∞ is the reference flow velocity and L is the total length of the channel (including the inlet domain). The reference velocity is given by the following relation:

$$U_{ref} = Ma\sqrt{\frac{P_{ref}\gamma}{\rho_{ref}}} = 0.8\sqrt{\frac{10^5 \times 1.4}{1}} \simeq 299.3\,\frac{m}{s} \tag{6.1}$$

Thus, the non-dimensional time that is needed for the flow to traverse the physical domain is

$$t = \frac{L}{U_{ref}} = \frac{84}{299.3} \simeq 0.28$$

It is also important to mention that the inlet conditions for the calculations of a compressible flow, in terms of the density and pressure, were different compared to those for an incompressible flow discussed in Chapter 4. Thus, the isentropic relations were taken into account for a flow at $M = 0.8$. According to them, the total-to-static ratios of density and pressure can be written as follows.

$$\frac{\rho_0}{\rho} = \left(1 + \frac{\gamma-1}{2}M^2\right)^{1/(\gamma-1)} = 1.351$$

$$\frac{p_0}{p} = \left(1 + \frac{\gamma-1}{2}M^2\right)^{\gamma/(\gamma-1)} = 1.524$$

The corresponding energy equation is given by:

$$E_0 = \frac{p_0}{\gamma-1} + \frac{1}{2}\rho_0\left(u_0^2 + \upsilon_0^2 + w_0^2\right)$$

The simulation is run for approximately 15 flow-trough-times (i.e., $\simeq 4.2$ non-dimensional time) to reach a statistically steady state. The mean and fluctuating flow properties are then computed for over 15 more flow-through times, and finally another 10 flow-through times are used to compute the higher-order statistics (turbulent kinetic energy, skewness, kurtosis).

The size of the mean reattachment vortices in the near wall regions of the channel is used as a key measure for determining the accuracy of the sudden-expansion calculations.

This parameter has been used in several studies dealing with separated and suddenly-expanded flows so as to validate the numerical approach to the problem. A comprehensive discussion on the reattachment lengths of these particular flows, found in the literature, was addressed in Chapter 4. The size of the recirculation area is characterised by the reattachment length, x_R. The reattachment length is defined as the distance from the wall (either the top or bottom wall of the channel, where recirculation vortices are formed) to the point where the wall shear stress or the velocity gradient with respect to the transverse direction are zero ($\tau_w = 0$ or $dU/dy = 0$). The reattachment point can be easily identified by means of the derivative dU/dy, which is defined as the change of the velocity in the streamwise direction with respect to y at the wall. At the wall, separated flow will give a negative dU/dy, whereas reattached flow has a positive dU/dy value. The location where the derivative is zero defines the reattachment point of the flow.

The streamlines of the time-averaged flow field inside the sudden expansion configuration for the three different grids are shown in Figure 6.1. It is noteworthy the fact that in all the three cases the flow appeared to bend upwards forming two recirculation areas of unequal size length in the near-wall region, with the shorter reattachment being close to the top wall and the larger one close to the bottom wall of the channel. The high-velocity core flow emanating from the step, keeps its trajectory several step heights downstream before impinging to the upper wall of the channel, changing that way direction and velocity magnitude (i.e., the streamwise velocity magnitude gradually decreases from the free-stream value as the flow approaches the upper wall).

However, it can be said that the reattachment lengths of the primary and secondary vortices are different among the three grid meshes used in the present study. It is evident that the size of the shorter reattachment decreases in length with increasing grid resolution. The opposite trend is observed for the larger recirculation zone, where its size increases with increasing grid resolution. This last observation is also ascertained by the evaluation of the locations where the mean streamwise velocity component $\langle U \rangle$ changes sign. The results of the mean positions of primary separation (L_1 and L_2) and secondary reattachment (L_3 and L_4) are presented in Table 6.1. As there is no experimental data to compare with, the sizes of the recirculation zones are compared against those addressed in Chapter 4 for an incompressible turbulent flow at $M = 0.1$ and $Re = 10^4$ (only the results obtained by the fine grid are presented).

It is evident that the free-stream Mach number has a significant effect on the reattachment locations of the two vortices in the near-wall region. Particularly, the reattachment

location of the shorter recirculation zone is closer to the step for the lower Mach number. However, this difference is not so substantial compared with that found for the reattachment length of the larger recirculation vortex between the two test cases. To be more specific, at $M = 0.8$ its length appears to be approximately 12.8% and 9.5% larger than that at $M = 0.1$ for the numerical and experimental case [17], respectively. The corresponding difference in terms of the length of the shorter reattachment is about 2.6% and 4.6%. The lengths of the secondary vortices are of about the same order of the step height h. In Section 6.3, the physical origin of the variation in reattachment length with Mach number will be addressed.

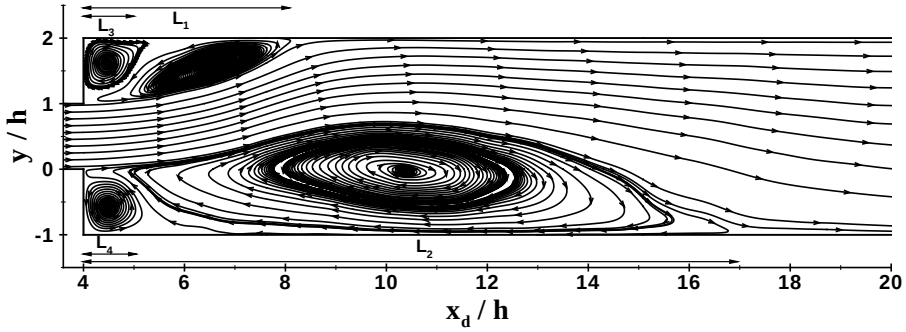

(a) Coarse Grid

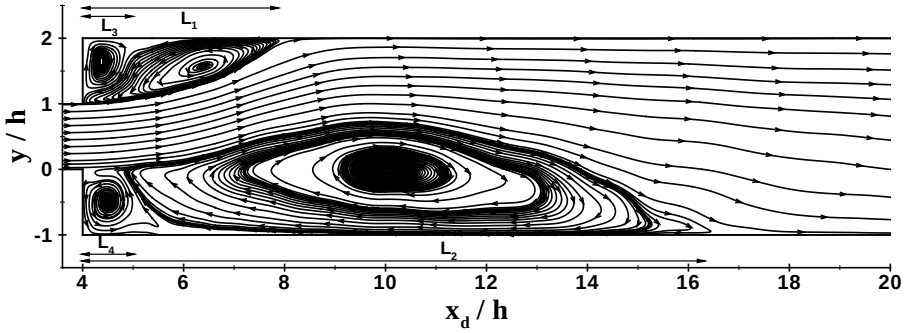

(b) Medium Grid

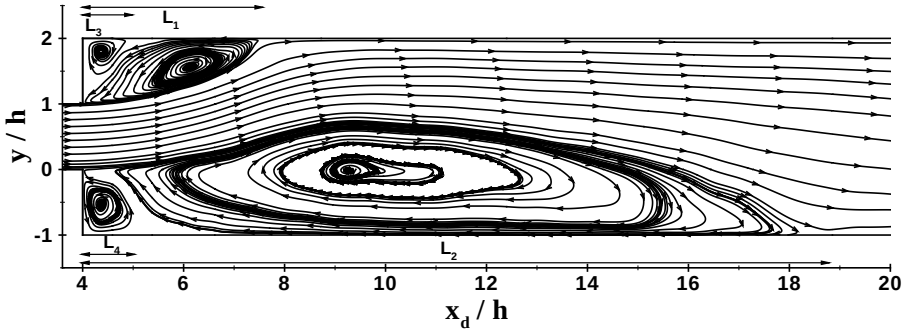

(c) Fine Grid

FIGURE 6.1: Streamlines of the mean flow at the center plane of the channel ($z/h = 2.5$) for three different grid meshes at $Re = 10^4$ and $M = 0.8$.

TABLE 6.1: Reattachment lengths of three different grid meshes at $M = 0.8$ and $Re = 10^4$ for the 5^{th}-order MUSCL scheme.

Grid	L_1/h	L_2/h	L_3/h	L_4/h
Coarse	4.12	13.06	1.25	1.08
Medium	3.93	13.16	0.88	1.01
Fine	3.51	15.88	0.79	0.98
ILES - ($M = 0.1$)	3.42	13.85	0.51	0.93

The mean streamwise and transverse velocities at three different wall-normal locations along the $x-$direction are shown in Figure 6.2. In the region of the shorter reattachment, at $y/h = 1.5$, all the three grids agree reasonably well with each other. There is only a small difference in grid 1, where the mean velocity profile (in both cases) is slightly shifted downstream. This last observation can be explained by the fact that the reattachment length of the shorter recirculation zone for grid 1 is larger compared to its counterparts, resulting in the reduction of the growth rate of the shear layer (see Table 6.1). In the high-velocity core flow region at the centerline of the channel, the mean flow is well resolved even with the lowest grid resolution. The curves of the mean velocity profiles match very well with each other, which indicates that the solution in that specific region has been successfully converged. The magnitude of the streamwise velocity component at $M = 0.8$ is, in general, higher than that found at a lower Mach number. The physical difference between the two Mach numbers under investigation is obviously compressibility. This argument is further supported in Figure 6.3, where the Favre averaged velocities for different Mach numbers are plotted. It can be said, therefore, that as the Mach number increases the averaged flow quantities can be significantly altered for the sudden expansion geometry.

The mean velocity profiles in the region of the larger recirculation zone ($y/h = -0.5$) are in fair agreement with each other. The maximum absolute value of the streamwise velocity at $x/h \simeq 6$ is approximately the same among the three grid meshes ($|U_{max}| \simeq 0.25$). However, a moderate discrepancy is observed between grid 3 and its counterparts close to the reattachment location and beyond that point, as the magnitude of the backflow for grid 3 remains high for a larger downstream distance.

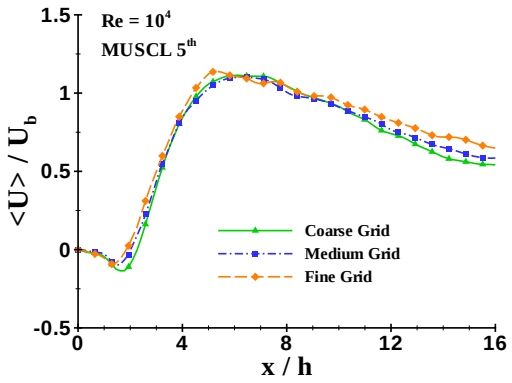

(a) U Velocity profile at Y = 1.5h

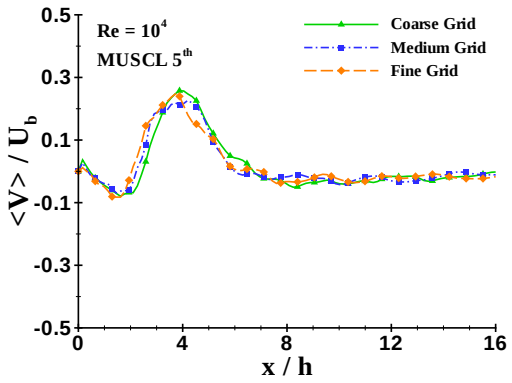

(b) V Velocity profile at Y = 1.5h

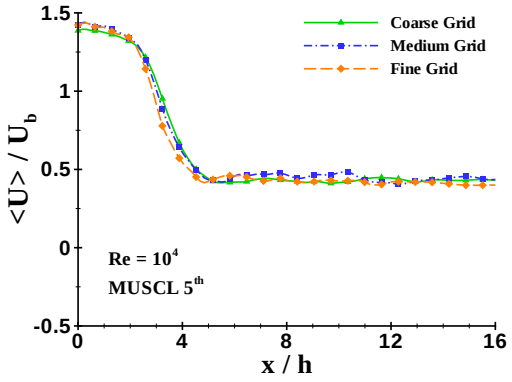

(c) U Velocity profile at Y = 0.5h

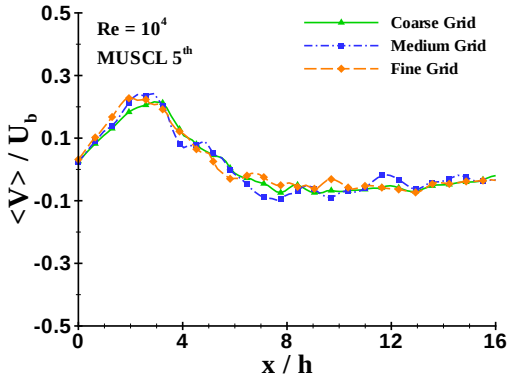

(d) V Velocity profile at Y = 0.5h

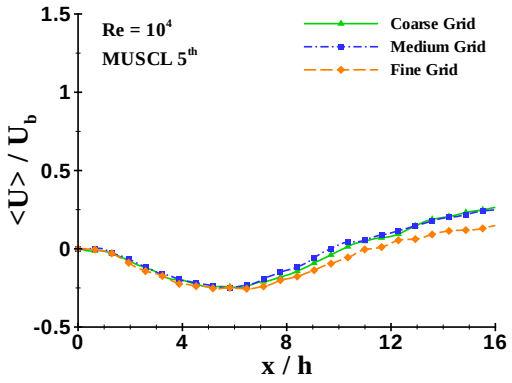

(e) U Velocity profile at Y = -0.5h

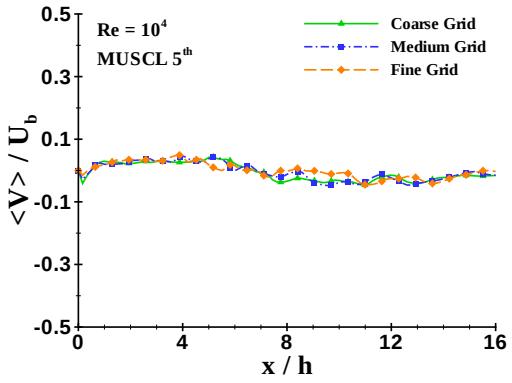

(f) V Velocity profile at Y = -0.5h

FIGURE 6.2: Time-averaged streamwise and transverse velocities along the x-axis (xy-plane) at $Re = 10^4$ and $M = 0.8$.

The magnitude of the wall-normal velocity is negative immediately after the step, and

close to the upstream wall in the streamwise range $x/h \simeq 0-1$. Further downstream, the mean transverse velocity takes values around zero, indicating that there is no significant vertical variation in the region of the larger reattachment.

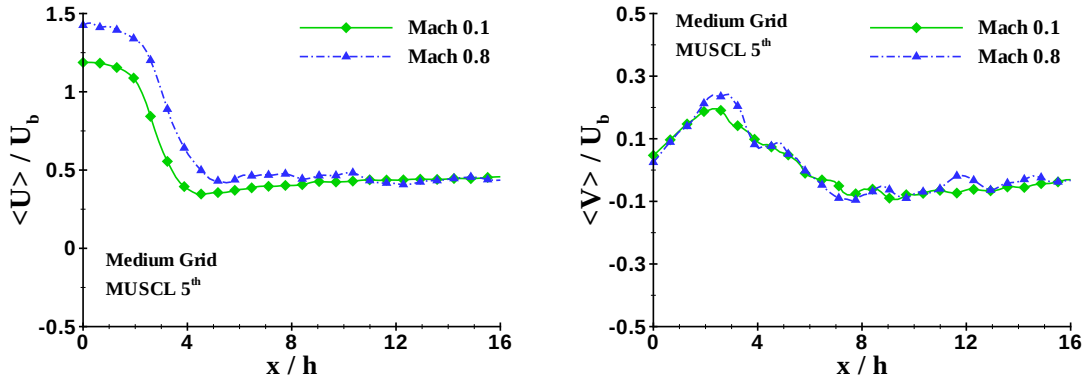

(a) Streamwise velocity (b) Wall-normal velocity

FIGURE 6.3: Time-averaged streamwise and wall-normal velocity profiles for two different flow regimes ($M = 0.1$ and $M = 0.8$) at $y/h = 0.5$ (centerline) using M5.

The rms velocity fluctuations (axial, u', and transverse, v') measured in three different locations in the xy-plane, are provided in Figure 6.4. It is known that in turbulent shear flows the second-order turbulent statistics are harder to predict than the averaged flow quantities (first-order statistics). For this reason, the numerical simulations were run for a reasonable amount of time so as for the flow to reach a statistically steady state.

The results indicate that the mean flow is well resolved, as grid 2 is, in general, closer to grid 3 than to grid 1. It is observed that the turbulence intensities exhibit a high turbulence level immediately downstream of the expansion. This high-turbulence zone is caused by the locally high mean-shear-rate in the region of the shear layers originating from the step. The mean fluctuating velocities, then, take their maximum values in the regions where the measurement lines cross the shear layers. This last feature is mostly prominent in the region towards the shorter recirculation zone at approximately 4 step heights downstream of the step. In these regions the flow exhibits the usual shear-flow anisotropy, with the streamwise velocity component being considerably larger than the transverse one.

The flow anisotropy was also observed in Chapter 4 for a turbulent incompressible flow over the sudden expansion configuration. However, the difference here between the two fluctuating velocity components is found to be much stronger. The flow anisotropy

of the mean normal stresses $\left(\left\langle u'u'\right\rangle, \left\langle v'v'\right\rangle, \left\langle w'w'\right\rangle\right)$ will be studied in the next section by means of the Reynolds stress anisotropy, in an attempt to investigate the turbulence behaviour in the shear-layer regions.

In Figure 6.5, the time-averaged Reynolds shear stress, $-\left\langle u'v'\right\rangle$, along with the turbulent kinetic energy, k, are shown. In the region of the shorter reattachment the maximum shear stress magnitude is observed at approximately $3.5h$ downstream of the step. At this specific location the turbulent kinetic energy takes its maximum value, which is consistent with the peak values detected there for the fluctuating velocity components u' and v', as shown in Figure 6.4. It is evident that grid 2 is in a very good agreement with grid 3, whereas grid 1 seems to underestimate both mean flow quantities. This last observation is mainly attributed to the poor mesh resolution provided by grid 1, resulting in the underprediction of the r.m.s. velocities, which in turn leads to lower magnitudes of the Reynolds shear stress and turbulent kinetic energy components.

The Reynolds shear stress in the region of the high-velocity core flow and that of the larger reattachment turns out to be almost identical for the three grids examined. However, this is not the case for the turbulent kinetic energy, where moderate variations of their peak intensity in the centerline of the channel at about $x/h \simeq 4$ were observed. Here again, grid 2 is much closer to grid 3 than to grid 1, which indicates that the solution is successfully converged in that particular measurement line. It is also important to underline that Mach 0.1 has significantly lower turbulent kinetic energy for $x/h \simeq 4$ compared to $M = 0.8$. For example at this location ($x/h = 4$ and $y/h = 0.5$) Mach 0.8 has a peak value of $\simeq 0.1$, whereas the peak for Mach 0.1 is only $\simeq 0.06$. This is, however, as expected, since the turbulence intensities are much higher for the larger Mach number.

The contour lines of the shear stress, in Figure 6.6, reveal two large flow regions of positive and negative $\left\langle u'v'\right\rangle$ in the upper and lower parts of the channel, respectively. The maximum absolute shear stress is observed in the region of the shorter reattachment close to the upper wall of the channel and at approximately $3h$ downstream of the constriction. On the other hand, turbulent kinetic energy contour lines show two high turbulence areas in the location of the shear layers immediately after the step. The turbulent kinetic energy magnitude appeared to be slightly higher across the upper shear layer. The same flow feature was also observed in Chapter 4 for an incompressible turbulent flow at $M = 0.1$, at considerably lower peak values, though. The increase in turbulent kinetic energy with Mach number, implies that the separated shear layer goes into transition earlier and hereupon grows faster as the free-stream Mach number is increased.

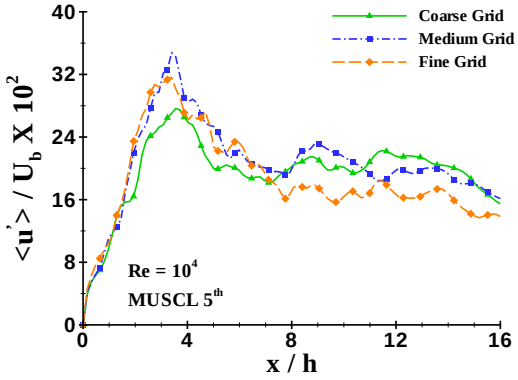

(a) U r.m.s. Velocity profile at Y = 1.5h

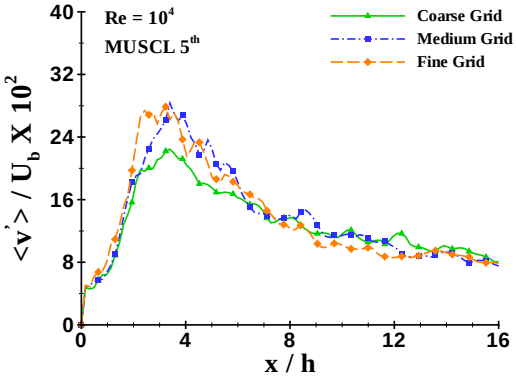

(b) V r.m.s. Velocity profile at Y = 1.5h

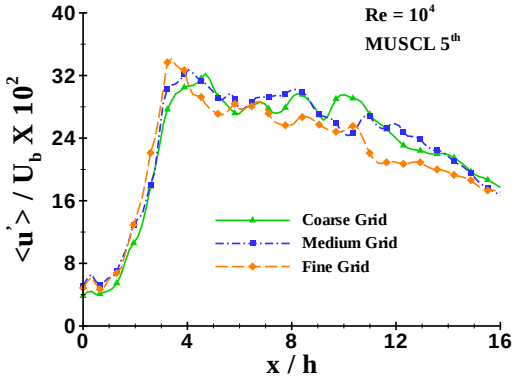

(c) U r.m.s. Velocity profile at Y = 0.5h

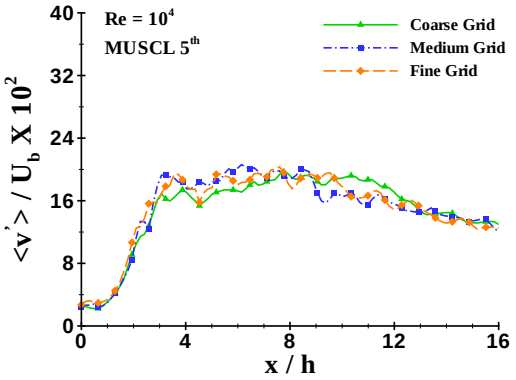

(d) V r.m.s. Velocity profile at Y = 0.5h

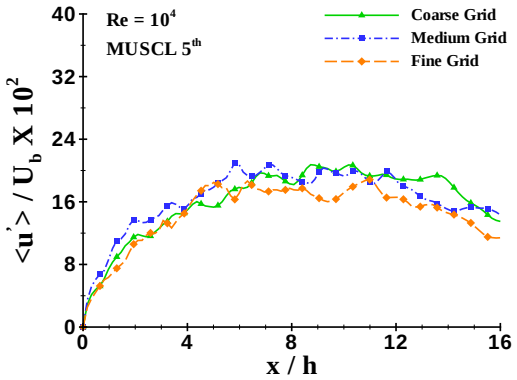

(e) U r.m.s. Velocity profile at Y = -0.5h

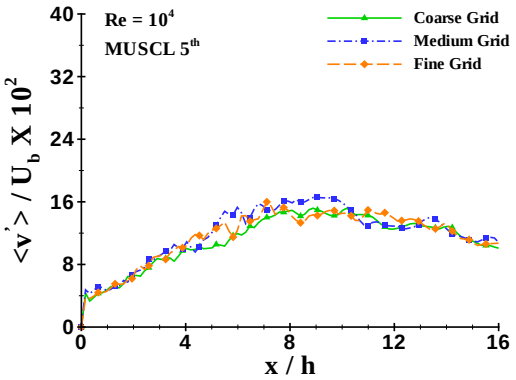

(f) V r.m.s. Velocity profile at Y = -0.5h

FIGURE 6.4: Time-averaged streamwise and transverse r.m.s. velocities along the x-axis (xy-plane) at $Re = 10^4$ and $M = 0.8$.

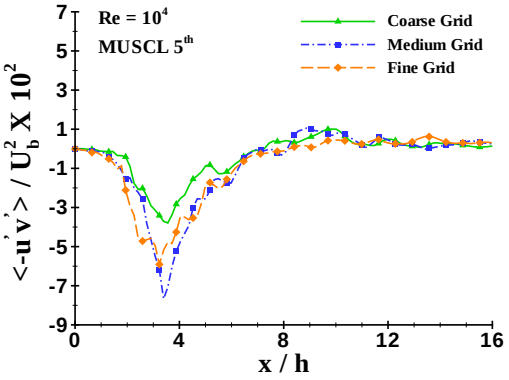

(a) Reynolds stress profile of u'v' at Y = 1.5h

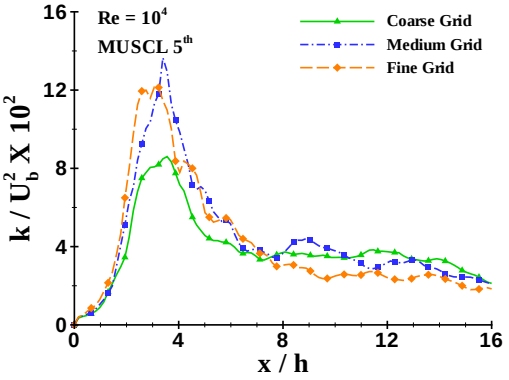

(b) Turbulent kinetic energy profile at Y = 1.5h

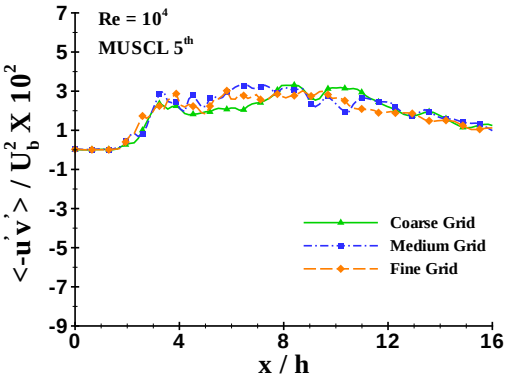

(c) Reynolds stress profile of u'v' at Y = 0.5h

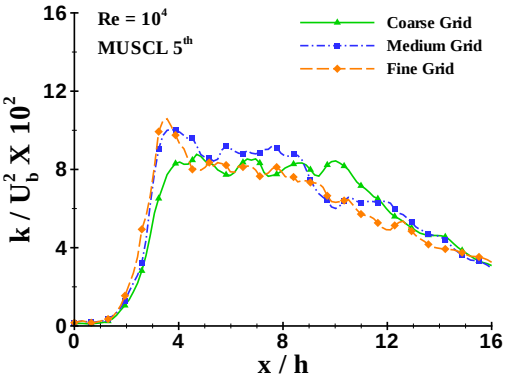

(d) Turbulent kinetic energy profile at Y = 0.5h

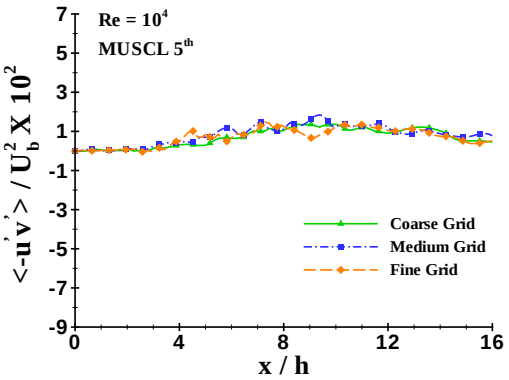

(e) Reynolds stress profile of u'v' at Y = -0.5h

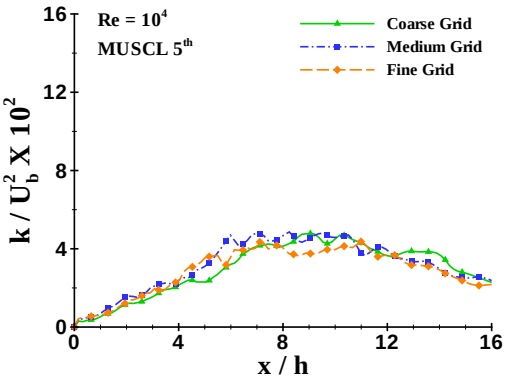

(f) Turbulent kinetic energy profile at Y = -0.5h

FIGURE 6.5: Time-averaged Reynolds stresses and turbulent kinetic energy along the x-axis (xy-plane) at $Re = 10^4$ and $M = 0.8$.

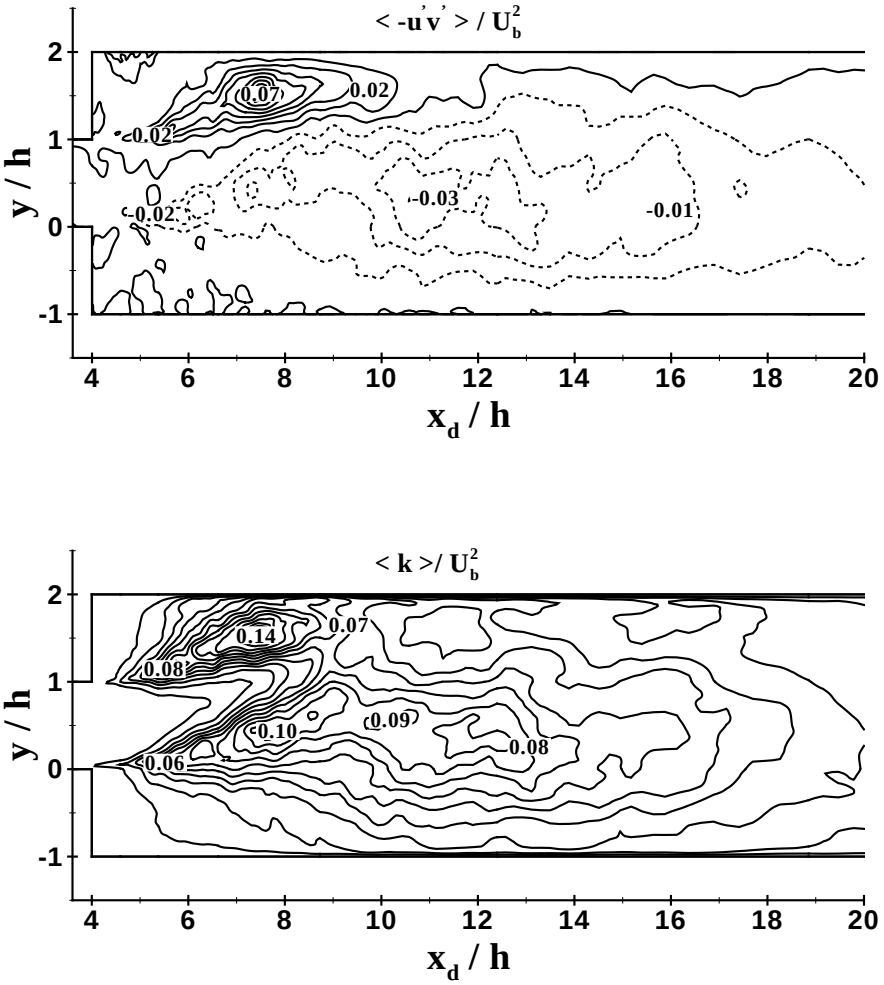

FIGURE 6.6: Contour lines (dotted lines for negative values; solid lines for positive values) of the time-averaged Reynolds shear stress and turbulent kinetic energy in the *xy*-midplane normalised by U_b^2.

Figure 6.7 shows the averaged wall pressure, C_P, and wall skin-friction coefficient, C_F, along the upper and lower part of the wall up to 30 step heights downstream of the step. It is taken as granted here that the high-velocity core flow originating from the inlet channel upstream of the step bends upwards, forming two recirculation zones of different size with the larger one taking place on the bottom wall and the shorter one on the opposite wall of the channel. These two flow quantities are of great importance when dealing with separated and reattached flows, as their values can determine the size of the primary and secondary reattachment lengths along the lower and upper part of

a sudden expansion geometry. The local wall pressure coefficient primarily decreases toward a local minimum immediately after the step and beneath the core flow region of the primary separation zones (i.e., near the location of the maximum backflow on each wall). Besides, a significant negative value is observed at the upper wall, and particularly in the range $x/h \simeq 0-3$. Further downstream and on the lower part of the channel the pressure gradually recovers, reaching a constant value.

On the other hand, along the upper-side wall, the pressure coefficient exhibits a local maximum and a second local minimum at streamwise positions of about $x/h \simeq 4.5$ and $x/h \simeq 6.5$, from the upper step, respectively. Note that the local pressure maximum on the upper wall almost coincides with the reattachment length of the shorter recirculation vortex. It can be also said that beyond $x/h \simeq 15$, the curves collapse, which indicates that the flow has recovered from the primarily shear layer instability.

As far as the wall-friction coefficient is concerned, the same peculiar behaviour as that observed at $M = 0.1$ is evident, confirming further the existence of the two secondary vortices at the corners of the wall. In the upper-wall region C_F exhibits a global maximum and a global minimum at $x/h \simeq 3$ and $x/h = 5.4$, respectively. The most important finding here is that the position where the wall skin friction coefficient changes sign, ($C_F = 0$), almost fits in with the reattachment location of the shorter vortex. To be more specific, the curve corresponding to grid 3 is shifted upstream, crossing the zero line in an earlier position than its counterparts (grid 2 follows and then grid 1). The reattachment lengths of the three grids demonstrated in Table 6.1 are in excellent agreement with the lengths arising from the wall skin-friction calculations. It was also observed that the maximum absolute value of C_F decreases in magnitude with increasing Mach number.

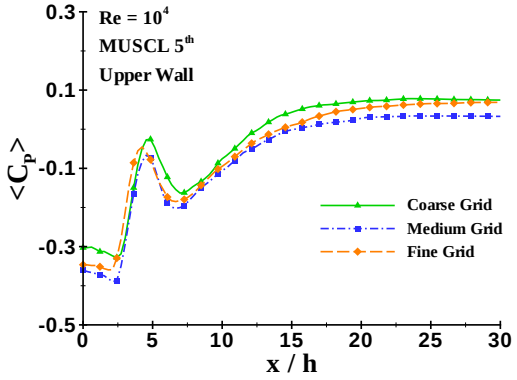

(a) Wall pressure coefficient along the upper wall

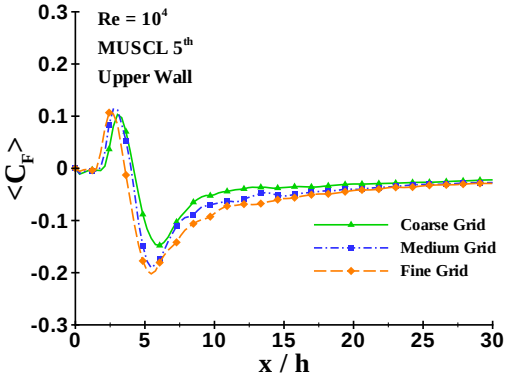

(b) Skin friction coefficient along the upper wall

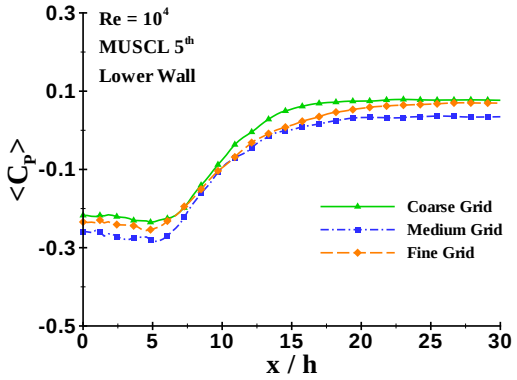

(c) Wall pressure coefficient along the lower wall

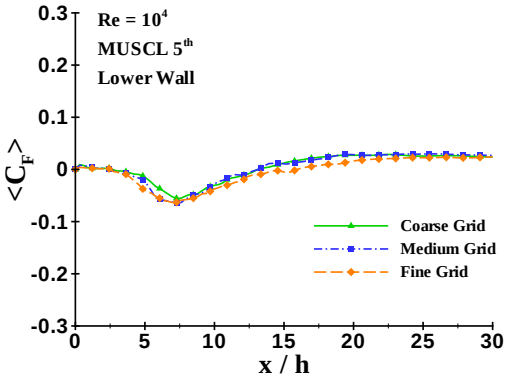

(d) Skin friction coefficient along the lower wall

FIGURE 6.7: Time-averaged pressure and skin friction coefficients along the upper and lower channel wall at $Re = 10^4$ and $M = 0.8$.

6.3 Flow Physics

Further to the previous discussions about turbulent flow statistics (fluctuating velocities and turbulent kinetic energy), in this section the evolution of the three normal stresses is addressed in an attempt to shed some light on the flow structure in the sudden expansion configuration. As already stated, the flow at the subsonic/transonic flow regime exhibit significant anisotropic behaviour, with the velocity fluctuations in the streamwise direction being considerably higher than those in the wall-normal one. Besides, the flow found to be more anisotropic with increasing Mach number, as the difference in magnitude between the streamwise and transverse velocity fluctuations is more intense at $M = 0.8$.

Calculations of the time-averaged normal stresses, $\overline{u'u'}, \overline{v'v'}, \overline{w'w'}$, at three measurement lines along the x-axis have been performed, using two different Reynolds numbers, as shown in Figure 6.8. The normal stresses were computed using the following formula:

$$\left\langle \rho u_i^{'} u_i^{'} \right\rangle \equiv \frac{1}{N} \sum_{n=1}^{N} [\rho (u_i - \overline{u_i})^2]$$

where $u_i = \{u, v, w\}$ is the instantaneous velocity vector.

The aim here is twofold: (a) to investigate the potential difference of the normal stresses in terms of their magnitudes, and (b) to study the influence of Re on the normal stress profiles inside the recirculation areas. It can be clearly seen that the mean streamwise normal stress, $\overline{u'u'}$, is the largest component for all the measurement positions examined. However, the streamwise evolution is similar for all the components. In the region of the shorter vortex, all the stress components increase up to approximately one step height before the reattachment, while further beyond that point a gradual reduction is followed, as the shear layer starts to reattach. A rapid decay of the normal stresses takes place in the recovery region up to $x/h \simeq 8$. Further downstream, their values turn out to be almost constant. In that particular region, $\overline{u'u'} > \overline{v'v'} > \overline{w'w'}$ for the case of $Re = 10^4$, whereas at $Re = 4 \cdot 10^4$ the spanwise normal stress component is slightly higher than the transverse one with $\overline{u'u'} > \overline{w'w'} > \overline{v'v'}$.

It is important to underline that the magnitudes of the normal stresses were found to be larger for the smaller Re under investigation, in all the measurement locations. A distinctly different evolution of the normal stresses was observed in the centerline of the channel, where, in both Re, the spanwise stress component turns out to be higher than the transverse one. The peak values of normal stresses in the high-velocity core flow region exhibit some significant variation between the two Re, with a percentage difference up to $\simeq 30\%$.

The structural changes of turbulence in shear flows are often studied by looking into the Reynolds stress anisotropy. The Reynolds stress anisotropy tensor, b_{ij}, which measures the departure of $\overline{u_i^{'} u_j^{'}}$ from isotropy (i.e., the complete lack of any directional preference), is given by the following expression:

$$b_{ij} = \frac{R_{ij} - \frac{2}{3} k \delta_{ij}}{2k} = \frac{R_{ij}}{2k} - \frac{1}{3}\delta_{ij} = \frac{\left\langle \rho u_i^{'} u_j^{'} \right\rangle}{\left\langle \rho u_l^{'} u_l^{'} \right\rangle} - \frac{1}{3}\delta_{ij} \tag{6.2}$$

where R_{ij} represents the Reynolds stresses, k is the turbulent kinetic energy, and δ_{ij} is the Kronecker delta given by:

$$\delta_{ij} = \begin{cases} 1, & if \quad i = j \\ \\ 0, & if \quad i \neq j \end{cases}$$

The turbulent kinetic energy can be written as follows:

$$k = \frac{R_{qq}}{2} = \frac{1}{2}\left\langle \rho u_l' u_l' \right\rangle = \frac{1}{2}\left(\left\langle \rho u' u' \right\rangle + \left\langle \rho v' v' \right\rangle + \left\langle \rho w' w' \right\rangle\right)$$

Thus the Reynolds stress anisotropy for the normal stresses can be obtained by:

$$\begin{aligned} b_{uu} &= \frac{\langle R_{uu}\rangle - \frac{2}{3}k}{2k} = \frac{\overline{\rho u' u'}}{2k} - \frac{1}{3} \\ \\ b_{vv} &= \frac{\langle R_{vv}\rangle - \frac{2}{3}k}{2k} = \frac{\overline{\rho v' v'}}{2k} - \frac{1}{3} \\ \\ b_{ww} &= \frac{\langle R_{ww}\rangle - \frac{2}{3}k}{2k} = \frac{\overline{\rho w' w'}}{2k} - \frac{1}{3} \end{aligned} \tag{6.3}$$

In Figure 6.9 the normal stress anisotropy at two streamwise locations ($x/h = 2$ and $x/h = 4$), is shown. Note that two different Re were used in order to examine further the influence of Re on the flow behaviour in the compressible regime. The anisotropy of wall-normal, $\overline{v'v'}$, and spanwise, $\overline{w'w'}$, stresses are larger in the near-wall region of the larger recirculation zone. On the other hand, the streamwise stress, $\overline{u'u'}$, becomes significant in the region close to the wall, in which the shorter reattachment is formed. In the shear layer regions (i.e., at $y/h = 0.2$ and $y/h = 1.2$) the anisotropy in all three stress components slightly increases with increasing Re. The maximum absolute values in the backflow region of the shorter recirculation vortex $1.3 < y/h < 1.9$ for b_{uu}, b_{vv} and b_{ww} are 0.17, 0.25 and 0.21, respectively for $Re = 10^4$. The corresponding values for $Re = 4 \cdot 10^4$ are 0.16, 0.21 and 0.19. Note also that the stress anisotropy tensor takes negative values almost everywhere in the flow field.

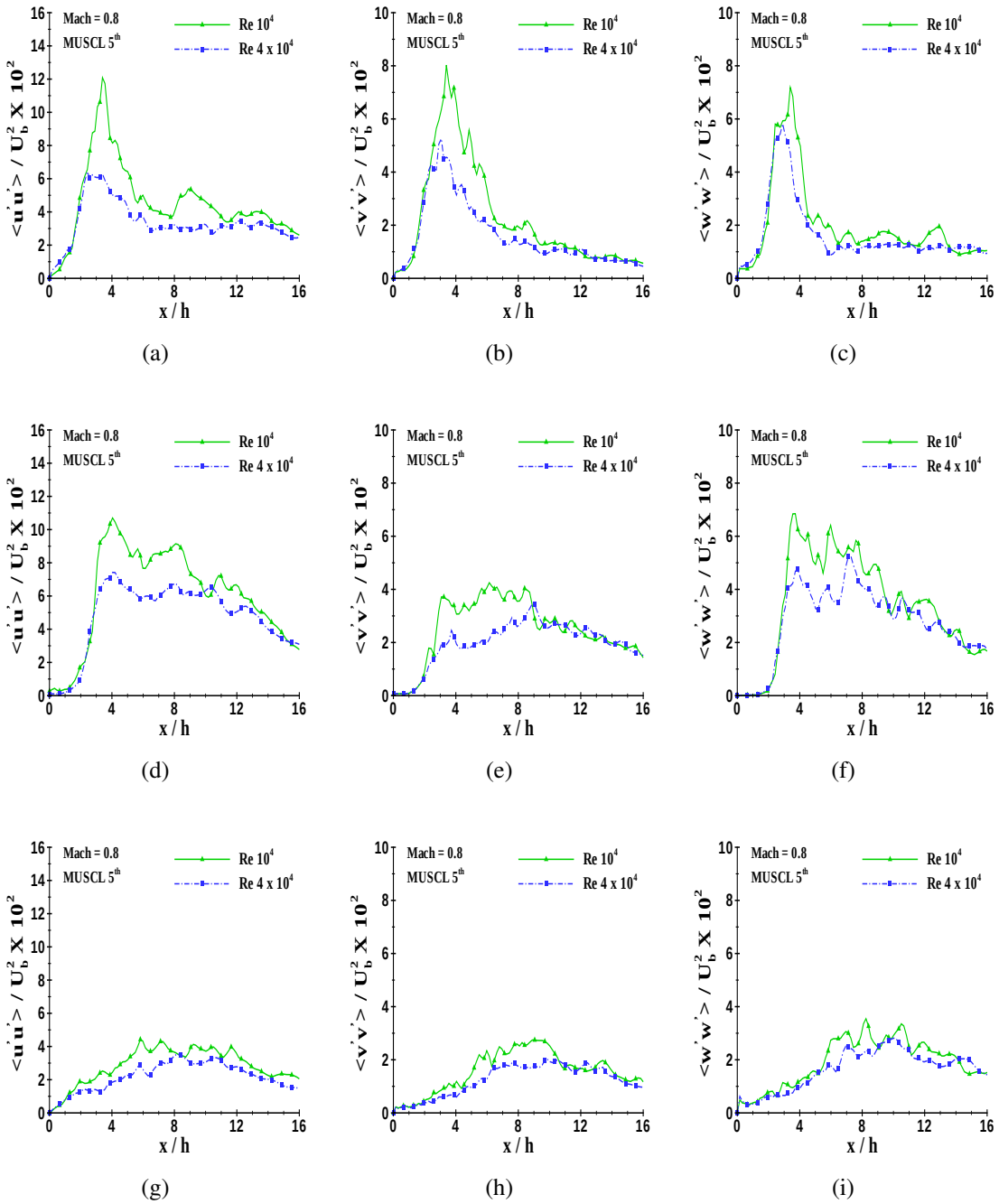

FIGURE 6.8: Streamwise evolution of mean normal stresses ($\overline{u'u'}, \overline{v'v'}, \overline{w'w'}$) at three wall-normal locations: (a),(b),(c) $y = 1.5h$, (d),(e),(f) $y = 0.5h$, and (g),(h),(i) $y = -0.5h$. Comparisons between $Re = 10^4$ and $Re = 4 \cdot 10^4$ at $M = 0.8$ are carried out.

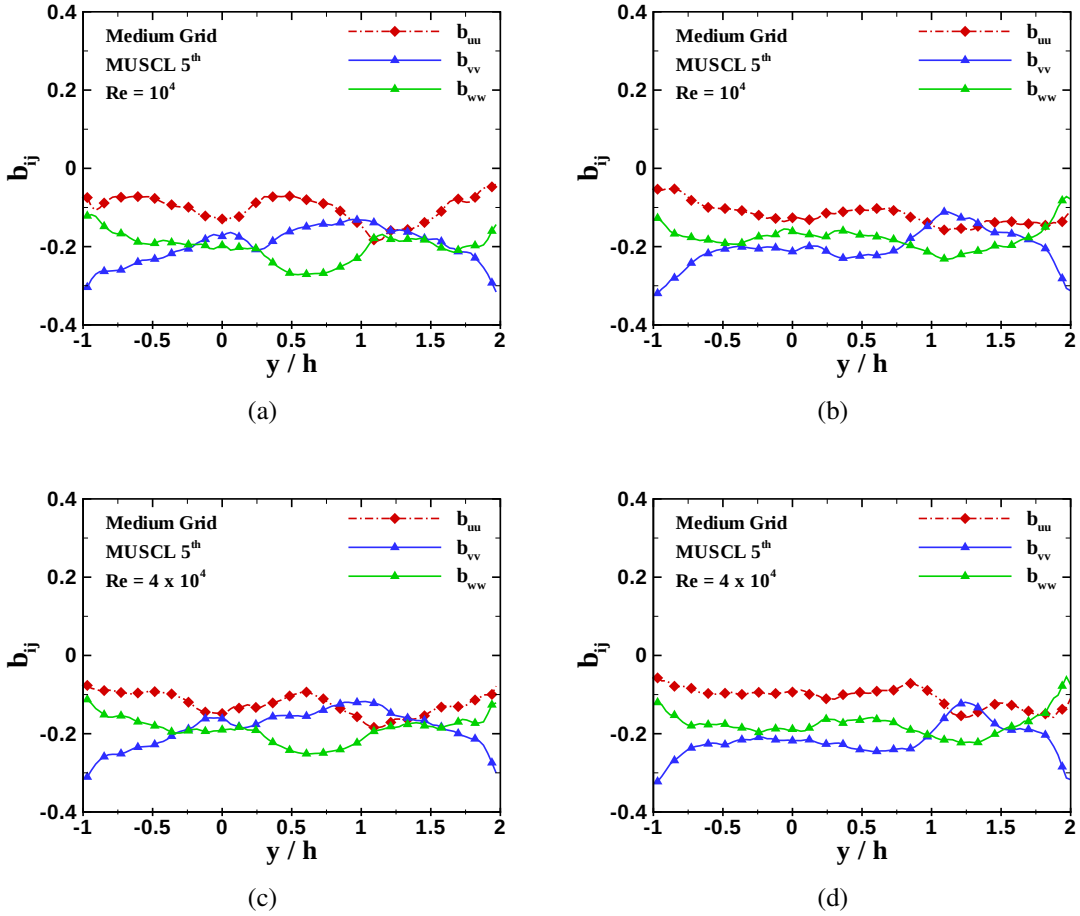

FIGURE 6.9: Anisotropy of normal stresses at (a),(c) $x/h = 2$ and (b),(d) $x/h = 4$ downstream of the step for two different Reynolds numbers at Mach 0.8.

The difference observed in the growth rate of the normal stresses and correspondingly in the growth rate of the turbulent kinetic energy can be explained by calculating the turbulent kinetic energy budget. The transport equation for the turbulent kinetic energy is derived by applying the Favre decomposition to the convective terms. The aim here is to reduce the convective terms to the same form as in the incompressible case. The Reynolds decomposition is applied to all the other terms involved in the turbulent kinetic energy budget. The resulting equation based on the research study of Huang et al. [57] for a compressible flow is as follows:

$$\frac{\partial k}{\partial t} = -\overline{U}_k \frac{\partial k}{\partial X_k} - \overline{\rho u_i'' u_k''} \frac{\partial \overline{U}_i}{\partial X_k} - \frac{\partial \overline{k'' u_k''}}{\partial X_k} - \nu \overline{\frac{\partial u_i''}{\partial X_k} \frac{\partial u_i''}{\partial X_k}} - \frac{\partial \overline{p'' u_i''}}{\partial X_i} + \nu \frac{\partial^2 k}{\partial X_k^2} \tag{6.4}$$

where k is the turbulent kinetic energy with $k = \frac{1}{2}\overline{\rho u_i' u_i'}$, and k' represents the fluctuating turbulent kinetic energy with $k' = \frac{1}{2}\rho u_i' u_i'$. The first term on the right-hand side of the above equation represents the turbulence convection; the second, energy production; the third, turbulent diffusion; the fourth, energy dissipation; the fifth, diffusion resulting from velocity-pressure interaction and the last one the viscous diffusion.

The turbulent kinetic budget terms calculated in three different streamwise locations along the wall-normal direction, are shown in Figure 6.10. These locations include the following flow regions: (a) the region immediately after the step at $x/h = 1$, (b) the re-circulation region corresponding to the shorter reattachment at $x/h = 2$, and (c) the recirculation region of the shorter reattachment and at the same time the backflow area of the larger vortex at $x/h = 5$. Note that all the concerned terms are normalised by the cube of the inlet bulk velocity over the characteristic length h, and then multiplied by 10^3. Furthermore, the results presented here were obtained using the 5^{th}-order MUSCL scheme at $Re = 4 \cdot 10^4$ and $M = 0.8$.

It can be said that at one step height downstream of the step the two most dominant terms in the energy budget are the turbulence production and the energy dissipation terms. The peak values of the aforementioned terms are found to be about the location of the two shear layer regions emanated from the step edges of the upstream channel. Considerable distribution to the energy budget is added by the turbulent diffusion and velocity-pressure correlation terms, especially away from the shear layers and towards the channel walls. Moreover, in the near-wall regions where the turbulence production is negligible, the energy dissipation term seems to be balanced by the viscous diffusion. Finally, the turbulence convection term contributes negatively to the energy budget. It is evident that the turbulence production, the turbulence convection along with the velocity-pressure interaction decrease in magnitude with increasing downstream distance. On the other hand, energy dissipation, viscous diffusion and turbulent diffusion increase with downstream distance. It is also important to underline that close to the reattachment location, the turbulence convection starts to contribute positively to the energy budget. This last phenomenon was also observed at the lower Mach number ($M = 0.1$). However, in the incompressible flow regime this last feature is not so prominent as, in general, the convection term remains negative throughout the computational domain. Most of the above flow properties and effects seem to attenuate with distance, as the magnitudes of the energy budget terms reduce considerably. Nevertheless, at $x/h = 5$ the energy dissipation and the viscous diffusion terms increase in magnitude close to the top and bottom wall of

the channel, as shown in Figure 6.10(c).

A more comprehensive study of each individual energy budget component is presented below, for two different flow regimes ($M = 0.1$ and $M = 0.8$) at $Re = 4 \cdot 10^4$. Note that all the calculations here were performed on grid 2, as the difference between grid 2 and grid 3 in terms of the mean flow statistics is not significant (the grid convergence study for the case of $Re = 4 \cdot 10^4$ is addressed in Appendix B).

The profiles of turbulent convection and production in three different downstream locations are presented in Figure 6.11. It can be clearly seen that the production increases with increase in Mach number up to $x/h = 2$. At $x/h = 5$ both cases $M = 0.1$ and $M = 0.8$ have similar profiles with their values being considerably lower than those detected close to the channel step. As the shear layers impinge on the top and bottom wall in the reattachment region, the swirly structures break up, resulting that way in the decrease of turbulent production. It is also evident that the rate at which turbulent production decreases at $M = 0.8$ is much higher than that at the lower Mach number under investigation.

As shown in Figures 6.11(a), 6.11(c), 6.11(e), the influence of the Mach number on the convection term is rather weak. It is evident that in both cases the convection term contributes negatively to the turbulent kinetic energy budget, which means that energy is removed from the mean flow and is diffused along the cross-stream direction. At $x/h = 1$, convection peaks at the high-speed side of the shear layers originating from the step edges, with the one closer to the shorter recirculation zone being higher than that located at the opposite wall. Moreover, the two curves match quite well in all the three measurement lines, with a small variation being detected at $x/h = 2$. Further downstream, the contribution of the convective term to the energy budget, in both cases, turns out to be low. It can be also seen that at this particular location, turbulent convection becomes positive with its magnitude being rather small along the wall-normal direction. Finally, in the near-wall region the magnitude of the turbulent convection is zero.

The energy dissipation and the viscous diffusion terms at two different Mach numbers are plotted in Figure 6.12. The peak values of the energy dissipation about the location of the two shear layers (i.e., the same location where the peak values of turbulent production were observed) found to be more than two times higher for the case of $M = 0.8$. This is mainly attributed to the larger peak values of turbulence production detected in that particular flow area for the larger Mach number. This last feature is present at $x/h = 1$ and $x/h = 2$, whereas farther downstream (at $x/h = 5$) the two curves collapse with their magnitudes approaching zero.

In the near-wall region, however, the opposite trend is observed. Specifically, the magnitude of the energy dissipation increases close to the upper and lower wall with increasing downstream distance. As far as the viscous diffusion term is concerned, it can be clearly seen that its contribution to the turbulent kinetic energy budget of the flow is almost negligible. However, immediately downstream of the step, its magnitude in the region of the free shear layers cannot be considered as totally negligible. Furthermore, in the near-wall region viscous diffusion has a dominant role as it balances the energy dissipation. In that particular location its peak value increases with increasing streamwise distance. Comparisons between $M = 0.1$ and $M = 0.8$ reveals that the influence of Mach number on the viscous diffusion along the cross-stream direction is not substantial, apart from the region close to the wall where the peak value of viscous diffusion at $M = 0.8$ is considerably higher than that observed at lower Mach number.

Figure 6.13 shows the turbulent transport quantities of the energy budget, and particularly the turbulent diffusion and the velocity-pressure correlation terms in the recirculation and reattachment regions. It can be clearly seen that the wall-normal profiles of turbulent diffusion have distinct crest and trough. The negative values at the bottom half of each shear layer indicate that energy is subtracted from the region, and transferred to the near-wall region, as well as to the top half of each shear layer. Comparisons of the profiles at three different streamwise locations, shows that as the shear layer grows, the region over which turbulent diffusion takes place widens in the wall-normal direction. Moreover, the turbulent diffusion profiles of the two Mach numbers examined, exhibit similar trend with their peak values at $M = 0.8$ being slightly higher than those at $M = 0.1$, as expected. It is important also to underline that at the reattachment location ($x/h = 5$) of the shorter recirculation vortex, the two turbulent diffusion profiles are in excellent agreement with each other.

In Figure 6.13, the diffusion due to velocity-pressure interaction is also shown, in the recirculation and reattachment regions. In turbulence modelling of compressible flows, the velocity-pressure diffusion term is usually neglected [129]. However, in the present study results revealed that the magnitude of the aforementioned term is comparable to turbulent diffusion term, and therefore its omission can lead to significant modelling errors. Pressure diffusion exhibits similar behaviour as that of turbulent diffusion, in the sense that there is a change from negative diffusion to positive diffusion, particularly in the region immediately downstream of the constriction and in the recirculation region (at

$x/h = 1$ and $x/h = 2$). The effect of compressibility on the pressure diffusion term cannot be considered as significant. Small variations occur mainly in the vortex core of the shorter reattachment.

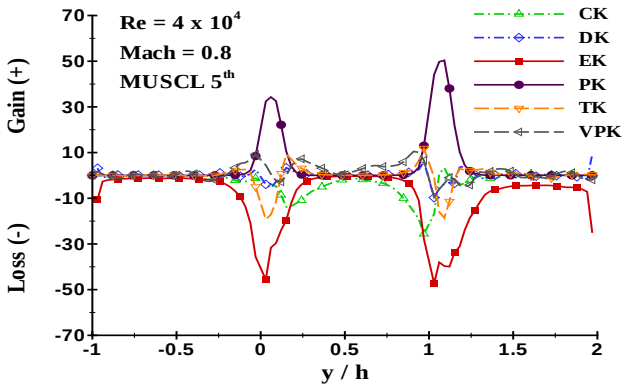

(a)

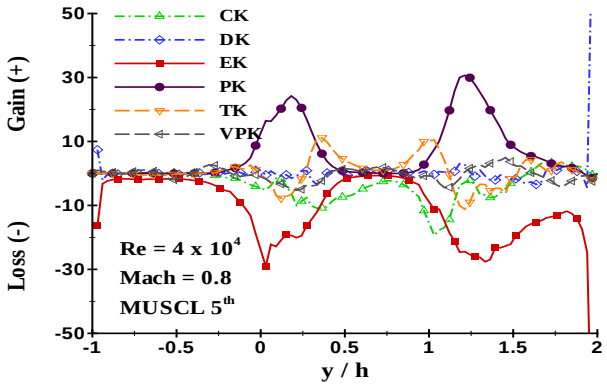

(b)

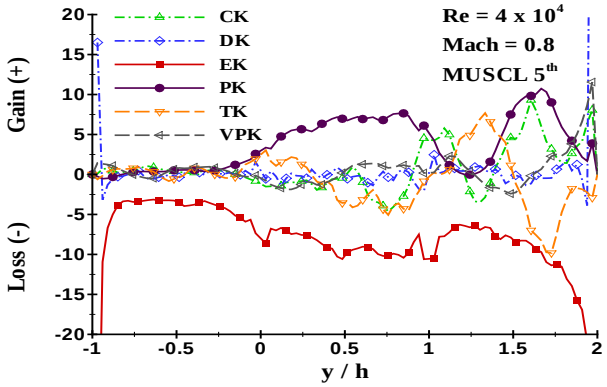

(c)

FIGURE 6.10: Turbulent kinetic energy budget terms across the wall-normal direction at three different streamwise locations downstream of the expansion: (a) $x = 1h$, (b) $x = 2h$, (c) $x = 5h$. All budget terms are normalised by U_b^3/h.

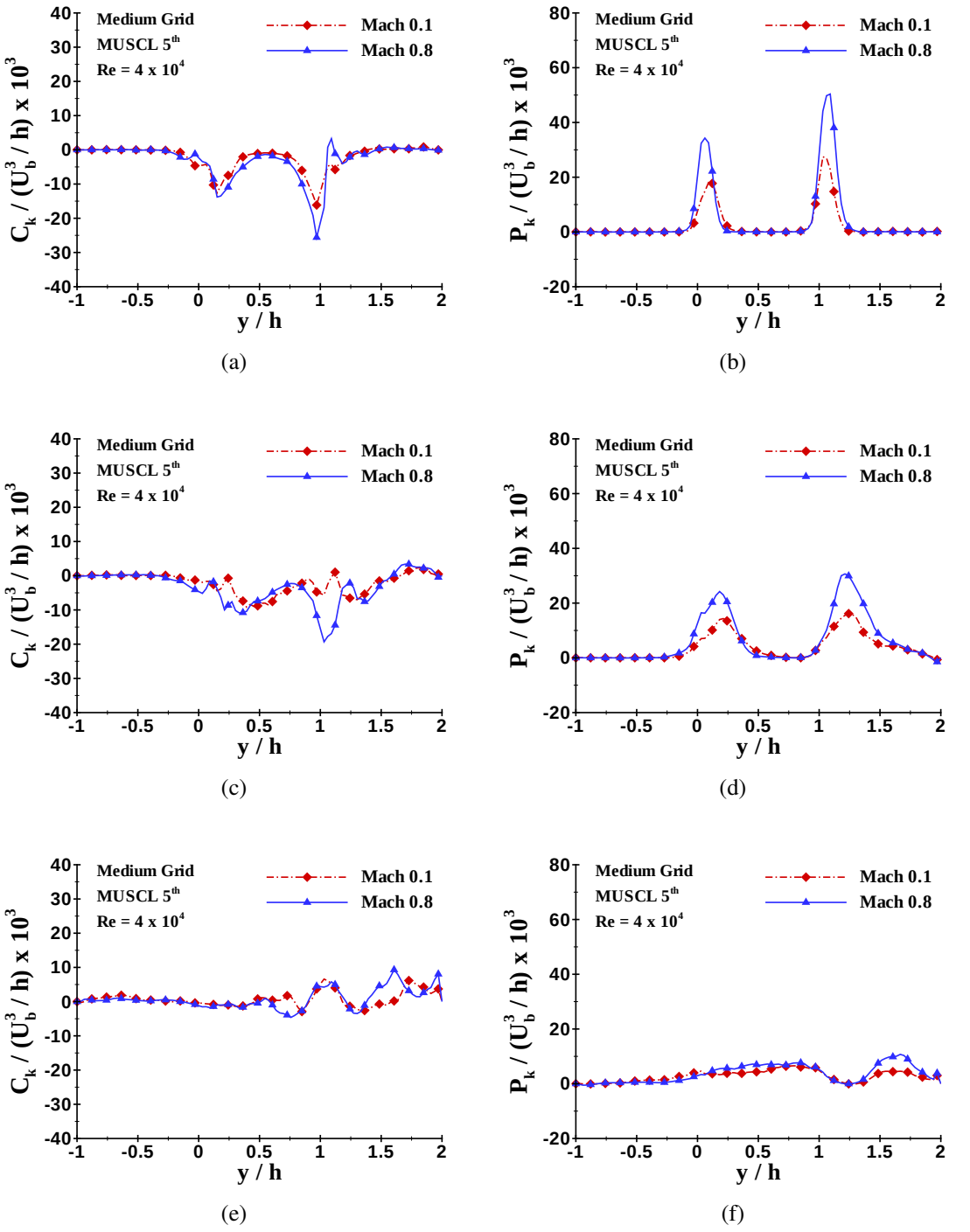

FIGURE 6.11: Convection term and Production of turbulent kinetic energy at (a),(b) $x/h = 1$, (c),(d) $x/h = 2$, (e),(f) $x/h = 5$ downstream of the step, for two different Mach number regimes ($M = 0.1$ and $M = 0.8$) at $Re = 4 \cdot 10^4$.

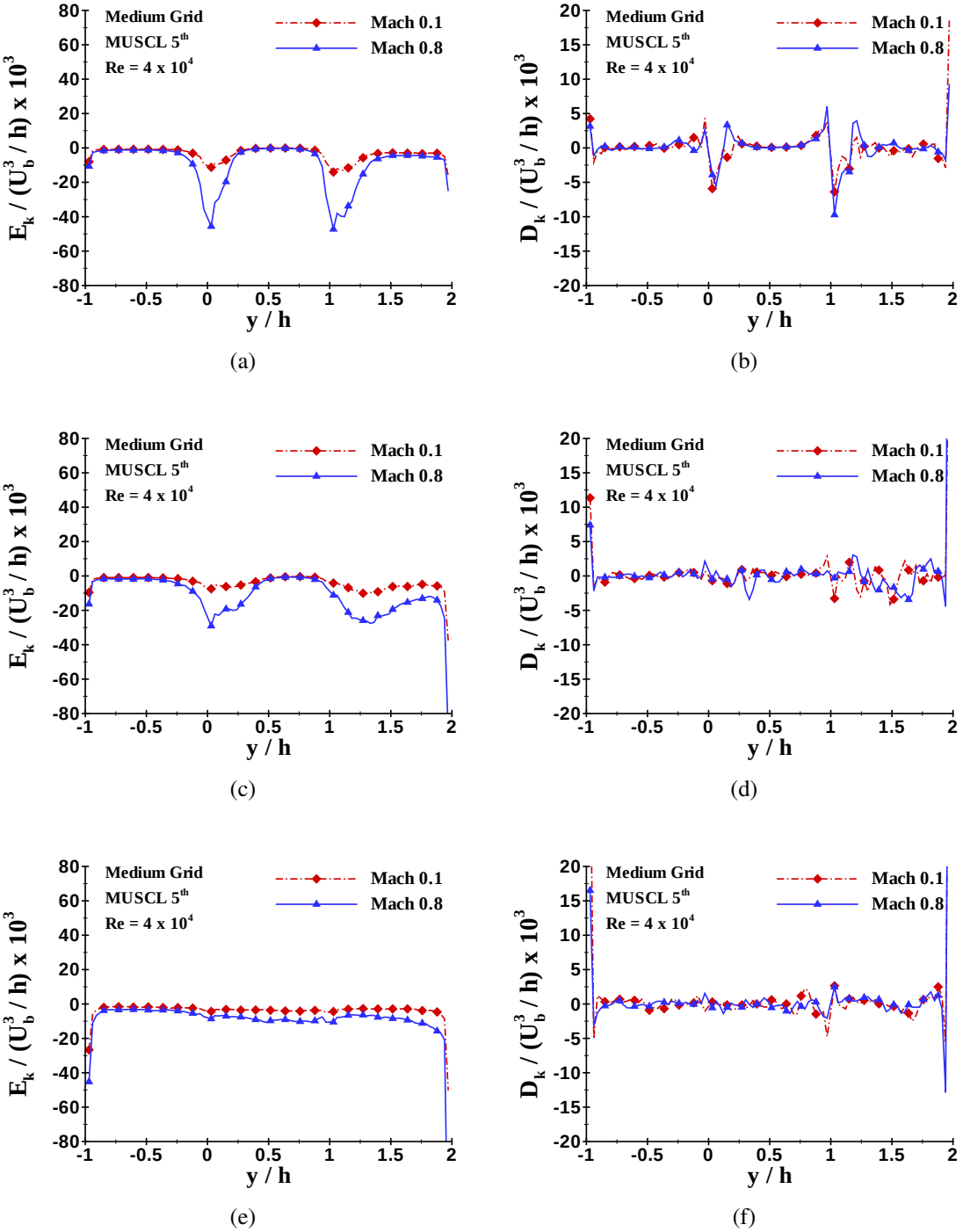

FIGURE 6.12: Dissipation and Viscous Diffusion terms at (a),(b) $x/h = 1$, (c),(d) $x/h = 2$, (e),(f) $x/h = 5$ downstream of the step, for two different Mach number regimes ($M = 0.1$ and $M = 0.8$) at $Re = 4 \cdot 10^4$.

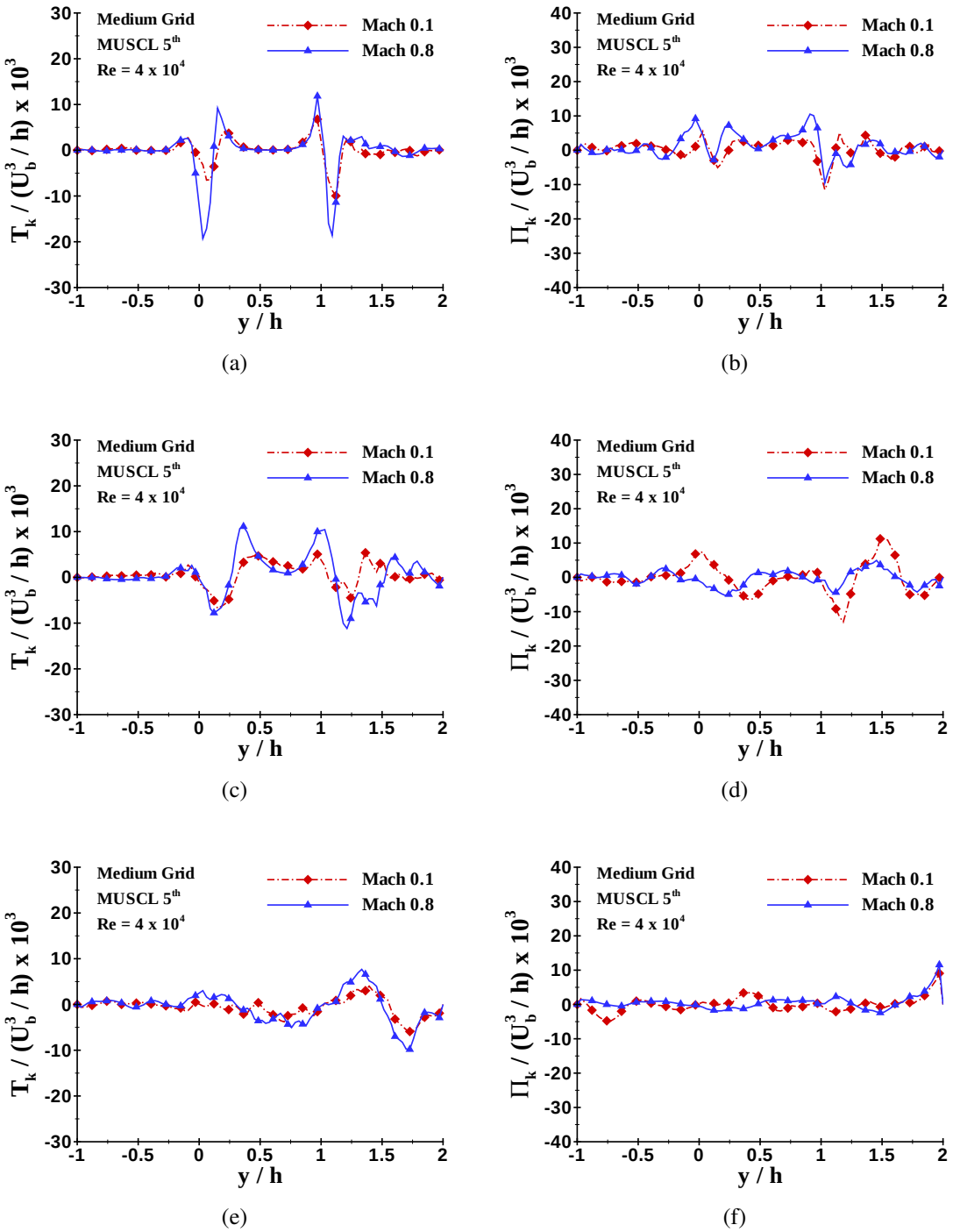

FIGURE 6.13: Turbulent Diffusion and Pressure Diffusion of k at (a),(b) $x/h = 1$, (c),(d) $x/h = 2$, (e),(f) $x/h = 5$ downstream of the step, for two different Mach number regimes ($M = 0.1$ and $M = 0.8$) at $Re = 4 \cdot 10^4$.

6.4 Summary

In this chapter, an investigation has been carried out of a turbulent compressible flow over a sudden expansion geometry in the framework of ILES. Comparisons of the numerical results with experimental data were not possible, as no previous study on this particular flow regime over the planar sudden expansion has been reported in the past. Nevertheless, results obtained at $M = 0.8$ were compared against those found at a lower Mach number (i.e., at $M = 0.1$ where the fluid can be assumed to be incompressible).

The results revealed that both averaged flow quantities and turbulent stresses are sensitive to the Mach number. The normalised mean streamwise velocity found to be approximately $\sim 10\%$ higher in the high-velocity core flow region for the higher Mach number. The difference in terms of the mean transverse velocity appeared to be less significant (less than 5%). Furthermore, the mean reattachment lengths of the primary recirculation zones increases with increase in Mach number. The length of the shorter vortex at $M = 0.8$ found to be of about the same length as that at lower Mach number. On the other hand, the length of the larger recirculation area for the case of $M = 0.8$ is approximately 12% longer. The increase in the mean reattachment length with compressibility implies that the separated shear layer (particularly that of the larger vortex) is more stable or grows less faster for higher Mach numbers. Note that this flow behaviour is similar to classical free-shear layers, where compressibility reduces growth rate.

In addition, calculations of the turbulent kinetic energy budget were performed to investigate the influence of compressibility on the budget terms. Turbulence production along with energy dissipation are the most dominant terms in the energy budget. Both terms found to significantly increase in magnitude with Mach number, thus resulting in a faster growth of turbulent kinetic energy. Among the transport terms, only turbulent diffusion and pressure diffusion appeared to contribute either positively or negatively to the energy budget, along the cross-steam direction. Turbulent diffusion removes energy from the mean flow, as it transports energy from the bottom half of each shear layer to the near-wall region and to the upper half of the shear layers. On the other hand, the magnitude of the viscous diffusion tends to zero in the free-shear layer region, whereas it becomes large close to the upper and lower wall of the channel. Finally, turbulence convection contributes negatively to the energy budget almost everywhere, apart from regions close to reattachment location where it becomes positive towards the upper wall.

7 Conclusion

7.1 Conclusion of Study

In this PhD thesis, high-order high-resolution numerical methods were used in the framework of Implicit Large Eddy Simulation (ILES), with aim at performing simulations of a turbulent flow in a planar sudden expansion configuration. The aim of this work was twofold: (a) to investigate, for the first time, ILES capability of capturing the flow physics in regions with strong separation and reattachment and (b) to study the influence of different Reynolds and Mach numbers on the mean flow structures.

For that purpose three different numerical schemes were used including the 3^{rd} order MUSCL, the 5^{th} order MUSCL and the 5^{th} order WENO method, along with two Reynolds numbers ($Re = 10000$ and $Re = 40000$). A novel low Mach number treatment (LMNT) approach was applied to the reconstructed values obtained from the limiters of the aforementioned schemes, in order to decrease the kinetic energy dissipation rate introduced in the limit of zero Mach number. In addition, simulations in the incompressible (Mach 0.1) and compressible (Mach 0.8) regime were performed to investigate further the flow behaviour in suddenly-expanded flows.

Synthetic turbulent boundary conditions (BCs) based on the digital filter (DF) generation technique were implemented on the CNS3D code and used throughout the numerical simulations. They produce a velocity signal in three directions by matching ad hoc first- and second-order moments, as well as lengths and time scales. The results indicated that the inflow synthetic BCs are able to produce realistic flow conditions, as the profiles of the mean and fluctuating velocity components match reasonably well both with direct numerical simulation (DNS) and experimental data.

The grid convergence study of a turbulent flow over a planar sudden expansion with expansion ratio $ER = 3$ and aspect ratio $AR = 5$ at $Re = 10^4$ revealed that the coarse grid is not capable of resolving the mean flow structures in such flows. Thus, measurements on first- and second-order statistics (in the streamwise and wall-normal direction) showed large discrepancies between numerical and experimental results, for several step heights downstream of the expansion. The flow was not well resolved there, due to the grid clustering performed in the streamwise direction, resulting in a much more rare grid resolution in that particular flow area. Considerably better results in terms of mean flow quantities were obtained from the medium and fine grid meshes examined. Note also that the same convergence study was carried out for a turbulent flow over a planar sudden expansion configuration at $Re = 4 \cdot 10^4$, using the same geometric properties with that at the lower Re. Similar results were obtained, with the coarse grid being rather inadequate of resolving the turbulent flow features.

A comprehensive study of the influence of the numerical schemes on the mean flow quantities (Reynolds shear stresses, turbulent kinetic energy, r.m.s. velocities), as well as on the reattachment lengths of the primary and secondary recirculation zones was undertaken. Results indicated that as the order of accuracy increases from 3^{rd} to 5^{th}, the time-averaged flow quantities are getting closer to the experimental data. Furthermore, it was observed that MUSCL schemes in conjunction with LMNT result in the overprediction of turbulence intensities, particularly in the regions of the recirculation vortices about the upper and lower wall of the channel. The same trend was also found for the WENO scheme at a lower intense level, though. It was made clear that W5 outperforms over its counterparts (M3, M5) in terms of first- and second-order (mean) statistics, almost everywhere in the flow field.

As previously mentioned, the effect of the Reynolds number on the mean flow properties was thoroughly investigated. Results on the mean flow paths, calculated by means of stream tracers, revealed that the larger recirculation zone is substantially influenced by

the different *Re* used, with its length turning out to be larger with increasing *Re*. On the other hand, the size of the shorter reattachment, along with the lengths of the secondary vortices formed about the corners of the channel walls, were not found to change dramatically. Further investigation on the time-averaged flow quantities showed that although the first-order statistics (i.e., streamwise and wall-normal velocity components) exhibit similar behaviour for the two cases, the profiles of the higher-order statistics (i.e., Reynolds shear stress, turbulent kinetic energy, turbulence intensity) are slightly affected by the increase in *Re*. Particularly, higher peak values of fluctuating velocity and turbulent kinetic energy were obtained at lower *Re*.

Turbulent kinetic energy budget measurements were conducted in a turbulent flow with sudden expansion at $Re = 10^4$ and $Re = 4 \cdot 10^4$. The main aim here was to shed some light on the flow physics encountered in such flows, and provide insight for turbulence modelling. Turbulence production appeared to be the most dominant term in the energy budget, as far as the region of the free-shear layers is concerned, being balanced by the energy dissipation term in that particular region. It was found that in some cases (depending on the numerical scheme and the *Re* used in the simulations) the ratio of the dissipation term to the production term approaches approximately the value of 0.6. In the near-wall region the production term tends to zero, whereas the viscous diffusion and the energy dissipation terms become more significant. The convection term contributes negatively to the energy budget, almost everywhere in the flow field. Finally, turbulent diffusion and pressure-velocity correlation terms (known also as the transport terms of the energy budget) appeared to subtract energy from the mean flow and transfer it in regions with low production rate towards the upper and lower wall of the channel.

Finally, the influence of compressibility on the mean values of a turbulent flow with a sudden expansion was examined, using two different Mach numbers at Mach 0.1 and 0.8. The grid independence study at Mach 0.8 revealed that the coarse grid can adequately resolve the mean flow values in terms of the first-order statistics (streamwise and transverse velocity components). As previously stated, this was not the case for the same coarse grid used to investigate the mean flow field in the incompressible regime. However, measurements on high-order statistics showed that the coarse grid underestimates the turbulent kinetic energy and the Reynolds shear stresses, considerably. It was also found that the reattachment length of the larger recirculation zone increases with Mach number (i.e., about 13% larger at Mach 0.8), whereas the length of the shorter recirculation vortex remains almost the same. Besides, the lengths of the secondary vortices do not appear to

vary significantly with Mach number.

7.2 Future Considerations

Based on the conclusions of this study, further investigation on turbulent flows with a sudden expansion needs to be undertaken, particularly in the three following fields:

1. Numerical analysis on separated and suddenly-expanded flows revealed that high-order high-resolution schemes in conjunction with ILES can lead to an underdissipative behaviour, particularly in flow regions with strong reversed motion. This resulted to the overprediction of the turbulence intensity and consequently of the turbulent kinetic energy, which in turn led to the underprediction of the primary and secondary reattachment lengths of the recirculation vortices. Thus, care should be taken to minimise the numerical error produced when high-resolution methods are combined with ILES. Simulations can then be conducted using a wide range of numerical methods extending from 2^{nd}- to even 9^{th}-order (MUSCL, WENO), with aim at clarifying the underlying reasons of the aforementioned overprediction of the high-order (mean) statistics.

2. Turbulent kinetic energy budget (TKEB) measurements showed that in the shear layer regions, the ratio of the energy dissipation to the turbulence production is in most cases less than 0.5. However, TKEB measurements on the backward-facing step (BFS), in the past, revealed that the contribution of the energy dissipation to the energy budget is much more prominent in this flow areas. Thus, numerical simulations of a turbulent flow over a BFS configuration could be conducted, using the same flow properties and boundary conditions, to investigate to what extent can ILES successfully resolve the mean flow structures, in flows with separation and reattachment of the shear layers. Comparisons between numerical and experimental results could indicate whether the underestimation of energy dissipation is due to the turbulence modelling, due to the numerical methods, or due to both of them.

3. The three-dimensionality of a turbulent flow in the sudden expansion configuration should be thoroughly examined, by means of side walls (at the spanwise direction), seeking to shed some insights into the effect of the walls on the coherent structures, which are developing in wall-bounded flows.

Appendices and References

References

[1] D.E. Abbott and S.J. Kline. Experimental investigation of subsonic turbulent flow over single and double backward facing steps. *J. Basic Eng*, 84:317–325, 1962.

[2] A. Acrivos and M.L. Schrader. Steady flow in a sudden expansion at high reynolds numbers. *Physics of Fluids*, 25:923–930, 1982.

[3] N.A. Adams. The use of les subgrid-scale models for shock capturing. *International Journal for Numerical Methods in Fluids*, 39(9):783–797, 2002.

[4] N. Alleborn, K. Nandakumar, H. Raszillier, and F. Durst. Further contributions on the two-dimensional flow in a sudden expansion. *Journal of Fluid Mechanics*, 330:169–188, 1997.

[5] F. Aloui and M. Souhar. Experimental study of turbulent asymmetric flow in a flat duct symmetric sudden expansion. *Journal of Fluids Engineering*, 122:174–177, 2000.

[6] B.F. Armaly, F. Durst, J.C.F. Pereira, and B. Schonung. Experimental and theoretical investigation of backward-facing step flow. *Journal of Fluid Mechanics*, 127:473–496, 1983.

[7] D.S. Balsara and C.W. Shu. Monotonicity preserving weighted essentially non-oscillatory schemes with increasingly high order of accuracy. *Journal of Computational Physics*, 160(2):405–452, 2000.

[8] J. Bardina, J.H. Ferziger, and W.C. Reynolds. Improved subgrid-scale models for large-eddy simulation. *Aeronaut. Astronaut. Paper*, 34:1111–1119, 1980.

[9] M. Barri, G.K. El Khoury, H.I. Andersson, and B. Pettersen. Dns of backward-facing step flow with fully turbulent inflow. *International Journal for Numerical Methods in Fluids*, 64(7):777–792, 2010.

[10] P.T. Barton. *A novel multi-dimensional Eulerian approach to computational solid dynamics*. PhD thesis, Cranfield University, 2010.

[11] F. Battaglia, S.J. Tavener, A.K. Kulkarni, and C.L. Merkle. Bifurcation of low reynolds number flows in symmetric channels. *AIAA journal*, 35(1):99–105, 1997.

[12] J. Blazek. *Computational fluid dynamics: principles and applications*. Elsevier Science Ltd, 2005.

[13] J.P. Boris, F.F. Grinstein, E.S. Oran, and R.L. Kolbe. New insights into large eddy simulation. *Fluid dynamics research*, 10(4-6):199–228, 1992.

[14] L. Bradbury. The structure of a self-preserving turbulent plane jet. *Journal of Fluid Mechanics*, 23(01):31–64, 1965.

[15] L. Browne, R.A. Antonia, and D.A. Shah. Turbulent energy dissipation in a wake. *Journal of Fluid Mechanics*, 179(1):307–326, 1987.

[16] S. Canbazoglu and O. Bozkir. Analysis of pressure distribution of turbulent asymmetric flow in a flat duct symmetric sudden expansion with small aspect ratio. *Fluid Dynamics Research*, 35(5):341–355, 2004.

[17] L. Casarsa and P. Giannattasio. Three-dimensional features of the turbulent flow through a planar sudden expansion. *Physics of Fluids*, 20:015103, 2008.

[18] W. Cherdron, F. Durst, and J.H. Whitelaw. Asymmetric flows and instabilities in symmetric ducts with sudden expansions. *Journal of Fluid Mechanics*, 84(01):13–31, 1978.

[19] T.P. Chiang, T.W.H. Sheu, and S.K. Wang. Side wall effects on the structure of laminar flow over a plane-symmetric sudden expansion. *Computers & Fluids*, 29(5):467–492, 2000.

[20] P.A. Davidson. *Turbulence: an introduction for scientists and engineers*. Oxford University Press, USA, 2004.

[21] V. De Brederode and P. Bradshaw. *Three-dimensional Flow in Nominally Two-dimensional Separation Bubbles: Flow Behind a Rearward-facing Step*. Department of Aeronautics, Imperial College of Science and Technology, 1972.

[22] S. De Zilwa, L. Khezzar, and J.H. Whitelaw. Flows through plane sudden-expansions. *International Journal for Numerical Methods in Fluids*, 32(3):313–329, 2000.

[23] J.W. Deardorff. A numerical study of three-dimensional turbulent channel flow at large reynolds numbers. *Journal of Fluid Mechanics*, 41(02):453–480, 1970.

[24] L. Di Mare, M. Klein, W.P. Jones, and J. Janicka. Synthetic turbulence inflow conditions for large-eddy simulation. *Physics of Fluids*, 18:025107, 2006.

[25] P.G. Drazin and W.H. Reid. *Hydrodynamic stability*. Cambridge Univ Pr, 2004.

[26] D. Drikakis. Bifurcation phenomena in incompressible sudden expansion flows. *Physics of Fluids*, 9:76–87, 1997.

[27] D. Drikakis. Embedded turbulence model in numerical methods for hyperbolic conservation laws. *International Journal for Numerical Methods in Fluids*, 39(9):763–781, 2002.

[28] D. Drikakis. Advances in turbulent flow computations using high-resolution methods. *Progress in Aerospace Sciences*, 39(6-7):405–424, 2003.

[29] D. Drikakis, F. Grinstein, and D. Youngs. On the computation of instabilities and symmetry-breaking in fluid mechanics. *Progress in Aerospace Sciences*, 41(8):609–641, 2005.

[30] D. Drikakis, M. Hahn, A. Mosedale, and B. Thornber. Large eddy simulation using high-resolution and high-order methods. *Philosophical Transactions of the Royal Society A: Mathematical, Physical and Engineering Sciences*, 367(1899):2985–2997, 2009.

[31] D. Drikakis, L.G. Margolin, and P.K. Smolarkiewicz. On 'spurious' eddies. *International journal for numerical methods in fluids*, 40(1-2):313–322, 2002.

[32] D. Drikakis and W. Rider. *High-resolution methods for incompressible and low-speed flows*. Springer Verlag, 2005.

[33] D. Drikakis and P.K. Smolarkiewicz. On spurious vortical structures. *Journal of Computational Physics*, 172(1):309–325, 2001.

[34] D. Drikakis and S. Tsangaris. On the solution of the compressible navier-stokes equations using improved flux vector splitting methods. *Applied Mathematical Modelling*, 17(6):282–297, 1993.

[35] F. Durst, A. Melling, and J.H. Whitelaw. Low reynolds number flow over a plane symmetric sudden expansion. *Journal of Fluid Mechanics*, 64(01):111–128, 1974.

[36] F. Durst, J. Pereira, and C. Tropea. The plane symmetric sudden-expansion flow at low reynolds numbers. *Journal of Fluid Mechanics*, 248:567–581, 1993.

[37] J.K. Eaton and J.P. Johnston. A review of research on subsonic turbulent flow reattachment. *AIAA J*, 19(9):1093–1100, 1981.

[38] G.K. El Khoury, B. Pettersen, H.I. Andersson, and M. Barri. Asymmetries in an obstructed turbulent channel flow. *Physics of Fluids*, 22:095103, 2010.

[39] M.P. Escudier, P.J. Oliveira, and R.J. Poole. Turbulent flow through a plane sudden expansion of modest aspect ratio. *Physics of Fluids*, 14:3641–3654, 2002.

[40] R.M. Fearn, T. Mullin, and K.A. Cliffe. Nonlinear flow phenomena in a symmetric sudden expansion. *Journal of Fluid Mechanics*, 211:595–608, 1990.

[41] G. Fischer. A survey of finite-difference approximations to the primitive equations. *Monthly Weather Review*, 93(1):1–10, 1965.

[42] E.A. Foumeny, D.B. Ingham, and A.J. Walker. Bifurcations of incompressible flow through plane symmetric channel expansions. *Computers & Fluids*, 25(3):335–351, 1996.

[43] C. Fureby and F.F. Grinstein. Large eddy simulation of high-reynolds-number free and wall-bounded flows. *Journal of Computational Physics*, 181(1):68–97, 2002.

[44] Y. Gagnon, A. Giovannini, and P. Hébrard. Numerical simulation and physical analysis of high reynolds number recirculating flows behind sudden expansions. *Physics of Fluids A: Fluid Dynamics*, 5:2377–2389, 1993.

[45] M. Germano. A proposal for a redefinition of the turbulent stresses in the filtered navier–stokes equations. *Physics of Fluids*, 29:2323, 1986.

[46] M. Germano. Turbulence: the filtering approach. *Journal of Fluid Mechanics*, 238:325–336, 1992.

[47] M. Germano, U. Piomelli, P. Moin, and W.H. Cabot. A dynamic subgrid-scale eddy viscosity model. *Physics of Fluids A: Fluid Dynamics*, 3:1760–1765, 1991.

[48] S. Ghosal. An analysis of numerical errors in large-eddy simulations of turbulence. *Journal of Computational Physics*, 125(1):187–206, 1996.

[49] S.K. Godunov. A difference method for numerical calculation of discontinuous solutions of the equations of hydrodynamics. *Matematicheskii Sbornik*, 89(3):271–306, 1959.

[50] F.F. Grinstein and C. Fureby. On monotonically integrated large eddy simulation of turbulent flows based on fct algorithms. *Flux-Corrected Transport*, pages 79–104, 2005.

[51] F.F. Grinstein and C. Fureby. Recent progress on flux-limiting based implicit large eddy simulation. In *European Conference on Computational Fluid Dynamics, ECCOMAS CFD*, 2006.

[52] F.F. Grinstein, L.G. Margolin, and W. Rider. *Implicit large eddy simulation: computing turbulent fluid dynamics*. Cambridge Univ Pr, 2007.

[53] A. Harten. Eno schemes with subcell resolution. *Journal of Computational Physics*, 83(1):148–184, 1989.

[54] A. Harten, P.D. Lax, and B. Van Leer. On upstream differencing and godunov-type schemes for hyperbolic conservation laws. *SIAM review*, pages 35–61, 1983.

[55] T. Hawa and Z. Rusak. The dynamics of a laminar flow in a symmetric channel with a sudden expansion. *Journal of Fluid Mechanics*, 436:283–320, 2001.

[56] J. Hinze. *Turbulence*. McGraw-Hill, 1975.

[57] P.G. Huang, G.N. Coleman, and P. Bradshaw. Compressible turbulent channel flows: Dns results and modelling. *Journal of Fluid Mechanics*, 305:185–218, 1995.

[58] H.J. Hussein, S.P. Capp, and W.K. George. Velocity measurements in a high-reynolds-number, momentum-conserving, axisymmetric, turbulent jet. *Journal of Fluid Mechanics*, 258(1):31–75, 1994.

[59] K. Iwamoto, Y. Suzuki, and N. Kasagi. Reynolds number effect on wall turbulence: toward effective feedback control. *International Journal of Heat and Fluid Flow*, 23(5):678–689, 2002.

[60] G. Jefferey. Instabilities and transition. http://media.efluids.com/galleries/instability?medium=105/, 2010.

[61] G.S. Jiang and C.W. Shu. Efficient implementation of weighted eno schemes. *J. Comput. Phys*, 126:202–228, 1996.

[62] M. Kadja and G. Bergeles. Numerical investigation of bifurcation phenomena occurring in flows through planar sudden expansions. *Acta Mechanica*, 153(1):47–61, 2002.

[63] L. Kaiktsis, G. Em Karniadakis, and S.A. Orszag. Unsteadiness and convective instabilities in two-dimensional flow over a backward-facing step. *Journal of Fluid Mechanics*, 321:157–187, 1996.

[64] L. Kaiktsis, G.E. Karniadakis, and S.A. Orszag. Onset of three-dimensionality, equilibria, and early transition in flow over a backward-facing step. *Journal of Fluid Mechanics*, 231:501–528, 1991.

[65] N. Kasagi and A. Matsunaga. Three-dimensional particle-tracking velocimetry measurement of turbulence statistics and energy budget in a backward-facing step flow. *International Journal of Heat and Fluid Flow*, 16(6):477–485, 1995.

[66] A. Kasahara and W.M. Washington. Ncar global general circulation model of the atmosphere. *Monthly Weather Review*, 95(7):389–402, 1967.

[67] K.H. Kim and C. Kim. Accurate, efficient and monotonic numerical methods for multi-dimensional compressible flows:: Part i: Spatial discretization. *Journal of Computational Physics*, 208(2):527–569, 2005.

[68] K.H. Kim and C. Kim. Accurate, efficient and monotonic numerical methods for multi-dimensional compressible flows:: Part ii: Multi-dimensional limiting process. *Journal of computational physics*, 208(2):570–615, 2005.

[69] M. Klein, A. Sadiki, and J. Janicka. A digital filter based generation of inflow data for spatially developing direct numerical or large eddy simulations. *Journal of Computational Physics*, 186(2):652–665, 2003.

[70] A.N. Kolmogorov. Local structure of turbulence in an incompressible viscous fluid at very high reynolds numbers. *Soviet Physics Uspekhi*, 10:734–736, 1968.

[71] A.N. Kolmogorov. Dissipation of energy in the locally isotropic turbulence. *Proceedings: Mathematical and Physical Sciences*, pages 15–17, 1991.

[72] L.D. Landau. On the problem of turbulence. *CR Acad. Sci. USSR*, 44:311–314, 1944.

[73] H. Le, P. Moin, and J. Kim. Direct numerical simulation of turbulent flow over a backward-facing step. *Journal of Fluid Mechanics*, 330:349–374, 1997.

[74] A. Leonard. Energy cascade in large-eddy simulations of turbulent fluid flows. *Adv. Geophys*, 18:237–248, 1974.

[75] M. Lesieur and O. Metais. New trends in large-eddy simulations of turbulence. *Annu. Rev. Fluid Mech*, 28:45–82, 1996.

[76] D.K. Lilly. A proposed modification of the germano subgrid-scale closure method. *Physics of Fluids A: Fluid Dynamics*, 4:633–635, 1992.

[77] X. Liu and F.O. Thomas. Measurement of the turbulent kinetic energy budget of a planar wake flow in pressure gradients. *Experiments in Fluids*, 37(4):469–482, 2004.

[78] X.D. Liu, S. Osher, and T. Chan. Weighted essentially non-oscillatory schemes. *Journal of Computational Physics*, 115(1):200–212, 1994.

[79] T.S. Lund, X. Wu, and K.D. Squires. Generation of turbulent inflow data for spatially-developing boundary layer simulations. *Journal of Computational Physics*, 140(2):233–258, 1998.

[80] L.G. Margolin and W.J. Rider. A rationale for implicit turbulence modelling. *International Journal for Numerical Methods in Fluids*, 39(9):821–841, 2002.

[81] LG Margolin, P.K. Smolarkiewicz, and A.A. Wyszogrodzki. Implicit turbulence modeling for high reynolds number flows. *Journal of Fluids Engineering*, 124:862–867, 2002.

[82] P.R. Mehta. Separated flow through large sudden expansions. *Journal of the Hydraulics Division*, 107(4):451–460, 1981.

[83] C. Meneveau and J. Katz. Scale-invariance and turbulence models for large-eddy simulation. *Annual Review of Fluid Mechanics*, 32(1):1–32, 2000.

[84] F.S. Milos and A. Acrivos. Steady flow past sudden expansions at large reynolds number. part i: Boundary layer solutions. *Physics of Fluids*, 29:1353–1359, 1986.

[85] F.S. Milos, A. Acrivos, and J. Kim. Steady flow past sudden expansions at large reynolds number. ii. navier–stokes solutions for the cascade expansion. *Physics of Fluids*, 30:7–18, 1987.

[86] J. Mizushima and Y. Shiotani. Structural instability of the bifurcation diagram for two-dimensional flow in a channel with a sudden expansion. *Journal of Fluid Mechanics*, 420:131–145, 2000.

[87] P. Moin and K. Mahesh. Direct numerical simulation: a tool in turbulence research. *Annual Review of Fluid Mechanics*, 30(1):539–578, 1998.

[88] A.S. Neto, D. Grand, O. Métais, and M. Lesieur. A numerical investigation of the coherent vortices in turbulence behind a backward-facing step. *Journal of Fluid Mechanics*, 256:1–25, 1993.

[89] S. Newhouse, D. Ruelle, and F. Takens. Occurrence of strange axiom a attractors near quasi periodic flows on t m, m 3. *Communications in Mathematical Physics*, 64(1):35–40, 1978.

[90] J.H. Nie and B.F. Armaly. Reverse flow regions in three-dimensional backward-facing step flow. *International Journal of Heat and Mass Transfer*, 47(22):4713–4720, 2004.

[91] N.R. Panchapakesan and J.L. Lumley. Turbulence measurements in axisymmetric jets of air and helium. part 1. air jet. *Journal of Fluid Mechanics*, 246:197–223, 1993.

[92] G. Papadopoulos and MV Otugen. Separating and reattaching flow structure in a suddenly expanding rectangular duct. *Journal of Fluids Engineering*, 117:17–23, 1995.

[93] U. Piomelli. Large-eddy simulation: achievements and challenges. *Prog Aerosp Sci*, 35(4):335–362, 1999.

[94] S.B. Pope. *Turbulent flows*. Cambridge Univ Pr, 2000.

[95] A. Restivo and J.H. Whitelaw. Turbulence characteristics of the flow downstream of a symmetric, plane sudden expansion. *ASME Transactions Journal of Fluids Engineering*, 100:308–310, 1978.

[96] D. Ruelle and F. Takens. On the nature of turbulence. *Communications in mathematical physics*, 20(3):167–192, 1971.

[97] Z. Rusak and T. Hawa. A weakly nonlinear analysis of the dynamics of a viscous flow in a symmetric channel with a sudden expansion. *Physics of Fluids*, 11(12):3629, 1999.

[98] P. Sagaut. *Large eddy simulation for incompressible flows*. Springer, 2001.

[99] E. Schreck and M. Schafer. Numerical study of bifurcation in three-dimensional sudden channel expansions. *Computers & Fluids*, 29(5):583–593, 2000.

[100] A. Scotti, C. Meneveau, and D.K. Lilly. Generalized smagorinsky model for anisotropic grids. *Physics of Fluids A: Fluid Dynamics*, 5:2306–2308, 1993.

[101] M. Shapira, D. Degani, et al. Stability and existence of multiple solutions for viscous flow in suddenly enlarged channels. *Computers & Fluids*, 18(3):239–258, 1990.

[102] C.W. Shu. Essentially non-oscillatory and weighted essentially non-oscillatory schemes for hyperbolic conservation laws. *Advanced numerical approximation of nonlinear hyperbolic equations*, pages 325–432, 1998.

[103] C.W. Shu and S. Osher. Efficient implementation of essentially non-oscillatory shock-capturing schemes. *Journal of Computational Physics*, 77(2):439–471, 1988.

[104] C.W. Shu and S. Osher. Efficient implementation of essentially non-oscillatory shock-capturing schemes, ii. *Journal of Computational Physics*, 83(1):32–78, 1989.

[105] A. Sideridis, K. Yakinthos, and A. Goulas. Turbulent kinetic energy balance measurements in the wake of a low-pressure turbine blade. *International Journal of Heat and Fluid Flow*, 32, 2010.

[106] J. Smagorinsky. General circulation experiments with the primitive equations. *Monthly weather review*, 91(3):99–164, 1963.

[107] J. Smagorinsky, S. Manabe, and J.L. Holloway Jr. Numerical results from a nine-level general circulation model of the atmosphere. *Monthly Weather Review*, 93(12):727–768, 1965.

[108] R. Smyth. Turbulent flow over a plane symmetric sudden expansion. *J. Fluids Eng.*, 101(3):348–353, 1979.

[109] I.J. Sobey and P.G. Drazin. Bifurcations of two-dimensional channel flows. *Journal of Fluid Mechanics*, 171:263–287, 1986.

[110] P.G. Spazzini, G. Iuso, M. Onorato, N. Zurlo, and G.M. Di Cicca. Unsteady behavior of back-facing step flow. *Experiments in fluids*, 30(5):551–561, 2001.

[111] C.G. Speziale. Galilean invariance of subgrid-scale stress models in the large-eddy simulation of turbulence. *Journal of fluid mechanics*, 156:55–62, 1985.

[112] R.J. Spiteri and S.J. Ruuth. A new class of optimal high-order strong-stability-preserving time discretization methods. *SIAM Journal on Numerical Analysis*, 40(2):469–491, 2002.

[113] K. Sugawara, H. Yoshikawa, and T. Ota. Les of turbulent separated flow and heat transfer in a symmetric expansion plane channel. *Journal of Fluids Engineering*, 127:865–871, 2005.

[114] K. Szymocha. An experimental analysis of the turbulent flow downstream of a plane symmetric sudden expansion. *Archiwum Mechaniki Stosowanej*, 36:705–713, 1984.

[115] H. Tennekes and J.L. Lumley. *A first course in turbulence*. The MIT press, 1972.

[116] B. Thornber, A. Mosedale, and D. Drikakis. On the implicit large eddy simulations of homogeneous decaying turbulence. *Journal of Computational Physics*, 226(2):1902–1929, 2007.

[117] B. Thornber, A. Mosedale, D. Drikakis, D. Youngs, and RJR Williams. An improved reconstruction method for compressible flows with low mach number features. *Journal of Computational Physics*, 227(10):4873–4894, 2008.

[118] E.F. Toro. *Riemann solvers and numerical methods for fluid dynamics: a practical introduction*. Springer Verlag, 2009.

[119] E.F. Toro, M. Spruce, and W. Speares. Restoration of the contact surface in the hll-riemann solver. *Shock waves*, 4(1):25–34, 1994.

[120] E. Touber and N.D. Sandham. Large-eddy simulation of low-frequency unsteadiness in a turbulent shock-induced separation bubble. *Theoretical and Computational Fluid Dynamics*, 23(2):79–107, 2009.

[121] A.A. Townsend. Momentum and energy diffusion in the turbulent wake of a cylinder. *Proceedings of the Royal Society of London. Series A. Mathematical and Physical Sciences*, 197:124–140, 1949.

[122] Y.Y. Tsui and H.W. Wang. Side-wall effects on the bifurcation of the flow through a sudden expansion. *International Journal for Numerical Methods in Fluids*, 56(2):167–184, 2008.

[123] B. Van Leer. Towards the ultimate conservative difference scheme iii. upstream-centered finite-difference schemes for ideal compressible flow. *Journal of Computational Physics*, 23(3):263–275, 1977.

[124] B. Van Leer. Towards the ultimate conservative difference scheme. iv. a new approach to numerical convection. *Journal of Computational Physics*, 23(3):276–299, 1977.

[125] B. Van Leer. Towards the ultimate conservative difference scheme. v. a second-order sequel to godunov's method. *Journal of Computational Physics*, 32(1):101–136, 1979.

[126] B. Van Leer. Flux-vector splitting for the euler equations. In *Eighth International Conference on Numerical Methods in Fluid Dynamics*, pages 507–512, 1982.

[127] I. Veloudis, Z. Yang, J.J. McGuirk, G.J. Page, and A. Spencer. Novel implementation and assessment of a digital filter based approach for the generation of les inlet conditions. *Flow, Turbulence and Combustion*, 79(1):1–24, 2007.

[128] E.M. Wahba. Iterative solvers and inflow boundary conditions for plane sudden expansion flows. *Applied Mathematical Modelling*, 31(11):2553–2563, 2007.

[129] D.C. Wilcox. *Turbulence modeling for CFD*. DCW industries La Canada, CA, 2006.

[130] R. Wille and H. Fernholz. Report on the first european mechanics colloquium, on the coanda effect. *Journal of Fluid Mechanics*, 23(04):801–819, 1965.

[131] Z.T. Xie and I.P. Castro. Efficient generation of inflow conditions for large eddy simulation of street-scale flows. *Flow, Turbulence and Combustion*, 81(3):449–470, 2008.

A

Appendix A

A.1 The Jacobian Matrix

In this appendix, the inviscid and viscous Jacobian matrices used for the linearisation of either the Euler or the Navier-Stokes equations will be addressed. Consider the conservation form of the governing equations represented by the generic form, written below.

$$\frac{\partial \mathbf{C}}{\partial t} + \frac{\partial \mathbf{F}(\mathbf{C})}{\partial x} = 0 \tag{A.1}$$

where

$$\mathbf{C} = \begin{bmatrix} u_1 \\ \\ u_2 \\ \vdots \\ u_m \end{bmatrix} \quad , \quad \mathbf{F}(\mathbf{C}) = \begin{bmatrix} f_1 \\ \\ f_2 \\ \vdots \\ f_m \end{bmatrix} \tag{A.2}$$

$\mathbf{C}$ is defined as the vector of the conserved variables and $\mathbf{F}$ =$\mathbf{F}(\mathbf{C})$ is the vector of fluxes. Note that each of $\mathbf{F}$ components f_i is a function of the components u_i of $\mathbf{C}$. The Jacobian matrix then of the flux function $\mathbf{F}(\mathbf{C})$ can be written as follows.

$$\mathbf{A}(\mathbf{C}) = \frac{\partial \mathbf{F}}{\partial \mathbf{C}} = \begin{bmatrix} \partial f_1/\partial u_1 & \cdots & \partial f_1/\partial u_m \\ \partial f_2/\partial u_1 & \cdots & \partial f_2/\partial u_m \\ \vdots & & \vdots \\ \partial f_m/\partial u_1 & \cdots & \partial f_m/\partial u_m \end{bmatrix} \tag{A.3}$$

The entries of $\mathbf{A}(\mathbf{C})$ are partial derivatives of the components f_i of flux vector $\mathbf{F}$ with respect to the components u_i of the conserved variables $\mathbf{C}$. Note also that the conservation laws of the form (A.1-A.2) can be written in quasi-linear form. This can be achieved by applying the chain rule of differentiation to the second term of Equation (A.1).

$$\frac{\partial \mathbf{F}(\mathbf{C})}{\partial x} = \frac{\partial \mathbf{F}}{\partial \mathbf{C}} \frac{\partial \mathbf{C}}{\partial x} \tag{A.4}$$

Thus Equation (A.1) can be also written as:

$$\frac{\partial \mathbf{C}}{\partial t} + \mathbf{A}(\mathbf{C}) \frac{\partial \mathbf{C}}{\partial x} = 0 \tag{A.5}$$

Now consider the non-dimensional equations of fluid motion expressed in a flux vector form as follows.

$$\frac{\partial \mathbf{C}}{\partial t} + \frac{\partial \mathbf{E}_{inv}}{\partial t} + \frac{\partial \mathbf{F}_{inv}}{\partial t} + \frac{\partial \mathbf{G}_{inv}}{\partial t} = \frac{\partial \mathbf{E}_{vis}}{\partial t} + \frac{\partial \mathbf{F}_{vis}}{\partial t} + \frac{\partial \mathbf{G}_{vis}}{\partial t} \tag{A.6}$$

where

$$\mathbf{C} = \begin{bmatrix} \rho \\ \rho u \\ \rho \upsilon \\ \rho w \\ \rho e_t \end{bmatrix}$$

$$\mathbf{E}_{inv} = \begin{bmatrix} \rho u \\ \rho u^2 + p \\ \rho u \upsilon \\ \rho u w \\ (\rho e_t + p)u \end{bmatrix} \quad \mathbf{E}_{vis} = \begin{bmatrix} 0 \\ \tau_{xx} \\ \tau_{xy} \\ \tau_{xz} \\ u\tau_{xx} + \upsilon\tau_{xy} + w\tau_{xz} - q_x \end{bmatrix}$$

$$\mathbf{F}_{inv} = \begin{bmatrix} \rho \upsilon \\ \rho \upsilon u \\ \rho \upsilon^2 + p \\ \rho \upsilon w \\ (\rho e_t + p)\upsilon \end{bmatrix} \quad \mathbf{F}_{vis} = \begin{bmatrix} 0 \\ \tau_{yx} \\ \tau_{yy} \\ \tau_{yz} \\ u\tau_{yx} + \upsilon\tau_{yy} + w\tau_{yz} - q_y \end{bmatrix} \tag{A.7}$$

$$\mathbf{G}_{inv} = \begin{bmatrix} \rho w \\ \rho w u \\ \rho w \upsilon \\ \rho w^2 + p \\ (\rho e_t + p)w \end{bmatrix} \quad \mathbf{G}_{vis} = \begin{bmatrix} 0 \\ \tau_{zx} \\ \tau_{zy} \\ \tau_{zz} \\ u\tau_{zx} + \upsilon\tau_{zy} + w\tau_{zz} - q_z \end{bmatrix}$$

In CFD simulations the equations of motion are transformed from the physical space (x, y, z) to the computational space (ξ, η, ζ) by the following relation.

$$\begin{aligned} \tau &= t \\ \xi &= \xi(t, x, y, z) \\ \eta &= \eta(t, x, y, z) \\ \zeta &= \zeta(t, x, y, z) \end{aligned}$$

For the Cartesian coordinates, the chain rule of partial differentiation can be applied providing the expressions below.

$$\begin{aligned}
\frac{\partial}{\partial t} &= \frac{\partial}{\partial \tau} + \xi_t \frac{\partial}{\partial \xi} + \eta_t \frac{\partial}{\partial \eta} + \zeta_t \frac{\partial}{\partial \zeta} \\
\frac{\partial}{\partial x} &= \xi_x \frac{\partial}{\partial \xi} + \eta_x \frac{\partial}{\partial \eta} + \zeta_x \frac{\partial}{\partial \zeta} \\
\frac{\partial}{\partial y} &= \xi_y \frac{\partial}{\partial \xi} + \eta_y \frac{\partial}{\partial \eta} + \zeta_y \frac{\partial}{\partial \zeta} \\
\frac{\partial}{\partial z} &= \xi_z \frac{\partial}{\partial \xi} + \eta_z \frac{\partial}{\partial \eta} + \zeta_z \frac{\partial}{\partial \zeta}
\end{aligned} \tag{A.8}$$

The derivatives of Equation (A.6) can be replaced by the derivatives of Equation (A.8). Applying that to the LHS of Equation (A.6) leads to:

$$\begin{aligned}
LHS \quad = \quad & \frac{\partial \mathbf{C}}{\partial \tau} + \xi_t \frac{\partial \mathbf{C}}{\partial \xi} + \eta_t \frac{\partial \mathbf{C}}{\partial \eta} + \zeta_t \frac{\partial \mathbf{C}}{\partial \zeta} + \xi_x \frac{\partial \mathbf{E}_{inv}}{\partial \xi} + \\
& + \eta_x \frac{\partial \mathbf{E}_{inv}}{\partial \eta} + \zeta_x \frac{\partial \mathbf{E}_{inv}}{\partial \zeta} + \xi_y \frac{\partial \mathbf{F}_{inv}}{\partial \xi} + \eta_y \frac{\partial \mathbf{F}_{inv}}{\partial \eta} + \\
& + \zeta_y \frac{\partial \mathbf{F}_{inv}}{\partial \zeta} + \xi_z \frac{\partial \mathbf{G}_{inv}}{\partial \xi} + \eta_z \frac{\partial \mathbf{G}_{inv}}{\partial \eta} + \zeta_z \frac{\partial \mathbf{G}_{inv}}{\partial \zeta}
\end{aligned} \tag{A.9}$$

However, the above equation is not in a conservative form, and to do so it needs to be divided by the Jacobian coefficient J, followed by an addition of a combination of terms which sums up to zero. The final equation expressed in a conservative form can be written as:

$$\frac{\partial \overline{\mathbf{C}}}{\partial \tau} + \frac{\partial \overline{\mathbf{E}}_{inv}}{\partial \xi} + \frac{\partial \overline{\mathbf{F}}_{inv}}{\partial \eta} + \frac{\partial \overline{\mathbf{G}}_{inv}}{\partial \zeta} = \frac{\partial \overline{\mathbf{E}}_{vis}}{\partial \xi} + \frac{\partial \overline{\mathbf{F}}_{vis}}{\partial \eta} + \frac{\partial \overline{\mathbf{G}}_{vis}}{\partial \zeta} \tag{A.10}$$

where

$$\overline{\mathbf{C}} = \frac{\mathbf{C}}{J}$$

$$\overline{\mathbf{E}}_{inv} = \frac{1}{J}\left(\xi_t \mathbf{C} + \xi_x \mathbf{E}_{inv} + \xi_y \mathbf{F}_{inv} + \xi_z \mathbf{G}_{inv}\right)$$

$$\overline{\mathbf{F}}_{inv} = \frac{1}{J}\left(\eta_t \mathbf{C} + \eta_x \mathbf{E}_{inv} + \eta_y \mathbf{F}_{inv} + \eta_z \mathbf{G}_{inv}\right)$$

$$\overline{\mathbf{G}}_{inv} = \frac{1}{J}\left(\zeta_t \mathbf{C} + \zeta_x \mathbf{E}_{inv} + \zeta_y \mathbf{F}_{inv} + \zeta_z \mathbf{G}_{inv}\right) \tag{A.11}$$

$$\overline{\mathbf{E}}_{vis} = \frac{1}{J}\left(\xi \mathbf{E}_{vis} + \xi_y \mathbf{F}_{vis} + \xi_z \mathbf{G}_{vis}\right)$$

$$\overline{\mathbf{F}}_{vis} = \frac{1}{J}\left(\eta_x \mathbf{E}_{vis} + \eta_y \mathbf{F}_{vis} + \eta_z \mathbf{G}_{vis}\right)$$

$$\overline{\mathbf{G}}_{vis} = \frac{1}{J}\left(\zeta_x \mathbf{E}_{vis} + \zeta_y \mathbf{F}_{vis} + \zeta_z \mathbf{G}_{vis}\right)$$

Note that J represents the Jacobian of transformation which is given by [32]:

$$J = \frac{\partial(\xi, \eta, \zeta)}{\partial(x, y, z)} = \frac{1}{x_\xi\left(y_\eta z_\zeta - y_\zeta z_\eta\right) - x_\eta\left(y_\xi z_\zeta - y_\zeta z_\xi\right) + x_\zeta\left(y_\xi z_\eta - y_\eta z_\xi\right)}$$

In order to numerically solve Equation (A.10), a linearisation process is applied, where all the flux vectors are expressed in terms of the flux vector $\overline{\mathbf{C}}$. Thus for the inviscid flux vector $\overline{\mathbf{E}}$ one can write:

$$\overline{\mathbf{E}}^{n+1} = \overline{\mathbf{E}}^{n} + \frac{\partial \overline{\mathbf{E}}}{\partial \overline{\mathbf{C}}} \triangle \overline{\mathbf{C}} + \mathscr{O}(\Delta\tau)^2 \tag{A.12}$$

$\frac{\partial \overline{\mathbf{E}}}{\partial \overline{\mathbf{C}}}$ is defined as the flux Jacobian matrix. The remaining inviscid Jacobian matrices are $\frac{\partial \overline{\mathbf{F}}}{\partial \overline{\mathbf{C}}}$ and $\frac{\partial \overline{\mathbf{G}}}{\partial \overline{\mathbf{C}}}$. Correspondingly, the viscous Jacobian matrices are $\frac{\partial \overline{\mathbf{E}}_{vis}}{\partial \overline{\mathbf{C}}}$, $\frac{\partial \overline{\mathbf{F}}_{vis}}{\partial \overline{\mathbf{C}}}$ and $\frac{\partial \overline{\mathbf{G}}_{vis}}{\partial \overline{\mathbf{C}}}$. Since flux vectors $\overline{\mathbf{C}}$ and $\overline{\mathbf{E}}$ are 5×1 vectors, each one of the Jacobian matrices will be 5×5 for problems in three dimensions. The inviscid Jacobian $\frac{\partial \overline{\mathbf{E}}}{\partial \overline{\mathbf{C}}}$ can then be written in the following form:

$$\frac{\partial \overline{\mathbf{E}}}{\partial \overline{\mathbf{C}}} = \frac{\partial\left(\overline{\mathbf{E}}_1, \overline{\mathbf{E}}_2, \overline{\mathbf{E}}_3, \overline{\mathbf{E}}_4, \overline{\mathbf{E}}_5\right)}{\partial\left(\overline{\mathbf{C}}_1, \overline{\mathbf{C}}_2, \overline{\mathbf{C}}_3, \overline{\mathbf{C}}_4, \overline{\mathbf{C}}_5\right)}$$

$$= \begin{bmatrix} \frac{\partial \overline{\mathbf{E}}_1}{\partial \overline{\mathbf{C}}_1} & \cdots & \frac{\partial \overline{\mathbf{E}}_1}{\partial \overline{\mathbf{C}}_5} \\ \vdots & & \vdots \\ \frac{\partial \overline{\mathbf{E}}_5}{\partial \overline{\mathbf{C}}_1} & \cdots & \frac{\partial \overline{\mathbf{E}}_5}{\partial \overline{\mathbf{C}}_5} \end{bmatrix} \tag{A.13}$$

The next step is to determine the elements of matrix A.13. This can be accomplished by expressing the flux vectors **E**, **F** and **G** in terms of the components of vector **C** according to:

$$\mathbf{E} = \begin{bmatrix} C_2 \\ \frac{C_2^2}{C_1} + (\gamma - 1)\left[C_5 - \frac{1}{2}\left(\frac{C_2^2}{C_1} + \frac{C_3^2}{C_1} + \frac{C_4^2}{C_1}\right)\right] \\ \frac{C_2 C_3}{C_1} \\ \frac{C_2 C_4}{C_1} \\ \gamma C_5 - \frac{(\gamma-1)}{2}\left[\left(\frac{C_2^2}{C_1} + \frac{C_3^2}{C_1} + \frac{C_4^2}{C_1}\right)\right]\frac{C_2}{C_1} \end{bmatrix} \tag{A.14}$$

$$\mathbf{F} = \begin{bmatrix} C_3 \\ \frac{C_2 C_3}{C_1} \\ \frac{C_3^2}{C_1} + (\gamma - 1)\left[C_5 - \frac{1}{2}\left(\frac{C_2^2}{C_1} + \frac{C_3^2}{C_1} + \frac{C_4^2}{C_1}\right)\right] \\ \frac{C_3 C_4}{C_1} \\ \gamma C_5 - \frac{(\gamma-1)}{2}\left[\left(\frac{C_2^2}{C_1} + \frac{C_3^2}{C_1} + \frac{C_4^2}{C_1}\right)\right]\frac{C_3}{C_1} \end{bmatrix} \tag{A.15}$$

$$\mathbf{G} = \begin{bmatrix} C_4 \\ \frac{C_2 C_4}{C_1} \\ \frac{C_3 C_4}{C_1} \\ \frac{C_4^2}{C_1} + (\gamma - 1)\left[C_5 - \frac{1}{2}\left(\frac{C_2^2}{C_1} + \frac{C_3^2}{C_1} + \frac{C_4^2}{C_1}\right)\right] \\ \gamma C_5 - \frac{(\gamma-1)}{2}\left[\left(\frac{C_2^2}{C_1} + \frac{C_3^2}{C_1} + \frac{C_4^2}{C_1}\right)\right]\frac{C_4}{C_1} \end{bmatrix} \tag{A.16}$$

Note that $C_1 = \rho$, $C_2 = \rho u$, $C_3 = \rho v$, $C_4 = \rho w$ and $C_5 = \rho e_t$. For instance, the first element of matrix A.13 is determined by:

$$\frac{\partial \overline{\mathbf{E}}_1}{\partial \overline{\mathbf{C}}_1} = \frac{\partial \left\{\frac{1}{J}\left[\xi_t C_1 + \xi_x C_2 + \xi_y C_3 + \xi_z C_4\right]\right\}}{\partial \left\{\frac{C_1}{J}\right\}} = \xi_t$$

The remaining elements of the first row are:

$$\frac{\partial \overline{\mathbf{E}}_1}{\partial \overline{\mathbf{C}}_2} = \xi_x \quad , \quad \frac{\partial \overline{\mathbf{E}}_1}{\partial \overline{\mathbf{C}}_3} = \xi_y \quad , \quad \frac{\partial \overline{\mathbf{E}}_1}{\partial \overline{\mathbf{C}}_4} = \xi_z \quad , \quad \frac{\partial \overline{\mathbf{E}}_1}{\partial \overline{\mathbf{C}}_5} = 0 \tag{A.17}$$

The elements of the second, third, fourth and fifth row are calculated in a similar manner.

B

Appendix B

B.1 Grid Convergence Study

In Chapter 6, numerical results were demonstrated of a compressible turbulent flow over a sudden expansion geometry. The simulations were conducted using a high-resolution method at two Reynolds numbers ($Re = 4 \cdot 10^4$ and $Re = 10^4$) and at Mach number $M = 0.8$. A grid convergence study was undertaken at $Re = 10^4$, for that purpose, in order to justify that the medium grid is adequate enough of successfully capturing the mean flow properties. However, for the higher Re the same study was not addressed in that particular Chapter. For the sake of consistency, therefore, a grid convergence study is carried out and presented in this appendix. The same initial and boundary conditions along with the same computational parameters were used in the study of the compressible turbulent flow at $Re = 4 \cdot 10^4$. Furthermore, as far as the the grid meshes are concerned, these are exactly the same as those used for the smaller Re (in terms of the total number of points, grid increments in the three directions, grid clustering, and the total number blocks used to separate the computational domain).

B.1.1 Mean flow paths

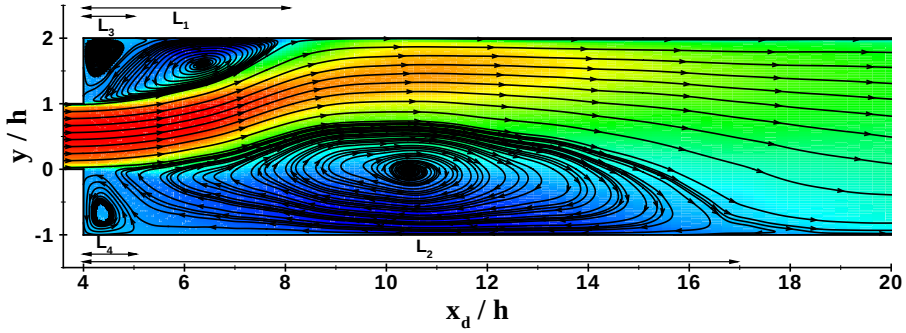

(a) Coarse Grid

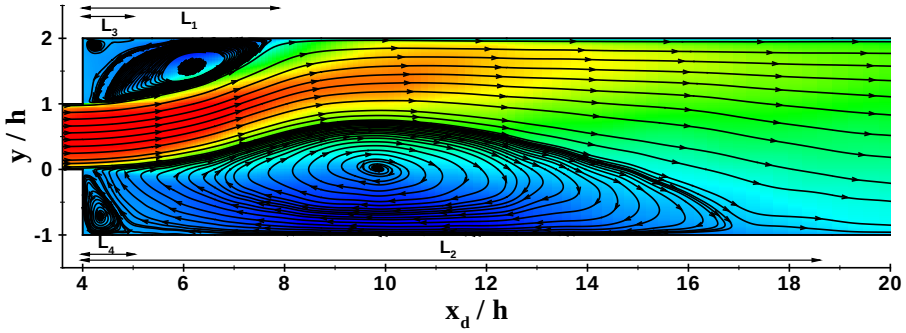

(b) Medium Grid

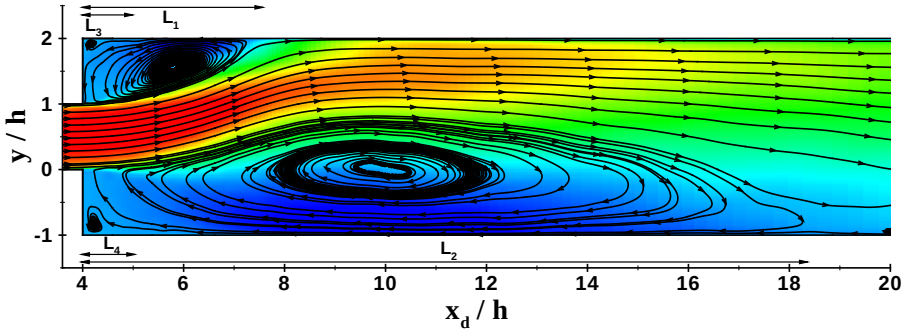

(c) Fine Grid

FIGURE B.1: Streamlines of the mean flow at the center plane of the channel ($z/h = 2.5$) for three different grid meshes at $Re = 4 \cdot 10^4$ and $M = 0.8$.

B.1.2 Time-averaged velocities

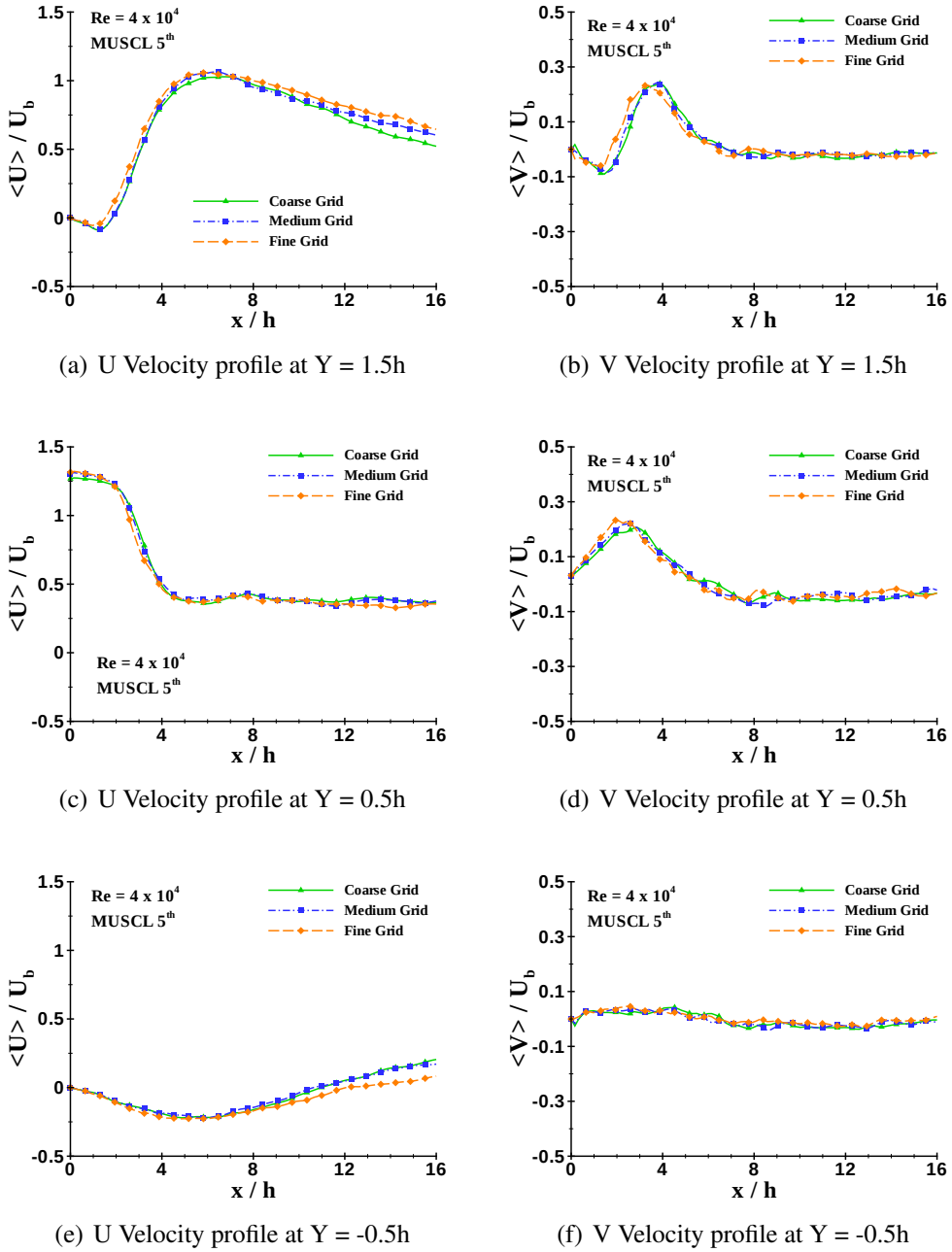

(a) U Velocity profile at Y = 1.5h

(b) V Velocity profile at Y = 1.5h

(c) U Velocity profile at Y = 0.5h

(d) V Velocity profile at Y = 0.5h

(e) U Velocity profile at Y = -0.5h

(f) V Velocity profile at Y = -0.5h

FIGURE B.2: Time-averaged streamwise and transverse velocities along the x-axis (xy-plane) at $Re = 4 \cdot 10^4$ and $M = 0.8$.

B.1.3 Time-averaged fluctuating velocities

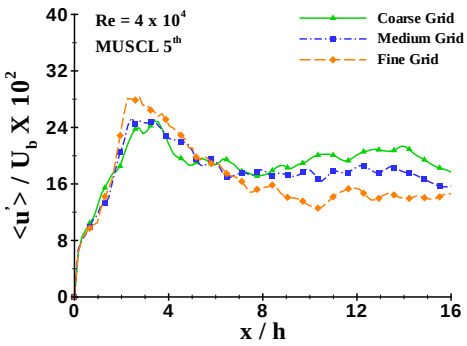

(a) U r.m.s. Velocity profile at Y = 1.5h

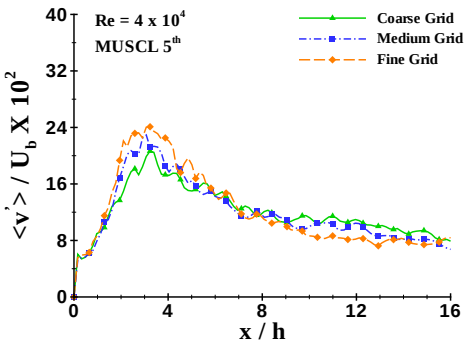

(b) V r.m.s. Velocity profile at Y = 1.5h

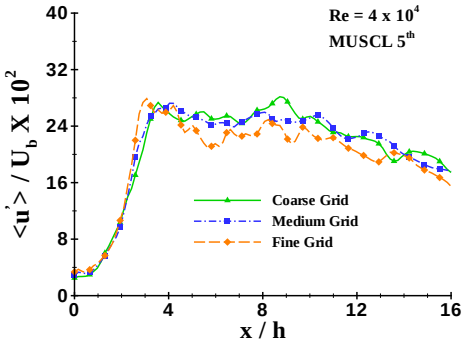

(c) U r.m.s. Velocity profile at Y = 0.5h

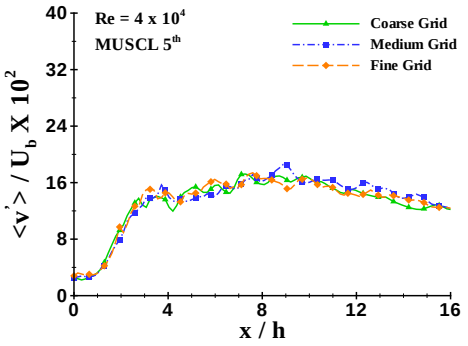

(d) V r.m.s. Velocity profile at Y = 0.5h

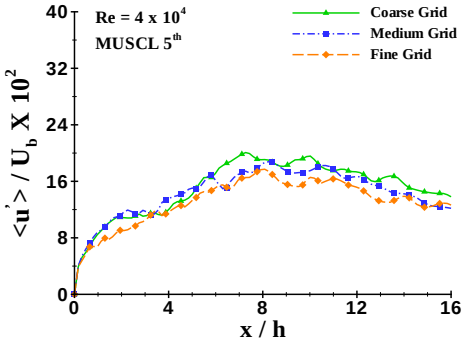

(e) U r.m.s. Velocity profile at Y = -0.5h

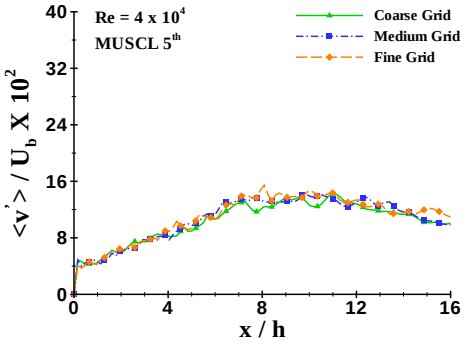

(f) V r.m.s. Velocity profile at Y = -0.5h

FIGURE B.3: Time-averaged streamwise and transverse r.m.s. velocities along the x-axis (xy-plane) at $Re = 4 \cdot 10^4$ and $M = 0.8$.

B.1.4 Mean Reynolds stresses and turbulent kinetic energy

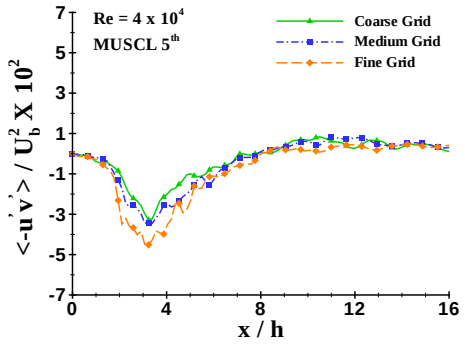

(a) Reynolds stress profile of $u'v'$ at Y = 1.5h

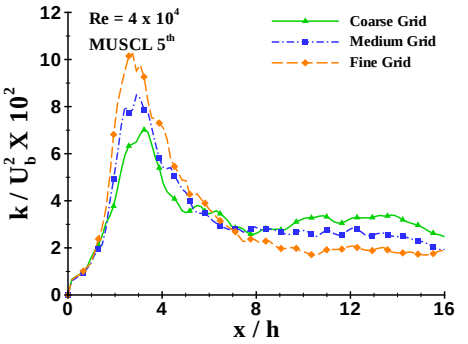

(b) Turbulent Kinetic Energy profile at Y = 1.5h

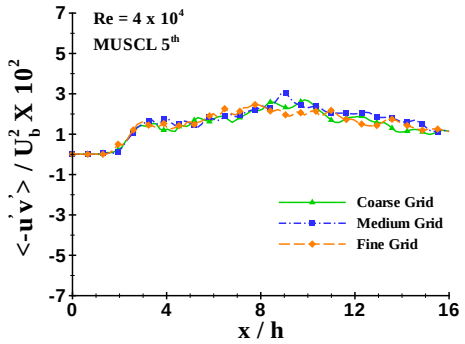

(c) Reynolds stress profile of $u'v'$ at Y = 0.5h

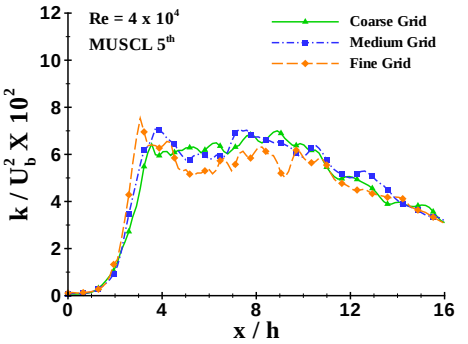

(d) Turbulent Kinetic Energy profile at Y = 0.5h

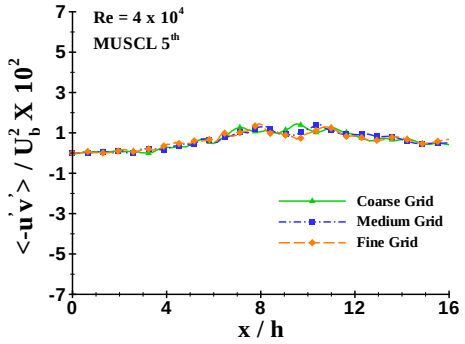

(e) Reynolds stress profile of $u'v'$ at Y = -0.5h

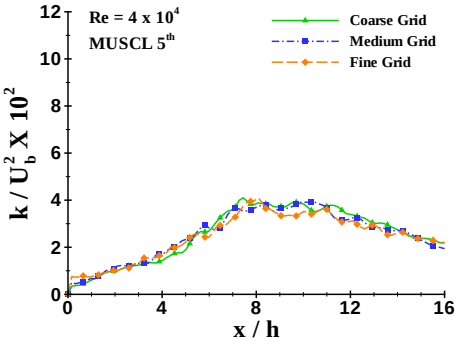

(f) Turbulent Kinetic Energy profile at Y = -0.5h

FIGURE B.4: Time-averaged Reynolds stresses and turbulent kinetic energy along the x-axis (xy-plane) at $Re = 4 \cdot 10^4$ and $M = 0.8$.

B.1.5 Skewness and kurtosis

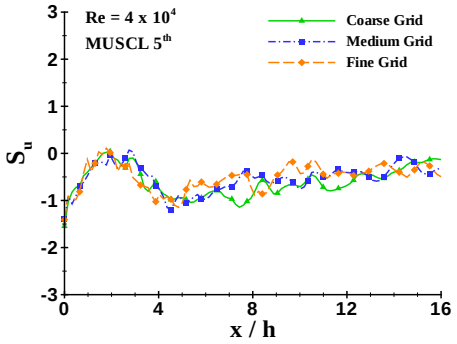

(a) Skewness of U-Velocity at Y = 1.5h

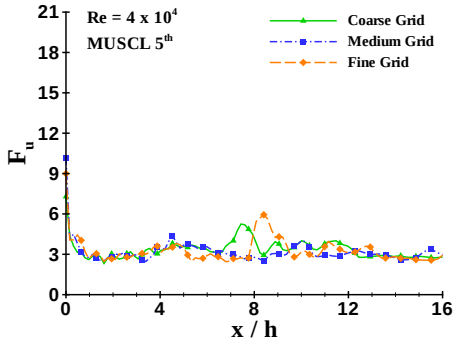

(b) Flatness of U-Velocity at Y = 1.5h

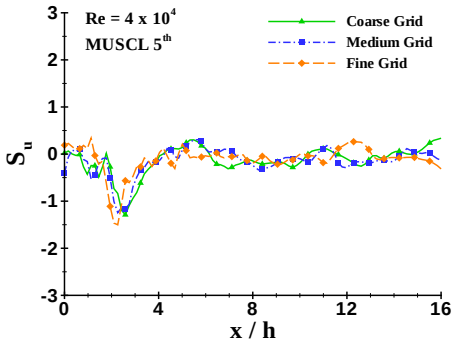

(c) Skewness of U-Velocity at Y = 0.5h

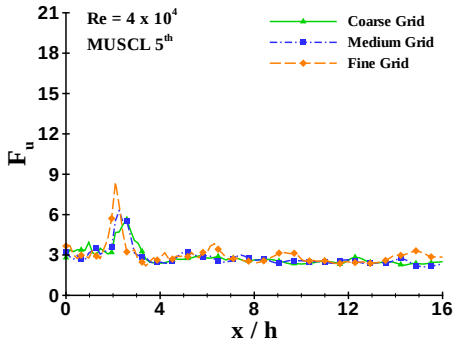

(d) Flatness of U-Velocity at Y = 0.5h

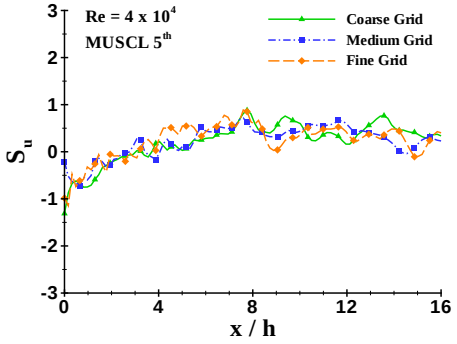

(e) Skewness of U-Velocity at Y = -0.5h

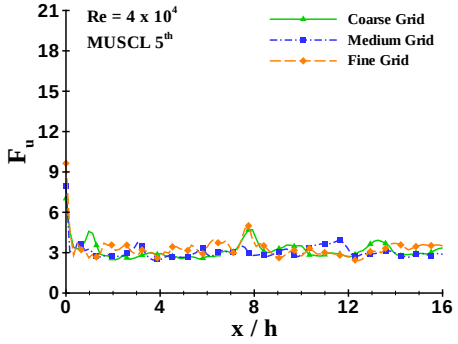

(f) Flatness of U-Velocity at Y = -0.5h

FIGURE B.5: Time-averaged Skewness and Flatness of the streamwise velocity U along the x-axis (xy-plane) at $Re = 4 \cdot 10^4$ and $M = 0.8$.

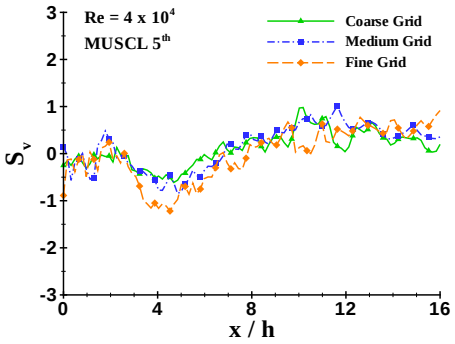

(a) Skewness of V-Velocity at Y = 1.5h

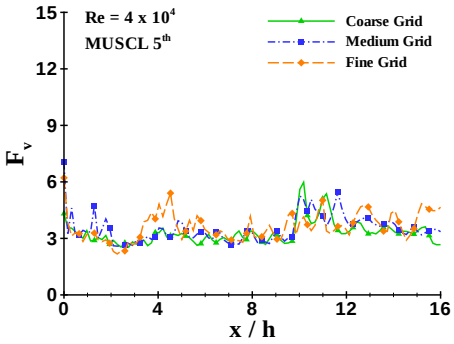

(b) Flatness of V-Velocity at Y = 1.5h

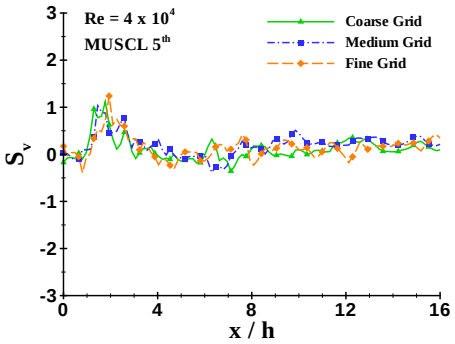

(c) Skewness of V-Velocity at Y = 0.5h

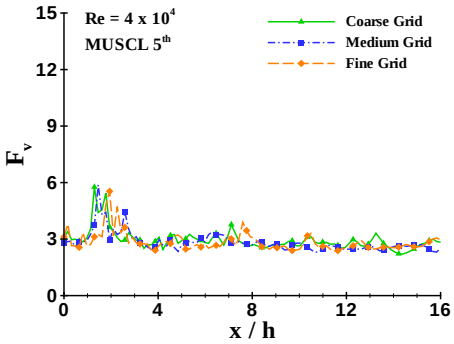

(d) Flatness of V-Velocity at Y = 0.5h

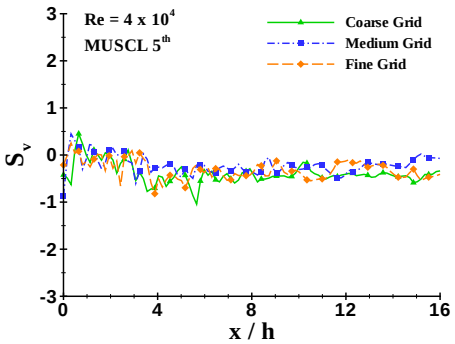

(e) Skewness of V-Velocity at Y = -0.5h

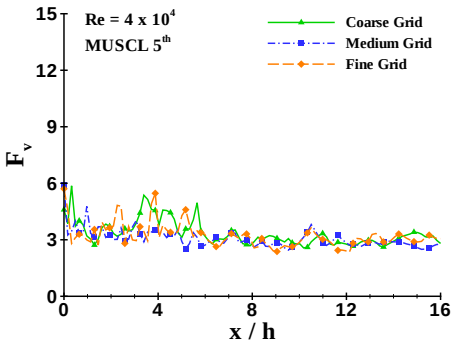

(f) Flatness of V-Velocity at Y = -0.5h

FIGURE B.6: Time-averaged Skewness and Flatness of the wall-normal velocity V along the x-axis (xy-plane) at $Re = 4 \cdot 10^4$ and $M = 0.8$.

C

Appendix D

C.1 Non-Dimensionalisation

The non-dimensional counterpart of a flow variable denoted by the superscript $(*)$ is used with aim at defining the non-dimensional Navier-Stokes equations which are necessary in order to compute flow parameters. The first step is to define reference variables l, U and ρ for the length, velocity and density, respectively. The resulting dimensionless variables in the Navier-Stokes equations (assuming an incompressible flow)

$$\frac{\partial u_j}{\partial x_j} = 0$$
$$\frac{\partial u_i}{\partial t} + \frac{\partial u_i u_j}{\partial x_j} = -\frac{1}{\rho}\frac{\partial p}{\partial x_i} + \nu \frac{\partial^2 u_i}{\partial x_j^2} \tag{C.1}$$

can be written as follows:

$$x_i^* = \frac{x_i}{l} \quad , \quad u_i^* = \frac{u_i}{U}$$
$$t^* = \frac{tU}{l} \quad , \quad p^* = \frac{p}{\rho U^2} \quad , \quad e^* = \frac{e}{U^2} \tag{C.2}$$

By replacing the variables u_i, t and p in Equation (C.1) with their dimensionless counterparts found in Equation (C.2), the following expression is obtained:

$$\frac{\partial u_j^*}{\partial x_j^*} = 0$$
$$\frac{\partial u_i^*}{\partial t^*} + \frac{\partial u_i^* u_j^*}{\partial x_j^*} = -\frac{\partial p^*}{\partial x_i^*} + \frac{\nu}{Ul}\frac{\partial^2 u_i^*}{\partial x_j^* \partial x_j^*} \tag{C.3}$$

The continuity equation in the above equation remains constant, however this is not the case for the momentum equation where on its right hand side a dimensionless parameter is formed. This parameter is known as the Reynolds number (Re) and is given by:

$$Re = \frac{Ul}{\nu}$$

The momentum equation can then be written as:

$$\frac{\partial u_i^*}{\partial t^*} + \frac{\partial u_i^* u_j^*}{\partial x_j^*} = -\frac{\partial p^*}{\partial x_i^*} + \frac{1}{Re}\frac{\partial^2 u_i^*}{\partial x_j^* \partial x_j^*} \tag{C.4}$$

For the sake of simplicity, the superscript $(*)$ was omitted throughout the thesis presentation.